Title
Microstrip Antennas with Polarization Diversity across a Wide Frequency Range and Phased Array Antennas for Radar and Satellite Communications

Author
Ho, Kevin Ming-Jiang

Publication Date
2014

UNIVERSITY OF CALIFORNIA, SAN DIEGO

Microstrip Antennas with Polarization Diversity across a Wide Frequency Range and Phased Array Antennas for Radar and Satellite Communications

A dissertation submitted in partial satisfaction of the
requirements for the degree
Doctor of Philosophy

in

Electrical Engineering (Electronic Circuits and Systems)

by

Kevin Ming-Jiang Ho

Committee in charge:

Professor Gabriel M. Rebeiz, Chair
Professor Peter M. Asbeck
Professor Gert Cauwenberghs
Professor William S. Hodgkiss
Professor Daniel F. Sievenpiper

2015

The Dissertation of Kevin Ming-Jiang Ho is approved, and it is acceptable in quality and form for publication on microfilm and electronically:

Chair

University of California, San Diego
2015

DEDICATION

To my mother Poh-Cheng Seah, and my wife Yee-Shian Lee.

TABLE OF CONTENTS

Signature Page iii

Dedication iv

Table of Contents v

List of Abbreviations x

List of Figures xiii

List of Tables xx

Acknowledgments xxi

Vita xxiv

Abstract of the Dissertation xxvi

Chapter 1 1

Introduction 1

1.1 Growing Demand for Mobile Connectivity 1

1.2 RF Front-End Miniaturization 2

1.2.1 Tunable and Reconfigurable Antennas for Wireless Communications 2

1.2.2 Low-Cost PCB Assembly 2

1.2.3 Shared Aperture Arrays 3

1.2 Scope of thesis 4

Chapter 2 6

L-Band Microstrip Antenna with Frequency Agility and Polarization Diversity 6

2.1 Overview 6

2.1.1 Tunable and Reconfigurable Antenna Elements 6

2.1.2 Antenna Re-Configurability with RF MEMS Switches 7

2.2 Omron RF MEMS Switches 7

2.2.1 Switch Details and Reliability Measurements 7

2.2.2 MEMS SPDT Modeling 10

2.3 Microstrip Antenna with Frequency Agility 12

2.3.1 Antenna Element with Dual Polarized Independent Tuning 12
2.3.2 Surface-Mount Series Capacitance Devices 14
2.3.3 Antenna Q and Bandwidth Approximation 16
2.4 Microstrip Antenna with Frequency Agility and Full Polarization Diversity 18
2.4.1 Re-configurable Feed Network with MEMS Switches 18
2.4.2 Alternate Reconfigurable Network with Frequency Resonance Offset 22
2.4.3 Polarization Diversity from Antenna Perturbation 23
2.4.4 Probe-fed Microstrip Antenna Cross Polarization Analysis 26
2.5 Hardware and Measurements 30
2.5.1 2 GHz Antenna Element 30
2.5.2 2 GHz Antenna with Full Polarization Diversity 32
2.5.3 Microstrip Antenna with Wide Frequency Span 35
2.5.4 Microstrip Antenna with Full Polarization Diversity across 1.15-1.55 GHz 37
2.5.5 Microstrip Antenna with Full Polarization Diversity and Frequency Agility with Single MEMS Switch 42
2.6 Conclusion 46
Chapter 3 47
Compact X-Band FMCW Phased Array Receiver with Packaged CMOS Phased Array RFIC chips 47
3.1 Overview 47
3.1.1 Compact T/R Modules and Integrated Phased Arrays 47
3.1.2 Chapter Overview 51
3.2 Phased-Array Antenna 52
3.2.1 Array Specifications and Overall Architecture 52
3.2.2 Antenna Element and Linear Array Design 53
3.3 RFIC Phased-Array Receiver Chips 56
3.4 RFIC-PCB interface 59
3.4.1 Wire-bond and QFN-packaged RFICs Assembly on PCB 59
3.4.2 Inter-channel Isolation 61

3.4.3 Input impedance 64
3.5 Commercial-Grade PCB for Antenna Arrays 65
3.5.1 Commercial Grade Laminates 65
3.5.2 Scan Blindness Prediction and Avoidance 67
3.5.3 Array Radiation Efficiency 75
3.5.4 Surface Roughness on Apparent ε_r Deviation 77
3.5.5 CPW Isolation and Losses 79
3.6 Hardware and Measurements 82
3.6.1 PCB Interface for RFIC phased arrays 82
3.6.2 Antenna Element and Linear Arrays 84
3.6.3 Phased Array Receiver 88
3.7 Conclusion 92
Chapter 4 93
Circularly Polarized Microstrip Antenna Array Performance Studies 93
4.1 Overview 93
4.1.1 Motivation 93
4.1.2 Scope 96
4.2 Microstrip Antenna Element and Array Setup 98
4.2.1 Microstrip Antenna Element Pattern 98
4.2.2 CP Array Setup 100
4.3 CP Arrays with LP Microstrip Antenna Elements 102
4.3.1 CP Broadside Array Xpol from LP Elements 102
4.3.2 CP Scanned Array Xpol from LP Elements 104
4.4 CP Arrays with CP Microstrip Antenna Elements 107
4.4.1 CP Broadside Array Xpol from CP Elements 107
4.4.2 CP Scanned Array Xpol from CP Elements 111
4.5 CP Arrays with Microstrip Antenna Elements 117
4.5.1 Summary of Key Observations 117
4.5.2 Array Implementation/Architecture for Large CP Arrays 118
4.6 Conclusion 119

Chapter 5 120

Dual-Band Components for Ku/Ka-Band Shared Aperture Antenna Arrays 120

5.1 Scope 120

5.2 Shared Apertures Array Implementation 121

5.2.1 Implementation Approaches 121

5.2.2 Multiple Arrays vs Wideband Arrays 122

5.2.3 Wideband versus Dual-Band Stacked Microstrip Antenna 123

5.2.4 Antenna Feed vs Board Routing Complexity 124

5.3 20/30 GHz Dual-band CP Antenna Element.. 125

5.3.1 20 GHz CP Antenna Parametric Study 125

5.3.2 20/30 GHz CP Antenna: Design 128

5.3.3 20/30 GHz CP Antenna: EM Simulations 130

5.4 Dual-Band 3-dB Couplers 132

5.4.1 General Classification 133

5.4.2 TLIN with LC implementation 135

5.4.3 Dual-band Couplers with Low-pass/Hi-pass TLINs.............................. 136

5.4.4 Extended Single-stage / Multi-stage Couplers Implementation............. 144

5.5 Conclusion.. 149

Chapter 6 150

Conclusion.. 150

6.1 Summary of Work 150

6.2 Future Work 151

Appendix A 152

Apparent Deviation of Microwave Materials Relative Permittivity 152

A.1 Introduction 152

A.2 3 Factors for Apparent ε_r deviation 153

A.2.1 X-band Stripline Test Resonator Standard.. 153

A.2.2 Dielectric Uniaxial Anisotropy 155

A.2.3 Surface Roughness 156

A.3 Fitted Design Parameters for RO4350 microstrip TLINs 158

A.4 Conclusion 161
Bibliography 162

LIST OF ABBREVIATIONS

AR	Axial-ratio
AUT	Antenna under test
BW	Bandwidth
C-band	Radar frequency band, 4-8 GHz
CAD	Computer-aided design
CCW	Counter-clockwise
CLRH	Composite left-right handed
CMOS	Complementary metal–oxide–semiconductor
COB	Chip on board
COTS	Commercial off-the-shelf
CP	Circular polarization / circularly polarized
Cpol	Co-polarized / Co-polarization
CPW	Coplanar waveguide
CTE	Coefficient of thermal expansion
CW	Clockwise
DBS	Direct broadcast satellite
DUT	Device under test
ED	Electro-deposited
EMC	Electromagnetic compatibility
EMI	Electromagnetic interference
ENIG	Electroless nickel, immersion gold
ESD	Electro-state discharge
FMCW	Frequency modulated continuous-wave
FFOV	Full field of view
FOV	Field of view
FR-4	Flame-retardant laminate, compliant to UL94V-0 standard
FSR	Full sheet resonance
GaAs	Gallium Arsenide

GPS	Global positioning system
GSG	Ground-signal-ground
HP	Linear-horizontal polarized / polarization
HiP	High-pass
HPA	High power amplifier
IP_3	3rd order intercept point
Ka-band	Radar frequency band, 26.5-40 GHz
K-band	Radar frequency band, 18-26.5 GHz
Ku-band	Radar frequency band, 12.4-18 GHz
L-band	Radar frequency band, 2-4 GHz
LCP	Liquid crystal polymer
LGA	Land grid array
LH	Left-handed
LHCP	Left-handed CP
LNA	Low noise amplifier
LoP	Low-pass
LP	Linear polarization / linearly polarized
LTCC	Low-temperature co-fired ceramic
MEMS	Micro-electrical-mechanical systems
MOM	Method-of-moments
MUT	Material under test
MMIC	Monolithic microwave integrated circuits
NF	Noise figure
P_{1dB}	1-dB compression point
PA	Power amplifier
PCB	Printed circuit boards
PCBA	PCB assembly
PIN	P-type, intrinsic, and n-type semiconductor interface
QFN	Quad-flat no lead (package)
RFIC	RF integrated circuits

RH	Right-handed
RHCP	Right-handed CP
Rx	Receive / Receiver
S-band	Radar frequency band, 2-4 GHz
SatComms	Satellite communications
SiO_2	Silicon oxide
SMA	Sub-miniature type-A
SMT	Surface-mount technology
SMTA	SMT-assembly
SPDT	Single-pole double-throw
TLIN	Transmission line
TSV	Through-silicon via
T/R	Transmit-receive
TRM	Transmit-receive module
Tx	Transmit / Transmitter
VP	Linear-vertical polarized / polarization
X-band	Radar frequency band, 8-12.4 GHz
Xpol	Cross-polarized / Cross-polarization

LIST OF FIGURES

Figure 2.1: Omron RF MEMS switches; (a) single switch device, (b) SPDT from 2 devices in (c) LGA plastic package. 8

Figure 2.2: Reliability measurements for Omron MEMS switches; (a) cold switching, (b) hot switching and (c) power handling. 9

Figure 2.3: Omron SPDT's (a) fitted small signal model, (b) modeled (dashed) and measured (solid) S-parameter response, and (c) 4 states of operation. 10

Figure 2.4: Simplified Omron SPDT model for direct CAD modeling; (a) down-state through, (b) up-state isolation, and (c) measured and modeled response. 11

Figure 2.5: (a) Differential-fed microstrip antenna with independent dual-polarized tuning, and (b) symmetry planes definition for VP excitation (left) and HP excitation (right). 13

Figure 2.6: (a) Simulated vs measured resonant frequency and capacitance loading for various bias voltages, and (b) implementation of tuning network using back-to-back diodes. 14

Figure 2.7: (a) Diode mounted on PCB and (b) model with transmission line stubs to account for parasitic series inductance (Zpkg) and shunt capacitance (Zpad) effects. 15

Figure 2.8: (a) Radiation efficiency simulations in HFSS, for cases of; antenna with matched feed at all frequencies, antenna loaded with MEMS tunable capacitors, and antenna loaded with tuning diodes, and (b) unloaded Q values for MEMS tunable capacitors and varactor diodes. 17

Figure 2.9: Reconfigurable feed network for (a) 3 polarization stages, and (b) 4 polarization stages. 21

Figure 2.10: (a) Alternate reconfigurable feed network for 4 polarization stages with 1 device, and (b) reflection phase and match at the antenna ports 22

Figure 2.11: (a) Antenna element with polarization diversity and frequency tuning, (b) capacitance tuning for high axial ratio in CP modes, and 2 possible configurations for (c) LHCP and (d) RHCP modes. 24

Figure 2.12: Normalized Xpol (in dB) for FOV of θ < (a) 30°, (b) 45° and (c) 60°, and (d) gain degradation (in dB), for differentially fed LP microstrip antenna with amplitude and phase offset. 27

Figure 2.13: Normalized Xpol (in dB) at (a) broadside, and FOV of θ < (b) 30° and (c) 45°, and (d) gain degradation (in dB), for quadrature fed CP microstrip antenna with amplitude and phase offset. 27

Figure 2.14: HFSS simulated normalized patterns for circularly polarized antenna with; (a) ideal probe feed, and (b) feed network in HFSS 29

Figure 2.15: Multi-layered PCB stack-up with commercial-grade laminates. 30

Figure 2.16: Hardware realization of 2 GHz microstrip antenna; (a) front view, back view of (b) reference antenna, and (c) antenna with feed network for full polarization diversity (MEMS devices shown in insert). 31

Figure 2.17: Measured return loss responses for 2 GHz antenna with full polarization diversity (Figure 2.16c). 33

Figure 2.18: Measured (a) gain, (b) efficiency, and normalized patterns for (c) HP, (d) VP, (e) LHCP and (f) RHCP modes, for 2 GHz antenna with full polarization diversity (Figure 2.16c). 34

Figure 2.19: Hardware realization of L-band microstrip antenna with frequency agility; (a) front view, back view of (b) reference antenna, and (c) antenna with feed network for full polarization diversity. 35

Figure 2.20: Measured return loss responses for reference antenna at various V_{bias} (LP, Figure 2.19b). 36

Figure 2.21: Measured gain and directivity for reference antenna versus (a) bias voltage and (b) frequency (LP, Figure 2.19b). 37

Figure 2.22: Measured return loss for the four polarization states with various bias conditions. 38

Figure 2.23: Measured antenna patterns of all four polarization modes for various bias cases: (a) 2 V bias, (b) 4 V bias, (c) 8 V bias and (d) 15 V bias. First column for HP modes, second column for VP modes, third column for LHCP, and last column for RHCP. 40

Figure 2.24: Measured and simulated axial-ratio for circular polarization modes. 41

Figure 2.25: Measured vs simulated directivity, gain, and efficiency for all cases of biasing and polarization modes. 42

Figure 2.26: Setup for conceptual verification of CP excitation (measurements in Figure 2.27). 43

Figure 2.27: Measured CP normalized patters, for cases of (a) 1.68 V bias, (b) 2.48 V bias, (c) 4.5 V bias, and (d) 9.76 V bias. 45

Figure 3.1: T/R modules (a) on LTCC for X-band application, and (b) FR-4 PCBs for L/C band [37]. 48

Figure 3.2: Compact X-band FMCW radar; (a) front view and (b) back view of antenna array and feed network, and (c) complete radar module [38]. 48

Figure 3.3: Phased array on PCB with end-fired slot antennas [41]. 49

Figure 3.4: Planar Ka-band phased array on LTCC; (a) cavity-backed antenna elements and (b) back-view with RF circuitry [43]. 49

Figure 3.5: Integrated 3D array on LCP for K-band [44]. 50

Figure 3.6: Phased array with RFIC on thin-film dielectric on silicon at wafer-level integration [45]. 50

Figure 3.7: Overall architecture of RFIC receive phased array antenna. 53

Figure 3.8: Theoretical calculations and IE3D simulations for (a) radiation efficiency and (b) fractional bandwidth vs substrate height, and IE3D simulations for (c) directivity, gain and (d) radiation and antenna efficiency for microstrip antenna on 0.032” and 0.06” thick RO4003 laminate. 54

Figure 3.9: 8-channel linear array with $0.53\lambda_0$ element spacing (blue), microstrip antenna H-plane (green), and microstrip array (red) normalized patterns; (a) 45° and (b) 60° scan with uniform distribution. 55

Figure 3.10: Feed network for 4-element linear array. 55

Figure 3.11: IBM8RF stack-up. 57

Figure 3.12: Block diagram (top) and microphotograph (bottom) of 4-channel phased-array receiver chip [47]. 58

Figure 3.13: (a) RFIC on PCB, and current flow from PCB to RFIC through wire-bond interface for (b) signal, (c) ground return for microstrip launch, and (d) ground return for CPW launch. 59

Figure 3.14: (a) QFN packaged RFIC on PCB, and current flow from PCB to RFIC through QFN package interface for (b) signal, (c) ground return for microstrip launch, and (d) ground return for CPW launch. 60

Figure 3.15: Isolation for PCB-RFIC interface with (a) wirebond, (b) plastic-moulded QFN package, and (c) air-cavity QFN package; for CPW-launch (left) and microstrip launch (right). 63

Figure 3.16: Simulated input impedance of RFIC-PCB interface with wire-bond and (plastic moulded and air-cavity) QFN, with matched termination at RFIC port. 64

Figure 3.17: Fitted RLC model for CPW-launch PCB-RFIC interface with (a) wirebond, (b) plastic-moulded, and (c) air-cavity QFN packages. 65

Figure 3.18: (a) Normalized surface waves propagation constant (β_{sw}/k_0) for various dielectric constant values, and (b) potential scan blindness and normalized surface waves propagation constant for $\varepsilon_r = 3.55$. 69

Figure 3.19: (a) Cut-off substrate thickness for higher order modes (red) and normalized surface waves propagation constant (β_{sw}/k_0) for TM_0 mode (blue) and (b) TE_1 mode, for various substrate ε_r and thickness. 70

Figure 3.20: Maximum conservative element spacing (a/λ_0) for maximum scan angle of (a) 15°, (b) 30°, (c) 45° and (d) 60°. 71

Figure 3.21: Return loss simulations with HFSS master-slave boundary conditions of an infinite array with element spacing of $0.53\ \lambda_0$ in the scan plane, for (a) both E and

H-planes scan at 9 GHz, H-plane scan (b) across frequency and (c) Smith Chart response. 74

Figure 3.22: Return loss simulations with HFSS master-slave boundary conditions of an infinite array of probe-fed (red) and slot-coupled (blue) element with element spacing of 0.53 λ_0 in the scan plane, for E-plane scan (left) and H-plane scan (right). 75

Figure 3.23: Computed radiation efficiency for various substrates at 9 GHz. 77

Figure 3.24: Apparent substrate height and ε_r arising from 2.8 µm of Cu surface roughness, for 0.0133” thick RO4350 laminate with 0.5 oz ED Cu cladding, evaluated at 9 GHz. 79

Figure 3.25: (a) Cross-section of CPW, showing nickel-gold plating on the sides of the signal-ground gap, and (b) simulated and measured line losses. 81

Figure 3.26: Relative permeability (μ_r) of nickel at microwave frequencies [71]. 81

Figure 3.27: (a) QFN-packaged CMOS RFIC - inside view, and (b) assembled on

PCB. 82

Figure 3.28: (a) Test structure for QFN on PCB, and (b) isolation of CPW feed network. 83

Figure 3.29: Multi-layered PCB stack-up for 4x8 active antenna array. 84

Figure 3.30: (a) Cross-section and dimensions, (b) hardware realization and (c) pattern measurements for slot-fed microstrip antenna element. 85

Figure 3.31: (a) Hardware realization, (b) return loss and (c) patterns measurements for 4-element linear array. 86

Figure 3.32: Linear array feed network (a) hardware verification and (b) measured insertion loss and relative phase. 87

Figure 3.33: 4x8 antenna array; (a) front-side, and (b) back-side microstrip feed network and QFN components. 89

Figure 3.34: Active receiver array (a) normalized pattern, and (b) azimuth plane scanned patterns at 9 GHz, and (c) gain across frequency. 91

Figure 4.1: (a) LP (top) and LHCP (bottom) microstrip antenna elements; sequential rotation and quadrature phase offset for LHCP operation with (b) LP and (c) LHCP antenna elements; LCHP antenna arrays with (d) LCHP elements in uniform array, (e) LP elements and (f) LHCP elements with sequential rotation and quadrature. 94

Figure 4.2: 2x2 unit cell for (a) square and (b) equilateral layout, and (c) square and (d) equilateral 2^Nx2^N array. 95

Figure 4.3: 20 GHz circular polarized microstrip antenna on 0.0307” thick RO4725 laminate; (a) layout, (b) return loss, (c) normalized cross-polarization, and (d) Smith chart response. 96

Figure 4.4: Elementary LP microstrip antenna element with E-plane aligned along (a) X-axis and (b) Y-axis. 99

Figure 4.5: Xpol of CP microstrip antenna arising from quadrature feed amplitude imbalance, with Δ_{Cir} = (a) 0, (b) 0.1, (c) 0.315, and (d) 0.5. 100

Figure 4.6: Normalized *broadside beam* patterns for LHCP *square array* with *LP* EP; Cpol (top row) and Xpol (bottom row) for (a) 2x2 (left column), 4x4 (middle column) and 8x8 arrays (right column), and Xpol for (b) 16x16 and (c) 32x32 arrays. 102

Figure 4.7: Normalized *broadside beam* patterns for LHCP *equilateral array* with *LP* EP; Cpol (top row) and Xpol (bottom row) for (a) 2x2 (left column), 4x4 (middle column) and 8x8 arrays (right column), and Xpol for (b) 16x16 and (c) 32x32 arrays. 103

Figure 4.8: Normalized *30° scan* patterns for LHCP *square array* with *LP* EP; Cpol (top row) and Xpol (bottom row) for 8x8 (left column), 16x16 (mid column) and 32x32 arrays (right column); with beam scan in (a) principle plane (ϕ = 0°) or in (b) diagonal plane (ϕ = 45°). 105

Figure 4.9: Normalized *30° scan* patterns for LHCP *staggered array* with *LP EP*; Cpol (top row) and Xpol (bottom row) for 8x8 (left column), 16x16 (mid column) and 32x32 arrays (right column); with beam scan in (a) principle Z-X plane (ϕ = 0°), (b) diagonal plane (ϕ = 45°); and Xpol for beam scan in (c) principle Y-Z plane.. 106

Figure 4.10: Location of Xpol spikes in elevation plane, for 30° beam scanned 8x8 LCHP array of *LP EP*; main beam in diagonal plane (ϕ = 45°) for square array (red), and in principle Z-X plane for equilateral array (blue). 107

Figure 4.11: Normalized *broadside beam* patterns for LHCP *square array* with *LHCP* EP; Cpol (top row) and Xpol (bottom row) for (a) 2x2 (left column), 4x4 (middle column) and 8x8 arrays (right column), and Xpol for (b) 16x16 array. 108

Figure 4.12: Normalized *broadside beam* patterns for LHCP *equilateral array* with *LHCP* EP; Cpol (top row) and Xpol (bottom row) for (a) 2x2 (left column), 4x4 (middle column) and 8x8 arrays (right column), and Xpol for (b) 16x16 array. 109

Figure 4.13: Normalized Xpol for *broadside beam* LHCP *square array* for 8x8 (left), 16x16 (middle) and 32x32 arrays (right) comprising of CP EP with Xpol of (a) -20 dB, (b) -10 dB and (c) -6 dB. 110

Figure 4.14: Normalized Xpol for *broadside beam* LHCP *equilateral array* for 8x8 (left), 16x16 (middle) and 32x32 arrays (right) comprising of CP EP with Xpol of (a) -20 dB, (b) -10 dB and (c) -6 dB. 111

Figure 4.15: Normalized *30° scan* patterns for LHCP *square array* with *LHCP* EP; Cpol (top row) and Xpol (bottom row) for 8x8 (left column), 16x16 (mid column) and 32x32 arrays (right column); with beam scan in (a) principle plane (ϕ = 0°) or in (b) diagonal plane (ϕ = 45°). 112

Figure 4.16: Normalized *30° scan* patterns for LHCP *equilateral array* with *LHCP* EP; Cpol (top row) and Xpol (bottom row) for 8x8 (left column), 16x16 (mid column) and 32x32 arrays (right column); with beam scan in (a) principle Z-X plane (ϕ = 0°) , (b) diagonal plane (ϕ = 45°); and Xpol for beam scan in (c) principle Y-Z. .. 113

Figure 4.17: Normalized Xpol for *30° bean scan in diagonal plane (ϕ=45°)* LHCP *square array* for 8x8 (left), 16x16 (middle) and 32x32 arrays (right) comprising of CP elements with Xpol of (a) -20 dB, (b) -10 dB and (c) -6 dB. 114

Figure 4.18: Normalized Xpol for *30° bean scan in Z-X plane (ϕ=0°)* LHCP *equilateral array* for 8x8 (left), 16x16 (middle) and 32x32 arrays (right) comprising of CP elements with Xpol of (a) -20 dB, (b) -10 dB and (c) -6 dB. 115

Figure 4.19: Normalized Xpol “spike” levels with varying element spacing and EP Xpol levels, for 30° beam scanned 8x8 LCHP array with LHCP elements, in (a) ϕ = 45° plane for square layout, and (b) ϕ = 0° plane for staggered layout, and (c) location of the Xpol spikes in the elevation plane. 116

Figure 5.1: Shared aperture implementation with (a) different antenna arrays for different frequencies and (b) wideband current-sheet array.................................. 122

Figure 5.2: Cross-section for (a) wideband and (b) dual-band layered microstrip antennas. 124

Figure 5.3: Feed network routing complexity for dual/multi-band array using antenna elements with (a) single feed point and (b) multiple feed points for multiple frequencies, and (c) multiple routings for separate antennas for different bands. .. 125

Figure 5.4: Layout of CP square microstrip antenna element. 126

Figure 5.5: Variation of input impedance with varying substrate thickness (*h*) for CP square microstrip antenna (*w* = *l*). 126

Figure 5.6: Variation of input impedance with varying feed offset (*s*) for CP square microstrip antenna (*w* = *l*) on 0.012” thick substrate. 126

Figure 5.7: Variation of input impedance with width/length ratio (*w*/*l*) CP microstrip antenna on 0.012” thick substrate. 127

Figure 5.8: Matched 20 GHz CP microstrip antenna on RO4003 substrate with various substrate thicknesses. 127

Figure 5.9: Dual-band microstrip antenna element (a) picture, (b) cross-section stack-up, and layout details for (c) top and (d) bottom metal layers. 129

Figure 5.10: Calculated (red trace, for LP) and IE3D simulated radiation efficiency for microstrip antennas on RO4003 at (a) 20 GHz and (b) 30 GHz. 130

Figure 5.11: Simulated reflection coefficient for dual-band antenna element; (a) in dB, and on Smith chart for case (b) with and (c) without via fencing. 131

Figure 5.12: Simulated AR for LHCP (solid line: w/o via-fencing, dashed line: with via fencing). 132

Figure 5.13: (a) Generic representation for couplers, (b) TLIN replacements with (LoP and HiP) slow-wave structures, and implementation with (c) loaded TLINs (π/T LoP network), or (d) cascade of LoP and HiP T network unit cells. 133

Figure 5.14: Single stage (a) branch-line, (b) rat-race couplers, and (c) lossless T-junction implementations for 3-dB splitting. 134

Figure 5.15: LoP (left) and HiP (right) TLIN implementation with LC networks; (a) basic L-section, (b) cascaded L-sections for wider bandwidth, (c) T- and (d) π-network implementation. 136

Figure 5.16: Unit-cell of (a) LoP and (b) HiP Tee-networks, and (c) TLIN comprising of 3-stage LoP/HiP ($N = 3$). 137

Figure 5.17: Simulated branch-line coupler response with 6-stage LoP/HiP TLINs. ... 139

Figure 5.18: Simulated extended T-junction splitter response (0/90°) with 6-stage LoP/HiP TLINs. 140

Figure 5.19: Simulated rat-race coupler response with 6-stage LoP/HiP TLINs. 141

Figure 5.20: Simulated extended T-junction splitter response (0/180°) with 6-stage LoP/HiP TLINs. 142

Figure 5.21: Quadrature-phased couplers with ideal TLINs; branch-line (left) and extended T-junction splitter (0/90°) (right). 143

Figure 5.22: Differential-phased couplers with ideal TLINs; rat-race (left), modified rat-race with $3\lambda/4$ TLIN replaced with $-\lambda/4$ (mid) and extended T-junction splitter (0/180°) (right). 144

Figure 5.23: Extension of single-stage branch-line couplers (a) with port extension [89], and (b) with cross-coupled TLIN [90]. 145

Figure 5.24: 2-section (a) branch-line and (b) rat-race couplers implementation. 146

Figure 5.25: Simulated branch-line response with 2-stage rat-race coupler. 147

Figure 5.26: Simulated rat-race response with 2-stage rat-race coupler. 148

Figure A.1: Stripline test resonator (a) layout and (b) assembly details [91]. 154

Figure A.2: Impact of $\varepsilon_{hori} > \varepsilon_{vert}$ on microstrip filter and EM modeling with (yellow trace) and without (green trace) uniaxial anisotropy [93]. 156

Figure A.3: Apparent dielectric constant values for ED 0.5 oz copper-cladded (a) RO4003 and (b) RO4350 laminates, with compensation for surface roughness. Data compiled from [94]. 157

Figure A.4: (a) Apparent substrate dielectric constant and (b) substrate height for use with conventional microstrip model, and (c) simulated characteristic impedance for microstrip TLINs on RO4350 with 35 µm copper thickness and 2.8 µm surface roughness. 159

LIST OF TABLES

Table 1.1: Common microwave frequency bands and applications for satellite communications [7]. 4

Table 2.1: Phase states at antenna feeds for various polarization states. 19

Table 2.2: RF MEMS SPDT bias states for 3 & 4 polarization modes. 20

Table 2.3: Configurations of tuning elements for performing polarization diversity for antenna in Figure 2.11. 23

Table 2.4: Combinations of feedpoints and polarization control devices for various polarization modes 25

Table 2.5: Feed excitation for Xpol analysis with probe-fed microstrip antenna. 28

Table 3.1: Commercial-grade laminates suited for FR-4-based multi-layered PCB lamination process and assembly. 66

Table 3.2: Antenna array gain 88

Table 4.1: List of normalized pattern plots for CP arrays 97

Table 4.2: Directivity and HPBW for square arrays with $0.59\lambda_0$ element spacing. 101

Table 5.1: Aperture sharing implementation methods. 121

Table 5.2: Physical dimensions (units in mils) for 20/30 GHz microstrip antenna. 131

Table 5.3: TLIN implementation with composite LH/RH comprising of Tee-network LoP/HiP unit cells 138

Table A.1: List of some Rogers laminates and dielectric constant values. 153

ACKNOWLEDGMENTS

Nothing can truly express my deepest heartfelt gratitude for my advisor, Prof. Gabriel Rebeiz, for his guidance, patience, support, and encouragement over the years. It is indeed my honor to be under his tutelage. Delving deep into his homework questions as his teaching assistant has empowered me with the insights for antennas which I would otherwise never achieve from books or courses. Repeated questioning of fundamental details over group meetings, deep mental consolidations for preparation of detailed weekly reports, emphasis on clarity and professionalism of verbal and visual presentations, and the atmosphere of civic responsibility and pro-activeness in the TICSG group; all of the factors that has deeply influenced me and equipped me with the technical and professional skills for facing the next wave of challenges ahead. Besides his concerns for his students' careers, his insights for impactful projects, and his passion and technical depth into various areas, what impressed me deeply is his constant monitoring of his students' development through various mechanisms, and timely provision of resources to allow his students to develop on their own, and in a conducive environment that he provides for the group. The time spent with my advisor and the TICSG group has been the most influential and rewarding for my professional and personal development.

Next, I would like to express my gratitude to my dissertation committee members, Prof. Peter Asbeck, Prof. Daniel Sievenpiper, Prof. Gert Cauwenberghs and Prof. William Hodgkiss, for their time off from their busy schedules to be in the committee, and their interest and valuable comments about my research.

The TICSG group is indeed a big group, with lots of movement over the years. I would like to thank all the TICSG members during this time for their friendship, encouragement, patience, and support; Chih-Hsiang “Elmer” Ko, Chenhui Niu, Tumay Kanar, Yang Yang, Hsin-Chang “Ken” Lin, Ozan Dogan Gurbuz, Bilgehan Avser, Abdullah Al-Azemi, Samet Zihir, Hasan Al-Rubaye, Hyunchul Chung, Kerim Kibaroglu, Bhaskara Rupakula, Hosein Zareie, Fatih Golcuk, Ozgur Inac, Donghyup Shin, Woorim Shin, Mehmet Uzunkol, Jennifer Edwards, Chirag Patel, Sang-Young

Kim, Hojr Sedaghat Pisheh, Alex Grichener, Berke Cetinoneri, Yu-Chin Ou, Yusuf Alparen Atesal, Isak Reines, Ramadan Alhalabi, Jason May, Mohammed El-Tanani, Tiku Yu, Kwang-Jin Koh, Michael Chang, Tao Yang, Bon-Hyun Ku, Youngho Cho, Hyun-Ho Yang, Mustafa Sayginer, Hong-Ming Lee, Choul-Young Kim, Yi-Chyun Chiou, Chih-Chieh Cheng, Rashed Mahameed, Dong-Woo Kang, Achref Yahiaoui, Belan Andres and Romain Stefanini. I would also like to thank all my friends in San Diego and UCSD for their friendship and support.

I would like to acknowledge Dr Alan Tran of Qualcomm Research Center for the use of the Satimo Stargate-32 near-field antenna chamber, and Sonsay Noimanivone for the assistance rendered in the measurements. I would like to acknowledge Prof. Dan Sievenpiper for the use of the ETS-Lindgren far-field antenna chamber, and Ryan Quarfoth and Jiang Long for the assistance rendered in the measurements.

Without the fellowship from DSO National Laboratories, I would not have considered doing my studies overseas. I would like to express my gratitude to Dr Siou-Teck Chew for roping me into RFL/DSO back in 2002, and his patience and guidance for my initial years with the organization. I would also like to express my gratitude to Dr Guan-Leng Tan, for his encouragement and guidance over the years when I was directly reporting to him, for building up a conducive environment that allows me to deeply focus and thrive upon my passion for microwave circuits with applied EM, and more importantly for actively encouraging me to work on my PhD in particularly with his previous advisor, Prof. Rebeiz. I would also like to thank my previous bosses in DSO for their guidance and patience, and also many of my co-workers in DSO for their support and friendship over the years; in particular Diana Chan and Josephine Lim for being my guarantors for the fellowship, and Diana too for providing critical and creative assembly support for the research projects.

I would like to acknowledge my mother, Poh-Cheng Seah, and my wife, Yee-Shian Lee, for their encouragement, support and patience over the years.

The material in this dissertation is based on the following papers which are either published, or under final process for publication.

Chapter 2 is based on and mostly a reprint of the following papers:

- K. M. Ho and G. M. Rebeiz, “A 0.9-1.5 GHz Microstrip Antenna with Full Polarization Diversity and Frequency Agility,” *IEEE Trans. Antennas Propag.*, May 2014.

- K. M. Ho and G. M. Rebeiz, “Tunable Microstrip Antenna with Circular Polarization across 1.4:1 Frequency Span,” *Proc. IEEE Antennas Propag. Symp.*, Jul. 2013.

- K. M. Ho and G. M. Rebeiz, “Microstrip Antennas with Full Polarization Diversity using Packaged RF MEMS Switches,” *Proc. IEEE Antennas Propag. Symp.*, Jul. 2012.

- K. M. Ho and G. M. Rebeiz, “Microstrip Patch Antennas with Frequency Agility and Polarization Diversity over a Wide Frequency Range,” *Proc. IEEE Antennas Propag. Symp.*, Jul. 2010.

Chapter 3 is based on and mostly a reprint of the following papers:

- K. M. Ho and G. M. Rebeiz, “A Low-Cost X-band Phased-Array Antenna using QFN-packaged CMOS RFIC Receivers,” *IEEE Trans. Microw. Theory Techn.*, submitted for publication.

- K. M. Ho, D. Shin and G. M. Rebeiz, “X-Band Phased Array Development on Teflon Laminates with CMOS RFIC Receivers,” *Proc. IEEE Antennas Propag. Symp.*, Jul. 2011.

Chapter 4, in part, is based on the following material as it appears in IEEE Antennas and Propagation Symposium, 2014:

- K. M. Ho and G. M. Rebeiz, “Limitations in Circularly Polarized Planar Arrays from Individual Element Cross Polarization Levels.”

Chapter 5, in part, is based on the following material as it appears in IEEE Antennas and Propagation Symposium, 2014:

- K. M. Ho and G. M. Rebeiz, “Dual-Band Circularly-Polarized Microstrip Antenna for Ku/Ka Band Satellite Communication Arrays.”

The dissertation author was the primary author of the work in these chapters, and coauthors (Prof. Gabriel M. Rebeiz, and Dr. Donghyup Shin) have approved the use of the material for this dissertation.

VITA

EDUCATION

2000	B.Eng. (Hons), National University of Singapore, Singapore
2002	M.Eng in Electrical and Computer Engineering, National University of Singapore, Singapore
2015	Ph. D. in Electrical Engineering, University of California, San Diego, USA

PROFESSIONAL EMPLOYMENT

2002 – present	Microwave Engineer, DSO National Laboratories, Singapore

PUBLICATIONS

K. M. Ho and G. M. Rebeiz, “A 0.9-1.5 GHz Microstrip Antenna with Full Polarization Diversity and Frequency Agility,” *IEEE Trans. Antennas Propag.*, vol. 62, no. 5, pp. 2398-2406, May 2014.

K. M. Ho and G. M. Rebeiz, “A Low-Cost X-band Phased-Array Antenna using QFN-packaged CMOS RFIC Receivers.,” *IEEE Trans. Microw. Theory Techn.*, submitted for publication.

K. M. Ho and G. M. Rebeiz, “Dual-Band Circularly-Polarized Microstrip Antenna for Ku/Ka Band Satellite Communication Arrays,” *Proc. IEEE Antennas Propag. Symp.*, Jul. 2014.

K. M. Ho and G. M. Rebeiz, “Limitations in Circularly Polarized Planar Arrays from Individual Element Cross Polarization Levels,” *Proc. IEEE Antennas Propag. Symp.*, Jul. 2014.

K. M. Ho, H. Lin and G. M. Rebeiz, “Improving 3G/4G Receiver Sensitivity (TIS) Using Antenna Impedance Matching Networks,” *IEEE Int. Microwave Symp. Digest*, Jun. 2014.

K. M. Ho and G. M. Rebeiz, “Tunable Microstrip Antenna with Circular Polarization across 1.4:1 Frequency Span,” *Proc. IEEE Antennas Propag. Symp.*, Jul. 2013.

K. M. Ho and G. M. Rebeiz, “Microstrip Antennas with Full Polarization Diversity using Packaged RF MEMS Switches,” *Proc. IEEE Antennas Propag. Symp.*, Jul. 2012.

K. M. Ho, D. Shin and G. M. Rebeiz, “X-Band Phased Array Development on Teflon Laminates with CMOS RFIC Receivers,” *Proc. IEEE Antennas Propag. Symp.*, Jul. 2011.

K. M. Ho and G. M. Rebeiz, “Microstrip Patch Antennas with Frequency Agility and Polarization Diversity over a Wide Frequency Range,” *Proc. IEEE Antennas Propag. Symp.*, Jul. 2010.

T. Yang, K. M. Ho and G. M. Rebeiz, “Compact Self-Shielded 2-3 GHz High Q Coaxial Fixed and Tunable Filters,” *IEEE Trans. Microw. Theory Techn.*, vol. 62, no. 12, pp. 3370-3379, Dec. 2014.

C. H. Ko, K. M. Ho, R. Gaddi and G. M. Rebeiz, “A 1.5-2.4 GHz Tunable 4-Pole Filter Using Commercial High-Reliability 5-Bit RF MEMS Capacitors,” *IEEE Int. Microwave Symp. Digest*, Jun. 2013.

C. H. Ko, K. M. Ho and G. M. Rebeiz, “An Electronically-Scanned 1.8-2.1 GHz Base-Station Antenna Using Packaged High-Reliability RF MEMS Phase Shifters,” *IEEE Trans. Microw. Theory Techn.*, vol. 61, no. 2, pp. 979-985, Feb. 2013.

G. M. Rebeiz, C.D. Patel, S. K. Han, C. H. Ko and K. M. Ho, “The Search for a Reliable MEMS Switch,” *IEEE Microwave Magazine*, vol. 14, no. 1, pp. 57-67, Jan. 2013.

Y. A. Atesal, B. Cetinoneri, K. M. Ho and G. M. Rebeiz, “A Two-Channel 8-20 GHz SiGe BiCMOS Receiver with Selectable IFs for Multibeam Phased-Array Digital Beamforming Applications,” *IEEE Trans. Microw. Theory Techn.*, vol. 59, no. 3, pp. 726-716, Mar. 2011.

ABSTRACT OF THE DISSERTATION

Microstrip Antennas with Polarization Diversity across a Wide Frequency Range and Phased Array Antennas for Radar and Satellite Communications

by

Kevin Ming-Jiang Ho

Doctor of Philosophy in Electrical Engineering (Electronic Circuits and Systems)

University of California, San Diego, 2015

Professor Gabriel M. Rebeiz, Chair

The thesis comprises of 3 projects; an L-band microstrip antenna with frequency agility and polarization diversity, X-band phased array antennas incorporating commercially packaged RFIC phased array chips, and studies for Ku/Ka-band shared aperture antenna array.

The first project features the use of commercially packaged RF-MEMS SPDT switches, that boasts of high reliability, high linearity, low losses, hermetically packaged and fully compatible for SMTA processes for mass-assembly and production. Using the switches in a novel manner for the feed network, microstrip antennas with polarization

diversity are presented. Frequency agility is achieved with the use of tuning diodes to provide capacitive loading to the antenna element. Additional inductance effects from surface-mounted capacitors, and its impact, is introduced. Theoretical cross-polarization of probe-fed antenna elements is presented for both linear and circular polarized microstrip antennas. Designs and measurements are presented, for microstrip antennas with polarization diversity, wide frequency tuning range, and both features. Replacement of the tuning diodes with commercially-packaged high Q RF MEMS tunable capacitors will allow for significant improvements to the radiation efficiency.

In another project, multi-channel CMOS RFIC phased-array receiver chips are assembled in QFN packages and directly integrated on the same multi-layered PCB stack-up with the antenna arrays. Problems of isolation from the PCB-QFN interface, and potential performance degradation on antenna array from the use of commercial-grade laminates for assembly requirements, namely potential scan blindness and radiation efficiency, are presented. Causes for apparent drift of dielectric constant for microstrip circuits, and high conductor losses observed in measurements, are introduced.

Finally, studies are performed for the design of a Ku/Ka-Band shared aperture array. Different approaches for developing dual-band shared apertures are considered. Design for single-fed circular-polarized dual-band antenna element operating at 20 GHz and 30 GHz is presented. Designs for dual-band quadrature and differential phased 3dB couplers are presented. Studies are performed on cross-polarization performances of circularly-polarized microstrip antenna arrays resulting from performance limitations of individual antenna elements. Results of the pattern studies and designs of the dual-band components can be combined to evaluate practical performance of dual-band array implementation and required component specifications and bandwidth constraints.

Chapter 1

Introduction

1.1 Growing Demand for Mobile Connectivity

With the internet permeating into all expects of the modern lifestyle, there is a growing demand for availability of internet and data-streaming on-the-go. Examples include availability of internet on both vehicular and hand-held mobile platforms with increasing bandwidth demand for real-time audio and video streaming. Other applications with real-time signal linkage to mobile platforms include global positioning and data communications. Signal transmission can be performed from cellular and broadcast base stations for land-based mobile platforms, and satellite broadcast for both land-based and air-borne platforms.

Impact on the RF front-end is the increase of functionality within a constrained form factor, to support the various applications while maintaining portability and user interface. Some possible developmental efforts from this impact includes

I - RF-front end tuning, for amplifiers, antennas, or both, for performance enhancement. This is in particular for devices on hand-held platforms.

II - Implementation of multi-functional integrated circuits (ICs) or micro-machined components on printed circuit boards (PCBs) with low developmental assembly cost.

III - Integration of multiple functionality or multiple operating frequencies in a shared platform. This is in particular for larger system platforms.

1.2 RF Front-End Miniaturization

1.2.1 Tunable and Reconfigurable Antennas for Wireless Communications

RF-front tuning with re-configurable matching networks for transmitter (Tx) power amplifier (PA) outputs and antenna inputs are actively looked into [1],[2], with the use of high Q RF MEMS switches [3] and tunable capacitors [4]-[5] in packaged form that are ready for automated PCB assembly (PCBA) facilities the most ideal tuning device for use.

Instead of an external matching network, antenna tuning can be integrated in the antenna element, support a wide frequency band through impedance tuning rather than serving only a single fixed frequency. As antenna elements on a mobile platforms (*esp.* for hand-held platforms) are the weakest link in the T/R signal chain, polarization configurability will allow better overall transmission link performance with matching polarization for the mobile platform with the base-station or direct satellite link.

For a small antenna which fits into a sphere of radius a, the 10-dB bandwidth (BW_{10dB}) limit is [6]:

$$BW_{10dB} = \frac{1}{\eta\sqrt{2}}\left(\frac{1}{ka} + \frac{1}{n(ka)^3}\right)^{-1} \tag{1.1}$$

where η is the radiation efficiency, k the free-space propagation constant, and n = 1 for linear polarized or *single-mode* antennas, or n = 2 for circular polarized or dual-mode antennas. Miniaturized antenna elements fitted in compact hand-held platforms, especially for frequencies at S-band (2-4 GHz) and below, will have low efficiency and small bandwidth. Tuning and re-configurability capabilities extend the antenna usability to a wider frequency range with higher performance efficiency beyond the theoretical limit.

1.2.2 Low-Cost PCB Assembly

Recent technological advances in micro-electronics thin-film and wafer fabrication processes has led to the development of dense multi-functional RF integrated circuits (RFICs), monolithic microwave integrated circuits (MMICs), micro-machining components and micro-electrical-mechanical systems (MEMS). These enabling technologies have allowed the advent of high performance components, or multi-functional systems within a small form factor, leading to products with various features within a small form factor which is previously considered as impossible.

The multi-functional miniaturized components will not be useful, until they are packaged for environmental protection and assembled on the PCBs. Available methods for doing so includes packages with land grid array (LGA) footprint for solder-reflow assembly, flip-chip assembly, and die-attach and wire-bond assembly. Solder-reflow with packaged components is the most ideal for mass-assembly, but may incur the loss for RF applications at high frequencies. Wire-bond assembly of die-attached on board, or chip-on-board (COB), potentially provides the best performance at microwave frequencies, but is the most involved in assembly efforts, and does not provide environmental protection for both the die and wire-bond transition.

Lastly, the requirements of multi-layered PCB fabrication processes (and preference of PCBA processes) dictates the PCB to be of certain commercial grade, for its mechanical strength and coefficient of thermal expansion (CTE) matching to copper's CTE, to avoid warpage of material under high heat condition. But such commercial grade laminates are generally lossy and seldom being considered for microwave applications traditionally, *esp.* for microwave antenna arrays.

1.2.3 Shared Aperture Arrays

A possible method of achieving RF miniaturization, at higher system level, is the use of shared aperture arrays. 2 or more different applications at different frequencies traditionally requiring separate antennas each can be using a common antenna aperture. This is particularly attractive for implementation on mini- or micro- “cube” satellites, where space for aperture implementation is a premium.

Some common frequency bands and applications for satellite communications are presented in Table 1.1 [7].

Table 1.1: Common microwave frequency bands and applications for satellite communications [7].

Band	Frequency	Applications
L	1-2 GHz	MSS, UHF TV, cellular phone, terrestrial microwave and studio television links.
S	4-4 GHz	MSS, Digital Audio Radio Service (DARS), NASA and deep space research.
C	4-8 GHz	FSS, fixed service terrestrial microwave.
X	8-12.4 GHz	FSS military communications, DARS feeder links, fixed service terrestrial, Earth observation satellites.
Ku	12.4-18 GHz	FSS, BSS, fixed service terrestrial microwave.
K	18-26.5 GHz	FSS, BSS, fixed service terrestrial microwave, local multi-channel distribution service (LMDS).
Ka	26.5-40 GHz	FSS, fixed service terrestrial microwave, LMDS, ISL, satellite imaging.
FSS	Fixed Satellite Service	Between Earth stations at any given positions, when one or more satellites are used; includes satellite-to-satellite links.
MSS	Mobile Satellite Service	Between mobile Earth stations and space stations.
BSS	Broadcast Satellite Service	A service in which signals transmitted or re-transmitted by space stations are intended for direct reception by the general public.
ISL	Inter-satellite Link	A service providing links between artificial satellites

1.2 Scope of thesis

The thesis presents on details from 3 separate projects, with the common theme of RF miniaturization and use of commercial-grade laminates.

Chapter 2 delves into the designs of microstrip antenna elements with polarization agility across wide frequency tuning range in L-band. Commercially packaged low loss metal contact RF micro-electrical-mechanical-systems (MEMS) switches are used in a novel reconfigurable feed network to achieve the pattern re-configurability. Transmission line loading effects for surface-mount components, and studies on theoretical cross-polarization of a square microstrip antenna for linear and circular polarization, are presented. Finally, hardware demonstrators are fabricated, with measured VSWR and radiation patterns presented.

Chapter 3 presents the development of an X-band phased array receiver antenna array, as part of a frequency-modulated continuous wave (FMCW) radar system. It features quad-flat no lead (QFN) assembled multi-channel CMOS RFIC receiver phased-array chips directly integrated on the same PCB stack-up as the antenna array. Channel-to-channel isolation degradation mechanism from the RFIC-QFN-PCB interface is studied. Problems for both the antenna elements (low efficiency, potential scan blindness) and the RF feed network (apparent dielectric constant change, losses) from the use of commercial grade laminates are presented. Finally, VSWR and pattern measurements are presented.

Chapters 4 and 5 presents on the preliminary studies for a Ku/Ka band circular polarized shared aperture antenna array, for satellite communications. Chapter 4 presents on studies on theoretical cross-polarization performance of circularly polarized arrays and degradation arising from the antenna element cross-polarization. Chapter 5 considers the various possible implementation methods for a dual-band shared-aperture array, and presents designs and simulations of dual-band antenna and couplers.

The thesis concludes with a summary and suggested future work.

Chapter 2

L-Band Microstrip Antenna with Frequency Agility and Polarization Diversity

2.1 Overview

2.1.1 Tunable and Reconfigurable Antenna Elements

An antenna element can be designed for operation with linear polarization (LP) or circular polarization (CP). The 2 orthogonal LP modes are vertical polarization (VP) and horizontal polarization (HP). Left-hand CP (LHCP) or clockwise (CW) polarization, and right-hand CP (RHCP) or counter-clockwise (CCW), are the 2 possible CP modes. Full pattern re-configurability allows the antenna to change its operating mode to any of these four cases for maximum power transfer in the communications link.

Prior art for planar antenna elements with frequency tuning and pattern re-configurability include; [8] for slot-ring antennas and [9] for cavity-backed microstrip antennas for independent frequency agility for dual-orthogonal LP modes; [10] with slots and control devices on the antenna element, [11] with slots perturbation on the ground plane, and [1] for switchable dual CP modes in dual operating frequencies, for re-configurable orthogonal CP modes.

Control devices for perturbations at corners of the antenna elements for linear & circular re-configurability include [13]-[15]. Antenna element with both frequency agility and polarization diversity was presented in [16], and a conceptual verification for both frequency agility and polarization diversity from a microstrip antenna element was presented in [17] with fixed lumped-element components.

2.1.2 Antenna Re-Configurability with RF MEMS Switches

With the use of 2 Omron RF MEMS switches and a novel feed network, [18] demonstrates design for achieving 4 polarization states from a single square microstrip antenna element. Complementing the design with dual-polarized tuning techniques from Carson ([8] for slot antennas and [9] for microstrip antennas), [19] demonstrates an antenna element with full polarization diversity *across* a wide frequency tuning range.

Conversely, restraining to one RF MEMS switch in the feed network, a dual-polarized tunable antenna is able to either have 3 polarization states across the frequency tuning range; vertical, horizontal, and circular. Or by having the orthogonal polarization frequencies offset with quadrature phase difference, retaining full polarization diversity across frequency tuning range can be retained [20].

Omron metal-contact RF MEMS switches are used for the reconfigurable feed network, and its model and reliability features will be first presented. Design concepts for a dual-polarized tunable microstrip antenna to achieving orthogonal dual-polarized frequency tuning across a wide bandwidth will be presented next, followed by details of the reconfigurable feed network for performing frequency agility. Theoretical LP and CP cross-polarization (Xpol) for a differential and quadrature phased probe-fed microstrip antenna is presented. Finally hardware realization and measured verifications are presented.

2.2 Omron RF MEMS Switches

2.2.1 Switch Details and Reliability Measurements

Figure 2.1a presents a metal-contact MEMS switch, developed by Omron [21]. 2 of these devices are packaged together to form a single-pole double-throw (SPDT) component (Figure 2.1b), in a land-grid array (LGA) package (Figure 2.1c) that allows for compatibility with pick-and-place automation process in printed circuit-board assemblies (PCBA). Key performance include insertion loss < 1 dB, isolation > 30 dB, < 2:1 VSWR up to 10 GHz, and measured third order intercept (IP_3) > 70 dBm. Actuation voltage required is ~ 30 V.

The Omron switch was tested at UCSD for 4 continuous months [22] and for billions of total cycles at 0.01-9 W, under cold switching conditions, and its resistance was constant at 1.1+/-0.1 Ω (Figure 2.2a). It was also tested under hot-switching conditions with an RF power of 300 mW, and operated up to 100M cycles (test stopped due to time limitations, Figure 2.2b). It was tested under continuous operation at 0.1-5 W (hours and days for each test) and its resistance was measured every few hours and remained constant to within +/-0.1 Ω (Figure 2.2c). The pull-down (28 V) and release voltage (15 V) were measured over 3 days of continuous actuation (once every hour) and no change was detected. All testing was done at 2 GHz and cycle testing was done at 1 kHz.

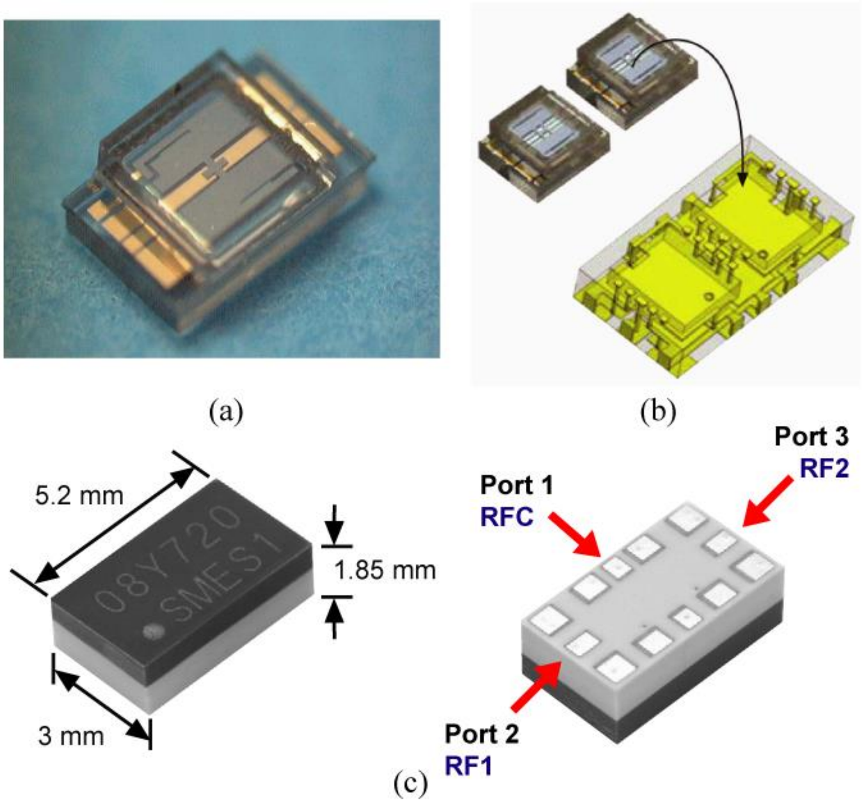

Figure 2.1: Omron RF MEMS switches; (a) single switch device, (b) SPDT from 2 devices in (c) LGA plastic package.

A distinctive feature of the Omron SPDT switch, as compared to transistor-based commercial SPDT parts, is its bias control which allows 4 states (instead of two). Since the switch is built using two independently controlled RF MEMS switches, power from input can be routed to a) either of the output channels with either switch turned on, b) both output channels with both switches turned on, or c) totally reflected at the input with both switches turned off (Figure 2.3c). This feature was utilized for the design of the reconfigurable feed network to allow for polarization diversity. With both switches turned on, the input impedance presented by the switch reduces to half of that as when either switch is turned on. This is due to the T-junction formed by both switches on, and the parallel loading of two identical loads.

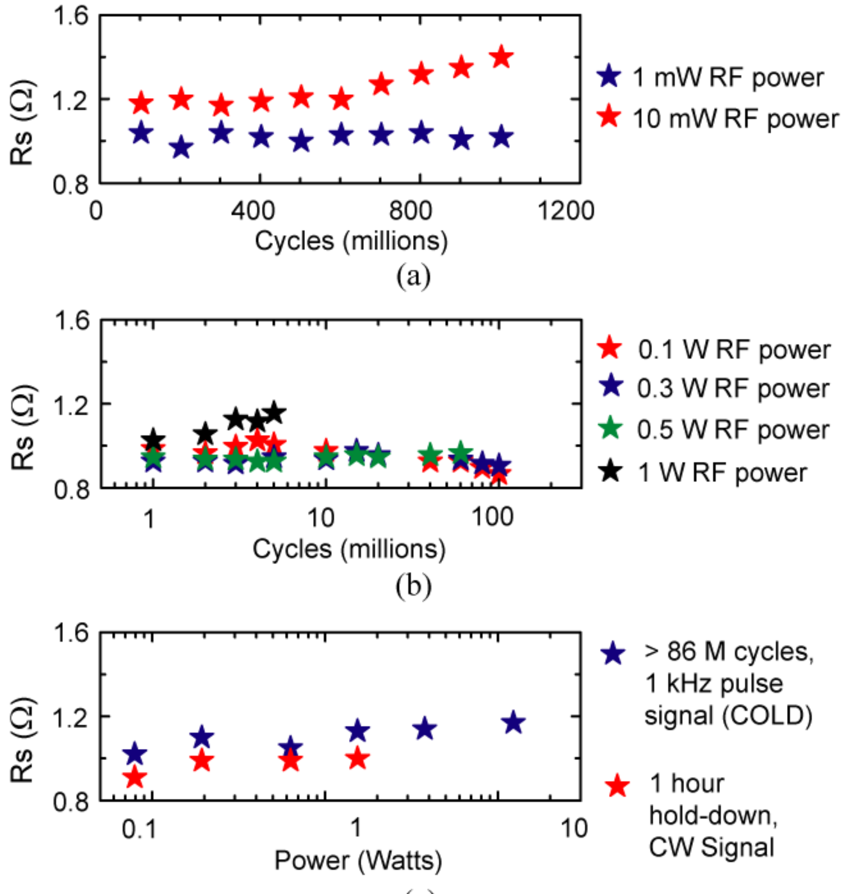

(a)

(b)

(c)

Figure 2.2: Reliability measurements for Omron MEMS switches; (a) cold switching, (b) hot switching and (c) power handling.

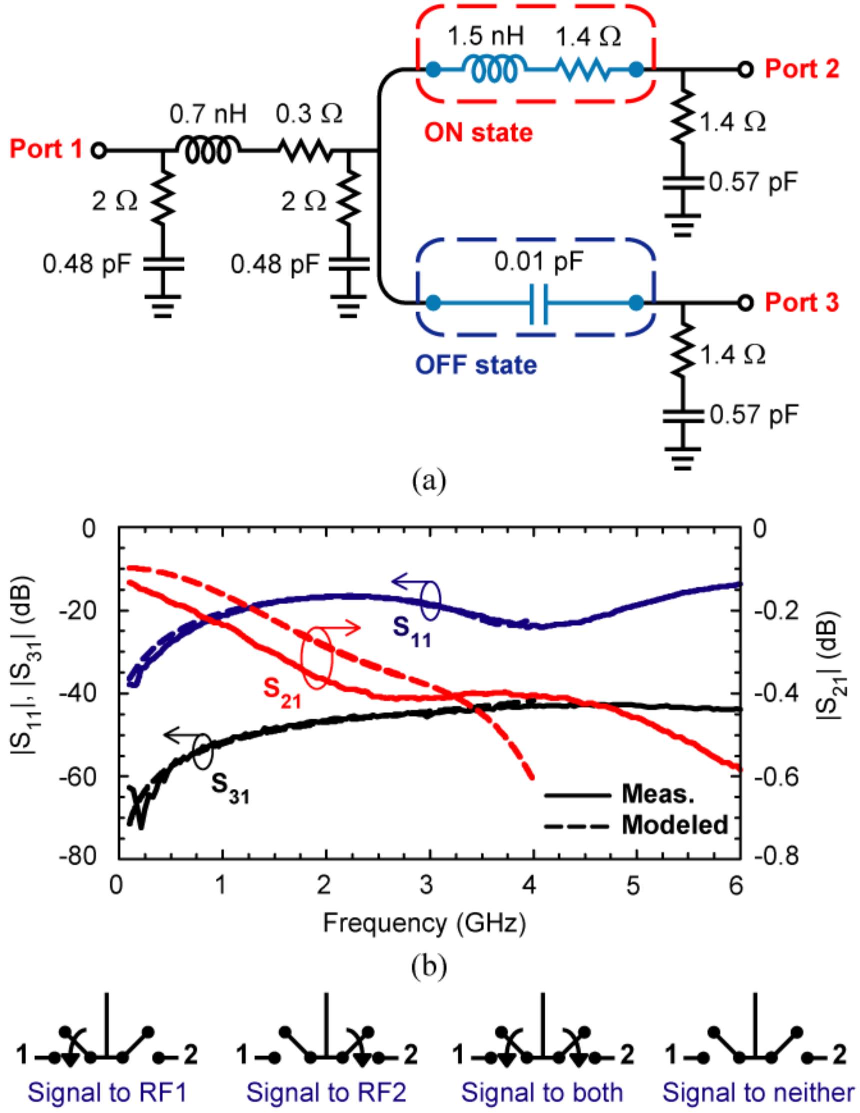

(a)

(b)

(c)

Figure 2.3: Omron SPDT's (a) fitted small signal model, (b) modeled (dashed) and measured (solid) S-parameter response, and (c) 4 states of operation.

2.2.2 MEMS SPDT Modeling

The packaged SPDT was mounted on a 0.01" thick Rogers RO4350 (ε_r 3.66, tanδ 0.0038) printed board, and measurements were taken with the assembled setup. The connectors and feed transmission lines (TLINs) were de-embedded using through and reflect standards, and the switch S-parameter response (in the 4 states) was fitted to an RLC model. Figure 2.3a presents the fitted model, and Figure 2.3b shows the modeled and measured SPDT response [23].

The measured S-parameter file or the circuit model can be used in circuit simulators. Unfortunately, these two methods may not be easily implemented in some EM solvers. Figure 2.4 presents a simple model suitable for all EM solvers: the individual switch up-state isolation or down-state transmission phase is modeled using the least number of reactance elements resulting in a compact model. The up-state isolation is modeled using a series capacitor (4 fF), and the down-state phase is modeled using a low-pass π-network for the TLIN segment (with characteristic impedance Z_0 and electrical length θ at frequency f) as:

$$L = \frac{Z_0 \cdot \sin\theta}{2\pi f}, \qquad C = \frac{1}{Z_0 \cdot 2\pi f}\sqrt{\left(\frac{1-\cos\theta}{1+\cos\theta}\right)} \tag{2.1}$$

In the down-sate position, the Omron switch has 45° phase delay at 2 GHz which corresponds to L = 2.8 nH and C = 0.66 pF (assuming matched to 50 Ω). This

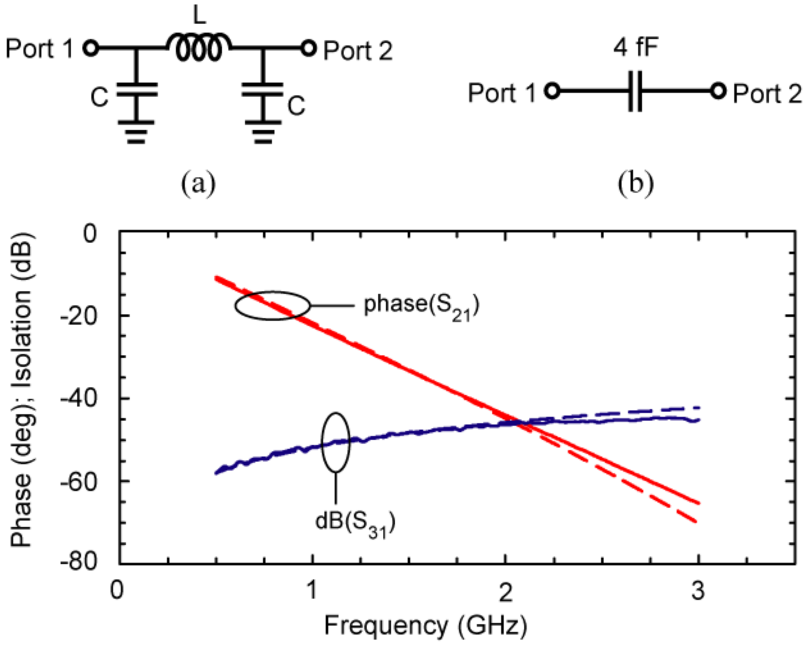

(a) (b)

(c)

Figure 2.4: Simplified Omron SPDT model for direct CAD modeling; (a) down-state through, (b) up-state isolation, and (c) measured and modeled response.

model can be directly implemented in all EM solvers, either as lumped components directly inserted in the geometry, or as surface impedance boundary conditions. In this work, it is used for modeling the cross-polarization radiation levels caused by the feed network [19].

Lastly, plastic packaged SPDTs in Figure 2.1a are used in this project. Using through-silicon-via (TSV) technology for packaging at wafer level, a highly miniaturized version has since been introduced [24], with size of 2.5 mm by 1.6 mm by 0.4 mm, and features an integrated charge pump which allows for ~ 3 V actuation bias voltages.

2.3 Microstrip Antenna with Frequency Agility

2.3.1 Antenna Element with Dual Polarized Independent Tuning

To insuring mode purity while independent frequency tuning for both orthogonal LP modes (VP and HP), [8] identified 3 conditions to be fulfilled;

I.- PMC symmetry along axis of operating mode

II.- PEC symmetry along axis orthogonal to operating mode

III.- Tuning element loading along axis of PMC symmetry

Requirements to enforce these conditions include differential feeds implementation (condition II), locating the feeds along the center of the element (condition I), and loading of antenna element at the center of the radiating edges (conditions I and III), and having equal reactance loading in both radiating slots (conditions I and II for both radiating and non-radiating modes).

Figure 2.5 shows a microstrip antenna element with differential ports for VP excitation (F_{V1} & F_{V2}) and HP excitation (F_{H1} & F_{H2}). Capacitance loading is introduced at the radiating edges (C_V and C_H for VP and HP respectively) for tuning the operating frequency from the natural resonance frequency for both linear modes. These two orthogonal LP modes can be simultaneously excited for independent operation at different frequencies across a wide frequency range, as demonstrated in [8]-[9].

With the origin at the center of the antenna, the Y-Z plane is the PMC symmetry plane for the VP mode (excitation at F_{V1} & F_{V2}), and the PEC symmetry plane for the HP mode (excitation at F_{H1} & F_{H2}). Conversely, the Z-X plane is the PEC plane of symmetry for the VP mode, and the PMC plane of symmetry for the HP mode (Figure 2.5b).

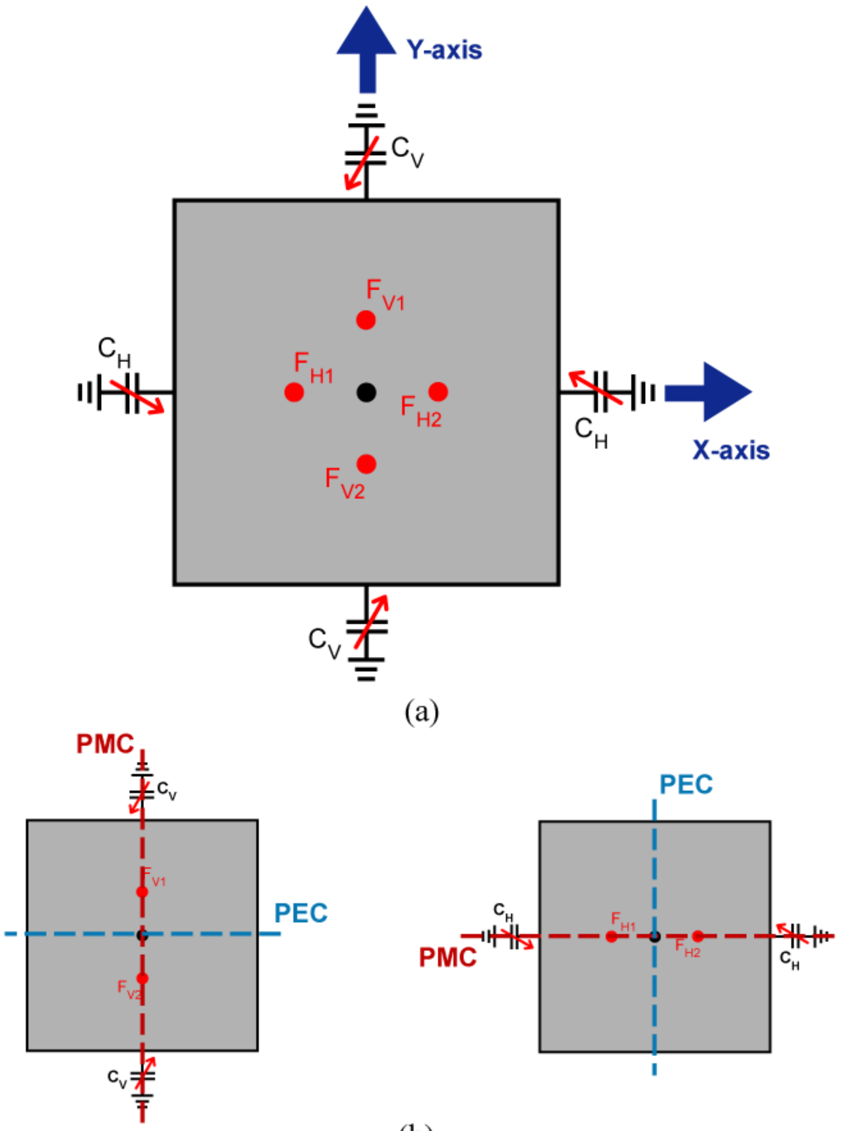

(a)

(b)

Figure 2.5: (a) Differential-fed microstrip antenna with independent dual-polarized tuning, and (b) symmetry planes definition for VP excitation (left) and HP excitation (right).

2.3.2 Surface-Mount Series Capacitance Devices

Tunable capacitance loading can be implemented using high Q RF MEMS tunable capacitors [25],[2] or switch capacitor banks using RF MEMS SPDTs presented above [23], but varactor tuning diodes are used in this concept demonstrator. To minimize the biasing requirements on the complexity of the antenna layout, a shorting via placed at the center of the antenna element enforces 0 V bias conditions for all four tuning devices (2 C_V and 2 C_H on all four radiating edges). Besides easing the biasing arrangements, the center ground via reduces Xpol radiation from the antenna element by 2-3 dB (for LP cases), and enhances isolation between both orthogonal linear modes by 4-6 dB.

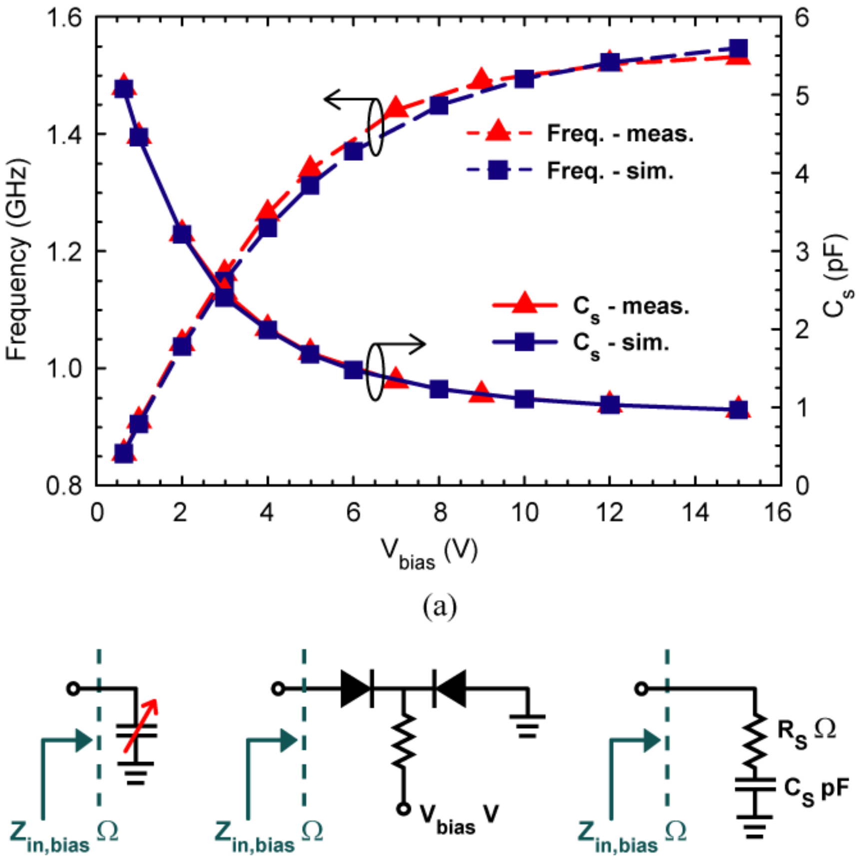

(a)

(b)

Figure 2.6: (a) Simulated vs measured resonant frequency and capacitance loading for various bias voltages, and (b) implementation of tuning network using back-to-back diodes.

Figure 2.6 presents the resonant antenna frequency when loaded with back-to-back varactor diodes (Skyworks SMV1234 silicon hyper-abrupt junction diodes in SC79 packages) [26]. The diodes have a series resistance of 0.8 Ω, a series package inductance of 0.7 nH, and a total capacitance of 1.3 - 9.6 pF. The diode Q is 8-80 at 1 GHz. The back-to-back arrangement is used to result in a smaller capacitance values, higher linearity and a wider tuning range, but unfortunately at the expense of the radiation efficiency with a higher series resistances. Surface-mount lumped elements were modeled using Modelithics CLR library components [27].

Surface-mount capacitors placed on a microstrip line have a parasitic component as shown in Figure 2.7. These include the shunt capacitance effects arising from the solder pads (line Z_{pad} with length l_{OC} below the package and l_{feed} extending beyond the package), and series inductance effects across the component (TLIN Z_{pkg} with length l_{pkg}). The latter forms a series resonance with the device's intrinsic capacitance which

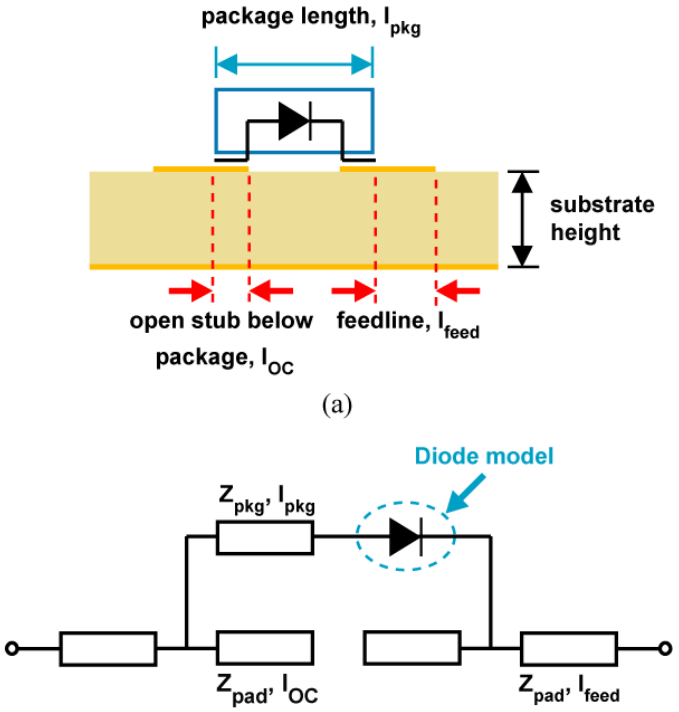

(a)

(b)

Figure 2.7: (a) Diode mounted on PCB and (b) model with transmission line stubs to account for parasitic series inductance (Zpkg) and shunt capacitance (Zpad) effects.

significantly reduces the first self-resonance frequency. The equivalent diode impedance has either a very high capacitance value at close to self-resonance, or behaves as an inductor above self-resonance. This accounts for measurements deviating from simulations in most tunable circuits.

2.3.3 Antenna Q and Bandwidth Approximation

With reconfigurable feed network loading the antenna ports, and input matching to 35 Ω for the input of the whole network (as will be presented in the next sub-section), bandwidth (and resonance too) of the antenna element cannot be easily identified from the return loss response. A reference antenna element (without the feed network) is required for resonance and bandwidth determination from measurements.

A possible way to estimate the bandwidth is from the unloaded Q (Q_u) of the antenna element. The microstrip antenna dielectric Q (Q_{di}) and conductor Q (Q_{cu}) can be calculated using [28]-[30]:

$$Q_{di} = \frac{1}{\tan\delta} \quad \text{and} \quad Q_{cu} = \frac{\eta_o \mu_r}{2}\left(\frac{k_o h}{R_s}\right) \tag{2.2}$$

where tanδ is the substrate loss tangent, h is the substrate height, η_o and k_o are the intrinsic impedance and wave number of free-space wave propagation respectively, and R_s the skin-depth resistivity of the conductor.

The space wave Q (Q_{sp}) can then be extracted from the simulated radiation efficiency (e) with no capacitance loading as:

$$Q_{sp} = \frac{1-e}{e} \Big/ \left(\frac{1}{Q_{cu}} + \frac{1}{Q_{di}}\right) \tag{2.3}$$

Using Q_{tune} to represent the diode Q (Q_{diode}) or the MEMS Q (Q_{MEMS}), and Q_u' to represent the unloaded Q for a microstrip antenna loaded with tuning elements, the radiation efficiency for a microstrip antenna loaded with tuning devices (e_{tune}) can be calculated using:

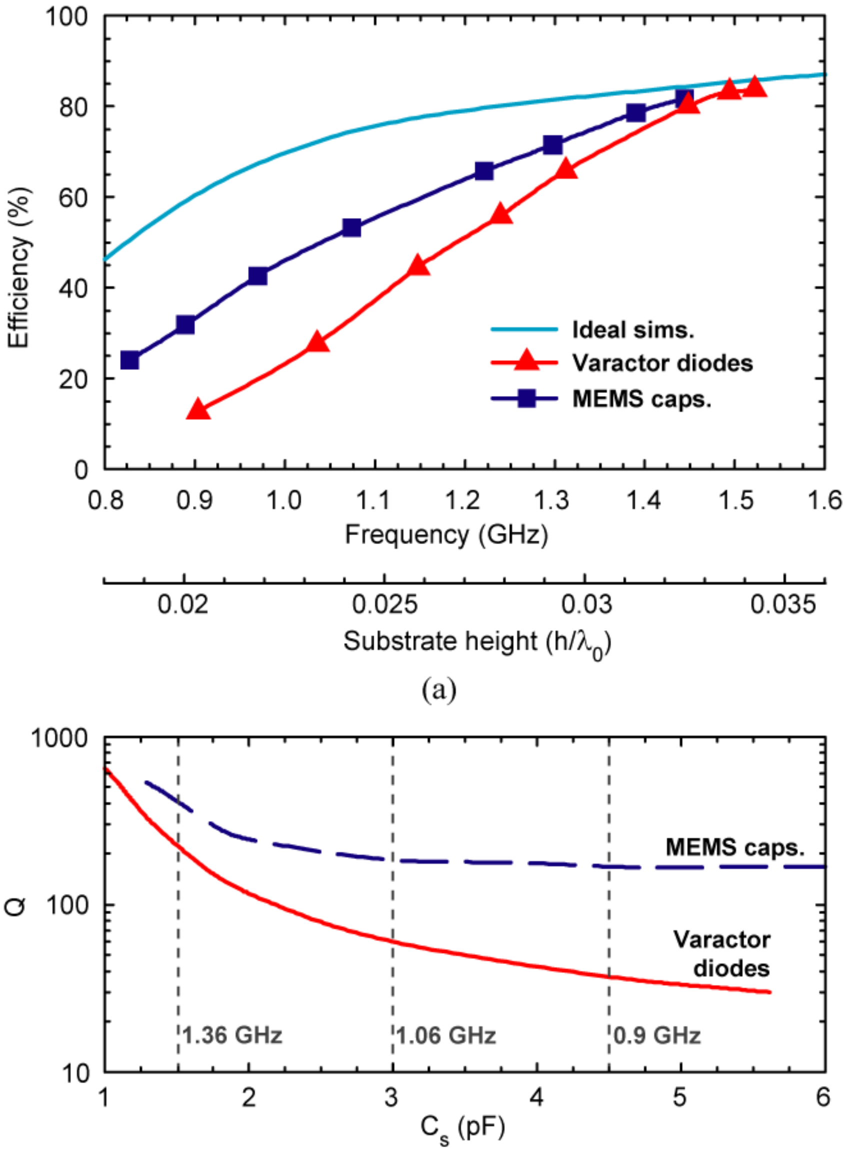

(a)

(b)

Figure 2.8: (a) Radiation efficiency simulations in HFSS, for cases of; antenna with matched feed at all frequencies, antenna loaded with MEMS tunable capacitors, and antenna loaded with tuning diodes, and (b) unloaded Q values for MEMS tunable capacitors and varactor diodes.

$$e_{tune} = \frac{Q_u'}{Q_{sp}} = \frac{1}{Q_{sp}} \bigg/ \left(\frac{1}{Q_{cu}} + \frac{1}{Q_{di}} + \frac{1}{Q_{tune}} \right) \qquad (2.4)$$

The estimated radiation efficiency using (2.4) with Q_{sp} from (3) and Q_{tune} from Figure 2.8b agrees well with HFSS simulated radiation efficiency values (Figure 2.8a), and can be a quick analysis tool. MEMS Q (Q_{MEMS}) values are derived from commercially packaged devices featured in [25] & [2], with 2 devices connected in shunt to obtain the desired capacitance (C_s) values at each radiating edge.

The low intrinsic efficiency of the antenna at lower frequencies is due to the electrically thin substrate and small antenna size at those frequencies, resulting in low resonator efficiency. The surface waves loss mechanism, usually not captured in HFSS, can be neglected for single antenna element applications, but should be considered if the design is to be extended to 1D or 2D microstrip antenna arrays.

The bandwidth of the microstrip antenna, for a given *VSWR*, can be defined as

$$BW_{LIN} = \frac{VSWR-1}{Q_u\sqrt{VSWR}} \tag{2.5}$$

for LP modes, and

$$BW_{CIR} = \frac{\sqrt{2(VSWR-1)}}{Q_u} \tag{2.6}$$

for CP modes, and

$$\frac{BW_{CIR}}{BW_{LIN}} = \frac{\sqrt{2\cdot VSWR}}{\sqrt{VSWR-1}} \tag{2.7}$$

or $BW_{CIR} = 2BW_{LIN}$, for $VSWR = 2$.

The calculated fractional bandwidth for LP is 1.5-2.5% at 0.9-1.5 GHz for varactor loading, as compared to < 1.5% for MEMS loading. The varactor diode low Q results in lower radiation efficiency but a wider bandwidth.

2.4 Microstrip Antenna with Frequency Agility and Full Polarization Diversity

2.4.1 Re-configurable Feed Network with MEMS Switches

Tuning both dual LP modes to the same frequency, Table 2.1 presents the phase excitation at the 4 inputs of antenna element presented in Figure 2.5 to achieve the desired polarization [31].

Table 2.1: Phase states at antenna feeds for various polarization states.

PHASE STATES FOR POLARIZATION EXCITATIONS

Polarization	F_{V1}	F_{V2}	F_{H1}	F_{H2}
Linear: Vertical	90^0	270^0	-	-
Linear: Horizontal	-	-	0^0	180^0
Circular: LHCP	90^0	270^0	0^0	180^0
Circular: RHCP	90^0	270^0	180^0	0^0

With one Omron SPDT as the polarization control device, one can achieve 3 states of polarization controls (Figure 2.9a & Table 2.2); VP, HP, and LHCP. LP is achieved as power is routed to either pair of the antenna feeds (either F_{V1} and F_{V2} for VP, or F_{H1} and F_{H2} for HP) using switch device (SW1) routing power to either RF1 or RF2 outputs. However, with switch device routing power to both RF1 and RF2 outputs, CP is obtained as power is transmitted to both sets of antenna feeds.

To reduce on complexity of feed inputs/outputs, differential feeds for each linear mode is to be fed with a single feed-point (or connector). They can be implemented with 0/180° rat-race couplers, baluns, Schiffman-type delay lines ([32], for reduced form factor) or in this case an additional transmission line segment of 180° at one of the feed ports. Though seemingly more narrowband, +/- 30° of phase deviation for the phase is acceptable before the cross-polarization (Xpol) degrades to -20 dB.

With 50 Ω matched terminations at both ports of the switch device, the common input port of the switch will present input impedance of 50 Ω and 25 Ω for LP and CP modes respectively. Matching to 35 Ω will allow for 1.4:1 VSWR of matched condition for all polarization modes. Hence the recommendation for bandwidth evaluation from the Q as presented in the preceding subsection. Zo_{IN} can be implemented with $\lambda_0/4$ impedance matching section, or alternatively using a series-line transformer to minimize its length, and is given by (matching a Z_L to a Z_S using a Z_0 and an electrical length θ) [33]:

Table 2.2: RF MEMS SPDT bias states for 3 & 4 polarization modes.

3 POLARIZATION STATES – 1 SPDT

Polarization	RF MEMS SW1
Linear – Vertical	Output to RF1
Linear – Horizontal	Output to RF2
Circular	Output to RF1 and RF2

4 POLARIZATION STATES – 2 SPDTS

Polarization	RF MEMS SW1	RF MEMS SW2
Linear – Vertical	Output to RF1	Not applicable
Linear – Horizontal	Output to RF2	Output to RF1 or RF2
Circular – LHCP	Output to RF1 and RF2	Output to RF1
Circular – RHCP	Output to RF1 and RF2	Output to RF2

$$Z_0 = \sqrt{A + \frac{BD}{C}}, \qquad \tan\theta = \frac{C \cdot Z_0}{B} \tag{2.8}$$

where

$$Z_L = R_L + jX_L$$
$$Z_S = R_S + jX_S$$

$$A = R_L R_S - X_L X_S$$
$$B = R_L X_S + R_s X_L$$
$$C = R_S - R_L$$
$$D = X_S - X_L$$

Adding a 2nd Omron SPDT (SW2), one can achieve all 4 polarization states (Figure 2.9b & Table 2.2); VP, HP, LHCP and RHCP. The CP modes (CW or CCW) is determined by device SW2. Switch SW2 acts as a 0/180° phase shifter, routing the signal via the λ/2 transmission line (Zo_{180} in Figure 2.9b) when output is set at RF2, or bypassing it when the output is set at RF1 for no phase lag. With the other half of the signal from the SW1 RF1 output routed through a λ/4 TLIN (Zo_{90} in Figure 2.9b) for a 90° relative phase lag, the two orthogonal pairs of antenna feeds are fed the required quadrature phase conditions for LHCP (output of SW2 to RF1) or RHCP (output of SW2 to RF2).

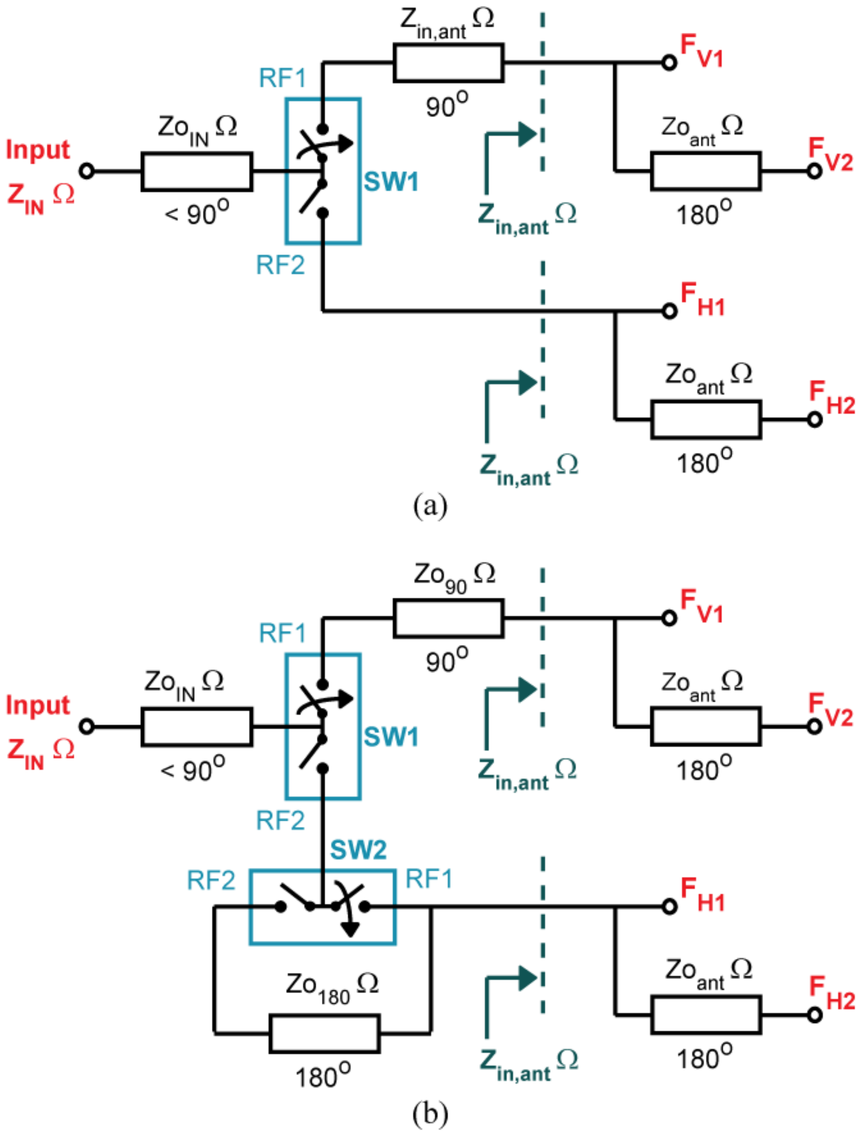

Figure 2.9: Reconfigurable feed network for (a) 3 polarization stages, and (b) 4 polarization stages.

Lastly, as there is no isolation between the two output paths out of SW1 for circular polarization modes, and output RF2 of SW1 is loaded with the 0/180° switch network, Zo_{90} thus serves as an impedance transformer between output RF1 switch SW1 and antenna feed network ($Z_{in,ant}$), to ensure balance of input impedance presented to both output ports of SW1, minimizing on the power imbalance for circular polarization excitations.

2.4.2 Alternate Reconfigurable Network with Frequency Resonance Offset

An alternate way to obtain 4 polarization modes with only 1 MEMS control device is to exploit the reflection phase offset of the two dual orthogonal LP modes of the antenna element. By removing the 90° TLIN segment in Figure 2.9a, and setting the frequency for HP mode (f_H) to be at quadrature phase difference with the VP mode (f_V), CP is achieved when switch device routes power to both RF1 and RF2 outputs (Figure 2.10a).

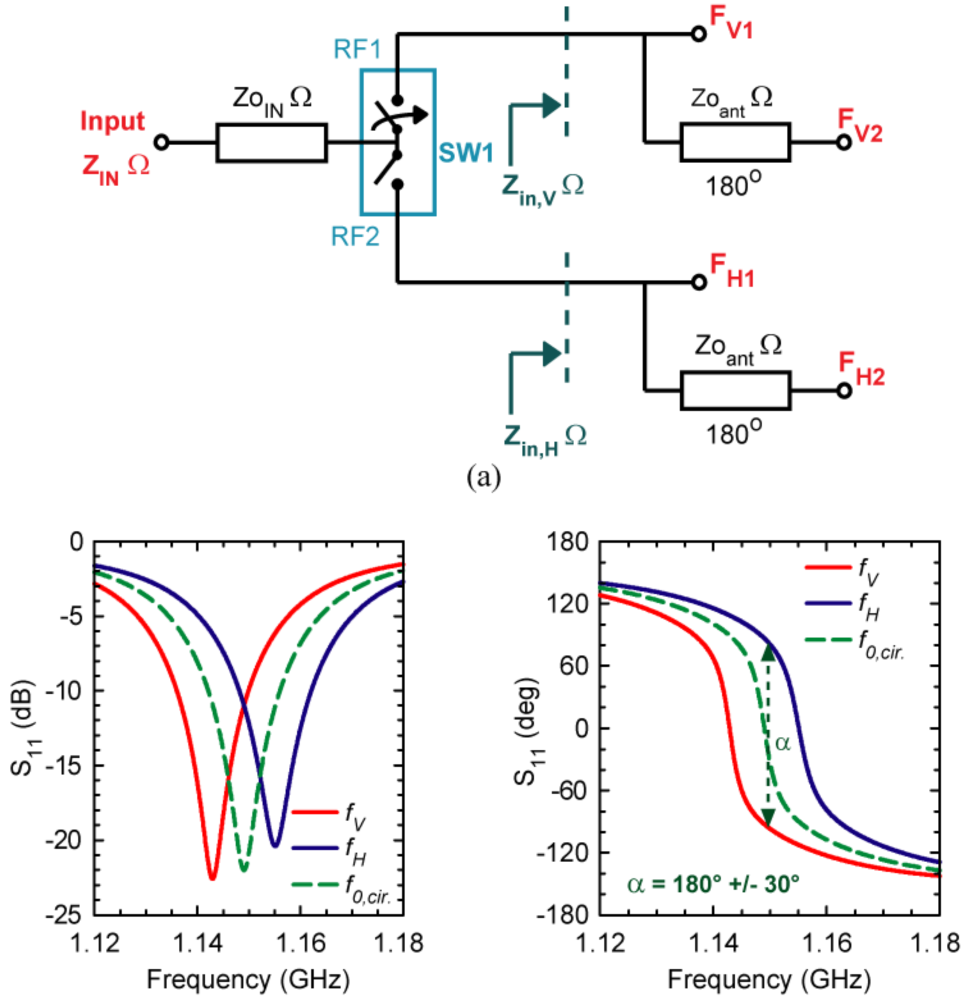

(a)

(b)

Figure 2.10: (a) Alternate reconfigurable feed network for 4 polarization stages with 1 device, and (b) reflection phase and match at the antenna ports

CW or CCW polarization modes is determined with $f_V > f_H$ for phase leading or $f_V < f_H$ for phase lagging. As S_{11} or return loss is an observation of the reflection phase condition, the phase difference for the two modes (observed at F_{V1} and F_{V2} for vertical mode and F_{H1} and F_{H2} for horizontal mode) has to be +/- 180° apart to obtain the quadrature phase difference condition and hence excitation of CP mode (Figure 2.10b).

This approach significantly reduces the complexity of the network, allowing the use of only 1 device for all 4 polarizations. Unfortunately the narrowband behavior of the antenna presents some additional challenges to ensure a good match for the CP states, and more effort is required to identify the required matching condition, namely for Zo_{IN} in Figure 2.10a, and possibly also between switch output ports and antenna input ports.

2.4.3 Polarization Diversity from Antenna Perturbation

Forgoing the use of re-configurable feed network involves the direct perturbation of the antenna element for achieving full polarization diversity, and a conceptual

Table 2.3: Configurations of tuning elements for performing polarization diversity for antenna in Figure 2.11.

LINEAR POLARIZATION STATES

polarization	Feed	T_{PA}	T_{PB}	C_H	C_V
Horizontal (x-axis)	F_{H1}, F_{H2}	S/C		C_F	-
Vertical (y-axis)	F_{V1}, F_{V2}	S/C		-	C_F

CIRCULAR POLARIZATION STATES

polarization	Feed	T_{PA}	T_{PB}	C_H	C_V
Left-handed (CW)	F_{H1}, F_{H2}	S/C	O/C or C_P	C_F	
	F_{V1}, F_{V2}	O/C or C_P	S/C	C_F	
Right-handed (CCW)	F_{H1}, F_{H2}	O/C or C_P	S/C	C_F	
	F_{V1}, F_{V2}	S/C	O/C or C_P	C_F	

REMARKS: C_F - Frequency determination capacitance
C_P - Circular polarization capacitance
S/C - short circuit; O/C - open circuit;

demonstrator was presented in [17], which is presented here. Considering the same square microstrip antenna element with dual independent polarization tuning from Figure 2.5a, the four corners are perturbed with slots, and tuning elements (T_{PA} and T_{PB}) placed across the slots (Figure 2.11a). The tuning elements provide control of polarization diversity for the antenna element.

With the four polarization tuning elements set at 0 Ω or shorted ($T_{PA} = T_{PB} = 0$ Ω) across the slots, the patch element operates in LP mode as a regular patch element. In this mode, the antenna acts as a dual LP mode antenna as described in Section 2.3.1.

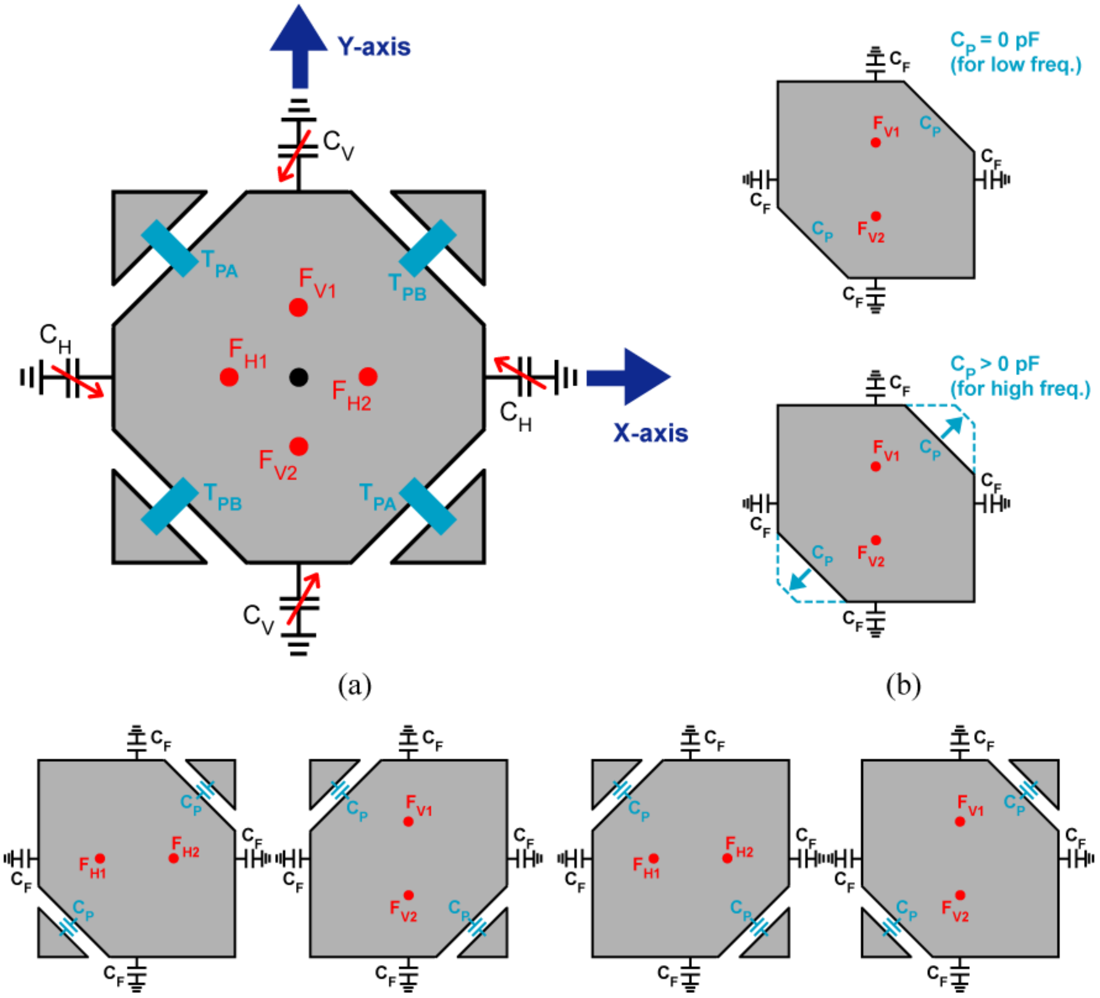

(a) (b)

(c) (d)

Figure 2.11: (a) Antenna element with polarization diversity and frequency tuning, (b) capacitance tuning for high axial ratio in CP modes, and 2 possible configurations for (c) LHCP and (d) RHCP modes.

For CP excitation, a set of two diagonally opposite polarization tuning elements are set at 0 Ω or shorted (e.g. T_{PA} = 0 Ω), and the other set of two diagonally opposite elements at open circuit or some capacitance across the slot to provide the required perturbation of the two orthogonal LP modes (e.g. $T_{PA} > 0$ pF). By interchanging the connections across the slots, for the same feed position, we can easily change the sense of CP mode. Similarly the change in the feed locations (e.g. F_{V1} & F_{V2} to F_{H1} & F_{H2}) will change the sense of CP mode. The other feed-pair is terminated with open loads.

For CP, the four frequency tuning shunt capacitors are set to the same value (i.e. $C_V = C_H = C_F$), and is used to provide frequency agility. Coupling between the orthogonal linear modes are controlled using polarization capacitors across the slots (e.g. $T_{PA} = C_P > 0$ pF), with capacitance values increasing as resonant frequency increases. It can be visualized as "shifting" of the slots outwards away from the patch center with increasing capacitance, thus reducing coupling between the two resonant modes at higher operating frequencies to ensure good axial-ratio (AR) across the frequency range (Figure 2.11b).

Table 2.4: Combinations of feedpoints and polarization control devices for various polarization modes

IMPLEMENTATION COMPLEXITY VS POLARIZATION CONFIGURATIONS

Complexity	Feeds & Pol. Controls	HP	VP	LHCP	RHCP
1 set feed 1 set pol. ctrl.	$F_{H1,2}$, T_{PA}	✓	✗	✗	✓
	$F_{H1,2}$, T_{PB}	✓	✗	✓	✗
	$F_{V1,2}$, T_{PA}	✗	✓	✓	✗
	$F_{V1,2}$, T_{PB}	✗	✓	✗	✓
1 set feed 2 set pol. ctrl.	$F_{H1,2}$, T_{PA} & T_{PB}	✓	✗	✓	✓
	$F_{V1,2}$, T_{PA} & T_{PB}	✗	✓	✓	✓
2 sets feed, 1 set pol. ctrl.	$F_{H1,2}$ & $F_{V1,2}$, T_{PA}	✓	✓	✓	✓
	$F_{H1,2}$ & $F_{V1,2}$, T_{PB}	✓	✓	✓	✓
Complete	$F_{H1,2}$ & $F_{V1,2}$, T_{PA} & T_{PB}	✓	✓	✓	✓

Table 2.3 lists the possible polarization modes for the antenna configuration presented. Possible implementation for frequency tuning elements (i.e. C_V and C_H) is discussed in Section 2.3.1 & 2.3.2. With 2 possible configurations for every CP mode, implementation complexity can be reduced to combinations of feed points and polarization control elements as presented in

Table 2.4. Though differential feeds are recommended for mode purity (esp for out of band response), the proposed concept works well with single-ended feeds.

Polarization tuning mechanisms (i.e. T_{PA} and T_{PB}) includes varactor diodes or RF MEMS tunable capacitors, used in shunt with PIN diodes or RF MEMS metal-contact switches. The antenna element can be shorted to ground with a ground via in the center of the element, providing some simplicity for biasing requirements. For more biasing simplicity (if required), the shorted requirements for polarization control elements (i.e. T_{PA} or $T_{PB} = 0\ \Omega$) can be substituted with large capacitance loading instead, with a penalty of reduced frequency tuning range.

2.4.4 Probe-fed Microstrip Antenna Cross Polarization Analysis

Studies on theoretical cross-polarization (Xpol) levels arising from non-ideal excitation conditions is performed, using an ideal probe-fed 2 GHz antenna element (Figure 2.5a) on a 0.25” thick RO4003 substrate ($\varepsilon_r = 3.55$, $\tan\delta = 0.0027$) in HFSS on an infinite ground plane. The infinite ground plane boundary condition in HFSS will generate patters corresponding to the theoretical microstrip antenna patterns presented in [34]. Simulated normalized cross-polarization and gain degradation resulting from amplitude and phase offset (Table 2.5) are presented in Figure 2.12 for LP from a differentially-phased equal amplitude fed antenna element, and Figure 2.13 for CP from a quadrature-phased fed equal amplitude antenna element.

- For ideal magnitude and phase excitation conditions, lowest Xpol level obtained = -35 dB, and = -39 dB with the presence of shorting via at center of element. Vertical currents on the probe feeds are sources for the Xpol.

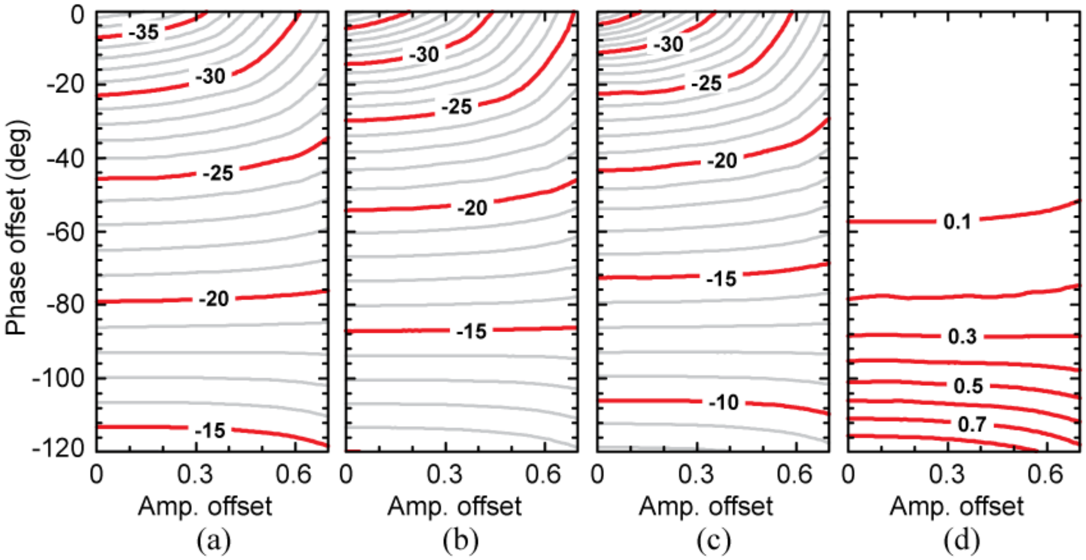

Figure 2.12: Normalized Xpol (in dB) for FOV of θ < (a) 30°, (b) 45° and (c) 60°, and (d) gain degradation (in dB), for differentially fed LP microstrip antenna with amplitude and phase offset.

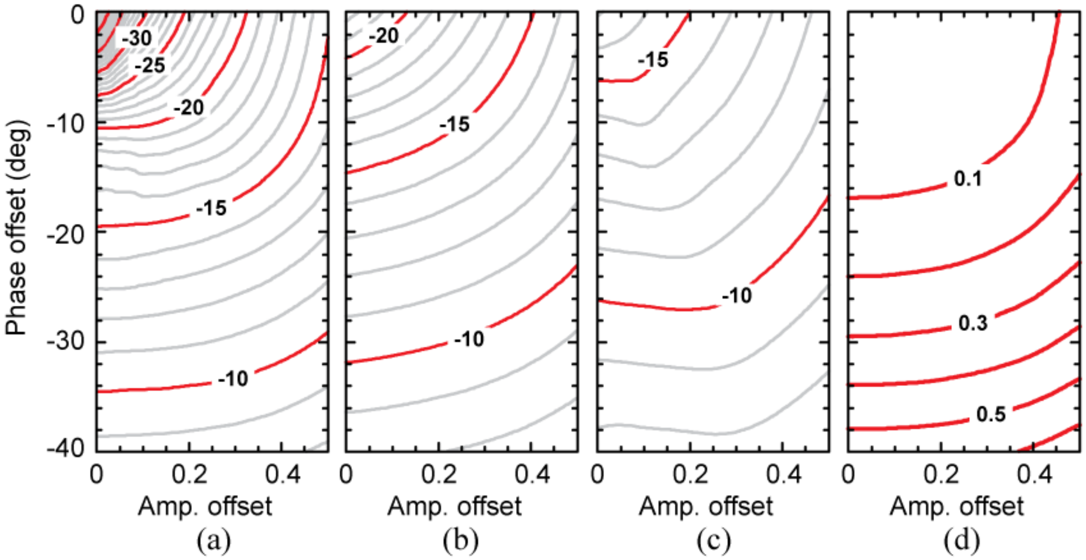

Figure 2.13: Normalized Xpol (in dB) at (a) broadside, and FOV of θ < (b) 30° and (c) 45°, and (d) gain degradation (in dB), for quadrature fed CP microstrip antenna with amplitude and phase offset.

Table 2.5: Feed excitation for Xpol analysis with probe-fed microstrip antenna.

DIFFERENTIAL FEEDS FOR LINEAR POLARIZATION

Feed	Excitation
F_{V1}	$1 \angle 0°$
F_{V2}	$1\text{-}A_D \angle 180° + \alpha_D°$

A_D: Amplitude Offset
α_D: Phase Offset

QUADRATURE FEEDS FOR CIRCULAR POLARIZATION

Feed	Excitation
F_{V1}	$1 \angle 0°$
F_{V2}	$1 \angle 180°$
F_{H1}	$1\text{-}A_C \angle 90° + \alpha_C°$
F_{H2}	$1\text{-}A_C \angle 270° + \alpha_C°$

A_C: Amplitude Offset
α_C: Phase Offset

- The E_θ Xpol component is a minimum at broadside direction, and increases for observation angle away from broadside; i.e. displaying an “M”-shaped pattern profile for top half space of $\theta < 90°$ as amplitude and phase excitation deviates from the ideal differential-phase condition.

- The E_ϕ Xpol component remains low despite of amplitude and phase deviations, reduces to zero at horizon (i.e. $E_{\phi,Xpol} = 0$ for $\theta = 90°$ or X-Y plane), and peaks at broadside direction (i.e. at $\theta = 0°$) with the same intensity as the minimum intensity of E_θ Xpol component.

CP quadrature-phased probe fed microstrip antenna element with similar physical characteristics shows the following cross-polarization pattern trends:

- For ideal quadrature-phased equal-amplitude excitation, lowest Xpol obtained is ~ -40dB at broadside direction (but *not* lower), and degrades *very rapidly* to > - 20 dB for field-of-view (FOV) region of $\theta < 30°$, and > -10 dB for FOV within $\theta < 60°$

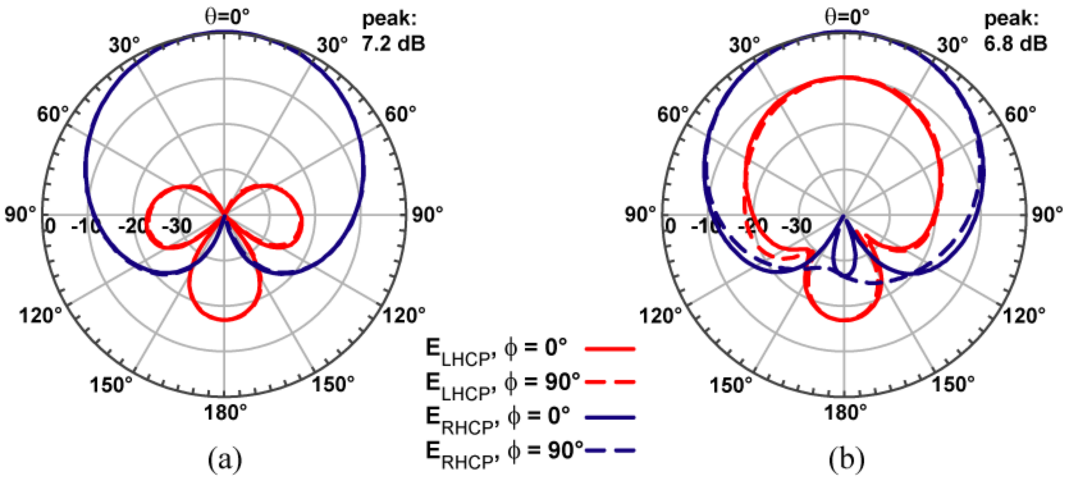

Figure 2.14: HFSS simulated normalized patterns for circularly polarized antenna with; (a) ideal probe feed, and (b) feed network in HFSS.

- Similar to case of E_θ for LP, Xpol component is a minimum at broadside direction, and increases for observation angle away from broadside; i.e. displaying a "M"-shaped pattern profile for top half space of $\theta < 90°$ for low amplitude and phase deviations from quadrature phase excitation, and *rapidly changes* to round profile as minimum Xpol approaches ~ -20 dB.

- Phase deviation from quadrature-phase excitation results in worst case Xpol in principle plane, whereas non-equal amplitude excitation results in worst case Xpol in diagonal plane.

Xpol = -20 dB for LP, and = -10 dB for CP, results in barely 0.2 dB of gain deviation, and will allow for 30% of phase deviation from the ideal differential/quadrature phased feed condition. And finally, expectation of Xpol = -40 dB is definitely not realistic for a single microstrip antenna element, though microstrip arrays can achieve high performance with cross-polarization cancellation techniques at an array level (presented in Chapter 4).

The re-configurable feed network is unfortunately a source of Xpol degradation. Figure 2.14 shows a comparison of HFSS simulated pattern for the same antenna (without the infinite ground plane assumption, and dimensions presented in Figure 2.16); with lumped-port excitation at the antenna probe vias (used for all simulations in this project), and with the feed network captured in HFSS, using the CAD model presented in Figure 2.4 for the MEMS switches. The latter simulation setup take into account the entire feed network, especially the signal splitting of in-phase and quadrature-phase components (needed for CP) results in ground return currents, and both the feed network and ground currents are radiating, causing a significant degradation in the Xpol level.

As such, with the design target for cross-polarization at <-20 dB below the main beam, expected measured values for CP modes will fall within -9 dB to -15 dB, with the network as the main Xpol radiating mechanism.

2.5 Hardware and Measurements

2.5.1 2 GHz Antenna Element

The PCB stack-up is shown in Figure 2.15, with the antenna elements on the top-side, the reconfigurable microstrip feed network on the bottom side, and an embedded layer for reference ground definition for both sides. The RO4000 laminates [35] have more loss and higher ε_r than typical PTFE-based laminates intended for antenna applications (e.g. RT/Duroid 5000 series), but cost a fraction of the RT5000 series, are

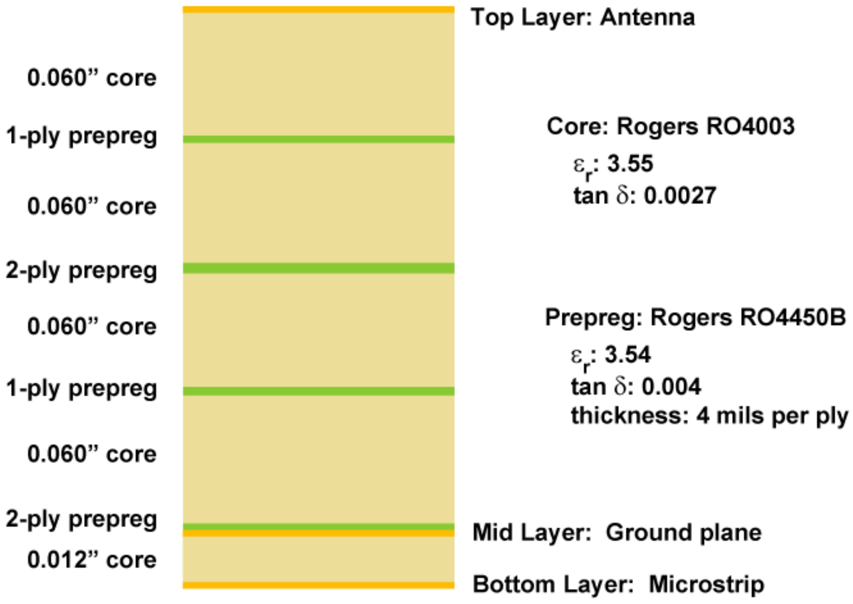

Figure 2.15: Multi-layered PCB stack-up with commercial-grade laminates.

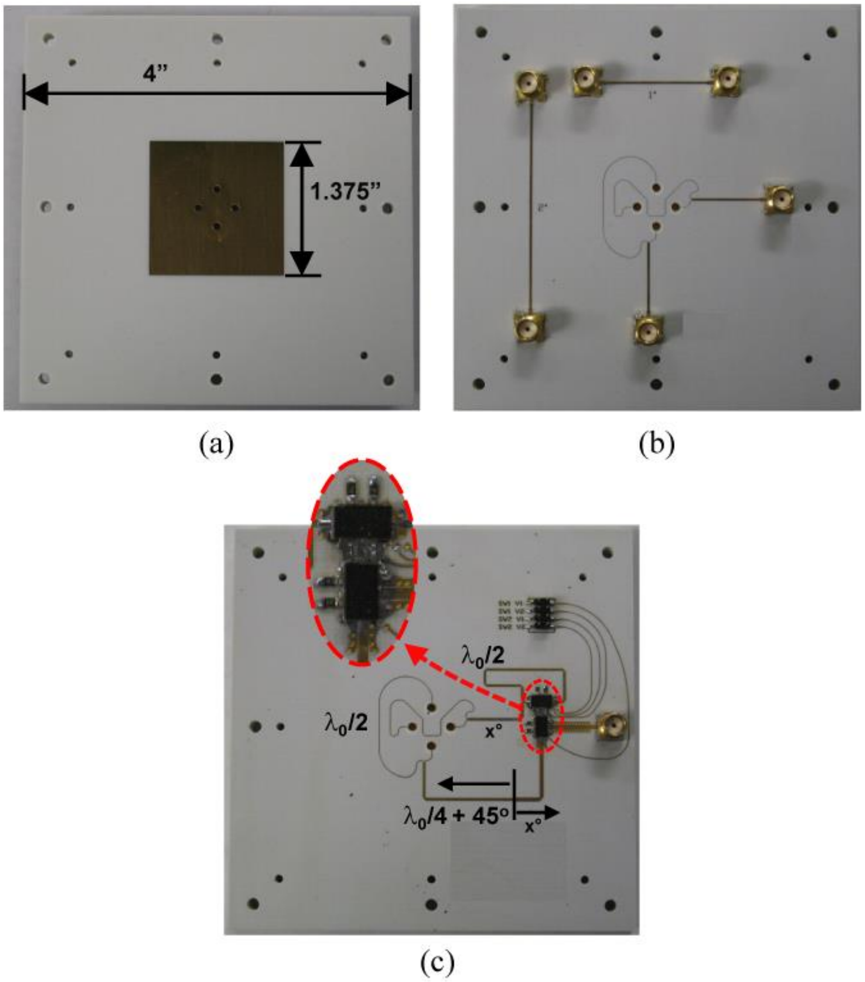

(a) (b)

(c)

Figure 2.16: Hardware realization of 2 GHz microstrip antenna; (a) front view, back view of (b) reference antenna, and (c) antenna with feed network for full polarization diversity (MEMS devices shown in insert).

compatible with conventional FR-4 PCB fabrication processes, do not suffer from warpage or de-lamination in multi-layered PCB lamination process, and are a good candidate for antenna elements with active circuitry, as used in satellite DBS receivers.

Substrate thickness of > 0.25” is required for good radiation efficiency, and can be achieved with customized laminates, or using the commercially-off-the-shelf (COTS) thickness of 0.06” and performing the stack-up as shown in the figure. The low loss ($\tan\delta = 0.0009$) and low relative permittivity ($\varepsilon_r = 2.2$) for Rogers RT/Duroid 5880 would render it the most suitable candidate for the laminate, but RO4003 was chosen instead for it low cost and compatibility with most typical FR-4 fabrication processes.

As such, the trade-off for the substrate choice is the degradation of the radiation efficiency, which approaches to 60% for an infinite substrate and ground plane. But as we are evaluating a single element in a truncated 4”x4” substrate, the simulated radiation efficiency in HFSS is ~ 90%, as the surface waves are not considered by the solver (and our measurements) for the single element on a finite substrate.

Figure 2.16 shows the hardware realization of a 2 GHz antenna on a 4”x4” substrate (corresponding to $0.68\lambda_0$ by $0.68\lambda_0$). Antenna size is 1.375” by 1.375” ($0.23\lambda_0$ by $0.23\lambda_0$), and each linear mode is fed by a pair of 0/180° feed-lines as shown in Figure 2.16b for simplicity. Measured radiation efficiency (with losses for feedlines de-embedded) is 86%, which is 0.3 dB lower than simulated radiated efficiency of 93%, mainly due to the losses from surface roughness in the antenna and feed vias not considered in the simulations.

2.5.2 2 GHz Antenna with Full Polarization Diversity

Hardware realization of a 2 GHz antenna element with full polarization diversity is shown in Figure 2.16c. The feed network corresponds to schematic in Figure 2.9b, with the following impedance conditions for the TLIN segments:

$Z_{in,ant} = 50\ \Omega$, $Zo_{ant} = 100\ \Omega$
$Zo_{90} = 29\ \Omega$, $Zo_{IN} = 31.5\ \Omega$, length 41°

Figure 2.17 presents the measured input reflection coefficient of the reconfigurable antenna at various switch configurations. It is seen that the antenna is well matched at 2 GHz in all four states. The match is > 14 dB for all polarizations, and is consistent with simulated response. Figure 2.18 presents the measured pattern, and they verify the proposed concept. Measurements are performed in Qualcomm Research Laboratory’s Satimo antenna chamber using Stargate-32 measurement system [36]. Peak directivity is ~ 5 dB for linear modes, and ~ 4 dB for circular modes.

Measured efficiency is ~ 67%, which includes ~ 0.76 dB of feed network losses. De-embedded radiation efficiency accounting for the network losses is ~ 80%. Good Xpol levels (<-20 dB) are obtained for the LP cases (Figure 2.18c & d) which corresponds well to simulations. Measured level of Xpol (-14 dB) for the CP cases are significantly higher than the simulated cases (<-20 dB), with reasons presented in the preceding section.

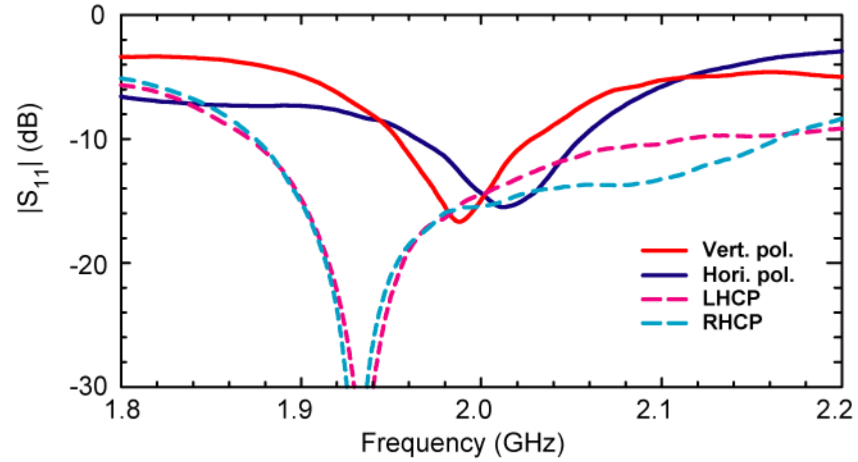

Figure 2.17: Measured return loss responses for 2 GHz antenna with full polarization diversity (Figure 2.16c).

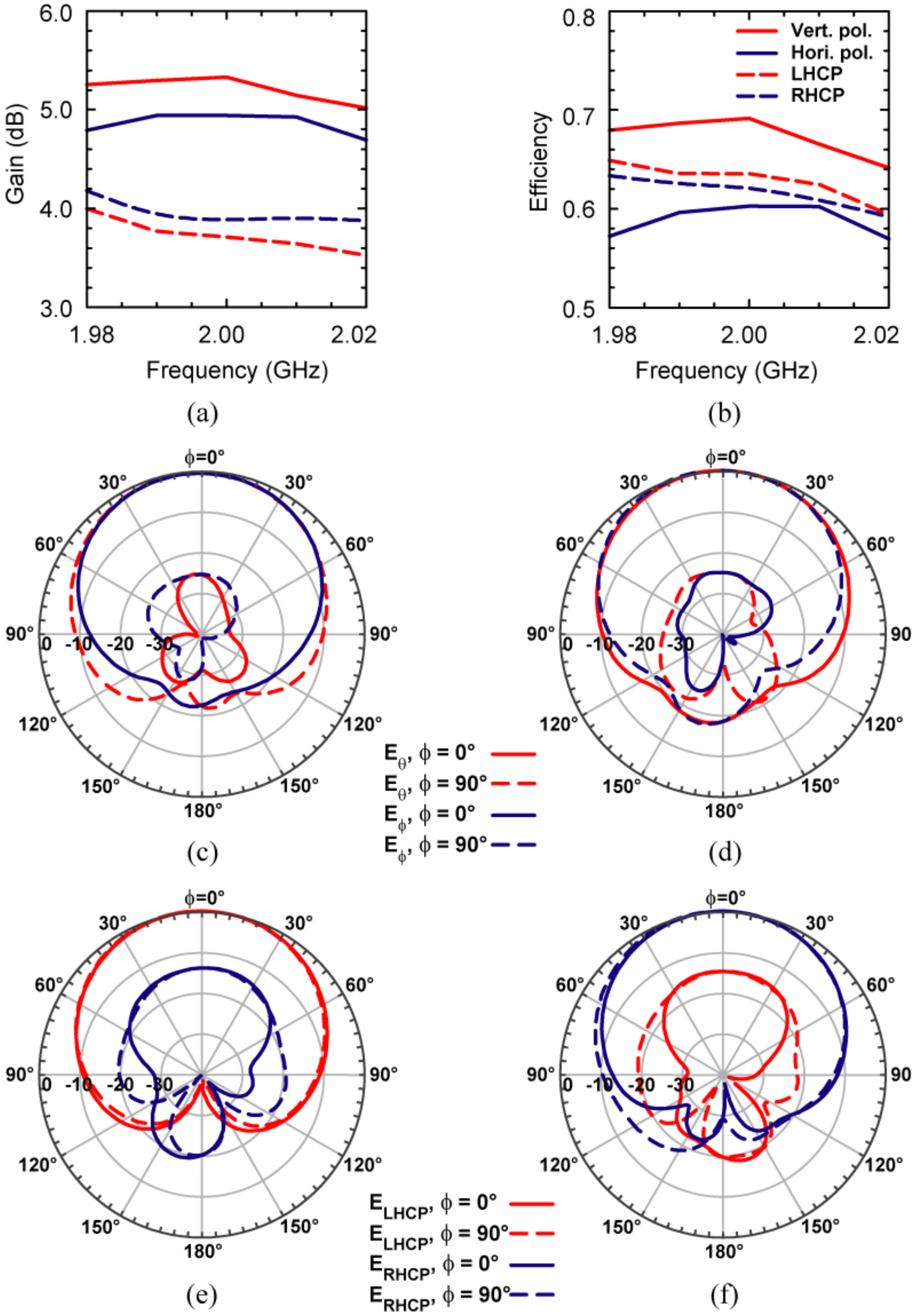

(a) (b)

(c) (d)

(e) (f)

Figure 2.18: Measured (a) gain, (b) efficiency, and normalized patterns for (c) HP, (d) VP, (e) LHCP and (f) RHCP modes, for 2 GHz antenna with full polarization diversity (Figure 2.16c).

2.5.3 Microstrip Antenna with Wide Frequency Span

Figure 2.19 shows the hardware realization of a 1” x 1” square microstrip antenna with frequency tuning loading (Figure 2.19b) with unloaded resonance of 2.1 GHz, and is used as reference antenna for measured center frequency and bandwidth. Substrate size of 4”x4” corresponds to 0.35-0.7 λ_0 at 1-2 GHz. The simulated radiation efficiency with a 3D EM solver is 93% at 2.1 GHz, and the measured radiation efficiency is ~86%, corresponding to ~0.34 dB of via and connector loss which are not accounted in simulations.

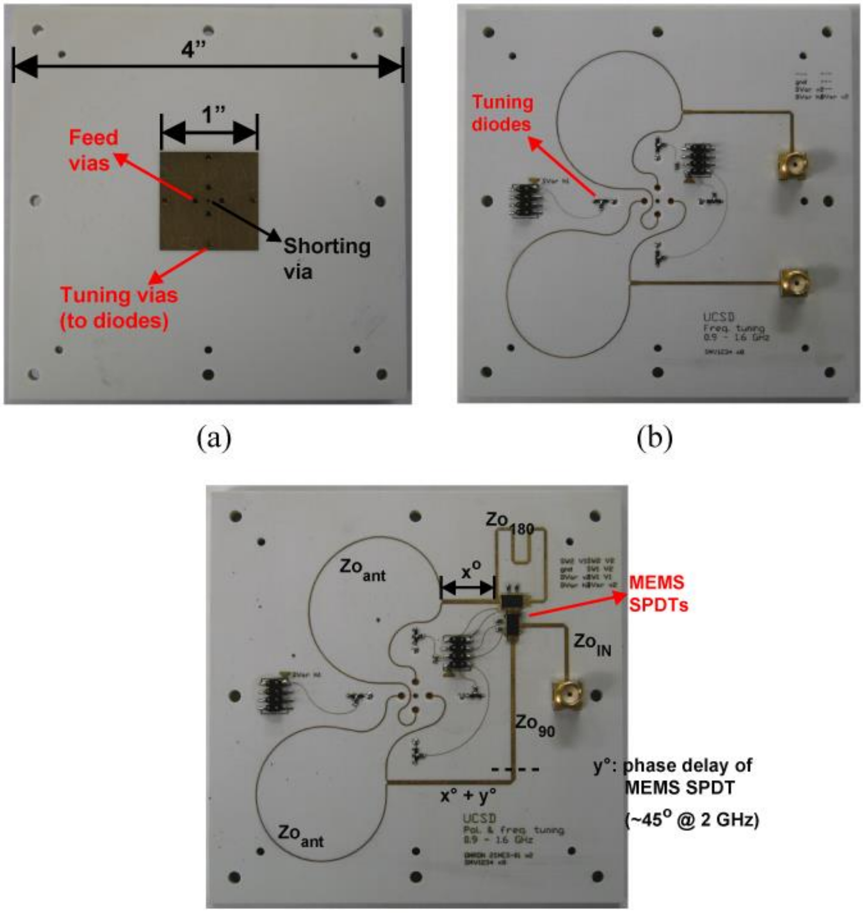

(a) (b)

(c)

Figure 2.19: Hardware realization of L-band microstrip antenna with frequency agility; (a) front view, back view of (b) reference antenna, and (c) antenna with feed network for full polarization diversity.

Skyworks SMV1234 tuning diodes are used in back-to-back configuration (Figure 2.6b), and are implemented on the microstrip feed network layer instead of the antenna layer, to reduce on the discrepancy between the simulated and measured bias voltages from the TLIN phenomenon (Figure 2.7). Plated via diameters of 0.06” are used for tuning diodes and feeds to reduce on via inductances. The antenna is at DC ground potential through the use of a ground via at the center of the antenna for convenience of diode biasing implementation.

Measured VSWR for the reference antenna is presented in Figure 2.20 for LP modes. Measured and simulated resonance frequency and series capacitance are compared in Figure 2.6a, and a good match for the resonances is obtained with measurements from the use of the TLIN models. Good match is obtained for 0.86-1.53 GHz (1.78:1 tuning range). Better VSWR for higher frequency region (higher V_{bias}) in measurements is due to higher diode losses in the measurements than captured from the suggested non-linear diode model in the datasheet [26]. Back-simulations from VSWR measurements reveal a series resistor with fixed value of 0.8 Ω adequately capturing the diode losses across full range of bias voltage conditions.

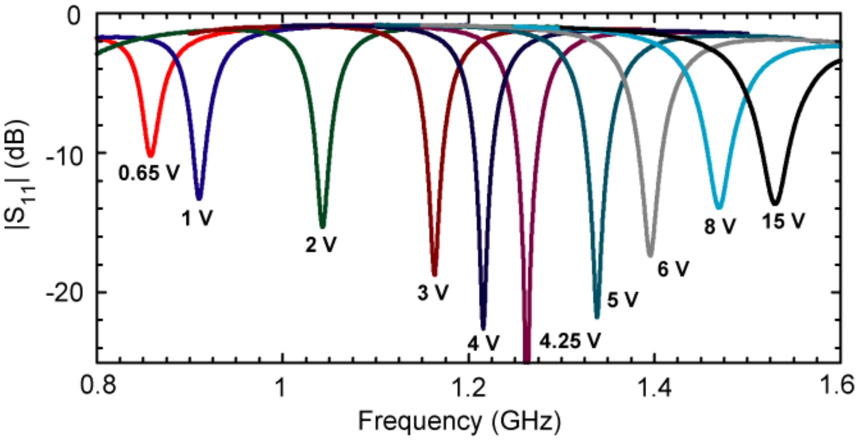

Figure 2.20: Measured return loss responses for reference antenna at various V_{bias} (LP, Figure 2.19b).

Gain measurements are presented in Figure 2.21 and they correspond well with HFSS simulations. Higher losses in measurements at higher frequencies/bias voltages are from the additional diode losses not accounted for in measurements. Measured Xpol of < -20 dB are obtained for all LP cases.

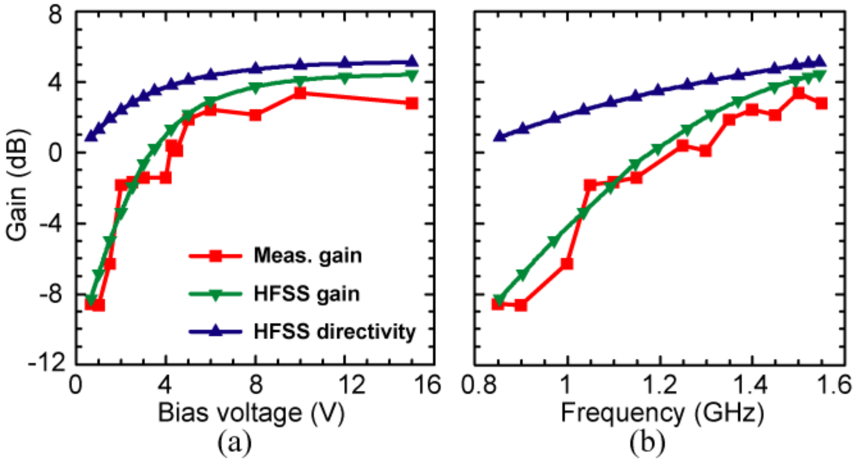

Figure 2.21: Measured gain and directivity for reference antenna versus (a) bias voltage and (b) frequency (LP, Figure 2.19b).

2.5.4 Microstrip Antenna with Full Polarization Diversity across 1.15-1.55 GHz

Hardware realization of a microstrip antenna element with full polarization diversity across a frequency span is shown in Figure 2.19c. The feed network corresponds to schematic in Figure 2.9b, with the following impedance conditions for the TLIN segments (center frequency = 1.3 GHz), which, together with the port impedance presented by the MEMS switches at all operating stages, provide the widest operating bandwidth:

$Z_{in,ant} = 35\ \Omega$, $Zo_{ant} = 70\ \Omega$

$Zo_{180} = 45\ \Omega$, $Zo_{90} = 36\ \Omega$

$Zo_{IN} = 37\ \Omega$, length 64°

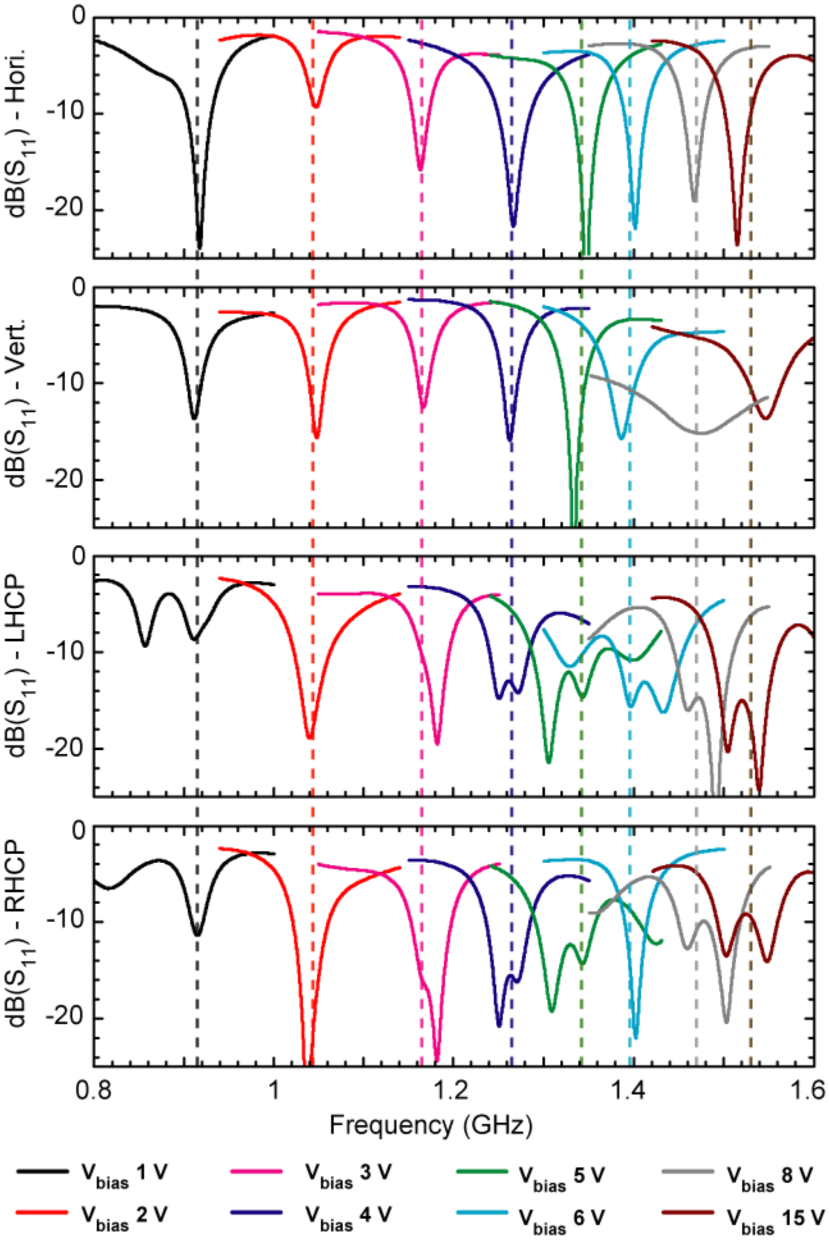

Figure 2.22: Measured return loss for the four polarization states with various bias conditions.

Measured return loss is presented in Figure 2.22 for various bias conditions. An excellent impedance match for (linear) VP and HP modes is obtained at 0.9-1.55 GHz (1.72:1 tuning range). Also, good impedance match for both CP modes are obtained at 1.15-1.55 GHz (1.4:1 turning range). As mentioned above, CP modes suffer a phase deviation of up to 30^{o} at 1.1 GHz due to the fixed feed network designed with 180^{o} at 1.3 GHz. S_{11} measurements agree well with simulations.

The pattern measurements were performed in a Satimo system antenna chamber with 50 MHz steps. The normalized pattern measurements are presented in Figure 2.23, and low Xpol levels are observed for the LP cases, which is consistent with simulations. Again, measurements agree well with simulations (not shown) except that Xpol levels of -9 to -15 dB are observed for the CP cases. Reasons for the Xpol levels are presented in the preceding section, and re-simulations of the antenna element with the feed-network effects are presented in Figure 2.24. In the future, proper packaging techniques to isolate the feed network should minimize this Xpol degradation.

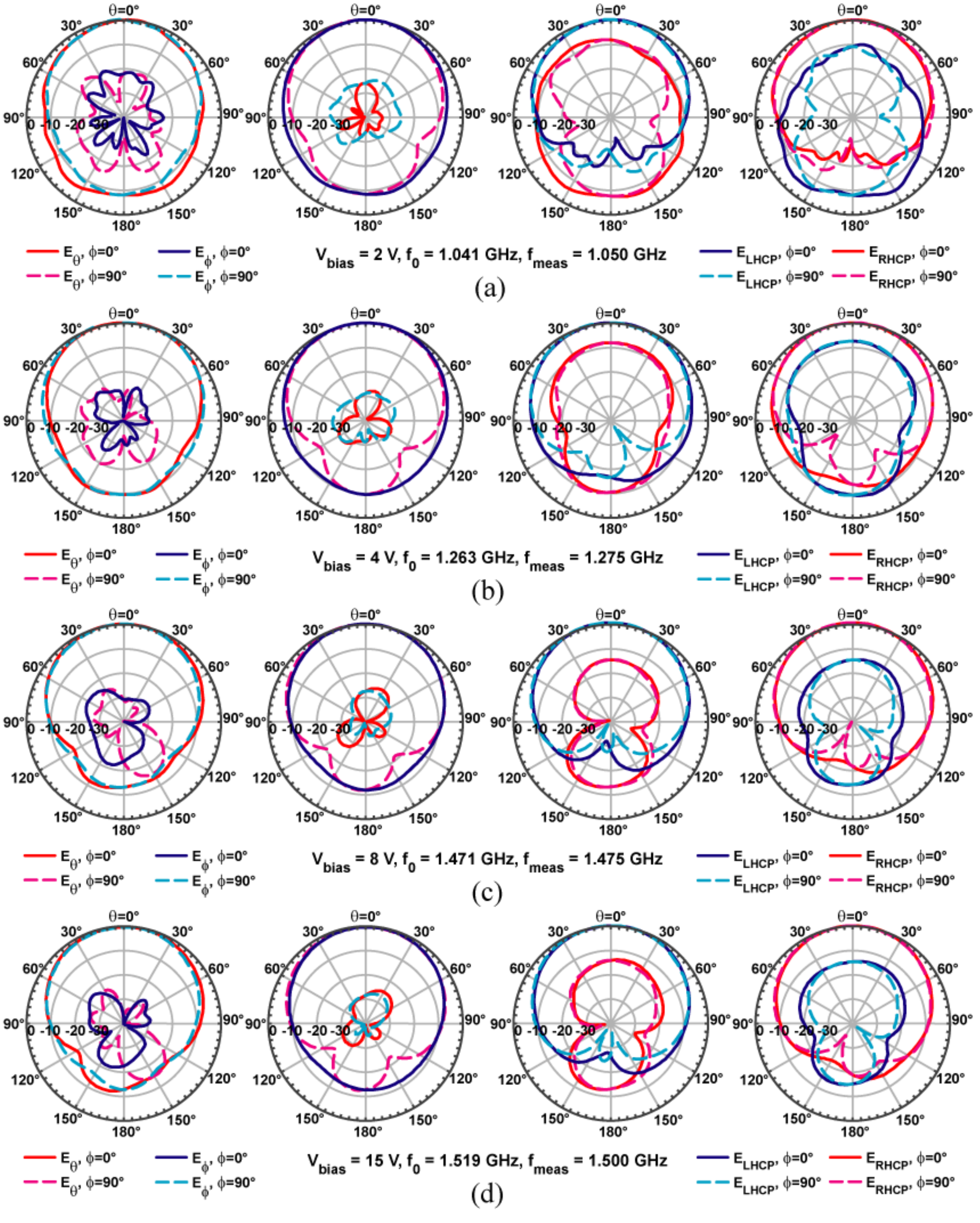

Figure 2.23: Measured antenna patterns of all four polarization modes for various bias cases: (a) 2 V bias, (b) 4 V bias, (c) 8 V bias and (d) 15 V bias. First column for HP modes, second column for VP modes, third column for LHCP, and last column for RHCP.

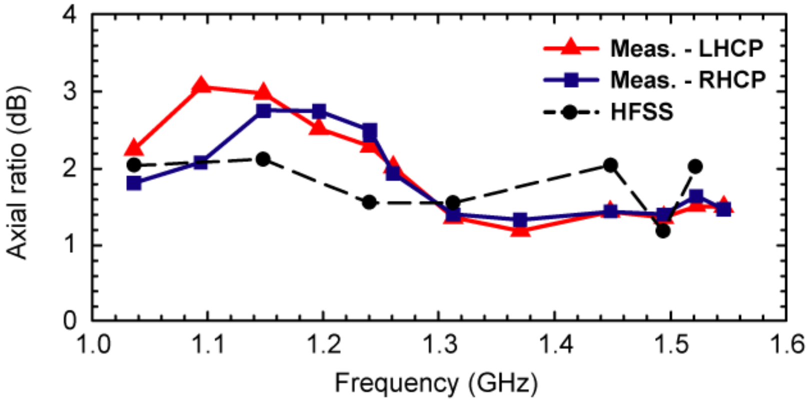

Figure 2.24: Measured and simulated axial-ratio for circular polarization modes.

Figure 2.25 presents the measured directivity, gain and efficiency. The directivity was obtained from the measured patterns in two ways with similar results: a) calculated from measured gain and measured efficiency, and b) performing 3D numerical integration of the measured pattern. The measured gain and efficiency are lower than simulations and this is due to the diode Q (typically lower than the data sheet at 1-2 GHz), surface roughness of the microstrip antenna and feed network not being considered in HFSS simulations, and higher Xpol levels obtained in the measurements than predicted in simulations. Unexpected additional losses from nickel-gold plating in the feed network will be presented in the following chapter. In comparison, the antenna efficiency using MEMS varactors should be ~30% at 1 GHz (Figure 2.8).

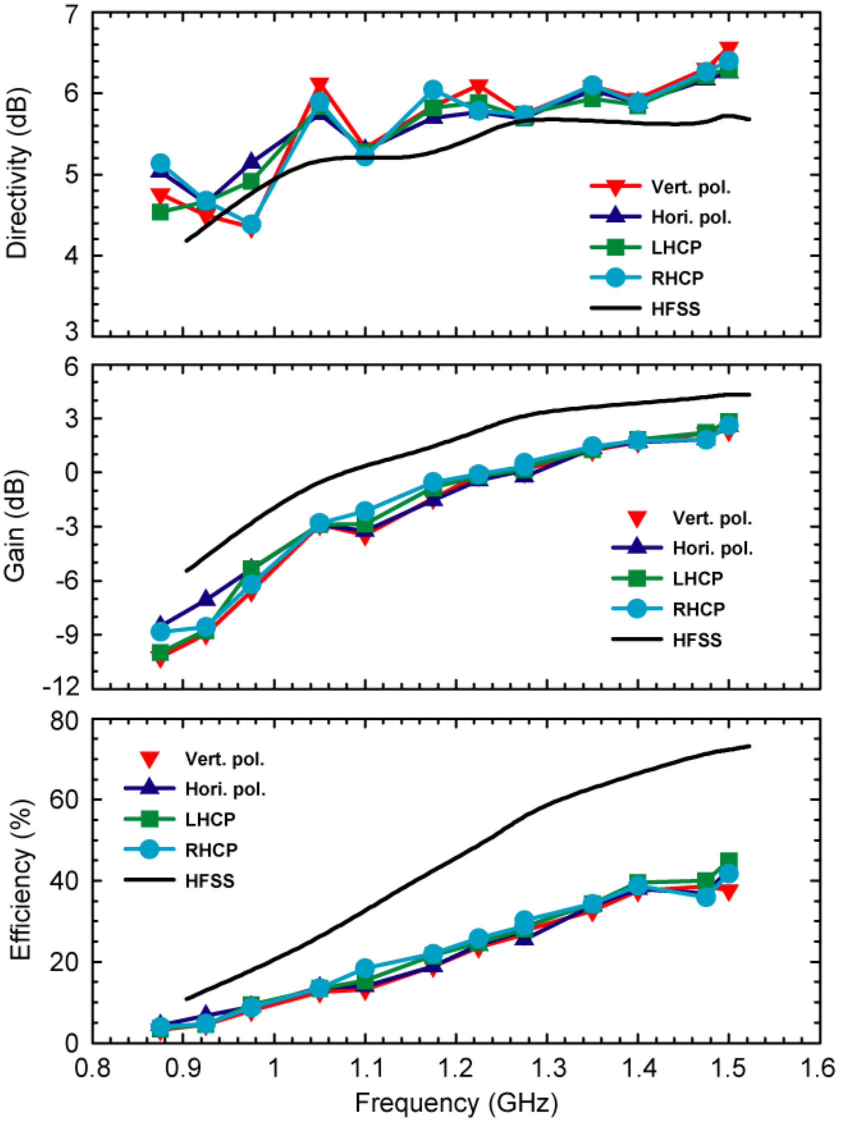

Figure 2.25: Measured vs simulated directivity, gain, and efficiency for all cases of biasing and polarization modes.

2.5.5 Microstrip Antenna with Full Polarization Diversity and Frequency Agility with Single MEMS Switch

By exploiting the phase difference from offset resonances of the two LP modes, Figure 2.10 presents an implementation for full polarization diversity with the use of only 1 MEMS switch. The setup in Figure 2.26 with the reference antenna from Figure

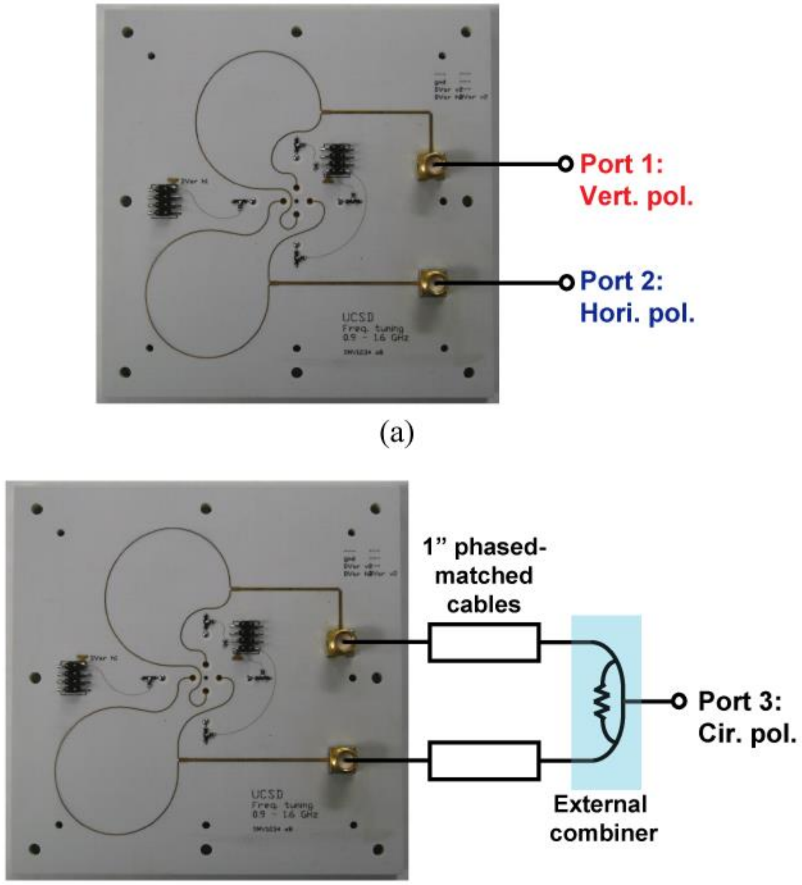

(a)

(b)

Figure 2.26: Setup for conceptual verification of CP excitation (measurements in Figure 2.27).

2.19b and external phase-matched cables and power combiner was implemented to identify the CP excitation.

Measured response for circular polarization is presented in Figure 2.27 for 1-1.5 GHz. Measured Xpol patters differ from those presented in Figure 2.23. Similar to the preceding case, the signal splitting of in-phase and quadrature-phase components (needed for CP) and ground return currents from the two connectors into the external cables and combiner, and the “extended” feed network are radiating together to form the resulting Xpol pattern. Planar implementation of the complete feed network (together with adequate EMI shielding) will reduce the Xpol effect.

A fixed bias offset (δV) was applied to both LP states in this demonstration. More precise bias offset values are required for higher frequency regions where V_{bias} changes rapidly for the same frequency shift.

Replacement of the setup in Figure 2.26 with an Omron MEMS switch on a demo board (as described in Section 2.2.2) was measured (but not presented for brevity). No additional matching was done for these measurements. Performances for linear cases are similar to those presented in Section 2.5.3, since the switch is matched for single output case. Pattern response for circular polarization cases are similar to those presented in Figure 2.27. Good VSWR was obtained for LP cases, but only ~ -4 to -6 dB match was obtained for the CP cases. Xpol for linear polarization cases are consistently < -20 dB, but ~ -9 dB to -13 dB for CP excitations, due to the additional co-radiation of the external feed network of cables and additional switch PCB containing the in-quadrature phase currents.

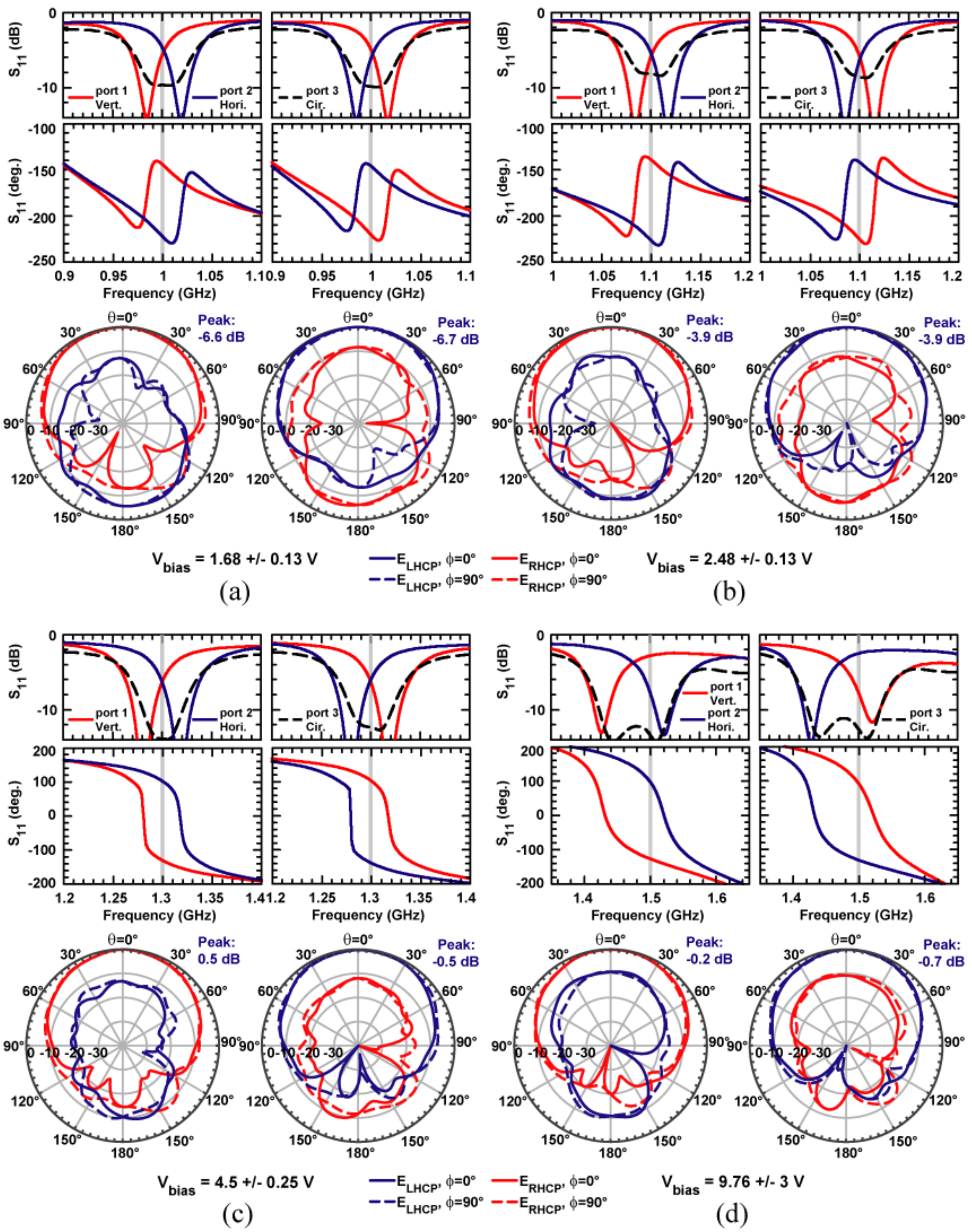

Figure 2.27: Measured CP normalized patters, for cases of (a) 1.68 V bias, (b) 2.48 V bias, (c) 4.5 V bias, and (d) 9.76 V bias.

2.6 Conclusion

A microstrip antenna with full polarization capabilities across a tuning range of 1.15 GHz to 1.55 GHz is presented. Conceptual demonstration for alternate solutions with single switch device for 3 or 4 polarization states are presented for 1 GHz to 1.5 GHz. Good correlation with simulations and measurements are obtained. The work can be extended to one and two-dimensional arrays of microstrip antennas. Better efficiencies, linearity and power handling can be obtained using RF MEMS switched capacitors which are now becoming commercially available for the 0.7-3 GHz range [4],[5].

Chapter 2 is based on and mostly a reprint of the materials that has been published in *IEEE Trans. Antennas Propag.* (May 2014) and *Proc. IEEE Antennas Propag. Symp.* (Jul 2013, 2012, 2010), Kevin M. Ho and Gabriel M. Rebeiz. The dissertation author was the primary author of these materials.

Chapter 3

Compact X-Band FMCW Phased Array Receiver with Packaged CMOS Phased Array RFIC chips

3.1 Overview

3.1.1 Compact T/R Modules and Integrated Phased Arrays

Utilizing the advances in packaging and assembly techniques, modern T/R modules are typically based on solid-state technologies for planar implementation and interface, and assembled on multi-layered platforms. Active and control devices are usually developed with gallium arsenide (GaAs) based monolithic microwave integrated circuit (MMIC) technology. Low-temperature co-fired ceramics (LTCC) exemplifies ceramic-based solutions for multi-layered planar technology (Figure 3.1a), and conventional FR-4 based printed circuit boards (PCBs) represents majority of organic-based counterparts (Figure 3.1b [37]).

Direct implementation of components and devices on the same planar platforms with the antenna elements allows for further size reduction and (depending on the details of the chosen process and materials) some degree of cost reduction. Examples of electronically scanned arrays with direct circuitry and planar antenna array integration (for broadside arrays) on PCB includes [38] at X-band for unmanned ground sensor (Figure 3.2), and [39] at X-band for satellite communications.

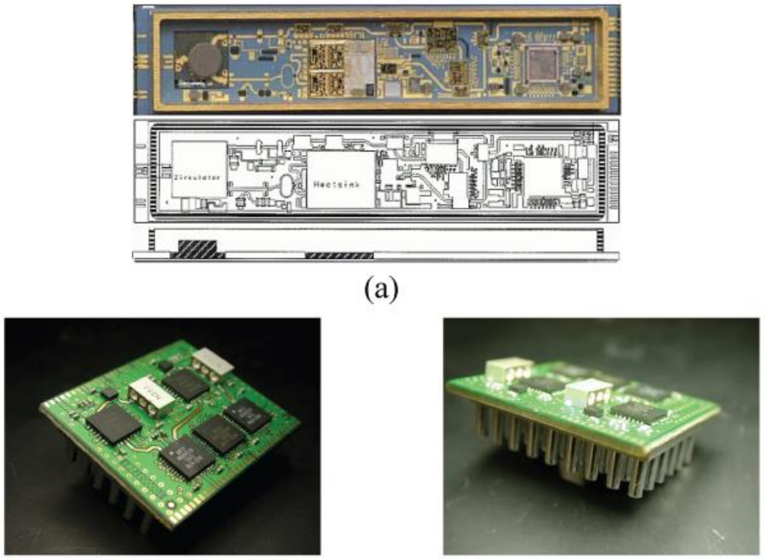

(a)

(b)

Figure 3.1: T/R modules (a) on LTCC for X-band application, and (b) FR-4 PCBs for L/C band [37].

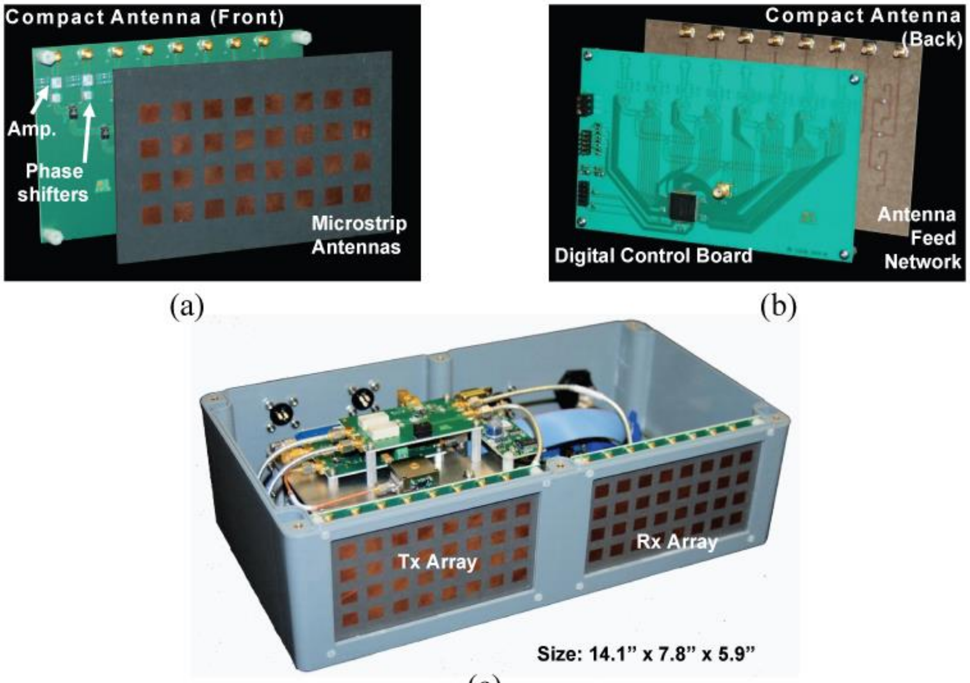

(a)

(b)

(c)

Figure 3.2: Compact X-band FMCW radar; (a) front view and (b) back view of antenna array and feed network, and (c) complete radar module [38].

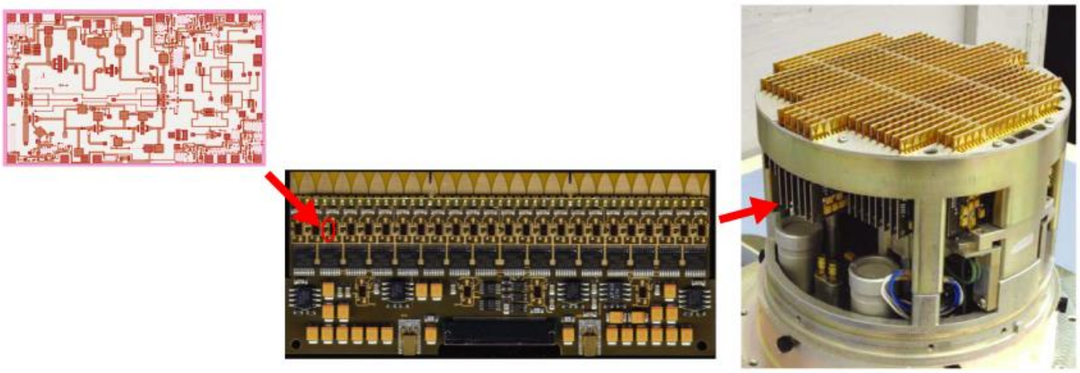

Figure 3.3: Phased array on PCB with end-fired slot antennas [41].

Figure 3.4: Planar Ka-band phased array on LTCC; (a) cavity-backed antenna elements and (b) back-view with RF circuitry [43].

Further PCB examples for wider bandwidth requirements include [40] with planar antenna arrays for multi-functional radar applications, and [41]-[42] with end-fire slot arrays for military airborne platforms. Demonstrations for alternative platforms include [43] on LTCC at Ka-band for mobile satellite communications, [44] on liquid crystal polymer (LCP), and [45] for a novel method of wafer-level integration with thin-film dielectric on silicon. Though [44] is not an electronically-scanned array, it is worth noting its novel 3D integration of all the functionalities in a very compact form factor using PCB and LCP materials.

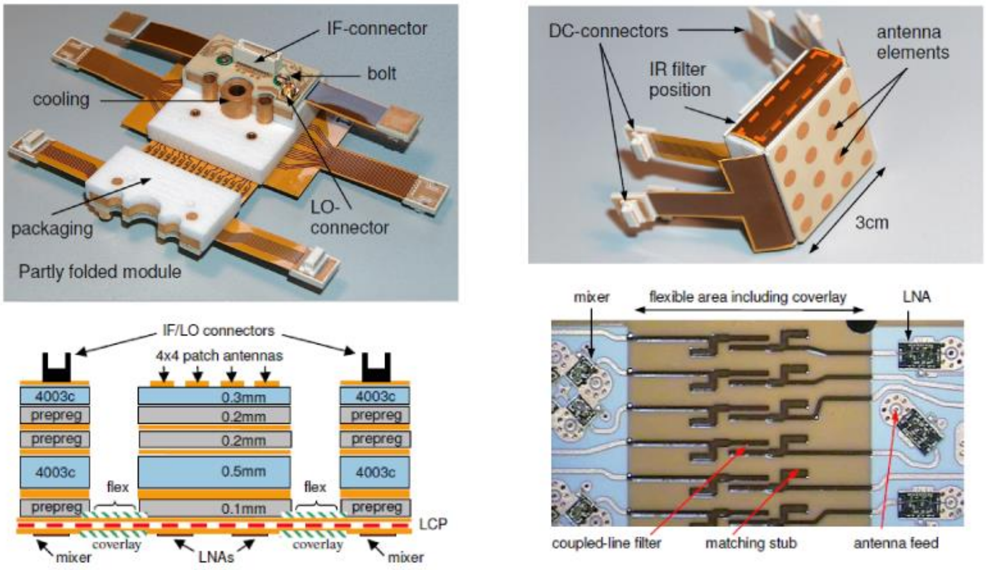

Figure 3.5: Integrated 3D array on LCP for K-band [44].

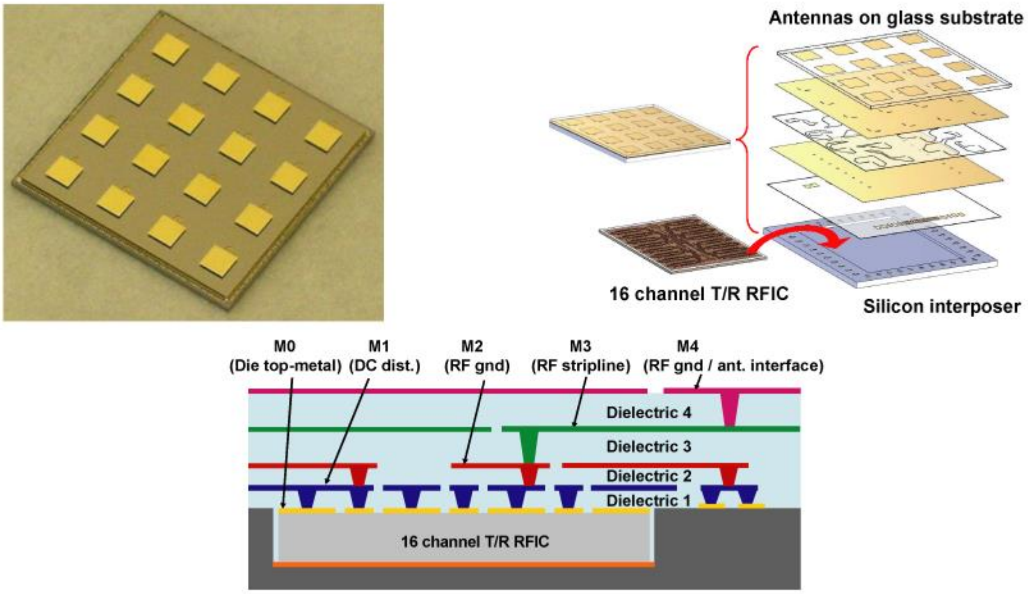

Figure 3.6: Phased array with RFIC on thin-film dielectric on silicon at wafer-level integration [45].

The recent advances of SiGe and CMOS for phased-array applications have resulted in very complex transmit/receive chips with 4-16 channels at X to W-band frequencies [46]-[54]. These chips not only provide multiple RF channels, but also, a Wilkinson combiner/divider, and advanced digital control functionality. This significantly reduces the complexity of the PCB routings allowing for phased-arrays with a short development time. Furthermore, these chips can be packaged in low-cost commercial plastic quad-flat no leads (QFN) packages, and can be placed on the PCB using automated surface-mount-technology assembly, thus eliminating manual assembly and increasing the reliability of the phased-array panel.

3.1.2 Chapter Overview

Directly integrating receiver phased-array RFIC chips presented in [47] on commercial-grade multi-layered PCB stack-up, this chapter presents the development efforts of a receiver phase array as part of an X-band FMCW unmanned portable compact radar shown in Figure 3.2 [38]. Focus for this work is on performance degradation arising from both RFIC-PCB integration for wire-bond and QFN packaged assembly solutions, and use of commercial-grade laminates for antenna arrays.

Requirements for the antenna array are first presented, followed by overall active array architecture implementation and simulated passive array performance. Linear array design methodology will be presented. Architecture and key performance for RFIC phased-array receiver chips are presented in brief, with the materials presented from [47]. Comparison of isolation and matching performance arising from both wire-bonded and QFN-packaged RFICs assembled on PCBs will be presented next.

Performance degradation from commercial laminates is presented next. Starting with the impact on antenna arrays, discussions are geared towards potential scan blindness and radiation efficiency. Focus is next on phase velocity deviations and apparent dielectric relative permittivity (ε_r) values of laminates with significant surface roughness. Findings on additional losses arising from gold-nickel plating for PCB surface finishing are presented. Finally, hardware realizations and measurements are presented for antenna element and active receiver array.

3.2 Phased-Array Antenna

3.2.1 Array Specifications and Overall Architecture

Targeted application for the receiver array was for unmanned ground sensor, with one dimensional scanning capability in the azimuth plane. Together with another transmit phased array, this receiver array is intended to be part of an FMCW compact radar system operating at X-band. Full radar hardware system is presented in Figure 3.2. Pattern requirements for the antenna array includes a fan beam with azimuth scanning of 45°, half-power beamwidth (HPBW) of ~12° in the scan azimuth plane, and ~25° in the fixed elevation plane. Operating frequency can be chosen to be at any frequency within 8.5-9.5 GHz, with instaneous operating bandwidth of 75 MHz. Array size should not exceed 5.9” by 3.7”, to fit to chassis aperture of an existing sensor system. Antenna gain required > 18 dB.

A linear array of 8 channels with physical channel separation of ~ 0.5 to $0.55\lambda_0$ satisfies the HPBW requirements in the azimuth plane while staying within 5.9” in size. Independent phase and amplitude control for these 8 channels allows for phase scanning ability and sidelobes reduction respectively in the azimuth plane. 2 4-channel CMOS RFIC receiver chips are used to provide the 8 channels of RF front-end circuitry for the receive array.

For higher gain and HPBW requirements in the fixed beam elevation plane, each channel comprises of 4 elements of in-phased microstrip antenna elements spaced ~ $0.6\lambda_0$ apart while staying within 3.7”. Figure 3.7 shows the proposed implementation for the 4x8 active receiver array, with a single PCB stack-up for the 4x8 antenna array, 2 RFIC phased-array chips, 2-way Wilkinson power combining, and all the required digital and DC routings. Implementation for transmitter array will be similar, with the RFIC receiver chips replaced with transmitter chips.

Finally, without any physical constrains imposed on the back side of the array, slot-coupled microstrip fed microstrip antenna array is implemented, allowing the choice of substate ε_r and thickness independently chosen to address problems or optimizing performance for both antenna elements and the feed network. The RFIC

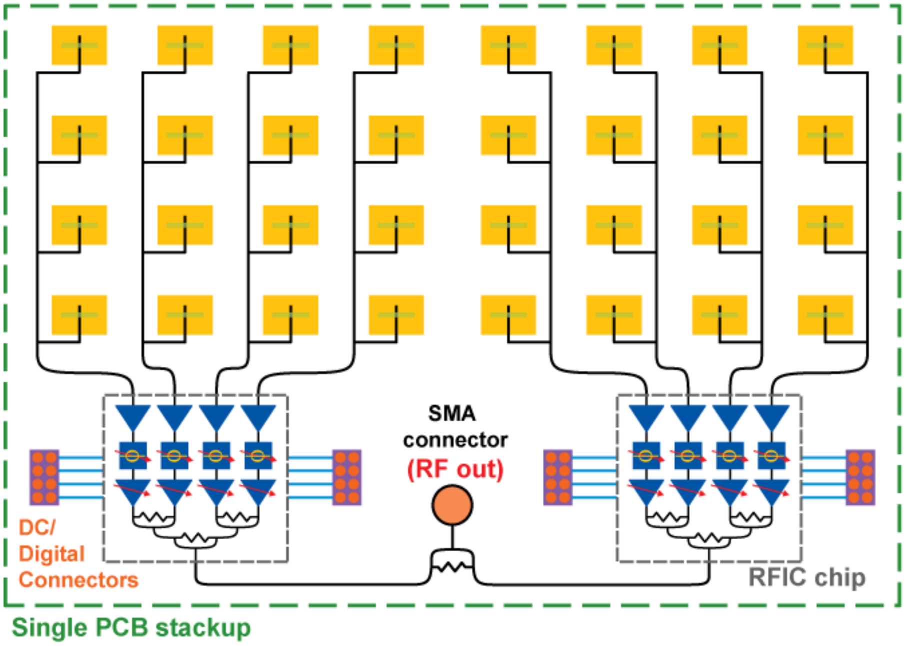

Figure 3.7: Overall architecture of RFIC receive phased array antenna.

receivers can be directly implemented on the same microstrip layer as the antenna feed network for minimizing on loss, as compared to requiring plated vias for layered interconnections for separate RFIC interface and antenna network layers.

3.2.2 Antenna Element and Linear Array Design

Figure 3.8a and Figure 3.8b presents calculated radiation efficiency and bandwidth for microstrip antenna on RO4003 laminate (ε_r = 3.55, tanδ = 0.0027). Theoretical calculations are based on [28]-[30] and [55], and they matches well with IE3D simulations. 2 ply of RO4450B prepreg (ε_r = 3.54, tanδ = 0.004, thickness = 0.004” per ply) are added to the laminate’s thickess for the IE3D simulations.

IE3D simulated directivity, gain (Figure 3.8c), radiation efficiency and antenna efficiency (Figure 3.8d) are presented for cases of implementation with 0.032” and 0.06” substrate thickness. Antenna efficiency considers the input impedance mismatch factor. 0.06” substrate thickness (= 0.068” in Figure 3.8 for additional 2 ply of prepreg) is chosen for its bandwidth of 600 MHz while having > 60% radiation efficiency (=

66%). Though operating bandwidth is only 75 MHz, the wider flat-band response for the will allow for operation at slight offseted frequencies, and less fluctuations to scan impedance variations. Normalized back-radiation is -15 dB.

Simulated normalized patterns for 8-channel array in the azimith scan plane are presented in Figure 3.9 for maximum scan angles, with rectangular antenna element size of 0.28λ_0 by 0.2λ_0, and element spacing of 0.53λ_0. Though intended application is up to 45° beam-scan away from broadside, case of 60° is also looked into for the studies, and

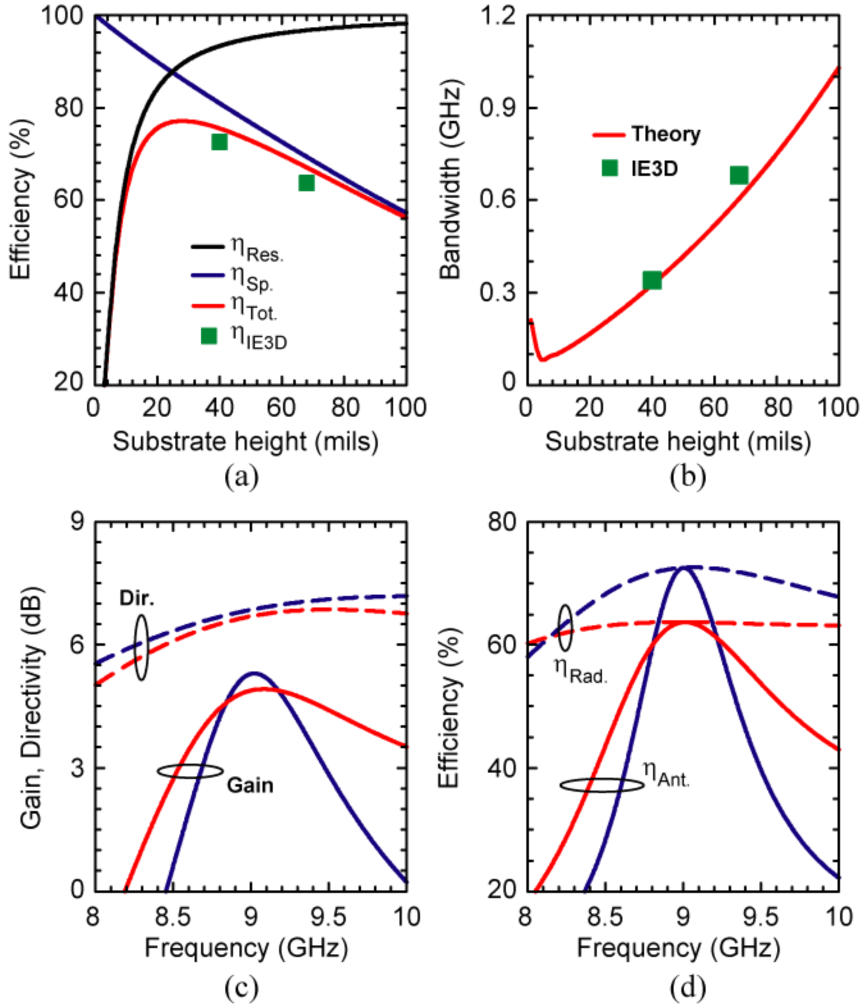

(a) (b)

(c) (d)

Figure 3.8: Theoretical calculations and IE3D simulations for (a) radiation efficiency and (b) fractional bandwidth vs substrate height, and IE3D simulations for (c) directivity, gain and (d) radiation and antenna efficiency for microstrip antenna on 0.032” and 0.06” thick RO4003 laminate.

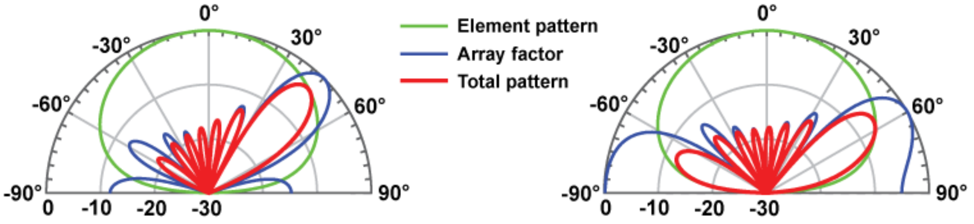

(a) (b)

Figure 3.9: 8-channel linear array with $0.53\lambda_0$ element spacing (blue), microstrip antenna H-plane (green), and microstrip array (red) normalized patterns; (a) 45° and (b) 60° scan with uniform distribution.

presented here.

Orientation of microstrip antenna element is such that scan plane is the H-plane to avoid potential scan blindness (as discussed in next section), and to minimize on grating lobes. For case of 45° beam scan, ~ 3.5 dB of truncation from the H-plane element pattern on the main beam will bring the first sidelobe to ~ -10 dB below the main beam (Figure 3.9a). For 60° scan cases, the edge truncation from the H-plane pattern is insufficient to sufficiently reduce the onset of the grating lobe (Figure 3.9b), and reducing element spacing to $0.5\lambda_0$ will reduce it to < -10 dB below main beam.

To minimize on both loss and complexity of design, the 4-element feed network can be independently designed from the antenna element in a serial feed manner as presented in Figure 3.10. With equal power division to each antenna element, the power split ratio in the N^{th} junction can be expressed as:

$$P_{split,dB} = 10 \cdot \log_{10} N \tag{3.1}$$

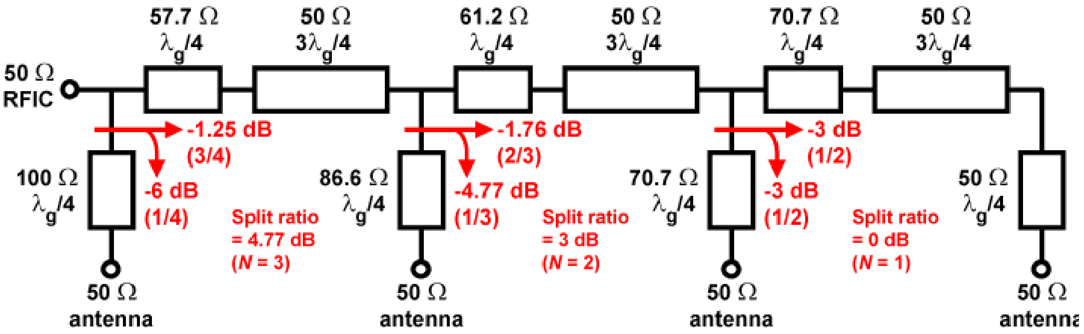

Figure 3.10: Feed network for 4-element linear array.

Main branch is maintained at 1 guided wavelength (λ_g) always, to optimize on bandwidth and minimize on losses and routing complexity. Substrate ε_r can be independently chosen to match to the range of desired spatial separation of the antenna elements (i.e ~ $0.6\lambda_0$ in this case).

A common phenomenon faced with commercial-grade laminates is the increase in effective permittivity arising from various factors (presented in next section). For case of $\varepsilon_r = 3.66$ (for RO4350), apparent ε_r of up to 4 leads to additional 15° of phase progression. For element spacing of $0.6\lambda_0$, that corresponds to 4° of tilt by the main beam, which can be determined based on the following expression:

$$\theta_{TB} = \sin^{-1}\left(\frac{\alpha_0 + \alpha'}{2\pi \frac{a}{\lambda_0}}\right) \tag{3.2}$$

where θ_{TB} is the new tilted main beam, α' the additional phase progression, α_0 the original phase progression (=0° in this case), and a the element spacing of the linear array.

3.3 RFIC Phased-Array Receiver Chips

The RFIC receiver (Rx) chips are fabricationed on a low-cost 0.13-μm CMOS technology, with an f_T of 100 GHz at bias current of 0.1 mA/μm and an minimum noise figure (NF_{min}) of 0.8 dB at 10 GHz (IBM8RF, Figure 3.11). Single-ended grounded coplanar-waveguides (CPW) are used in the receiver chip, and differental CPW for the transmitter chip. Typical Q of ~ 15 are obtained for inductors, which are simulated in Sonnet. Capacitors are implemented with metal-insulator-metal (MIM) capacitors, and have Q > 20 at 10 GHz. nMOS capacitors are used primarily for decouping and isolation purposes, together with trenches as isolation walls for the latter intents. Digital signal routings are done using M2 or M3 layers, and are shielded by M1, MQ and LY layers as ground planes to isolate the digital switching noise from the RF analog path.

Block diagram for Rx chip is presented in Figure 3.12a. Featuring *all-RF* architecture design (phase shifting and signal combining in the RF domain), the Rx chip features 5-bit phase shifter with lowest bit as a trim-bit, and 4-bit variable gain to reduce on r.m.s. gain errors. After correcting for gain errors of ~2-3 dB, ~ 4-5 dB of gain variation is available for antenna pattern shaping & sidelobe suppression. Microphotograh of the chip is presented in Figure 3.12b, and chip size is 2.9x2.5 mm^2.

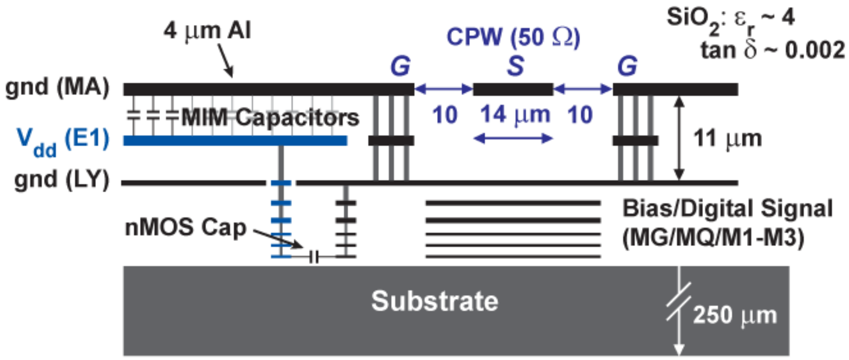

Figure 3.11: IBM8RF stack-up.

The measured on-chip performance is summarized in [47] and shows a gain of ~10 dB per channel, an input P_{1dB} of -12 dBm (input IP_3 of -3 to -4 dBm), and a NF < 3.7 dB at 9-9.5 GHz. The CMOS chip can be used together with a GaAs LNA (on every antenna) with 17 dB gain and 0.6 dB NF and results in a total channel gain of 27 dB, input P_{1dB} of -26 dBm and a receiver NF < 0.8 dB (not including the antenna loss). The combined GaAs+silicon receiver would be competitive for point-to-point communications, and in long-range FMCW radars for perimeter detection.

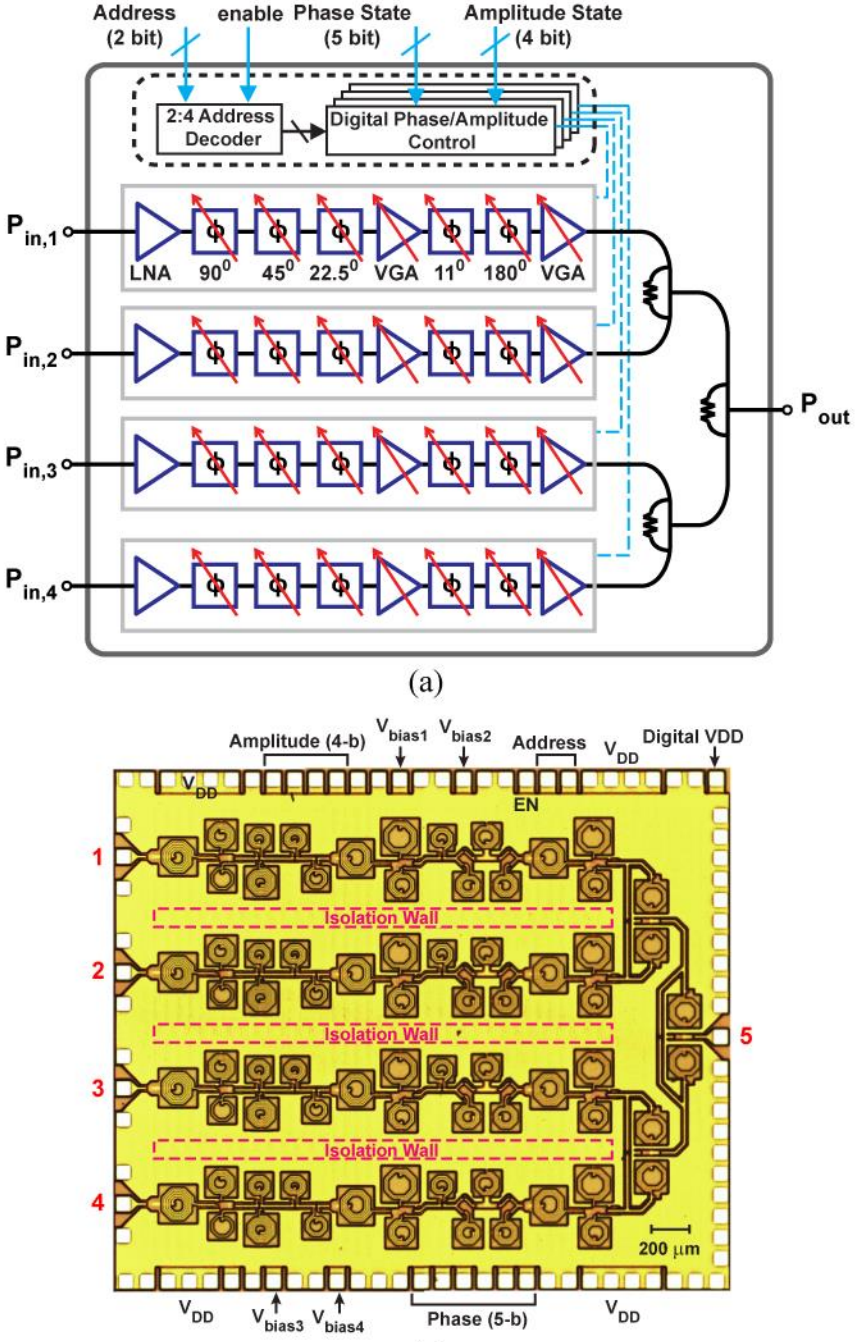

(a)

(b)

Figure 3.12: Block diagram (top) and microphotograph (bottom) of 4-channel phased-array receiver chip [47].

3.4 RFIC-PCB interface

3.4.1 Wire-bond and QFN-packaged RFICs Assembly on PCB

Both impedance matching for every channel, and isolation between adjacent channels, are concerns for PCB-RFIC interface of phased array RFICs, with performance degradation through the PCB or through the package too for implementation of packaged chips. Matching degradation is primarily from the bondwire inductance, followed by any shunt capacitance from PCB pads or packaging material which brings the response to a distributed behaviour.

The return ground current forms the primarily source of isolation degradation, and has to be adequately identified for high isolation performance. As compared to MMICs, signal reference for RFICs may not be as obvious. Unlike microstrip on PCBs or MMICs where the bottom-most of the substrate or die is the microstrip signal's ground plane, RF routings for RFICs resides in a thin silicon-oxide (SiO_2) layer of ~ 10 um above a 250 µm thick silicon die. Signal reference is introduced from the ground

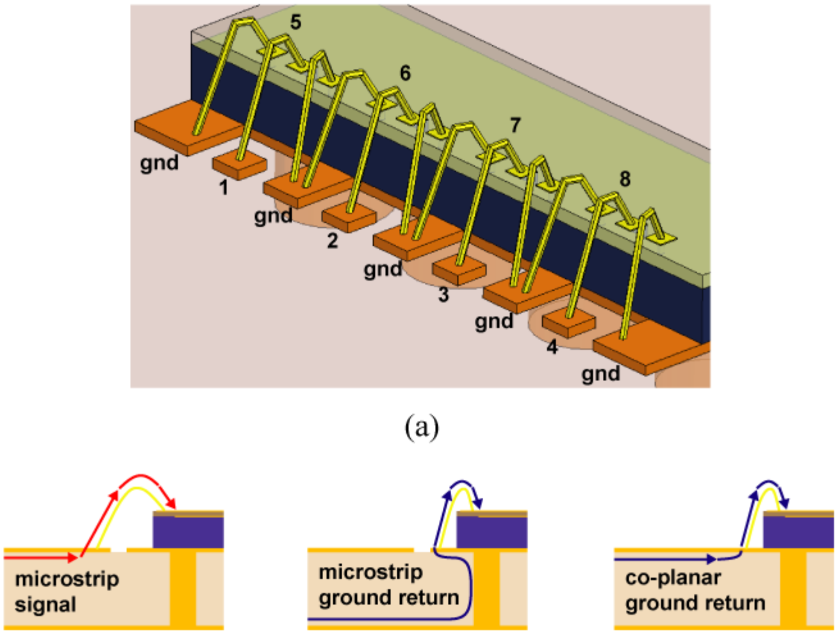

(a)

(b) (c) (d)

Figure 3.13: (a) RFIC on PCB, and current flow from PCB to RFIC through wire-bond interface for (b) signal, (c) ground return for microstrip launch, and (d) ground return for CPW launch.

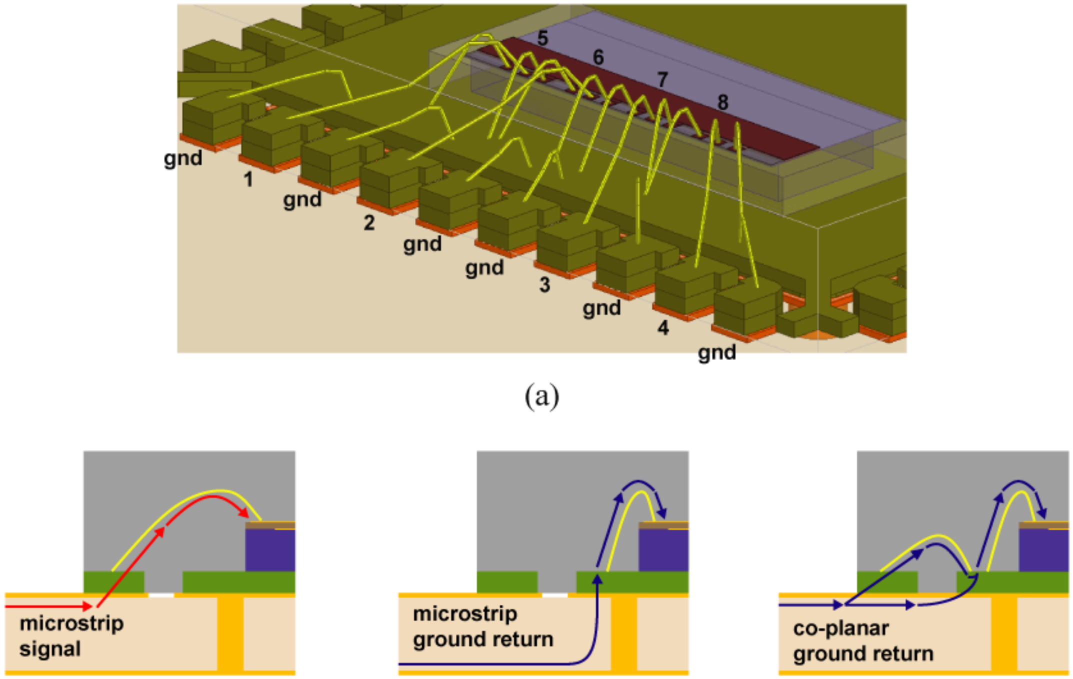

(a)

(b) (c) (d)

Figure 3.14: (a) QFN packaged RFIC on PCB, and current flow from PCB to RFIC through QFN package interface for (b) signal, (c) ground return for microstrip launch, and (d) ground return for CPW launch.

pads in the ground-signal-ground (GSG) launch, which may not necessarily be of the same potential as the die's bottom-most ground plane.

Figure 3.13a shows a 4-channel RFIC directly assembled on a PCB with bondwire-interface. Typical length of the bondwire is 0.025", corresponding to free-space self-inductance of ~0.45 nH. Similarly, Figure 3.14a shows a QFN package assembled on PCB, together with the 4 input channels of the assembled RFIC in the package. The bond-wires for ground potential are bonded directly on the package pedestal, to minimize on the bond-wire length and hence on the bondwire inductance. Typical bondwire length ranges from 0.055" to 0.066", corresponding to ~1.2-1.6 nH inductance for a wire of that length in free-space. 0.0133" thick RO4350 substrate is used in the simulations ($\varepsilon_r = 3.66$, $\tan\delta = 0.0038$).

The QFN package is a commercially available 6x6 mm^2 40-lead QFN package, and its model is directly available from Amkor as an ADS Design Kit library component [57]. Both plastic-moulded and air-cavity packages are considered in the studies. Plastic moulding material is found between the package leads for air-cavity packages. Electrical properties of the moulding compound are $\varepsilon_r \sim 3.7$ and $\tan\delta \sim 0.009$.

Figure 3.13b and Figure 3.14b shows the flow of an RF signal from the PCB to the RFIC, and Figure 3.13c and Figure 3.14c the path undertaken by the signal return if microstrip transmission lines are used for the PCB interface to the die/package. This ground return path is negligible at lower frequencies and deviates more significantly from the signal path with decreasing wavelengths.

Coplanar waveguides (CPWs) allows most of the ground return to propagate at the top PCB surface together with the RF signal (i.e. “co-planar ground”), and (Figure 3.13d and Figure 3.14d) the ground return now undertakes a shorter path. As such, lead pads has to be dedicated for facilitating mechanism of ground returns (shown as “gnd” in both figures). This limits the availability of leads available for routing other signals, and in some cases dictates the package side required based on the lead-count, having the package to be much bigger than the actual chip size and much longer bondwires required for the chip-package interface. Nevertheless, significant improvement in isolation across a wider frequency band is observed with such CPW launch (esp for QFN case in Figure 3.14d) as compared to conventional microstrip lauch.

3.4.2 Inter-channel Isolation

Figure 3.15 presents on the inter-channel isolation resulting from the various PCB-RFIC interface implementation methods. CPW launch and microstrip lauch cases are presented in the left column and right column respectively. These simulations assumes the presence of internal vias in the RFIC chips across the 250 µm thick silicon layer to the die bottom-most layer.

Isolation for wire-bond implementation setup in Figure 3.13a is presented in Figure 3.15a. 40 dB of isolation or better is obtained for CPW launch (Figure 3.13d) for worst case of adjacent channels. The absence of internal vias shorting RFIC intermediate ground layer to the die bottom-most layer corresponds to ~ 10 dB of relative degradation, as presented in [54] of ~ 30-40 dB for all cases across X-band. Microstrip launch (Figure 3.13c) further degrades isolation to 28 GHz at 9 GHz, and worst case of within 20 dB at 20 GHz. The short wire-bonds ensures the highest possible isolation for adjacent channels/pads interface from chip to board.

Setup for isolation investigations is presented in Figure 3.14a for QFN-packaged RFIC chips on PCB, and HFSS simulated responses for plastic-moulded and air-cavity QFN packages presented in Figure 3.15b and Figure 3.15c respectively. For plastic-moulded QFN packages, isolation is ~ 35 dB at 9 GHz for worst case of adjacent channels with CPW launch, as compared to 27 dB for microstrip launch. This isolation quickly degrades to < 10 dB at > 16 GHz for case of microstrip lauch, while staying constant at > 32 dB up to 20 GHz for case of CPW launch, illustrating the growing importance of the ground return routings for increasing operating frequencies.

Slight improvements in isolation (~1 dB at 9 GHz) are observed for air-cavity QFN packages. As the dominant coupling mechanism arises from inductive coupling between the bond-wires in the package, absence of plastic-mould materials will have minimal impact on the isolation. The dominant coupling mechanism can be further verified with the forward-wave coupling reflecting phase for adjacent channel or port at DC (i.e. $\angle S_{16}$ in Figure 3.13a), which is lagging (i.e. = -90°) for dominant inductive coupling, and not leading (i.e. = +90°) which is the case for dominant capacitive coupling.

For microstrip launch on wire-bond interface, with sufficient shorting vias in the RFIC shorting the intermediate ground plane to the die bottom-most layer, and located located close to the RFIC launch pads, up to 12 dB of worst case isolation can still be achieved at 20 GHz, and 27 dB at 9 GHz (Figure 3.15a, right column). Note these values varies with substrate variations. Also, for QFN implementation, though offering 27 dB of worst case isolation at 9 GHz, direct microstrip launch degrades significantly at higher frequencies in Ku-band region, with the plastic moulding material offering some sufficienly high capacitance for invoking resoanace. The partial removal of plastic moulding material in the air-cavity region allevates the problem to some extent.

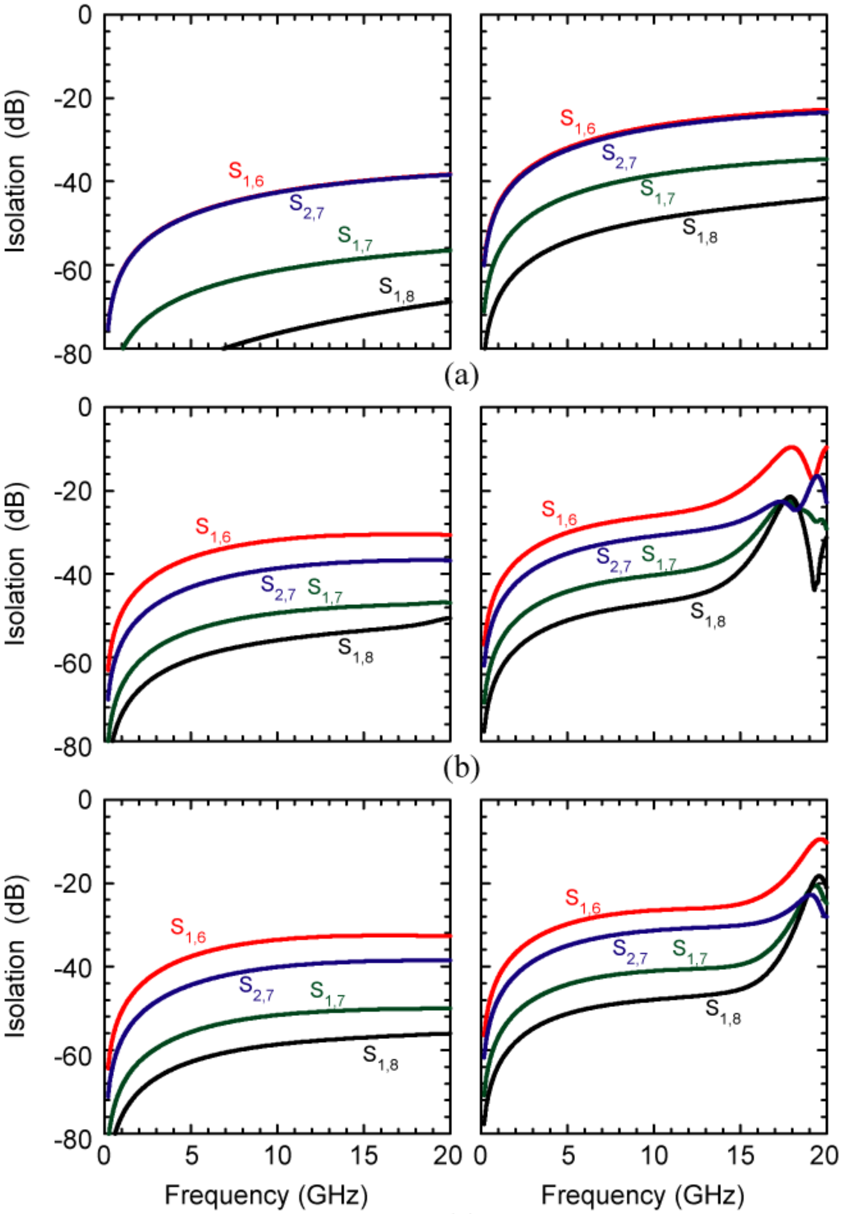

(a)

(b)

(c)

Figure 3.15: Isolation for PCB-RFIC interface with (a) wirebond, (b) plastic-moulded QFN package, and (c) air-cavity QFN package; for CPW-launch (left) and microstrip launch (right).

CPW launch with minimal differences in the signal-ground path will be strongly recommended for best isolation performance with QFN package interface.

3.4.3 Input impedance

Terminating the RFIC port with 50 Ω match, input impedance seen from the PCB port for individual channel is presented in Figure 3.16. 0.45 nH of series inductance is obtained for case of wirebond with CPW launch. That same bondwire translates to > 0.55 nH with microstrip launch, with the additional inductance arising from the path difference between the signal (Figure 3.13b) and the ground return (Figure 3.13c). Inadequate grounding within the RFIC die will further degrade this value to ~ 0.7 nH, which is the commonly encounted bondwire inductance approximation.

Resonance is encountered for QFN package interface, at 12 GHz and 14 GHz for plastic-moulded and air-cavity packages respectively. The plastic moulding material (especially at the leads) forms a shunt capacitance component, which self-resonates with the series inductance from the long bondwires, and presents a high impedace to the PCB input. Though successfully implemented for X-band in [53], caution and careful design is to be exercised for Ku-band implementation.

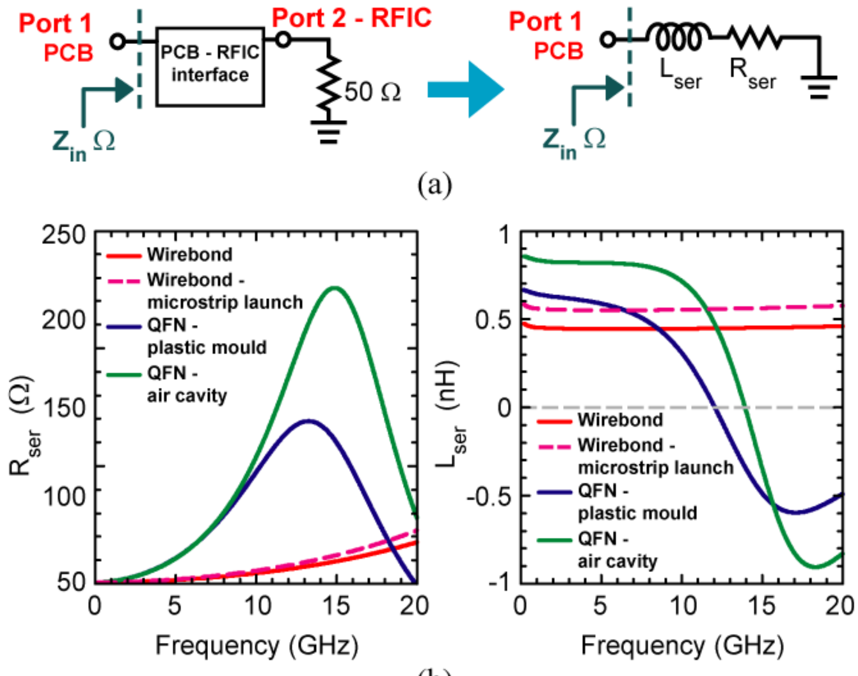

(a)

(b)

Figure 3.16: Simulated input impedance of RFIC-PCB interface with wire-bond and (plastic moulded and air-cavity) QFN, with matched termination at RFIC port.

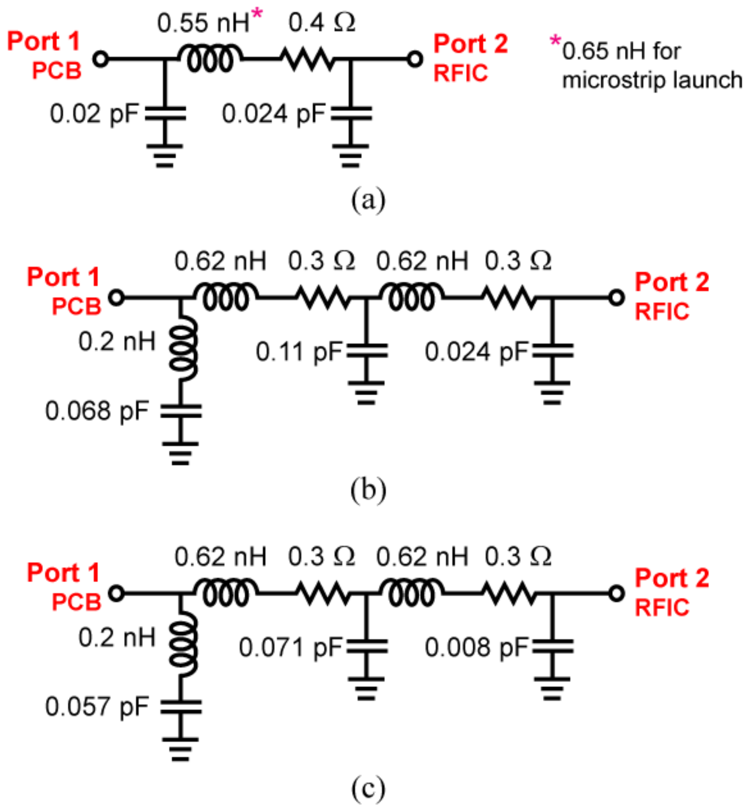

Figure 3.17: Fitted RLC model for CPW-launch PCB-RFIC interface with (a) wirebond, (b) plastic-moulded, and (c) air-cavity QFN packages.

A better tool for performing on-board matching is to use the fitted RLC model, presented in Figure 3.17. Distributed models fits the S-parameter responses perfectly for cases with QFN packages (Figure 3.17b for plastic-moulded QFN, and Figure 3.17c for air-cavity QFN). Though these models fits the S-paramters well and are adequate for most matching purposes and frequency-domain simulations, they are not necessary causal, and are not appropriate for time-domain transient simulations.

3.5 Commercial-Grade PCB for Antenna Arrays

3.5.1 Commercial Grade Laminates

Commerical grade laminates for high frequency applications includes Rogers' RO4000 series, Nelco's N4000-series, Panasonic's Magtron 6 and Isola GigaSync. Table 3.1 lists some of these laminates. Typical ε_r values are 3-4.4, and tanδ of 0.003-

Table 3.1: Commercial-grade laminates suited for FR-4-based multi-layered PCB lamination process and assembly.

Manufacturer	Series	ε_r	tan δ	Remarks
Rogers	RO4003	3.55	0.0027	hydrocarbon/ceramic, glass-reinforced
	RO4350	3.66	0.004	
	RO4450B	3.3-3.54	0.004	prepreg
Panasonic	Megtron 6: R-5775	3.4	0.004	epoxy-resin
	Megtron 6: R-5670	3.2	0.004	prepreg
Isola	GigaSync	4.13	0.0066	epoxy-resin
Taconic	Orcer RF35P	3.5	0.0037	organic-ceramic woven glass
Nelco	N4000-13 SI	3.7	0.007	epoxy-resin
	N4800-20 SI	3.55	0.006	

0.009. These boards are usually epoxy-resin based, or hydro-carbon ceramic based for materials from Rogers, and are more firm for handling and process-compatible with FR-4 fabrication facilities, translating to higher fabrication and lamination successes for multi-layered sequential lamination processes. These materials will be strongly recommended for complex multi-layered planar construction, and is required for low-cost development of phased arrays through the goal of direct integration of the antenna elements with active devices.

For the same operating frequency, higher ε_r translates to increase in substrate electrical thickness, which results in higher normalized propagation constant for the TM_0 surface waves mode. Problems associated with surface waves includes onset of scan blindness possibilities, and reduction in space-wave efficiency.

Microstrip antennas benefits from laminates with low ε_r and low $\tan\delta$. Low ε_r allows for wider scan angles or thicker substrates without triggering surface waves (and scan blindness). Both factors (low ε_r and low $\tan\delta$) allows for high radiation efficiency.

For these reasons, RT5880 (ε_r = 2.2, tanδ = 0.001) and RT5880LZ (ε_r = 1.96, tanδ = 0.0013) laminates are the most ideal for microstrip antenna arrays and phased array antennas. Using commercial grade laminates increases the chances for scan blindness triggering and unexpected degradation in full-array efficiency.

Other problems involves the microstrip feed network. They includes apparent increase in ε_r values (and decrease in measured phase velocity) and higher conductor losses. The surface roughness between the copper-dielectric interface is responsible for both phenomenon, and the microscopic layer of nickel arising from gold-plating of the copper surface is a dominant factor for the latter.

The microstrip feed network for the 4x8 phased array antennas comprises of 4-element linear array microstrip feed network, CPW feed network from the linear arrays to the input of the RFIC receivers, and microstrip feedlines from the RFIC receivers output to a Wilkinson combiner to the array connector. For the 4-element linear array (Figure 3.10), accurate determination of transmisison line phase velocity is of paramount interest, to ensure the elements are excited in phase. Isolation and losses are of some importance for the CPW feed network.

3.5.2 Scan Blindness Prediction and Avoidance

Possibilities of incurring scan blindness increases with increasing substrate dielectric constant and thickness. Knowledge of its occurance and avoidence through design will avoid this problem. Two methods of easily predicting the possibilties of scan blindness arising from the choice of substrate dielectric constant and thickness are

I - calculations of Floquet modes as presented in [58], and

II - simulation of single antenna element with the use of master-slave boundary conditions in HFSS, or similar features in any 3D EM solvers for infinite array calculations.

The first approach does not need licenses for any EM solvers, and is adequate for most design purposes and (with pre-computed coefficients or curves) can be determined almost instantly. Besides providing confirmation of the presence of scan blindness, the latter approach with HFSS presents deeper insights through the variation of active impedance seen by the antenna element. It is also noted that 1D scanning is performed in the H-plane for the 8-channels array, resulting in a zero possibility of incurring scan blindness due to the mismatch of polarization of the radiation fields and the surface waves modes, and can be easily verified with the latter method.

Potential scan blindness for a principle plane can be easily derived from the Floquet modes, starting from the following expression [58]:

$$\frac{\beta_{sw}}{k_0} = \left(\frac{k_x}{k_0}\right)^2 + \left(\frac{k_y}{k_0}\right)^2 = \left(\frac{m}{a/\lambda_0} + u\right)^2 + \left(\frac{n}{b/\lambda_0} + v\right)^2 \tag{3.3}$$

where

$$u = \sin\theta \cdot \cos\phi, \qquad k_x = \frac{2\pi m}{a} + k_0 u,$$

$$v = \sin\theta \cdot \sin\phi, \qquad k_y = \frac{2\pi n}{b} + k_0 v,$$

and *a* and *b* referring to the array spacing, and *m* and *n* the order of the Floquet modes along the X-axis and Y-axis orientation respectively. Propagation constants for free-space and surface waves are indicated by k_0 and β_{sw} respectively. Considering a fundmental mode of $m = 1$ and $n = 0$ for beam scanning along X-axis in a rectangular grid array, (3.3) is re-written as

$$\frac{\beta_{sw}}{k_0} - \frac{m}{a/\lambda_0} = \sin\theta_{sb} \tag{3.4}$$

or

$$\theta_{sb} = \sin^{-1}\left(\left|\frac{\beta_{sw}}{k_0} - \frac{1}{a/\lambda_0}\right|\right) \tag{3.5}$$

with θ_{sb} the potential scan angle resulting in scan blindness. With the TM_0 mode surface wave propagation constant (β_{sw}) known, this expression serves as a useful quick evaluation for predicting potential scan blindness for any given substrate and element spacing. For equilateral grid arrays with equal spacing (*a*) between every element, a factor of 2/√3 to the element spacing can be included in (3.5), which now reads as

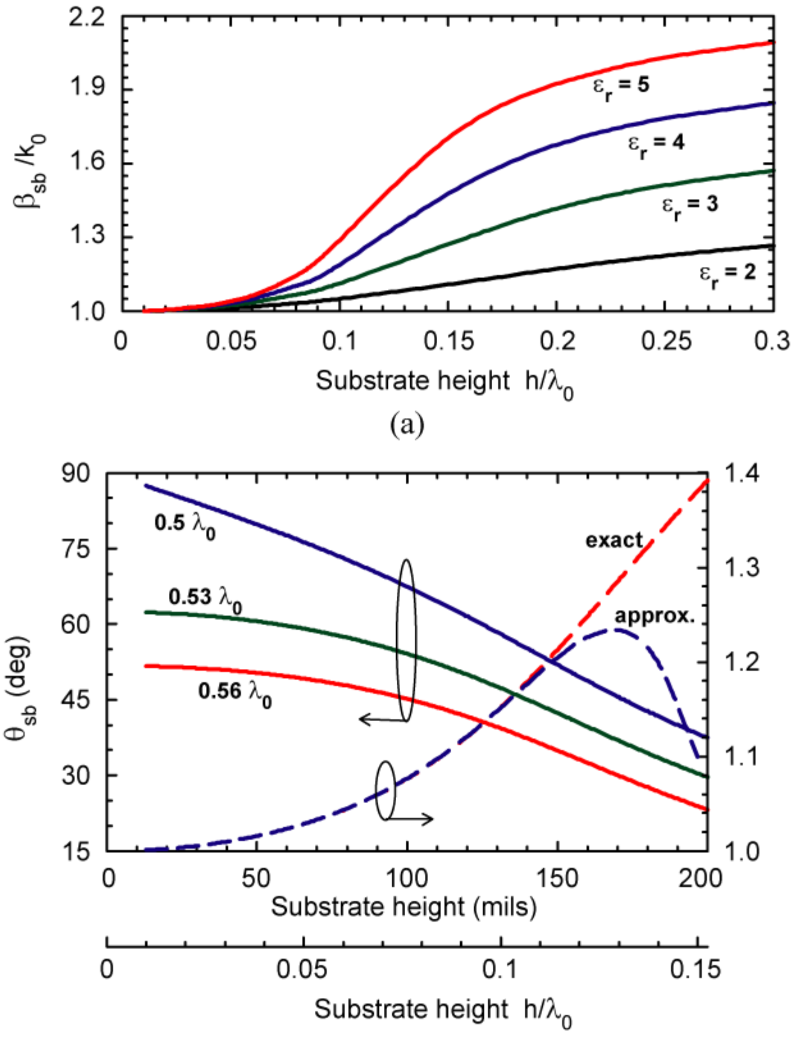

(a)

(b)

Figure 3.18: (a) Normalized surface waves propagation constant (β_{sw}/k_0) for various dielectric constant values, and (b) potential scan blindness and normalized surface waves propagation constant for $\varepsilon_r = 3.55$.

$$\theta_{sb} = \sin^{-1}\left(\left|\frac{\beta_{sw}}{k_0} - \frac{2}{\sqrt{3}}\cdot\frac{1}{a/\lambda_0}\right|\right) \tag{3.6}$$

The 2/√3 factor arising from the equilateral spacing of elements translates to the 1.155 times increase in element spacing for the same scan blindness angle.

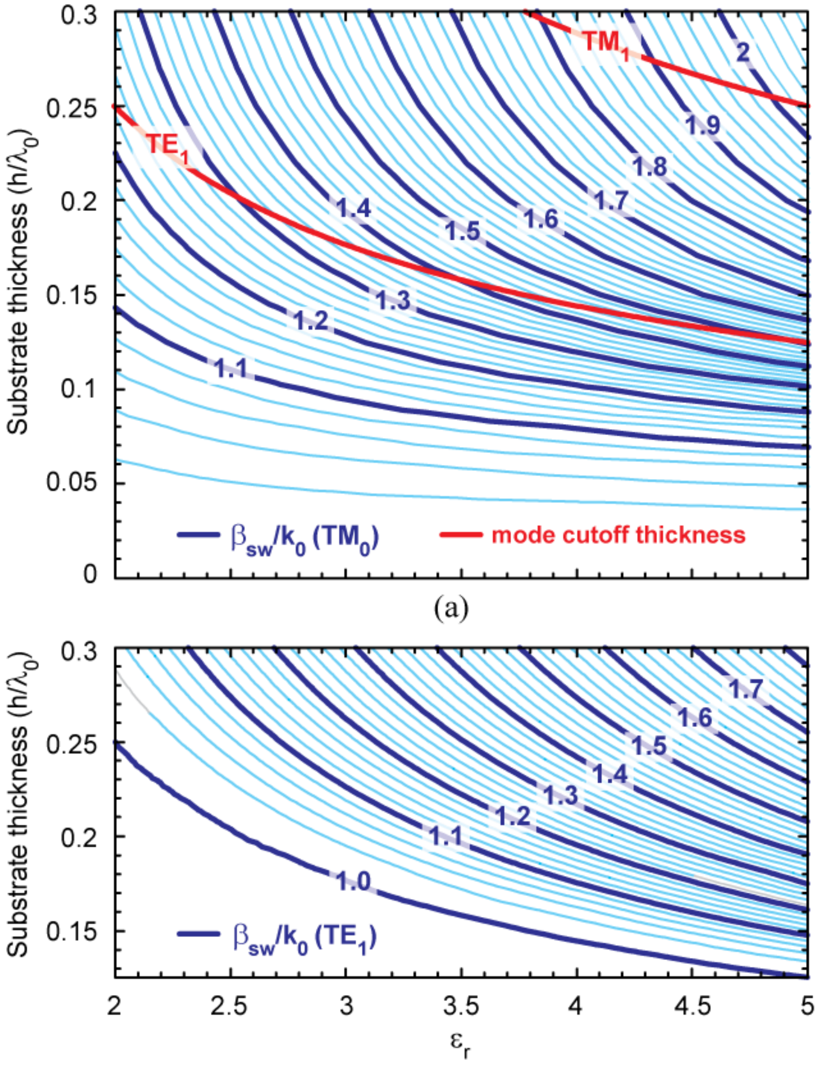

(a)

(b)

Figure 3.19: (a) Cut-off substrate thickness for higher order modes (red) and normalized surface waves propagation constant (β_{sw}/k_0) for TM_0 mode (blue) and (b) TE_1 mode, for various substrate ε_r and thickness.

Evaluation and approximation of β_{sw} for TM_0 surface wave mode is found in [59] and [55] respectively. Normalized β_{sw} is pre-computed and presented in Figure 3.18a for ε_r = 2-5 vs substrate height h. A steady increase of β_{sw} is observed with increasing substrate ε_r and height. Figure 3.18b presentes exact and approximate values of β_{sw} for ε_r = 3.55 (for RO4003 laminates), with the approximate values valid till substrate thickness of $0.13\lambda_0$.

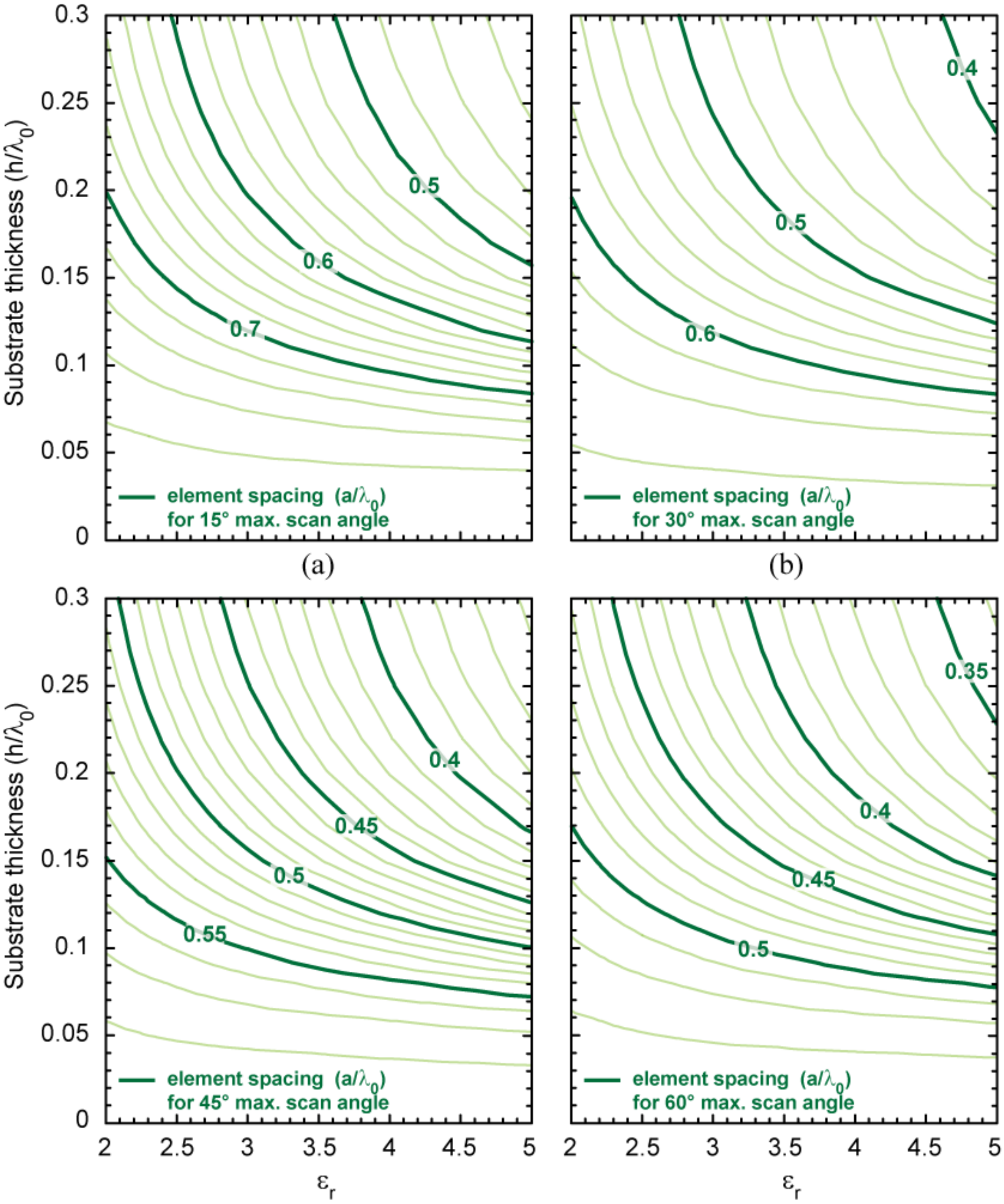

(a) (b)

(c) (d)

Figure 3.20: Maximum conservative element spacing (a/λ_0) for maximum scan angle of (a) 15°, (b) 30°, (c) 45° and (d) 60°.

With the normalized surface wave propagation constants evaluated, potential scan blindness is easily computed with (3.5) for rectangular grid arrays, and Figure 3.18b shows the maximum scan angle off broadside allowed before potential scan blindness is triggered, for case of $\varepsilon_r = 3.55$. The maximum possible scan angle reduces most significantly with the reduction of element spacing from $0.5\lambda_0$ to $0.53\lambda_0$ and with increase of substrate thickness from 0.01" to 0.08".

$$\frac{h_{TMn}}{\lambda_0} = \frac{n}{2\sqrt{\varepsilon_r - 1}}, \quad n = 0,1,2... \tag{3.7}$$

for the TM modes, and

$$\frac{h_{TEn}}{\lambda_0} = \frac{2n-1}{4\sqrt{\varepsilon_r - 1}}, \quad n = 0,1,2... \tag{3.8}$$

for the TE modes.

Figure 3.19 replots, in greater resolution, normalized surface waves (β_{sw}/k_0) for TM_0 and TE_1 modes, and cut-off substrate thickness (h/λ_0) for TE_1 and TM_1 surface-waves modes. TE_1 mode can be avoided for $\varepsilon_r = 5$, with substrate height $< 0.1\ \lambda_0$ always. Cutoff frequencies for the higher order modes can be easily calculated from

Though H-plane scan does not excite the lowest order surface wave modes (TM_0), it does excites the next (TE_1) mode and scan blindness may still occur for H-plane scan arrays on thick substrates. Rearranging (3.5), most conservative element spacing (a/λ_0) for any maximum scan angle (θ_{max}) without incurring scan blindness can be evaluated with

$$\frac{a}{\lambda_0} = \frac{1}{\frac{\beta_{sw}}{k_0} + \sin\theta_{\max}} \tag{3.9}$$

Figure 3.20 presents the calculated maximum element spacing for scan angles of 15°, 30°, 45° and 60°, based on (3.9) for the lowest order surface waves mode from Figure 3.19. Without bandwidth requirements, a recommended practice is ensuring substrate height to be within $\lambda_d/21$ (or 0.3 rad), with λ_d the dielectric wavelength [60]-[61], i.e.

$$\begin{aligned} &\beta_d h = 0.3 \\ => &\frac{2\pi}{\lambda_d} h = 0.3 \\ => &\frac{h}{\lambda_0} = \frac{0.3}{2\pi\sqrt{\varepsilon_r}} \end{aligned} \tag{3.10}$$

Though most microstrip antenna may be built on substrate with thickness < 0.1 λ_0, there are instances when the substrate thickness is intentionally increased to > 0.1 λ_0, e.g. for microstrip antennas with U- (or E-) shaped slots for typically > 15-20% bandwidth, or with a laminate at the top of the antenna, acting as a superstrate for wideband matching or as a radome for practical purposes. In these instances both Figure 3.19 and Figure 3.20 serves as good quick references for scan blindness prediction with commercial grade laminates.

Potential scan blindess can be further evaluated in HFSS using master-slave boundary conditions for an element in an infinite array. Figure 3.21 shows the simulated return loss for scanning in both E and H-planes separately for an infinite array, with element separation of $0.53\lambda_0$ and $0.6\lambda_0$ for the scanning and fixed-beam planes respectively. For the case of E-plane scan, scan blindness is revealed in the form of almost 0 dB of return loss at the operating frequency with increasing beam scan angle.

With the polarization mismatch of the radiating elements with the surface waves in the H-plane, scan blindness will not occur for case of H-plane scan from the lowest order TM_0 mode. Instead, increasing scan angles degrades the input match condition to ~ -6 dB of return loss for 60° (Figure 3.21b). Figure 3.21c presents the S_{11} loci for the various scan cases for H-plane scan array, and the input impedance becomes increasingly capacitive with increasing scan angles in the H-plane. If choice of substrate parameters and element spacing is limited by other factors, for wide H-plane scan angle requirements, the individual antenna element can be designed with an inductive match at broadside, allowing for a 2:1 VSWR match for all scan angles required. Antenna elements with wider bandwidth than the intended operating frequency will also allow for a better match condition across all scan angles.

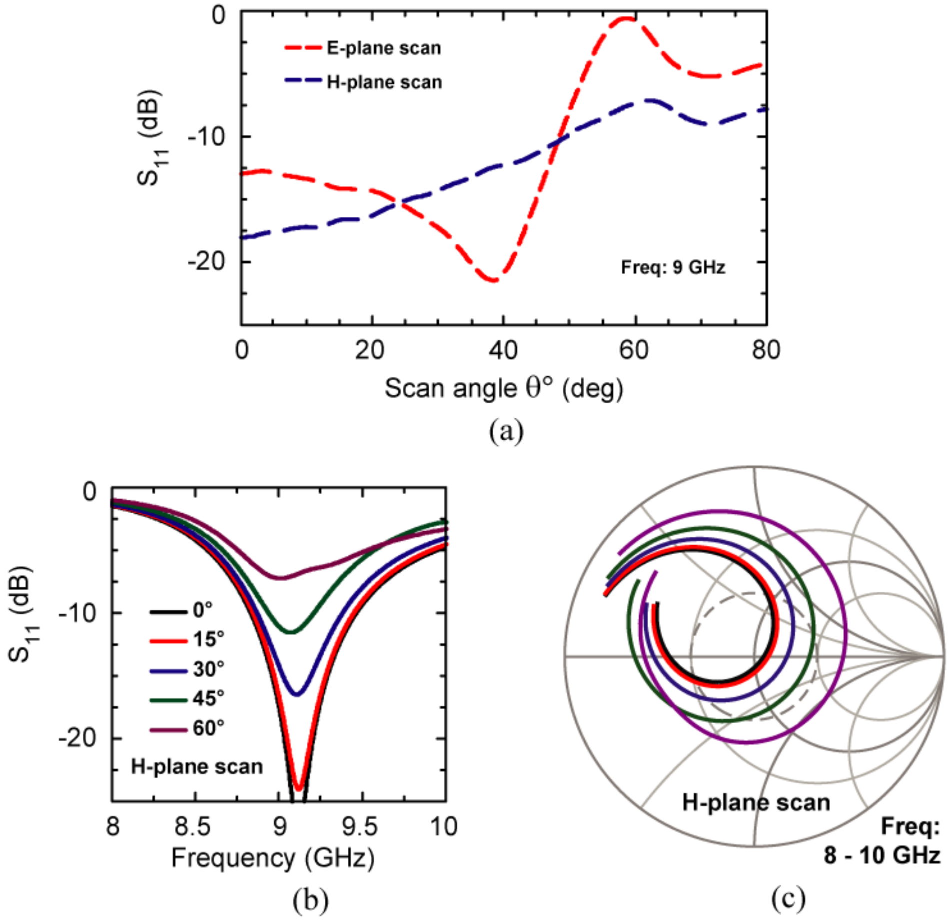

Figure 3.21: Return loss simulations with HFSS master-slave boundary conditions of an infinite array with element spacing of 0.53 λ_0 in the scan plane, for (a) both E and H-planes scan at 9 GHz, H-plane scan (b) across frequency and (c) Smith Chart response.

Further degradation arising from probe-fed antenna arrays are presented in [62], which discusses on the presence of a leaky-wave mode that brings the scan blindness occurrence at smaller scan angles than those presented in Figure 3.19 and Figure 3.20. Singled ended probe-fed antenna element was designed on the same substrate, simulated with similar conditions (infinite array, E- and H-plane scan arrays), and return loss simulations from HFSS presented in Figure 3.22. Different probe configurations were considered (from 0.012” via diameter, to 0.001” width line source) and similar results were obtained, and they do not revel any significant impact from the leaky wave modes on the scan blindness.

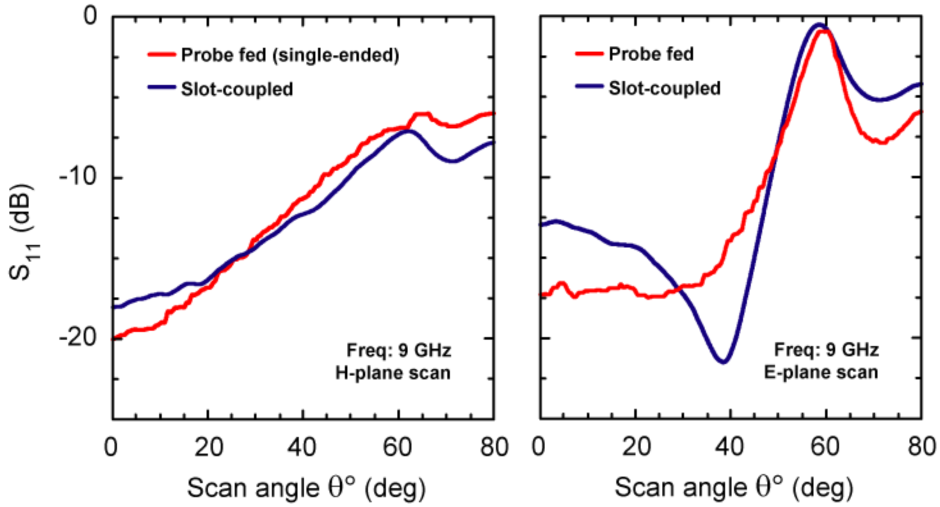

Figure 3.22: Return loss simulations with HFSS master-slave boundary conditions of an infinite array of probe-fed (red) and slot-coupled (blue) element with element spacing of 0.53 λ_0 in the scan plane, for E-plane scan (left) and H-plane scan (right).

3.5.3 Array Radiation Efficiency

While designing a single microstrip antenna element as part of a electrically large array, both resonator loss and surface-wave loss should be considered in depth. Resonator efficiency relates to the stored energy of the microstrip patch as a resonator, and increases with increasing substrate height. Conversely, surface wave losses [55] increases with increasing substrate height, and is captured as space wave efficiency with the following equation:

$$\eta_{sp} = \frac{P_{sp}}{P_{sp} + P_{sw}} \tag{3.11}$$

where η_{sp} refers to the space wave efficiency, and P_{sp} and P_{sw} power radiated to space-wave and propagated as surface-waves respectively. Total efficiency (η_{tot}) for microstrip antennas can be easily computed from computer-aided design (CAD) formulas [28]-[30], and is related to space-wave efficiency and resonator efficiency (η_{re}) with:

$$\eta_{tot} = \eta_{re} \cdot \eta_{sp} \tag{3.12}$$

Surface waves losses are more significant and severe in large microstrip antenna arrays as compared to individual antenna elements. As single antenna elements, the power trapped as surface wave mechanism will be re-radiated back to free-space as it reaches the edges of the substrate, which ranges from $0.5\lambda_0$ to $3\lambda_0$ in length for each side. But for large arrays, the power trapped in the surface waves are not able to easily re-radiate, as they transverses along the substrate surface. Besides incurring lower total radiated power, they causes higher mutual coupling between the elements, resulting in larger deviations in the active impedance. For an aperture size of 12 λ_0 by 12 λ_0 for application in Ku-band, -3 dB of radiation efficiency (i.e. 50%) could potentially incur up to 6 dB of additional total array gain degradation.

To complicate matters further, for single antenna elements, use of EM solvers which computes the field intensity directly in 3D space (e.g. HFSS and CST Microwave Studio) will not be able to identify surface wave mechanism. Most users will be designing a single element with some finite substrate size, and the surface waves will be either terminated at the substrate boundary, or re-radiated as part of overall radiation energy. As such, the EM simulated efficiency will consistently reflect as ~ 90% radiation efficiency, which is the resonator efficiency mechanism. Space-wave efficiency can only be identified from using methods-of-moments (MOM)-based EM solvers solving the Sommerfeld equations directly with assumptions of infinite substrate and ground plane lateral size (e.g. IE3D and Momentum), or computing CAD formulas derived in [28]-[30] for the various efficiency values.

Figure 3.8a shows the various radiation efficiency mechaisms for RO4003 substrate, and some IE3D EM verifications. As resonator efficiency increases with increasing substrate thickness to ~ 90%, the overall efficiency is dominated by the decreasing space wave efficiency. Figure 3.23 presents the comupted radiation efficiency for various substrate cases. With increasing substrate thickness, space wave efficiency decreases more significantly with higher dielectric constant substrates.

For case of 0.1” substrate thickness, implementation with Teflon-based RT5880 (ε_r = 2.2) incurrs only 78% efficiency, as compared to < 50% for epoxy-resin based GigaSync (ε_r = 4.15) laminates. For most other laminates (e.g. Megtron-6 or RO4350)

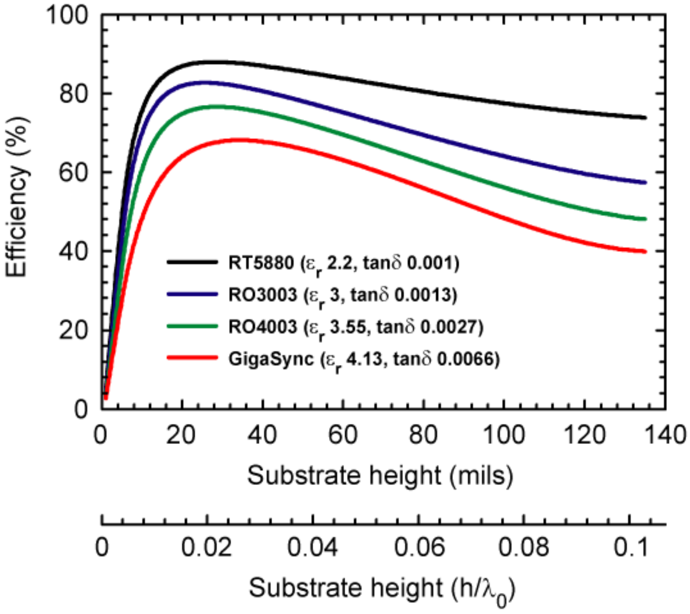

Figure 3.23: Computed radiation efficiency for various substrates at 9 GHz.

the expected efficiency can be approximated from these curves. In *most* cases HFSS will typically reflect *only* the resonator efficiency mechanism, and in this examples reporting radiation efficiency of > 90%. Without the awareness of low efficiency from surface-waves mechanism, unexpected degradation of the full array gain from the use of GigaSync (or similar epoxy-resin laminates) will be so much more impactful as compared to the use of RT5880.

Finally, it is worth noting that the simulated return loss from the MOM-based solvers will deviate significantly from HFSS simulations, with a consistently larger deviation observed for increasing surface waves losses. Measurements of *single* antenna elements always corresponds much better to HFSS simulations than MOM-based solvers for both return loss and antenna gain, leading to the negligence of space-wave efficiency in many cases.

3.5.4 Surface Roughness on Apparent ε_r Deviation

RO4000-series laminates with 0.5 oz per-square-feet (psf) of electro-deposited (ED) copper cladding (corresponding to 17.5 μm of copper thickness) have a surface roughness of 2.8 μm [63]. This surface roughness resides in the copper-laminate interface, and impacts on the propagation by increasing in both losses and inductance-per-unit-length (L_{PUL}) of the TLIN [64]-[65].

Impact of the surface roughness on L_{PUL} is not widely appreciated at this time. Causing a decrease in the propagation phase velocity, the apparent guided wavelength increases and causing measured resonances to consistently occur at lower frequencies from intended designs. A way to identify this mechanism for apparent ε_r deviation, is the observation of decreasing resonant frequency with decreasing substrate thickess for the same substrate ε_r.

Increase in dielectric constant values used in simulations is suggested for ensuring consistency in modeled and measured resonance frequency [66]-[67]. Unfortunately this method increases the capacitance-per-unit length (C_{PUL}) of the transmission line model instead of L_{PUL} which is the true culprit for the change in phase velocity. A consequence is the greater inconsistency of modeled and measured characteristic impedace of TLINs, at the cost of accurately reproducing the TLIN phase velocity in simulations.

A more appropriate correction factor to use in existing Jansen and Hammerstad's microstrip TLIN model [68], for consistency in measurements and modeling for *both* the characteristic impedance and phase velocity, is to increase *both* the apparent dielectric constant and substrate height from the values of the actual physical entity. Sonnet's surface roughness model accounts for L_{PUL} effects accurately [69],[70] and is used to compute for the effective dielectric constant and phase velocity for our implementation of the 4-element linear array.

For the case of a 0.0133" thick RO4350 ($\varepsilon_r = 3.66$, $\tan\delta = 0.0037$) laminate with 0.5 oz of ED copper cladding, back-calculations from Sonnet's surface roughness results to identify the apparent dielectric constant and thickness of the standard microstrip TLIN model is presented in Figure 3.24, which shows the apparent thickness of substrate significantly thicker than the physical 0.0133" thickness for the consistent characteristic impedance values. There are a total of 3 distinct factors causing an

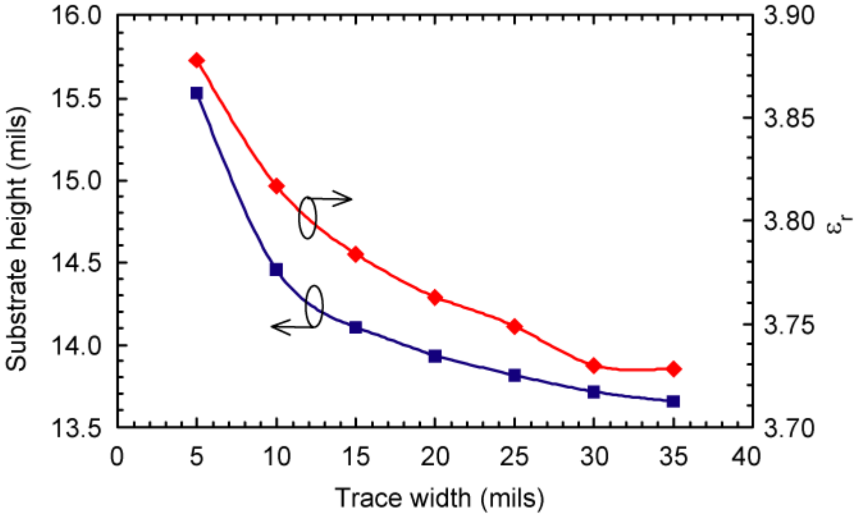

Figure 3.24: Apparent substrate height and ε_r arising from 2.8 µm of Cu surface roughness, for 0.0133” thick RO4350 laminate with 0.5 oz ED Cu cladding, evaluated at 9 GHz.

apparent change in material permittivity, based on measured resonances of microstrip cicuits, and are presented in Appendix A.

3.5.5 CPW Isolation and Losses

Grounded CPW feed transmission lines are utilized between the 8 4-element linear arrays and the inputs to the RFIC receviers for insuring high isolation between the channels. Simulations for grounded CPW transmission lines for isolation evaluation can be computationally intensive especially in predominantly planar solvers cause of the ground vias. From forward-waves coupling of a pair of coupled lines, a quick simple solution for evaluation of isolation performance can be extacted from the of the odd-even mode phase velocities for a short segment of a pair of transmission lines routed parallel to each other using

$$P_{iso} = \sin^2\left(\frac{(\beta_e - \beta_o)l_p}{2}\right) \tag{3.13}$$

where P_{iso} is the isolation power (or the square of *forward coupling* in a 4-port coupled line model), l_p the length of transmisison lines routed in parallel, and β_e and β_o the propagation constants for the even-mode and odd-mode respectively. Ensuring isolation of > 40 dB in all segments allows for ~40 dB of isolation in the CPW network, which is above the isolation of 35 dB incurred by PCB to RFIC through the QFN package interface. Also, the gap in the CPW configuration was kept to a minimum of 0.005” of signal-ground spacing to further ensure high isolation within a compact board area.

Unfortunately the 0.005” signal-ground gap incurs much higher insertion loss than expected, due to the nickel introduced in the electroless nickel gold immersion (ENIG) plating finish. Figure 3.25a shows the zoom-in of a cross-section of grounded CPW implementation on PCB, where besides the top of the traces, the nickel and gold plating covers the side walls of the copper traces too. Field (and hence current) concentration on the side-walls for CPW is higher than that for microstrip and increases with decreasing signal-ground gap, and thus the ENIG plating impact on losses for CPW is significantly higher than that for microstrip.

The additional losses can be captured in HFSS using layered impedance boundary conditions with the nickel and gold layered added as shown in Figure 3.25b on CPW with dimensions shown at the top of the figure, for cases of bare copper finish, layered boundary conditions (modeling ENIG finishing) at top of traces, and layered boundary conditions at top and side of traces. Measured losses generally corresponds to these simulations well. Unfortunately that may be due to *consistent coincidences*, and is currently lacking of theoretical backings, as the additional loss mechanism is derived from the relative permeability (μ_r) values used in HFSS (default $\mu_r = 600$ in HFSS, $\mu_r = 100$ used in simulations for Figure 3.25b), and μ_r to converge to unity as frequency increases to microwave region [71]-[73] (Figure 3.26, [71]).

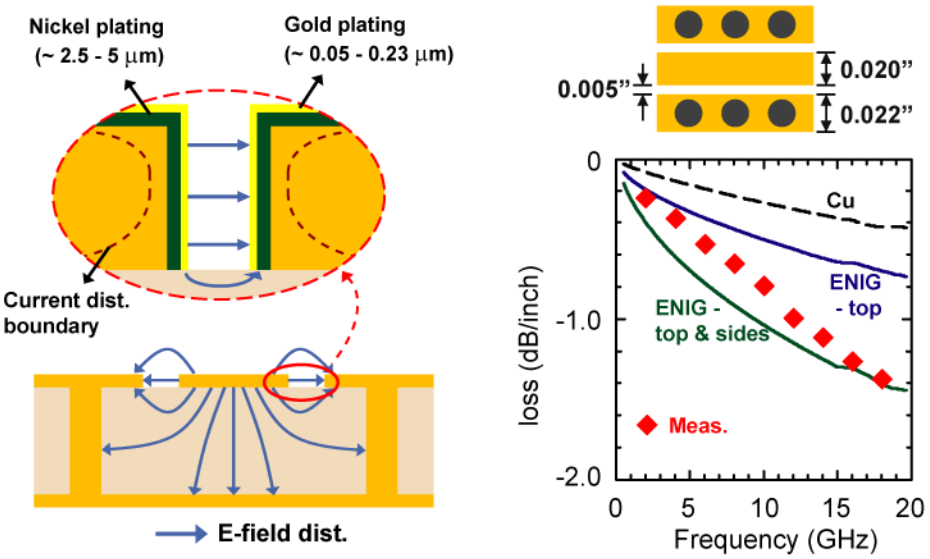

(a) (b)

Figure 3.25: (a) Cross-section of CPW, showing nickel-gold plating on the sides of the signal-ground gap, and (b) simulated and measured line losses.

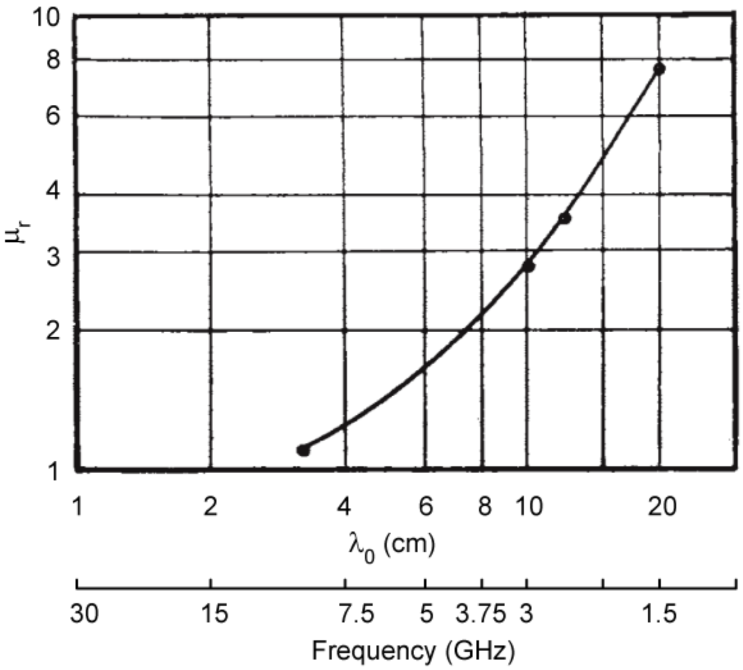

Figure 3.26: Relative permeability (μ_r) of nickel at microwave frequencies [71].

3.6 Hardware and Measurements

3.6.1 PCB Interface for RFIC phased arrays

Figure 3.27 present the QFN packaged RFIC receivers assembled to the PCB, with bias supply decoupling capacitors and electro-static discharge (ESD) protection diodes surrounding the chip. Also, RF ESD is provided on the main transmission-lines using λ/4 shorted stubs.

Figure 3.28 presents a test structure of the 4-element feed network with coaxial connectors used in-place of the 1x4 antenna elements. The CPW feed length on each antenna is 1.3” with a measured insertion loss of ~1.1 dB at 9 GHz. The measured isolation is > 40 dB between the different feed lines. The lines are well balanced in phase (< 5° variation over 4 lines).

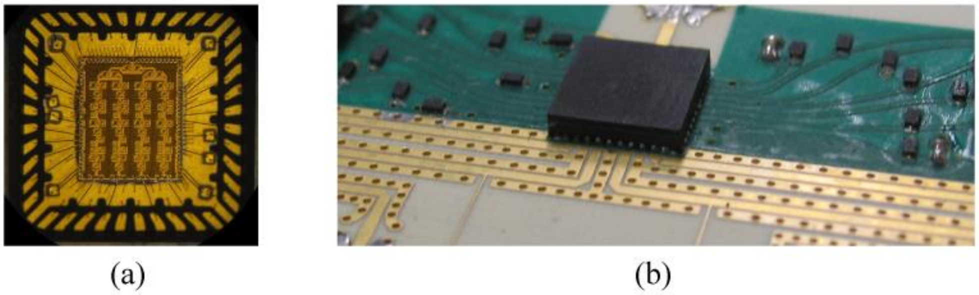
(a) (b)

Figure 3.27: (a) QFN-packaged CMOS RFIC - inside view, and (b) assembled on PCB.

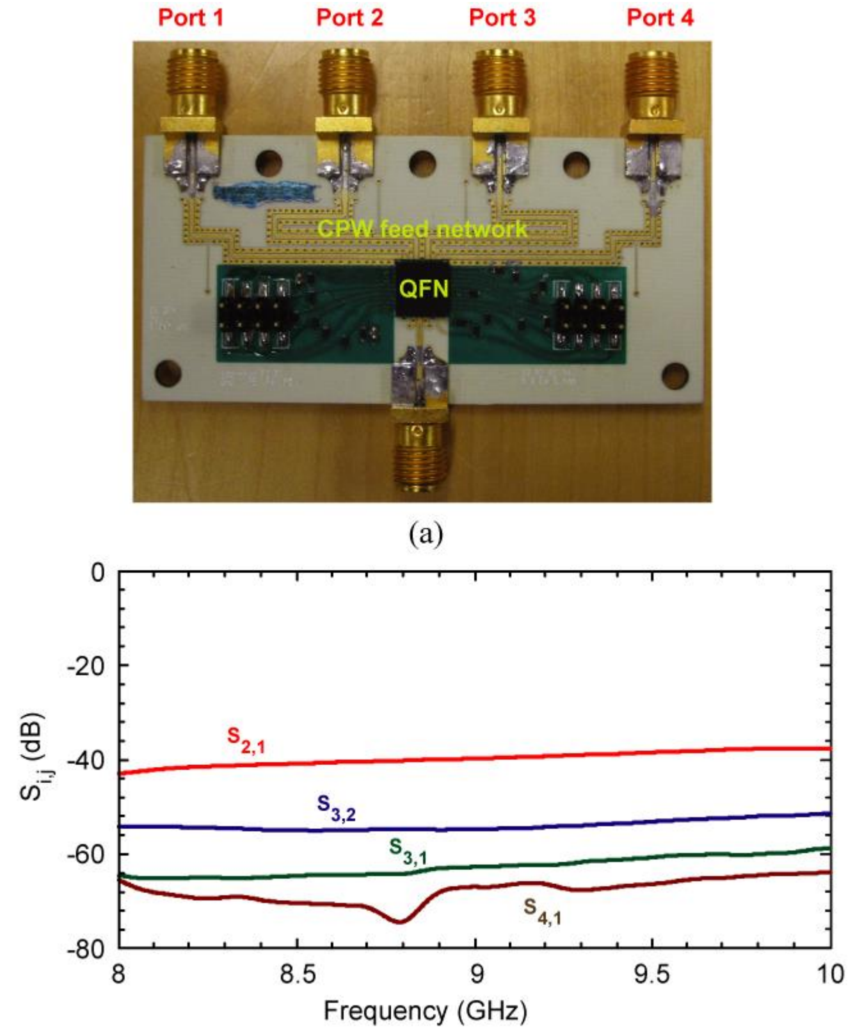

(a)

(b)

Figure 3.28: (a) Test structure for QFN on PCB, and (b) isolation of CPW feed network.

3.6.2 Antenna Element and Linear Arrays

Figure 3.29 presents the final PCB stackup implemented for both transmitter and receiver arrays. Rogers RO4003 (ε_r = 3.55, tanδ = 0.0027) is used for the microstrip antenna elements, RO4350 (ε_r = 3.66, tanδ = 0.0037) for the microstrip feed network and interface for surface-mount components, and RO4450B (ε_r = 3.54, tanδ = 0.004, thickness = 0.004" per ply) for the prepreg or thermoset bonding films. Choice of RO4450 over RO4003 for the feed network is to allow for the guided wavelength to be $< 0.6\lambda_0$ to allow for ease of routing of the 4-element linear array (Figure 3.10).

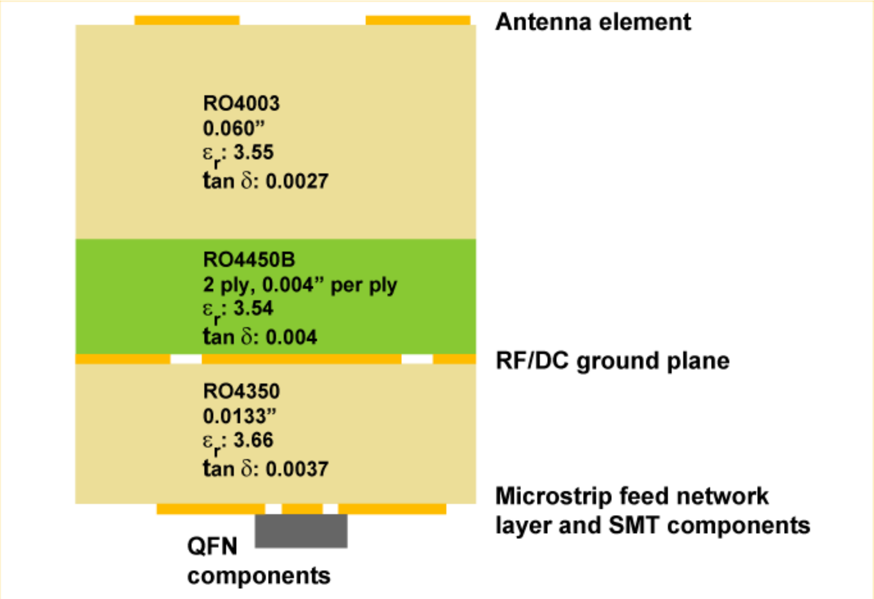

Figure 3.29: Multi-layered PCB stack-up for 4x8 active antenna array.

Details and pattern measurements for a single antenna element are presented in Figure 3.30, and return loss measurements in Figure 3.31. With substrate size of $2\lambda_0$ by $2\lambda_0$, measured return loss matches well with IE3D simulations, with IE3D considering infinite substrate and ground plane size in the lateral (i.e.X-Y plane) dimension. It is noted, for a smaller substrate size (e.g. $1\lambda_0$ by $1\lambda_0$), the measured S_{11} locus on the Smith chart becomes more inductive, as the resonance shifts to slightly below intended frequency of 9 GHz, which matches HFSS simulations perfectly. Measured gain of 4.5 dB corroborates well with IE3D simulated gain of 4.9 dB. Measured normalized cross-polarization is < -20 dB, which, together with the back-radiation, is due to uncertainties from measurement setup and test fixtures.

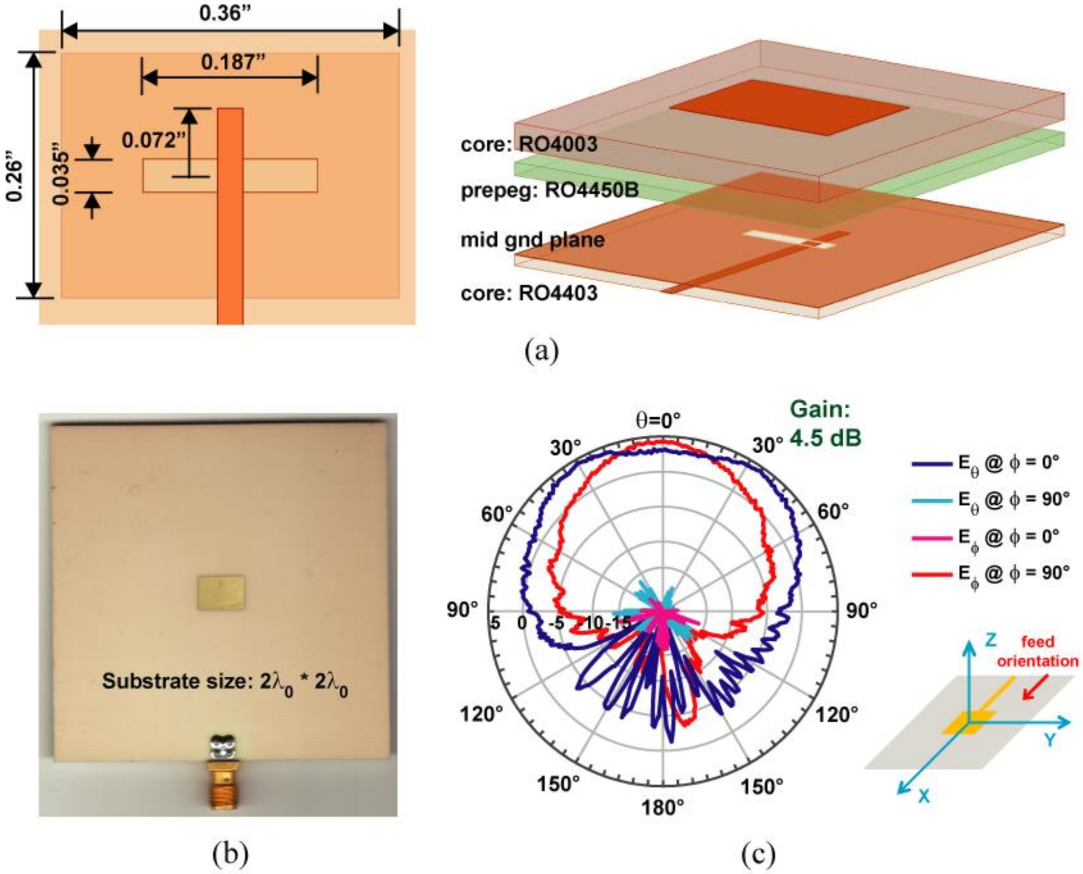

(a)

(b) (c)

Figure 3.30: (a) Cross-section and dimensions, (b) hardware realization and (c) pattern measurements for slot-fed microstrip antenna element.

Figure 3.31 presents the hardware realization and measurements of a 1x4 E-plane linear array. The 4-element array has a measured 3-dB beamwidth of 22 deg. in the E-plane. The simulated 1x4 antenna gain is 12.0 dB at 9 GHz (the vertical feed network loss is 0.9 dB at 9 GHz).

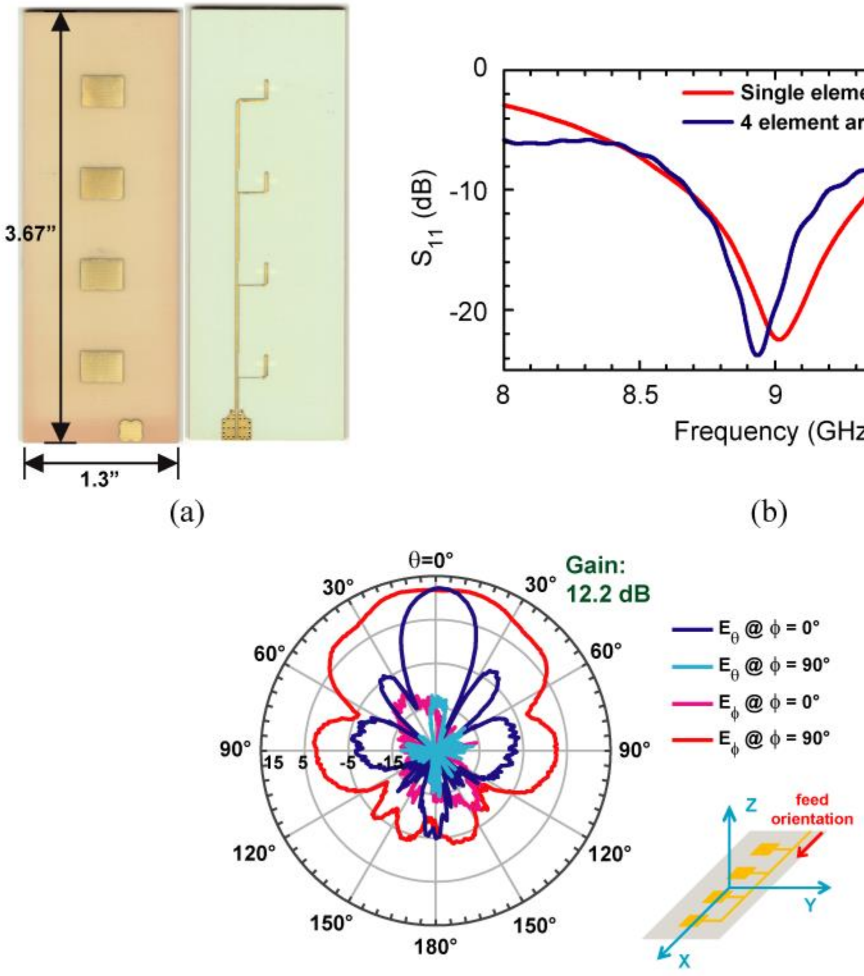

(a) (b)

(c)

Figure 3.31: (a) Hardware realization, (b) return loss and (c) patterns measurements for 4-element linear array.

Figure 3.32 presents the hardware and measured verification of the feed network for the 4-element linear array, and < +/- 2° of relative phase deviation was obtained at 9 GHz. The measured split ratio is also acceptable, as there is no isolation resistors for every split Tee junction, resulting in a theoretical +/- 0.2 dB variation from practical measurements of the split ratio. These measurements successfully verified our modified transmission line model presented in Figure 3.24.

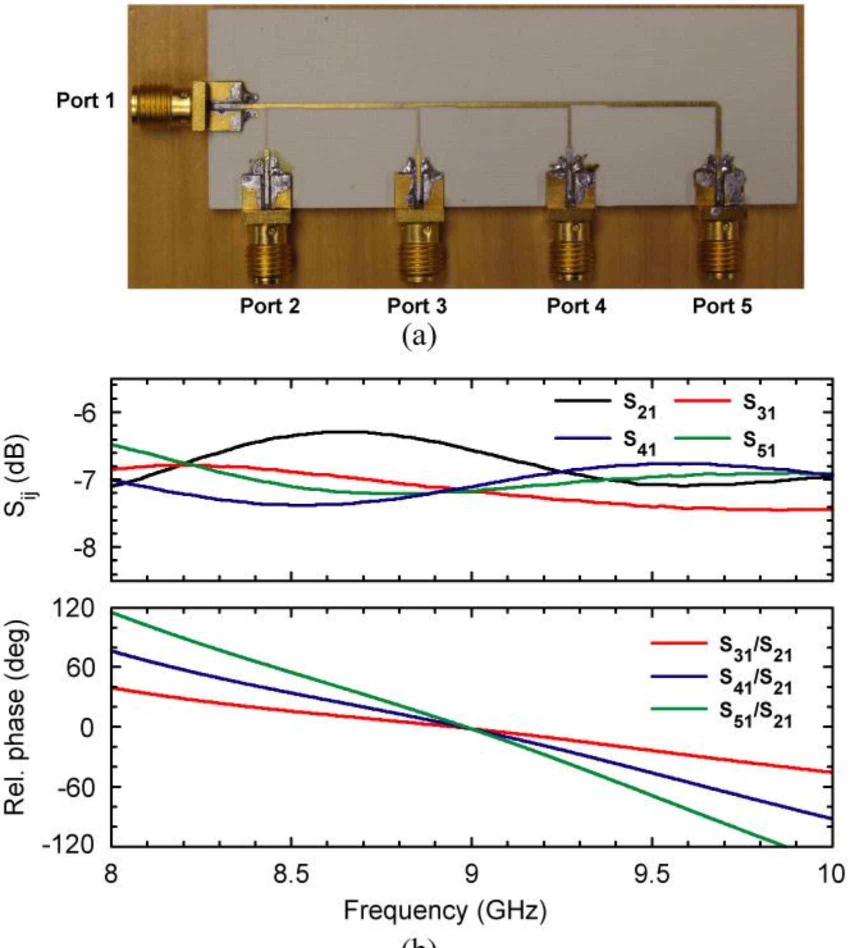

(a)

(b)

Figure 3.32: Linear array feed network (a) hardware verification and (b) measured insertion loss and relative phase.

3.6.3 Phased Array Receiver

The simulated 4x8 antenna directivity with $0.6\lambda_0$ vertical sepearation and $0.53\lambda_0$ horizontal separation (5.8"x3.4" size) is 21.06 dB at 9 GHz with a 3-dB beamwidth of 12° and 25° in the vertical and azimuthal planes, respectively (see Figure 3.33 for array details). The 4x8 antenna gain referenced to the input of the QFN CMOS chip is 18.4 dB due to the antenna and feed network losses (see Table 3.2). Once the QFN CMOS chip gain (~7 dB average with VGA control), and the transmission-line and Wilkinson combiner loss (1.2 dB) at the output of the CMOS chip are included, the active antenna gain is ~24 dB at 9 GHz.

If a passive antenna is used as a reference with an 8:1 Wilkinson summing network (loss of 1.7 dB), then the 4x8 antenna gain becomes 16.7 dB at 9 GHz. Such a passive array has been built and the measured gain was 17.6+/-0.5 dB at 9 GHz. The difference is due to errors in gain measurements and standing waves in the relatively

Table 3.2: Antenna array gain

Description	Gain/Loss (dB)
Antenna Directivity	21.06
Microstrip Antenna Loss	0.7
Vertical Feed Network Loss	0.9
CPW Feed Network Loss	1.1
Total Losses	2.7
Antenna Gain[1]	18.4
Antenna Gain[2]	24
Antenna Gain[3]	16.7

1 Gain defined to the input of the QFN CMOS pacakge.

2 Gain defined at the coaxial port and includes the CMOS chip gain and after-CMOS transmission-line loss.

3 Gain defined for a passive array only includes the 8:1 Wilkinson combiner network.

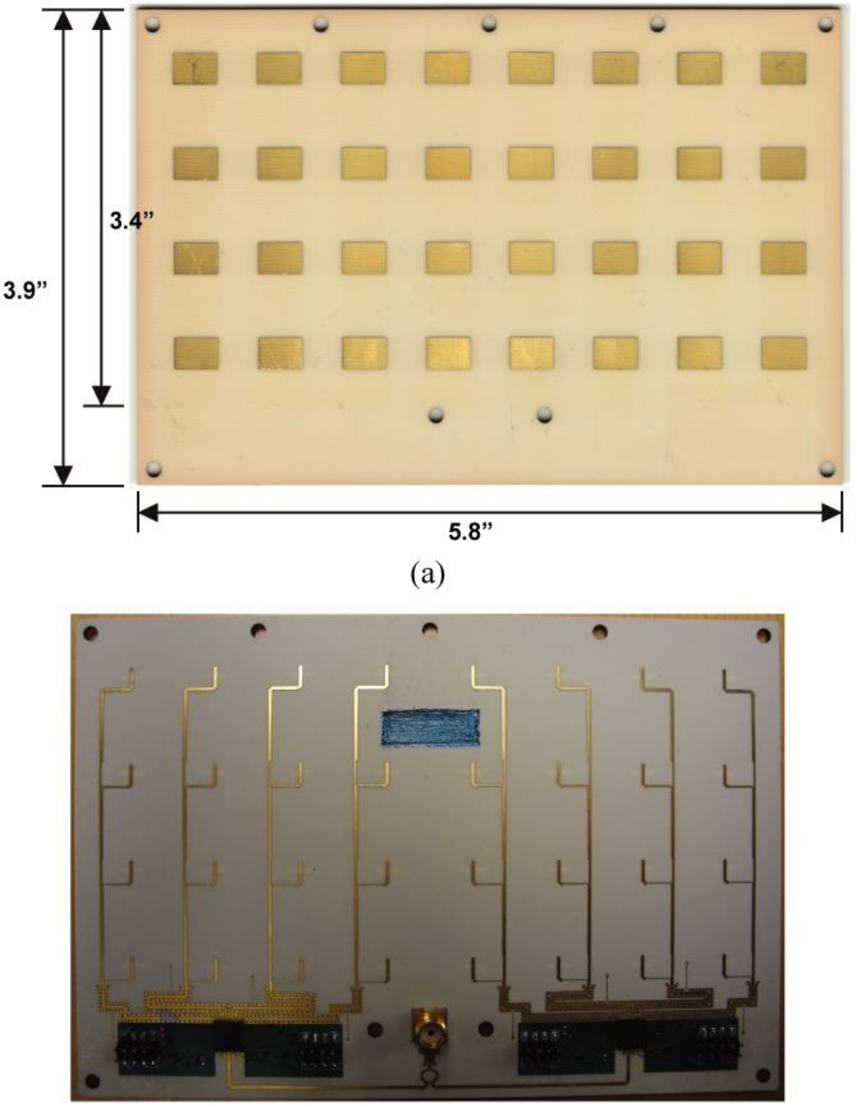

(a)

(b)

Figure 3.33: 4x8 antenna array; (a) front-side, and (b) back-side microstrip feed network and QFN components.

small antenna measurement chamber (2 meters in length).

The measured patterns are shown in Figure 3.34 for the elevation and azimuth (scanned) planes. In all cases, the cross-polarization components is < -25 dB due to scanning in one of the principal planes. Note that at turn-on, without any calibration whatsoever, the array showed an active broadside gain of 19.0 dB, but it was determined that the registers in the CMOS chips randomly set the phase states with +/-30-90° errors between the channels. After calibrating out the phase errors and setting the amplitude to be uniform across the array, an active gain of 23.0+/-0.5 dB was measured which compares well with the expected value of ~24 dB. Measurements agree well with the simulated patterns (and are not shown). The scanning performance of the array shows ~2 dB gain drop up to 45° in agreement with simulations, and a 5 dB drop at 60° scan angle due to the triggering of a grating lobe.

Figure 3.34c presents the measured antenna gain vs. frequency and scan angle. The bandwidth performance is dominated by both the 1x4 vertical microstrip antennas and the CMOS chip, and the ripples are most probably due to mismatch between the 1x4 vertical antenna impedance and the CMOS QFN package input impedance. This ripple will be reduced in the future (or become inconsequential for system G/T) if a 17 dB GaAs LNA is used at every vertical antenna.

Besides the single PCB stack-up, no other hardware is required for the 4x8 active phased array, demonstrating the compactness of the array design when using QFN packaged chips.

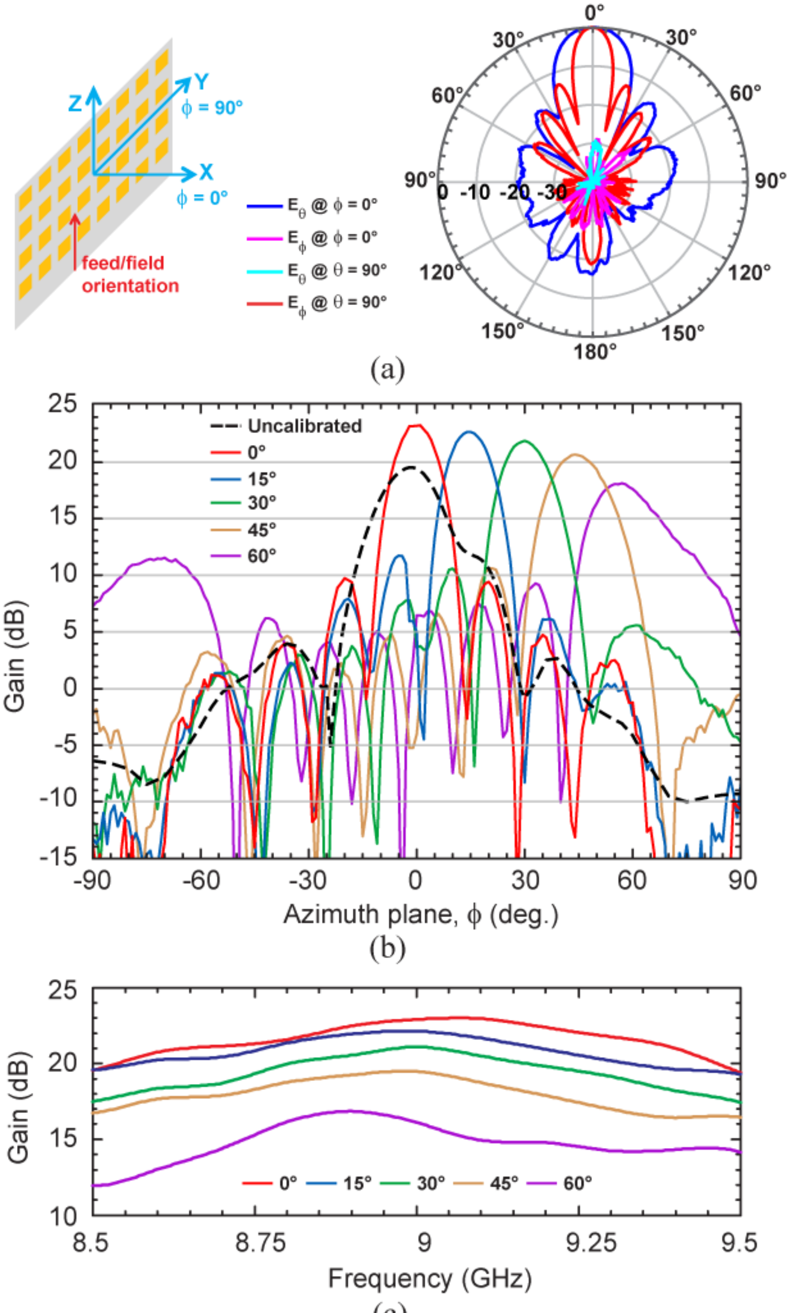

(a)

(b)

(c)

Figure 3.34: Active receiver array (a) normalized pattern, and (b) azimuth plane scanned patterns at 9 GHz, and (c) gain across frequency.

3.7 Conclusion

An 8-channel active electronically scanned phased array is presented at 8.5-9.5 GHz. The phased-array uses only two CMOS chips, QFN packaged, and a simple PCB stack-up. The high integration density of silicon chips (SiGe, CMOS) greatly simplifies phased-array development, and allows for commercial high-volume techniques to be used. We believe that, together with built-in self-test (BIST) capabilities for silicon RFIC arrays [74], large-scale phased arrays can be developed at low-cost, using automated manufacturing techniques and test, which will greatly advance the state-of-the art for phased-array panels.

Chapter 3 is based on and mostly a reprint of the material that has been submitted in *IEEE Trans. Microw. Theory Techn.* (2015), and material that has been published in *Proc. IEEE Antennas Propag. Symp.* (Jul 2011), Kevin M. Ho, Donghyup Shin and Gabriel M. Rebeiz. The dissertation author was the primary author of this material.

Chapter 4

Circularly Polarized Microstrip Antenna Array Performance Studies

4.1 Overview

4.1.1 Motivation

Circularly polarized (CP) antenna patterns can be obtained from linearly polarized (LP) microstrip antenna elements [75], with a unit cell of every 4 elements laid out in a 2x2 square grid, physically rotated clockwise (CW) or counter-clockwise (CCW) by 90° in a sequential manner (i.e. sequential rotation), and excited with quadrature phase offset (Figure 4.1b). With LP antenna elements replaced by CP elements, the same arrangement of sequential rotation and quadrature phase offset (Figure 4.1c) will enhance the axial ratio (AR) of the 2x2 array in CP mode.

As such, Figure 4.1d-f presents 3 methods of achieving CP for large arrays;

I - uniform array of CP antenna elements (Figure 4.1d).

II - array of LP antenna elements with sequential rotation and quadrature phase offset for every 2x2 unit cell (Figure 4.1b & e).

III - array of CP antenna elements with sequential rotation and quadrature phase offset for every 2x2 unit cell (Figure 4.1c & f).

Existing work for sequential rotation and quadrature phase excitation of antenna elements for circular polarized arrays includes [75] for LP elements, and [76]-[78] for array analysis with CP elements. Details for the following are not adequately presented:

- Combination of sequential element rotation and quadrature phase excitation, while performing beam scanning.
- Xpol performance of square and equilateral arrays (Figure 4.2)
- Impact of LP elements on CP array (Figure 4.1e).

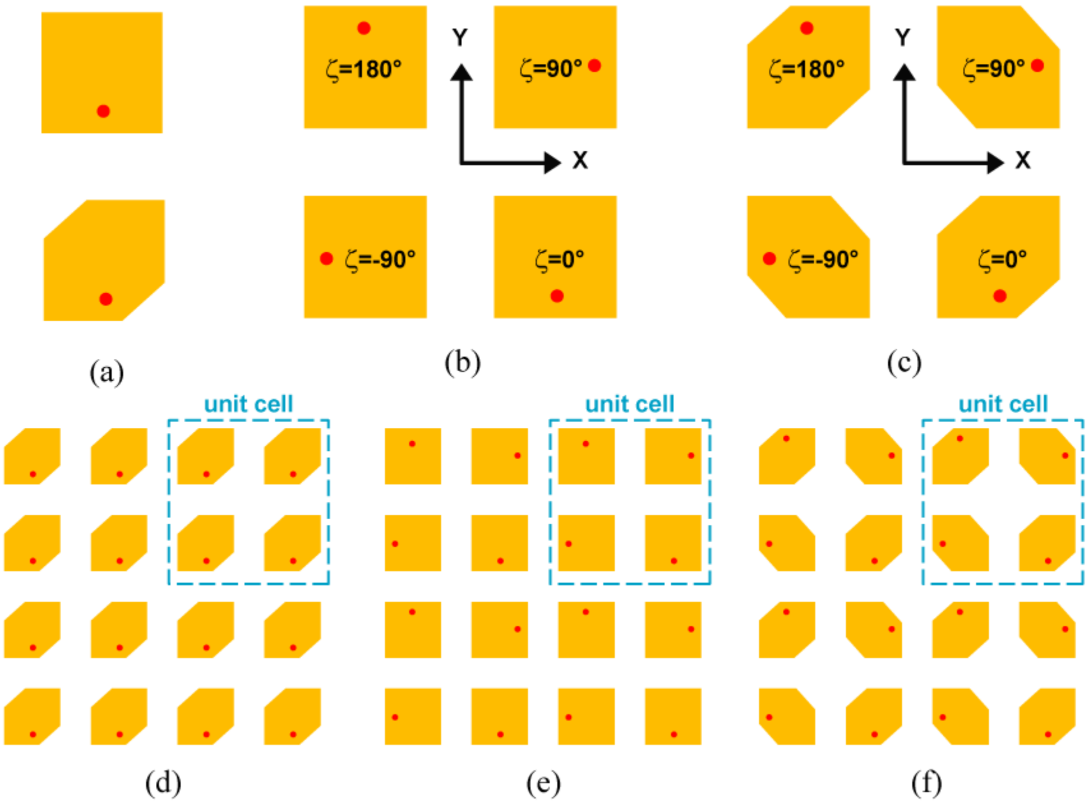

(a) (b) (c)

(d) (e) (f)

Figure 4.1: (a) LP (top) and LHCP (bottom) microstrip antenna elements; sequential rotation and quadrature phase offset for LHCP operation with (b) LP and (c) LHCP antenna elements; LCHP antenna arrays with (d) LCHP elements in uniform array, (e) LP elements and (f) LHCP elements with sequential rotation and quadrature phase offset.

- Impact of CP element Xpol on CP array (Figure 4.1f).

Bandwidth widening for CP antennas leads to high Xpol and poor AR performance. As an example, Figure 4.3 presents the design of a 20 GHz circularly polarized antenna element with a single feed-point on a 0.0307” thick RO4725 laminate (ε_r = 2.55, tanδ = 0.0026). Normalized Xpol is ~ -10 dB for 1 GHz of operating bandwidth, and ~ -6.5 dB for 2 GHz bandwidth. Insights of the influence of element Xpol impact on the full CP array will allow for determination of bandwidth and AR performance for individual elements without any performance sacrifice on the final array Xpol.

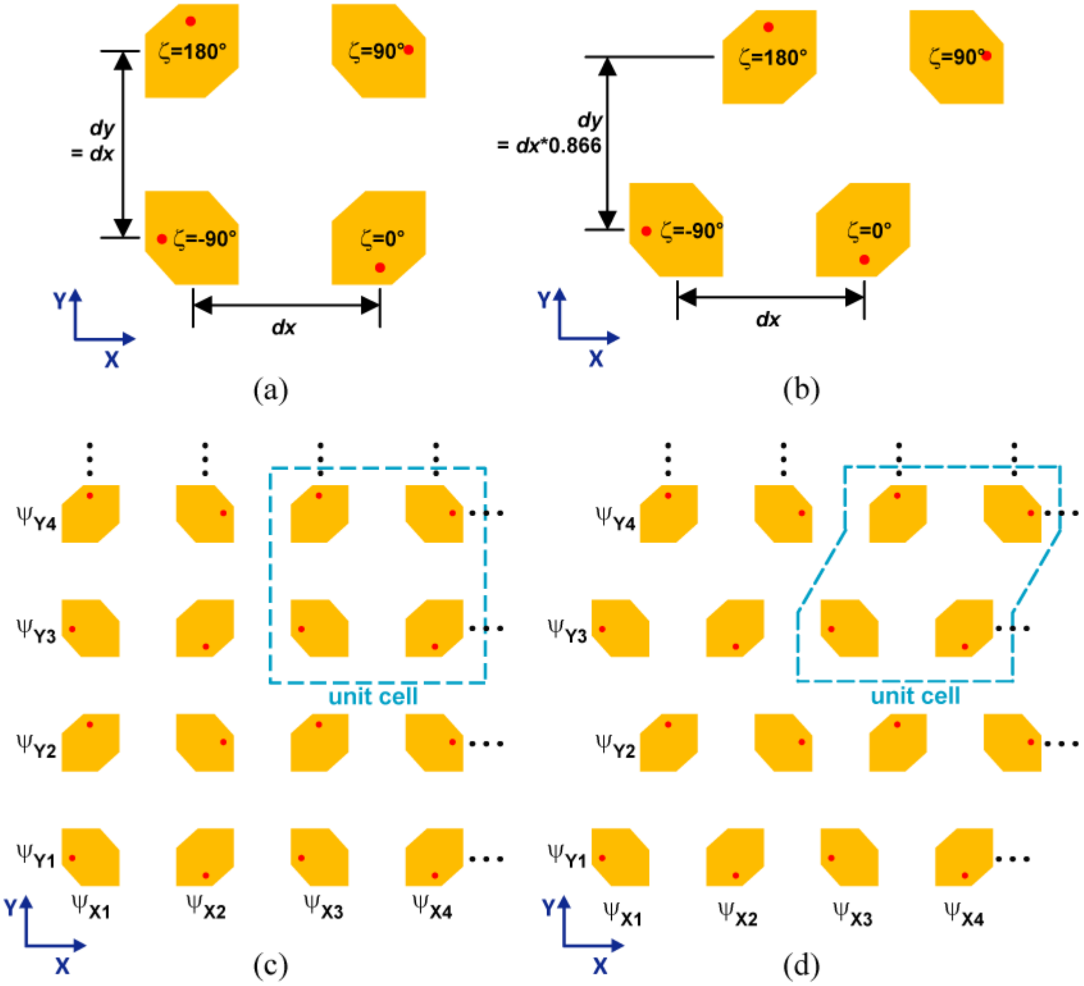

(a) (b)

(c) (d)

Figure 4.2: 2x2 unit cell for (a) square and (b) equilateral layout, and (c) square and (d) equilateral 2^Nx2^N array.

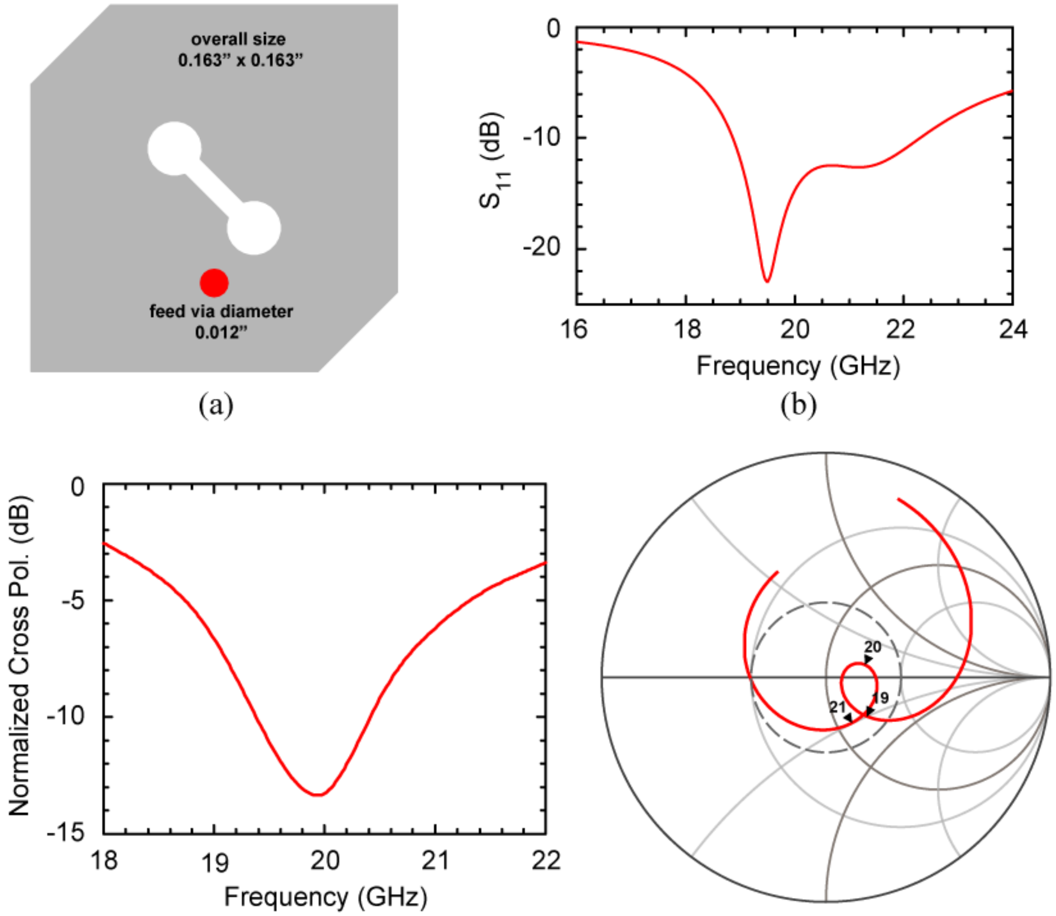

(a) (b)

(c) (d)

Figure 4.3: 20 GHz circular polarized microstrip antenna on 0.0307" thick RO4725 laminate; (a) layout, (b) return loss, (c) normalized cross-polarization, and (d) Smith chart response.

4.1.2 Scope

With pattern superposition of elementary microstrip antenna element pattern, this chapter presents calculated co-polarization (Cpol) and Xpol array patterns for various cases as presented in Table 4.1.

Elementary element pattern (EP) with array factor (AF) multiplication techniques are presented, instead of detailed and massive EM simulated results, to distinguish fundamental impact of pattern degradation intrinsic to the element or unit-

Table 4.1: List of normalized pattern plots for CP arrays

EP	Main beam	Array layout	Element Xpol	Figure ref.
LP	Broadside	Square	N.A.	Figure 4.6
		Staggered		Figure 4.7
	θ = 30°	Square	N.A.	Figure 4.8
		Staggered		Figure 4.9
CP	Broadside	Square	N.A.	Figure 4.11
		Staggered		Figure 4.12
		Square	-20, -10, -6 dB	Figure 4.13
		Staggered		
	θ = 30°	Square	N.A.	Figure 4.15
		Staggered		Figure 4.16
		Square	-20, -10, -6 dB	Figure 4.17
		Staggered		Figure 4.18

cell pattern, and removing the extrinsic factors of surface waves triggering, mutual coupling of elements, and impact of finite substrate and ground plane.

LP and CP microstrip antenna element will be presented, followed by CP arrays using LP and CP elements with sequential rotation and quadrature excitations (methods II and III). Performance for CP arrays with uniform layout of CP elements (i.e. method I) is consistent with CP element performance (direct scalar multiplication of element pattern to the array), and will not be presented.

Cases of broadside arrays and scanned arrays are presented. Main beam scan of up to 30° elevation in any azimuth plane is desired for the intended application. Results from the studies will aid in the choice of array architecture and definition of element performance, for the development of CP wideband or shared aperture electronically scanned arrays.

4.2 Microstrip Antenna Element and Array Setup

4.2.1 Microstrip Antenna Element Pattern

An elementary form of microstrip antenna pattern representation is that of a pair of radiating slots [34], with the following equations for an antenna with length *L* and width *W*:

$$\vec{E}_X = \frac{\sin(k\frac{W}{2}\sin\theta\sin\phi)}{k\frac{W}{2}\sin\theta\sin\phi}\cos(k\frac{L}{2}\sin\theta\cos\phi)\cdot\left(-\cos\phi\hat{\theta}+\cos\theta\sin\phi\hat{\phi}\right) \tag{4.1}$$

for case of E-plane oriented along X-axis (i.e. radiating slots oriented along Y-axis, and array factor of slots along X-axis, Figure 4.4a), and

$$\vec{E}_Y = \frac{\sin(k\frac{W}{2}\sin\theta\cos\phi)}{k\frac{W}{2}\sin\theta\cos\phi}\cos(k\frac{L}{2}\sin\theta\sin\phi)\cdot\left(\sin\phi\hat{\theta}+\cos\theta\cos\phi\hat{\phi}\right) \tag{4.2}$$

for case of E-plane oriented along Y-axis (i.e. radiating slots oriented along X-axis, and array factor of slots along Y-axis, Figure 4.4b).

These patterns (4.1) and (4.2) reflects excitation from radiating slots, and will inherently have no Xpol components (i.e. $|E_\theta| = |E_\phi|$ along diagonal plane for LP). These patterns can also be generated from HFSS, with "infinite ground plane" option selected for the finite conductivity boundary condition as the bottom ground plane, with almost negligible impact of the radiation from non-radiating slots. More complicated patterns can be found in [28]-[30], which relates the impact of the substrate thickness on the pattern, and corresponds well to IE3D simulated patterns.

With the X- and Y-axis oriented LP microstrip antenna element pattern defined, a practical LP antenna element pattern with Xpol can be derived from

$$\vec{E}_{Lin} = |X_{Lin}|e^{j\angle X_{Lin}}\cdot\vec{E}_X + |Y_{Lin}|e^{j\angle X_{Lin}}\vec{E}_Y = E_{Lin,\theta}\hat{\theta}+E_{Lin,\phi}\hat{\phi} \tag{4.3}$$

where X_{Lin} and Y_{Lin} corresponds to the excitation for the ideal X- and Y-axis oriented LP components. Defining $|X_{Lin}| = 1 - \Delta_{Lin}$, $|Y_{Lin}| = \Delta_{Lin}$, and $\angle X_{Lin} = \angle Y_{Lin} = 0°$, pattern for a HP (or LP along X-axis) antenna element is defined, with the Xpol at broadside = $|E_{Lin,cross}| = 20log_{10}[\Delta_{Lin} / (1- \Delta_{Lin})]$.

Similarly, CP excitation can be defined with the following:

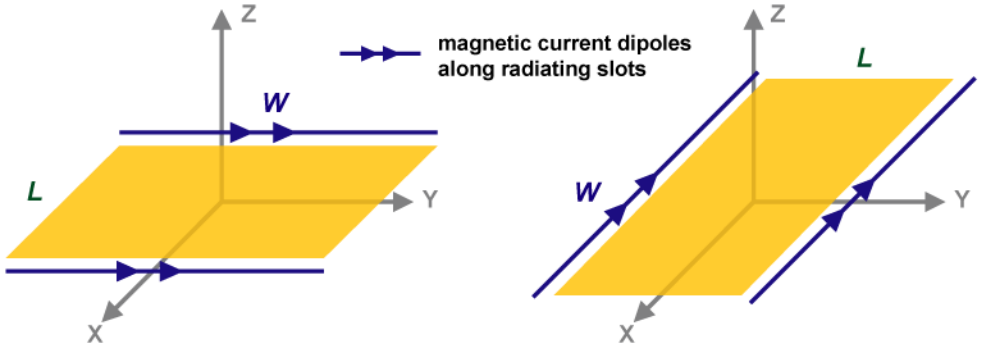

(a) (b)

Figure 4.4: Elementary LP microstrip antenna element with E-plane aligned along (a) X-axis and (b) Y-axis.

$$
\begin{aligned}
\vec{E}_{Cir} &= |X_{Cir}| e^{j\angle X_{Cir}} \cdot \vec{E}_X + |Y_{Cir}| e^{j\angle Y_{Cir}} \vec{E}_Y = E_{Cir,\theta}\hat{\theta} + E_{Cir,\phi}\hat{\phi} \\
E_{LHCP} &= \frac{1}{\sqrt{2}}\left(E_{Cir,\theta} - jE_{Cir,\phi}\right) \\
E_{RHCP} &= \frac{1}{\sqrt{2}}\left(E_{Cir,\theta} + jE_{Cir,\phi}\right)
\end{aligned}
\tag{4.4}
$$

Defining $|X_{Cir}| = 1$ +/- Δ_{Cir}, $|Y_{Cir}| = 1$ -/+ Δ_{Cir}, and $|\angle X_{Cir} - \angle Y_{Cir}| = 90°$, Xpol at broadside (i.e. $\theta = 0°$) arising from quadrature feed amplitude imbalance is defined as $|E_{Cir,cross}| = 20log_{10}(\Delta_{Cir})$.

Figure 4.5a presents normalized pattern of an ideal CP microstrip element with excitation based on (4.4) and $\Delta_{Cir}=0$, (i.e. ideal CP element with no Xpol excitation). Normalized Xpol of < -30 dB is found in visible field-of-view (FOV) of $\theta < 30°$ ("30-for-30"), and < -20 dB within FOV of $\theta < 45°$. This figure represents the theoretical limit for lowest possible CP from a single microstrip antenna element using quadrature excitation of orthogonal linear modes. Any better Xpol performance from a *single element* for a wider region can only be achieved with true circular polarized antenna element (e.g. helical or spiral antennas).

Figure 4.5b-d presents normalized patterns for CP microstrip elements with various Xpol excitations (i.e. Δ_{Cir} = 0.1, 0.315, and 0.5), for normalized cross-polarization levels of -20 dB, -10 dB, and -6 dB respectively. Square geometry of

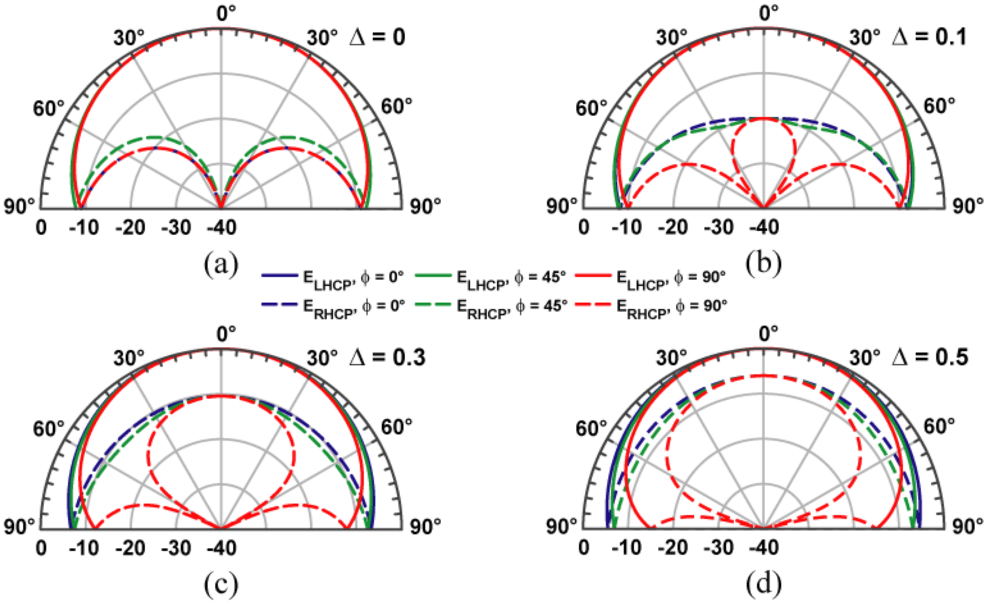

(a) (b) (c) (d)

Figure 4.5: Xpol of CP microstrip antenna arising from quadrature feed amplitude imbalance, with Δ_{Cir} = (a) 0, (b) 0.1, (c) 0.315, and (d) 0.5.

$0.25\lambda_0$ is considered for the antenna element (i.e. $W = L = 0.25\lambda_0$), which corresponds to implementation on RO4003 laminates ($\varepsilon_r = 3.55$, $\tan\delta = 0.0027$).

Finally, AR for CP pattern is defined as

$$AR = \frac{Cpol + Xpol}{Cpol - Xpol} \tag{4.5}$$

and AR of 2 (or 3 dB) and 3 (or 4.8 dB) corresponds to Xpol of -10 dB and -6 dB respectively.

4.2.2 CP Array Setup

With the basic antenna pattern defined, an array layout is formally defined next. Full array pattern is obtained with pattern multiplication of microstrip EP as defined above, with the AF of the layout as defined herewith.

Requirements for the layout include the need for performing beam scanning and cross-polarization cancellation. A LP or LHCP microstrip element (top and bottom of Figure 4.1a respectively) is arranged as a LHCP unit cell (Figure 4.1b and c for LP and LHCP elements respectively) with the elements sequentially rotated and fed with

Table 4.2: Directivity and HPBW for square arrays with $0.59\lambda_0$ element spacing.

Array size	No of Elements	Directivity	HPBW
4 x 4	16	18.4 dB	21.7°
8 x 8	64	24.4 dB	10.7°
16 x 16	256	30.5 dB	5.4°
32 x 32	1024	36.5 dB	2.7°

quadrature phase progression (ζ). The unit cells are then combined to form a large square array of 2^N by 2^N elements (Figure 4.2c), or with every alternate row along the array offset to form a equilateral (or staggered) array (Figure 4.2b,d) with row-offset along X-axis for the studies presented. Cases of N = 1-5 will be considered, corresponding to 2x2 unit cell, 4x4, 8x8, 16x16, and 32x32 arrays (Table 4.2). Layout dimensions for the equilateral array is defined in Figure 4.2b, which also corresponds to equidistant (= *dx*) element separation throughout the array.

Progressive phase distribution is introduced (ψ_{xp}, ψ_{yp}, with $p = 1, 2, .. 2^N$) to the elements for electronic beam scan off array broadside. Element spacing for all cases presented henceforth is at $0.59\lambda_0$ (i.e. $dx = 0.59\lambda_0$ in Figure 4.2a-b) unless otherwise stated. This spacing corresponds to 30° beam scan without incurring surface waves excitation on RO4003 substrates (with $\varepsilon_r = 3.55$, Figure 3.18).

Only one hierarchy of element rotation and quadrature phase offset is performed for at a level of every 2x2 unit cell. Broadside CP array performance can be further enhanced with a 2nd hierarchical level of sequential rotation and quadrature phasing i.e. treating every 2x2 unit cell as a 2nd level of EP, and performing layout rotation and quadrature phasing for every “2x2” groups of unit cells. That is not considered for the studies, as the 2nd level of hierarchy will invalidate electronic beam scan capabilities.

4.3 CP Arrays with LP Microstrip Antenna Elements

4.3.1 CP Broadside Array Xpol from LP Elements

Figure 4.6 presents normalized patterns from LHCP *broadside arrays*, for cases of 2x2 unit cell (Figure 4.2a), 4x4, 8x8, 16x16 and 32x32 *square layouts* (Figure 4.2c), and comprising of *LP antenna elements* defined from (4.3) with $\Delta_{Lin} = 0$ for no EP Xpol.

For a 2x2 unit cell (Figure 4.6a), the theoretical Xpol in the diagonal plane (ϕ = 45°) is barely -10 dB for FOV of $\theta < 30°$, despite having ideal EP with no Xpol. 2x2 unit cell forms as an "EP" at a higher hierarchy for large arrays, and the diagonal plane Xpol will have an impact for applications requiring beam scanning in the diagonal plane. Normalized Xpol in the principle planes (Z-X and Y-Z planes, for ϕ = 0° and 90° respectively) < -30 dB within FOV of $\theta < 60°$.

With larger array sizing, Xpol cancellation impact from the sequential layout arrangement further suppresses the CP array Xpol to < -30 dB across full visible half-

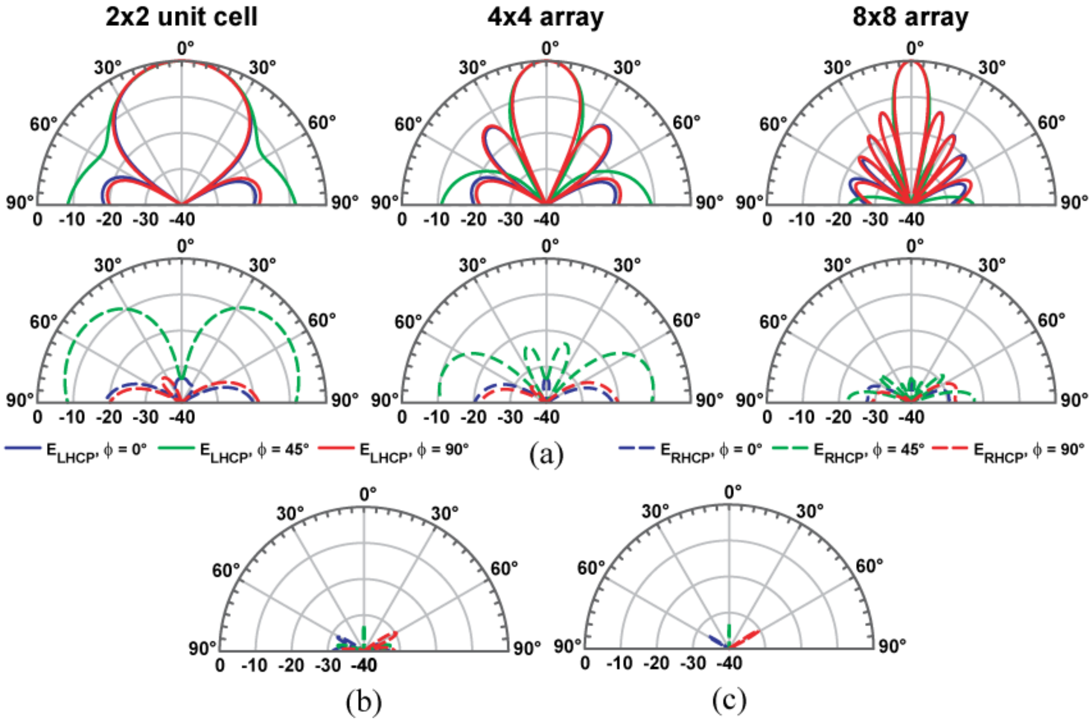

Figure 4.6: Normalized *broadside beam* patterns for LHCP *square array* with *LP* EP; Cpol (top row) and Xpol (bottom row) for (a) 2x2 (left column), 4x4 (middle column) and 8x8 arrays (right column), and Xpol for (b) 16x16 and (c) 32x32 arrays.

space. This forms the theoretical limits for minimum Xpol expectations from *CP broadside arrays* with *LP elements*. Xpol from individual LP elements has no further impact on these patterns presented.

Similarly, Figure 4.7 presents normalized patterns from LHCP *broadside arrays*, for cases of 2x2 unit cell (Figure 4.2a), 4x4, 8x8, 16x16 and 32x32 *equilateral layouts* (Figure 4.2d), and comprising of *LP antenna elements* defined from (4.3) with $\Delta_{Lin} = 0$ for no EP Xpol. For case of 2x2 array (Figure 4.7a-left column), staggered or equilateral arrays further degrades the Xpol patterns to > -10 dB in both diagonal plane ($\phi = 45°$) and plane of row-staggering (Z-X plane, $\phi = 0°$). A strong Xpol component at elevation angle of $\theta = 60°$ is found in the Z-X plane for all arrays cases. The row-staggering mechanism breaks the symmetry of the 2x2 unit cell symmetry in the orthogonal principle planes, with the plane of row-staggering having less CP Xpol pattern truncation at elevations angles beyond $\theta > 60°$ which it otherwise would had

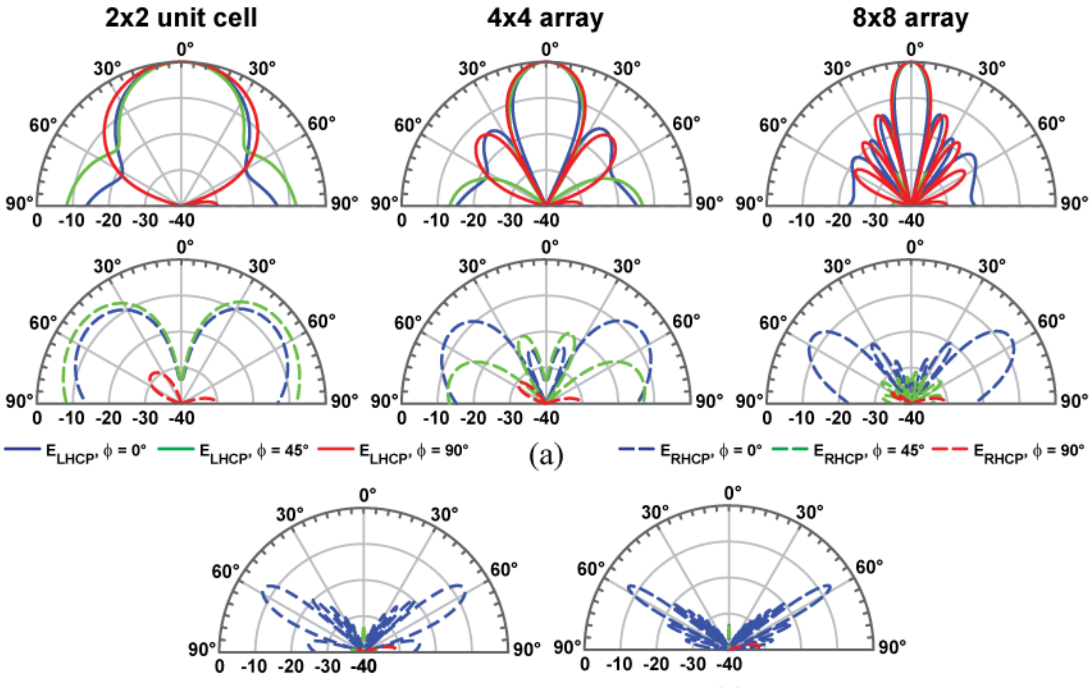

(b) (c)

Figure 4.7: Normalized *broadside beam* patterns for LHCP *equilateral array* with *LP* EP; Cpol (top row) and Xpol (bottom row) for (a) 2x2 (left column), 4x4 (middle column) and 8x8 arrays (right column), and Xpol for (b) 16x16 and (c) 32x32 arrays.

from a square array layout. This may not be of concern, as generally full-FOV (FFOV) is typically defined as within θ < 60°.

Element Xpol has little impact on the CP array performance. These verifies, for LP elements in CP arrays, with fixed broadside beams, square arrays provides much better cross-polarization performance than the equilateral layout, with normalized Xpol of < -30 dB to be expected.

4.3.2 CP Scanned Array Xpol from LP Elements

Figure 4.8 presents normalized patterns from LHCP *scanned arrays*, for cases of 8x8, 16x16 and 32x32 *square layouts* (Figure 4.2c), and comprising *of LP antenna elements* defined from (4.3) with $\Delta_{Lin} = 0$ for no EP Xpol. Main beam is scanned to θ = 30° in the principle plane (Z-X plane, ϕ = 0°, Figure 4.8a) and in the diagonal plane (ϕ = 45°, Figure 4.8b). With beam scanned in principle plane, Xpol levels decreases with increasing array size, to worst case of -25 dB for large array (Figure 4.8a). A strong Xpol "spike" is found when the beam scan is performed in the diagonal plane, which corresponds to the high 2x2 unit cell Xpol level presented in Figure 4.6a. Xpol degradation of individual LP elements has minimal impact on CP array Xpol performance.

Similarly, Figure 4.9 presents normalized patterns from LHCP *scanned arrays*, for cases of 8x8, 16x16 and 32x32 *equilateral layouts* (Figure 4.2d), and comprising *of LP antenna elements* defined from (4.3) with $\Delta_{Lin} = 0$ for no EP Xpol. Main beam is scanned to θ = 30° in the principle plane of row-staggering (Z-X plane, ϕ = 0°, Figure 4.9a), in the orthogonal principle plane (X-Y plane, ϕ = 0°, Figure 4.9c), and in the diagonal plane (ϕ = 45°, Figure 4.9b). Strong Xpol is now observed in the equilateral array, for beam scanned in the plane of row-staggering (i.e. Z-X plane, ϕ = 0°), shown in bottom row of Figure 4.9a. Xpol degradation of individual LP elements has minimal impact on CP array Xpol performance.

These plots highlights potential limitations for CP beam scanned arrays with LP microstrip antenna elements. A possible way to reduce this strong Xpol "spike" response is to decrease the element spacing, as shown in Figure 4.10, for its angle of inclination away from Z-axis. For case of square arrays, the spike moves away from broadside towards the X-Y plane (θ = 90°) as the element spacing decreases to below $0.45\lambda_0$ (blue trace in Figure 4.10). Case of 8x8 array size is presented in Figure 4.10, and is representative for all cases. Values vary within 1° for larger arrays with larger spacing, and up to 5° for decreasing element spacing.

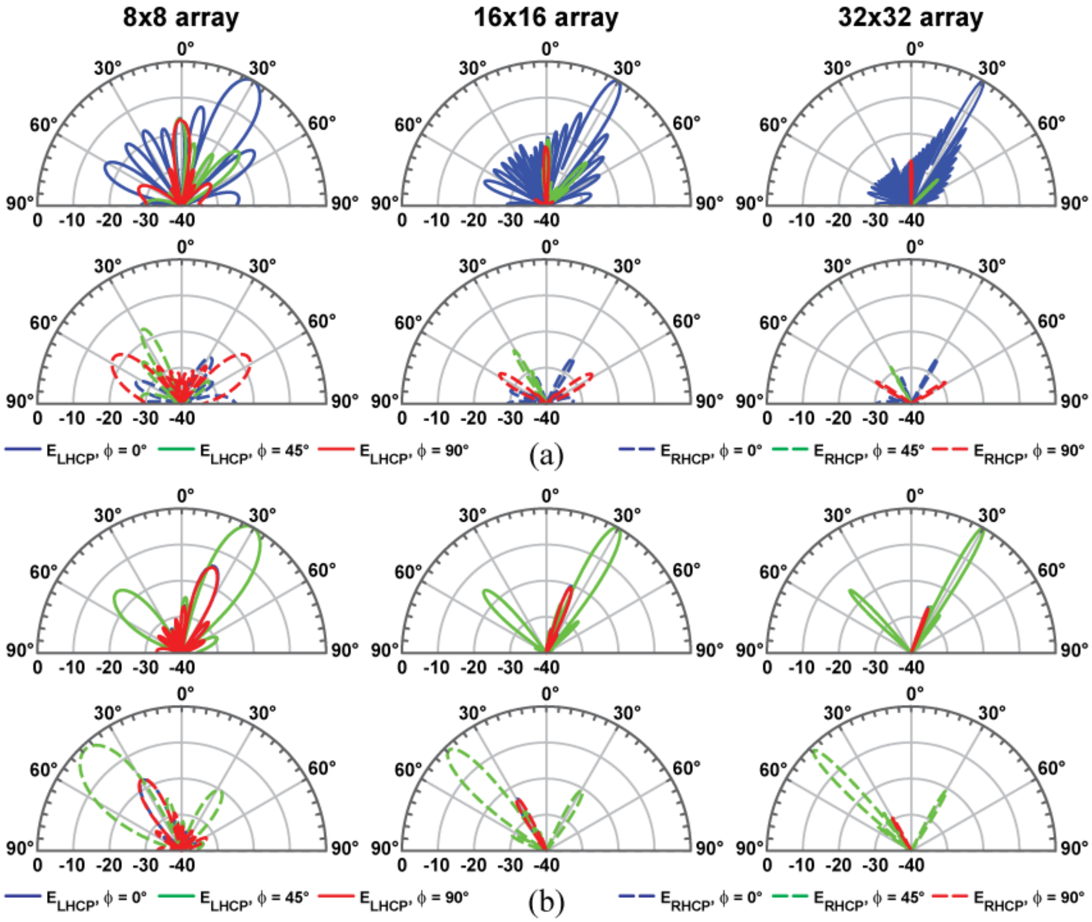

Figure 4.8: Normalized *30° scan* patterns for LHCP *square array* with *LP* EP; Cpol (top row) and Xpol (bottom row) for 8x8 (left column), 16x16 (mid column) and 32x32 arrays (right column); with beam scan in (a) principle plane (ϕ = 0°) or in (b) diagonal plane (ϕ = 45°).

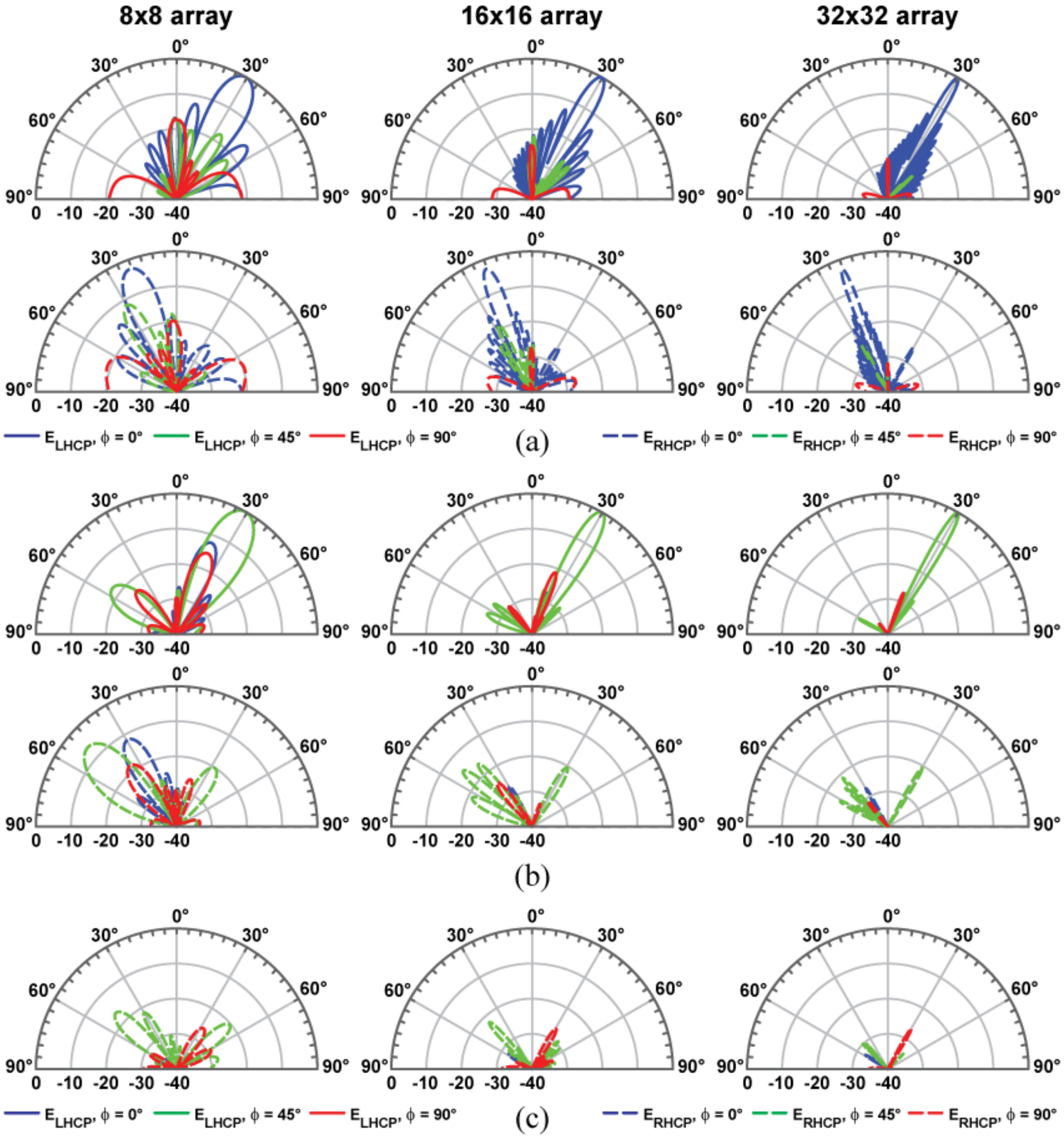

Figure 4.9: Normalized *30° scan* patterns for LHCP *staggered array* with *LP EP*; Cpol (top row) and Xpol (bottom row) for 8x8 (left column), 16x16 (mid column) and 32x32 arrays (right column); with beam scan in (a) principle Z-X plane (ϕ = 0°), (b) diagonal plane (ϕ = 45°); and Xpol for beam scan in (c) principle Y-Z plane (ϕ = 90°).

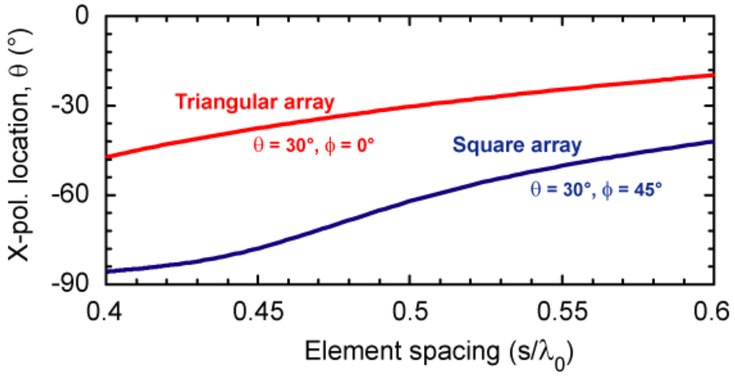

Figure 4.10: Location of Xpol spikes in elevation plane, for 30° beam scanned 8x8 LCHP array of *LP EP*; main beam in diagonal plane (ϕ = 45°) for square array (red), and in principle Z-X plane for equilateral array (blue).

4.4 CP Arrays with CP Microstrip Antenna Elements

4.4.1 CP Broadside Array Xpol from CP Elements

Figure 4.11 presents normalized patterns from LHCP *broadside arrays*, for cases of 2x2 unit cell (Figure 4.2a), 4x4, 8x8 and 16x16 and 32x32 *square layouts* (Figure 4.2c), and comprising of *LHCP antenna elements* defined from (4.4) with Δ_{Cir}=0 for no EP Xpol. Similarly, Figure 4.12 presents normalized patterns from LHCP *broadside arrays*, for cases of 2x2 unit cell (Figure 4.2a), 4x4, 8x8 and 16x16 and 32x32 *equilateral layouts* (Figure 4.2d), and comprising of *LHCP antenna elements* defined from (4.4) with Δ_{Cir}=0 for no EP Xpol. For both sets of patterns, Xpol consistently reduces for CP array reduces with increasing array size, till below -40 dB for 16x16 arrays.

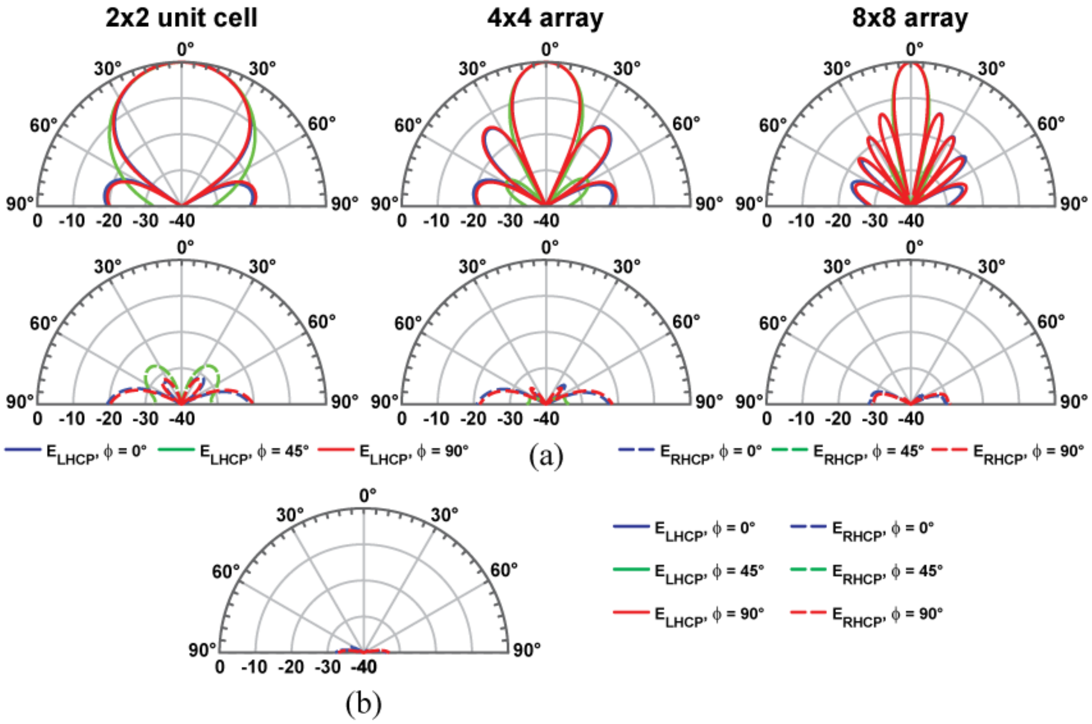

Figure 4.11: Normalized *broadside beam* patterns for LHCP *square array* with *LHCP* EP; Cpol (top row) and Xpol (bottom row) for (a) 2x2 (left column), 4x4 (middle column) and 8x8 arrays (right column), and Xpol for (b) 16x16 array.

The array cross-polarization degrades with every element having a cross-polarization component. Figure 4.13 and Figure 4.14 presents normalized Xpol patterns from LHCP *broadside arrays*, for cases of 8x8, 16x16 and 32x32 *square* and *equilateral layouts* respectively, and comprising of *LHCP antenna elements* defined from (4.4) with Δ_{Cir}=0.1, 0.315, and 0.5 for EP Xpol of -20dB, -10 dB, and -6 dB respectively.

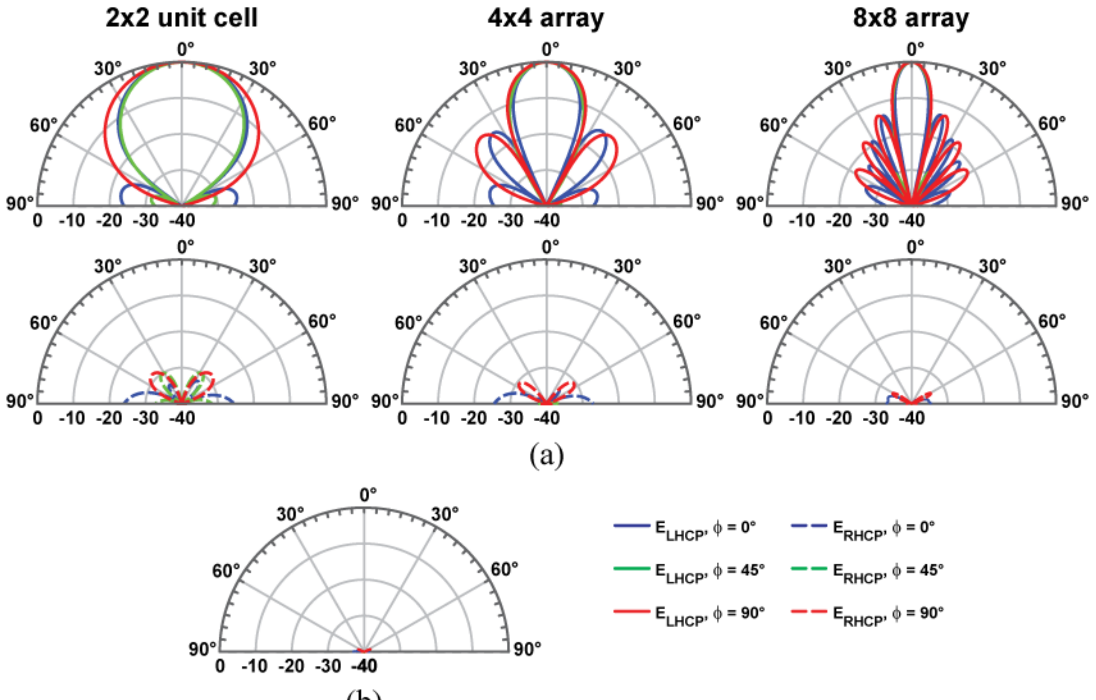

(a)

(b)

Figure 4.12: Normalized *broadside beam* patterns for LHCP *equilateral array* with *LHCP* EP; Cpol (top row) and Xpol (bottom row) for (a) 2x2 (left column), 4x4 (middle column) and 8x8 arrays (right column), and Xpol for (b) 16x16 array.

CP Xpol are within <-30 dB for all square array cases. This verifies, for case of *broadside* CP array with CP elements, EP Xpol levels are not critical, and AR of 3 more (for element Xpol of -6 dB or higher) can be tolerated for achieving wide impedance bandwidth while maintaining CP array Xpol of <-35 dB.

Similar to the case for staggered arrays with LP EP (Figure 4.7), Xpol degradation is observed for equilateral arrays, at elevation angle of θ = 60° in the plane of row-staggering (Z-X plane, ϕ = 0°), at level of ~ 6 dB below EP Xpol of CP element. In most cases, Xpol for regions at θ = 60° may fall out of the FFOV of θ < 60°

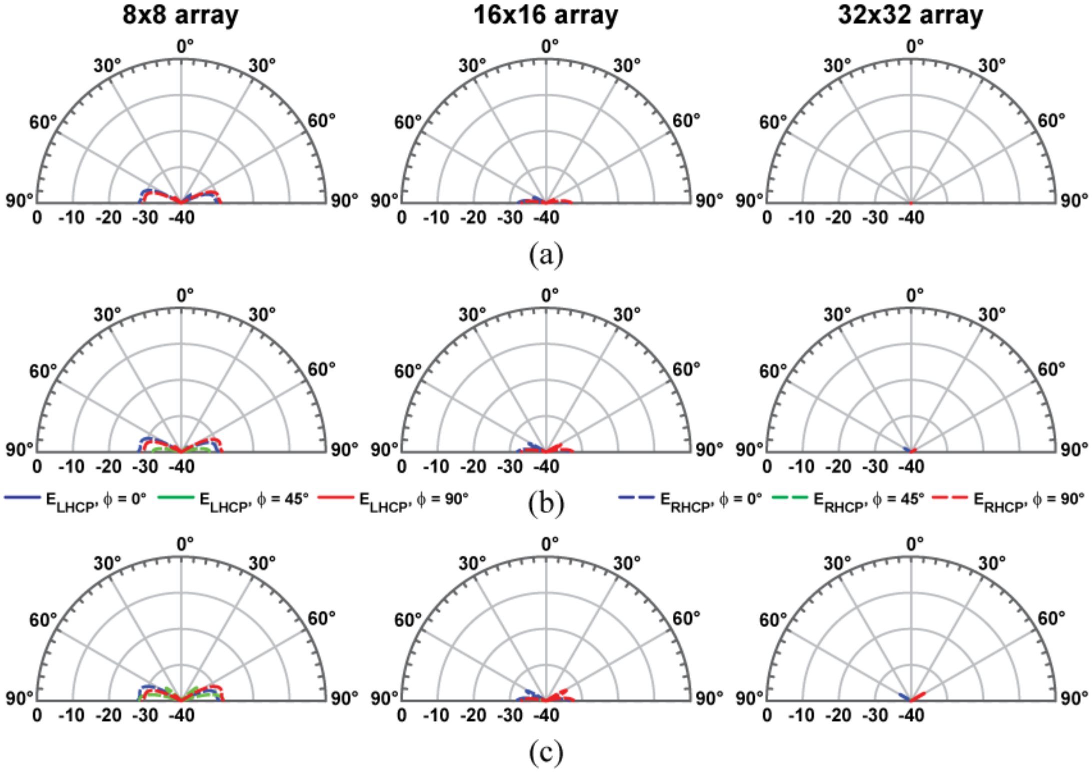

(a)

(b)

(c)

Figure 4.13: Normalized Xpol for *broadside beam* LHCP *square array* for 8x8 (left), 16x16 (middle) and 32x32 arrays (right) comprising of CP EP with Xpol of (a) -20 dB, (b) -10 dB and (c) -6 dB.

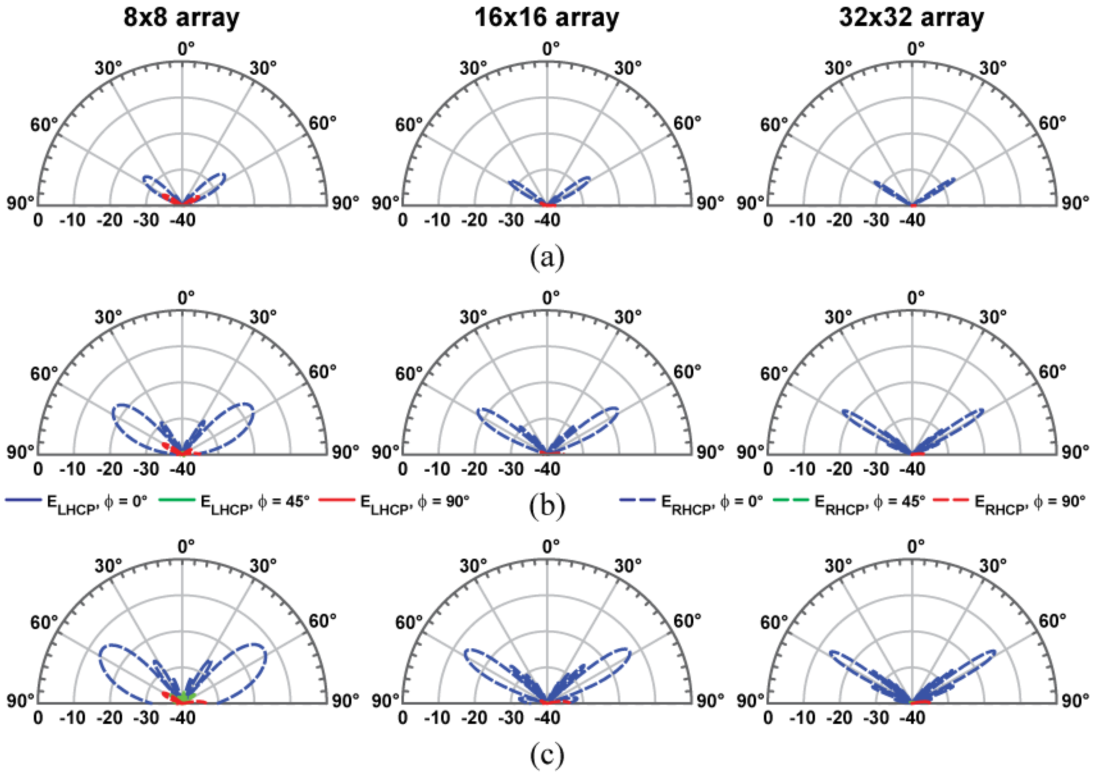

(a)

(b)

(c)

Figure 4.14: Normalized Xpol for *broadside beam* LHCP *equilateral array* for 8x8 (left), 16x16 (middle) and 32x32 arrays (right) comprising of CP EP with Xpol of (a) -20 dB, (b) -10 dB and (c) -6 dB.

4.4.2 CP Scanned Array Xpol from CP Elements

Figure 4.15 presents normalized patterns from LHCP *scanned arrays*, for cases of 8x8, 16x16 and 32x32 *square layouts* (Figure 4.2c), and comprising *of LHCP antenna elements* defined from (4.4) with Δ_{Cir}=0 for no EP Xpol. Main beam is scanned to θ = 30° in the principle plane (Z-X plane, ϕ = 0°, Figure 4.15a) and in the diagonal plane (ϕ = 45°, Figure 4.15b). Unlike the case of scanned CP arrays with LP elements (Figure 4.8b), there is no strong Xpol spike observed. Highest Xpol observed is generally at ~-23 dB in the same direction as the main beam.

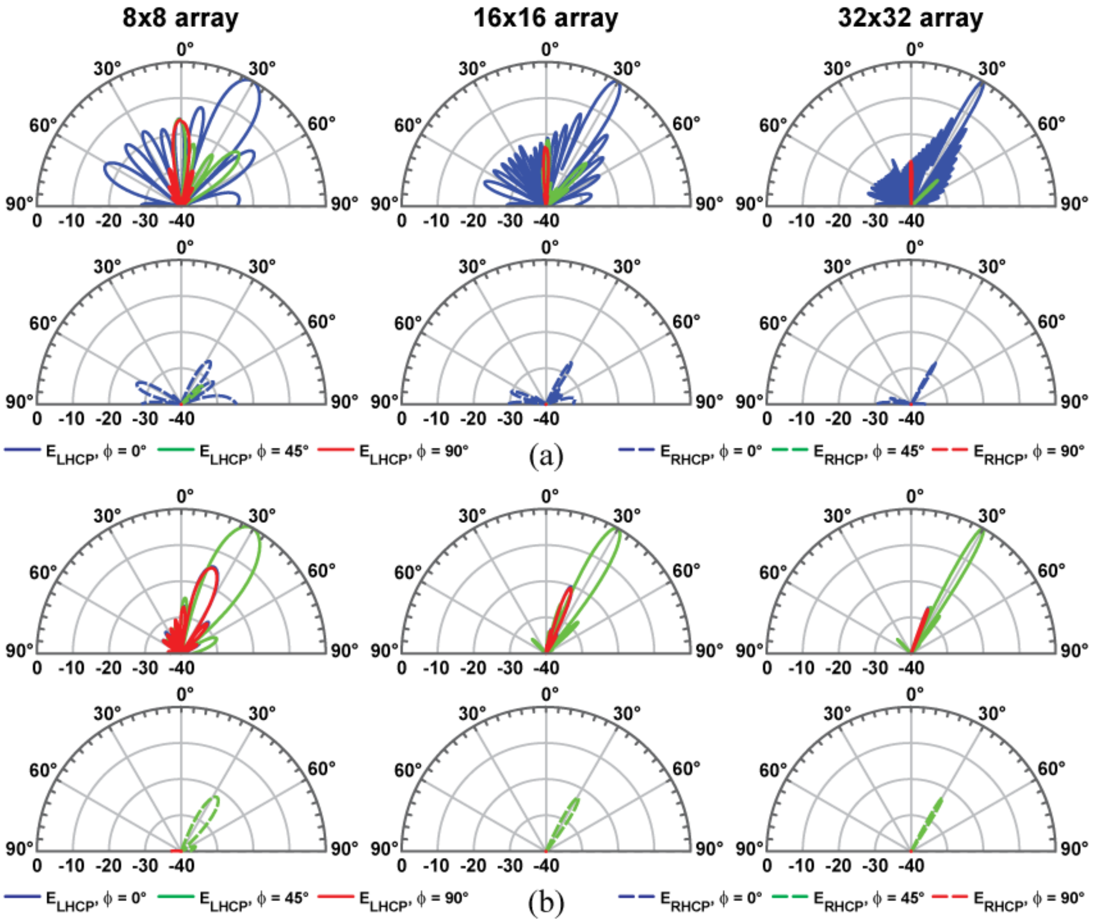

Figure 4.15: Normalized *30° scan* patterns for LHCP *square array* with *LHCP* EP; Cpol (top row) and Xpol (bottom row) for 8x8 (left column), 16x16 (mid column) and 32x32 arrays (right column); with beam scan in (a) principle plane ($\phi = 0°$) or in (b) diagonal plane ($\phi = 45°$).

In a similar fashion, Figure 4.16 presents normalized patterns from LHCP *scanned arrays*, for cases of 8x8, 16x16 and 32x32 *equilateral layouts*, and comprising *of LHCP antenna elements* defined from (4.4) with $\Delta_{Cir}=0$ for no EP Xpol. Main beam is scanned to $\theta = 30°$ in the principle plane of row-staggering (Z-X plane, $\phi = 0°$, Figure 4.16a), in the orthogonal principle plane (X-Y plane, $\phi = 0°$, Figure 4.16c), and in diagonal plane ($\phi = 45°$, Figure 4.16b). And similarly to the prior case, strong Xpol spikes found in cases of equilateral arrays of LP elements (Figure 4.9a) are not encountered for this case with CP elements, and worst case Xpol is ~ -23 dB in the orientation of the main beam.

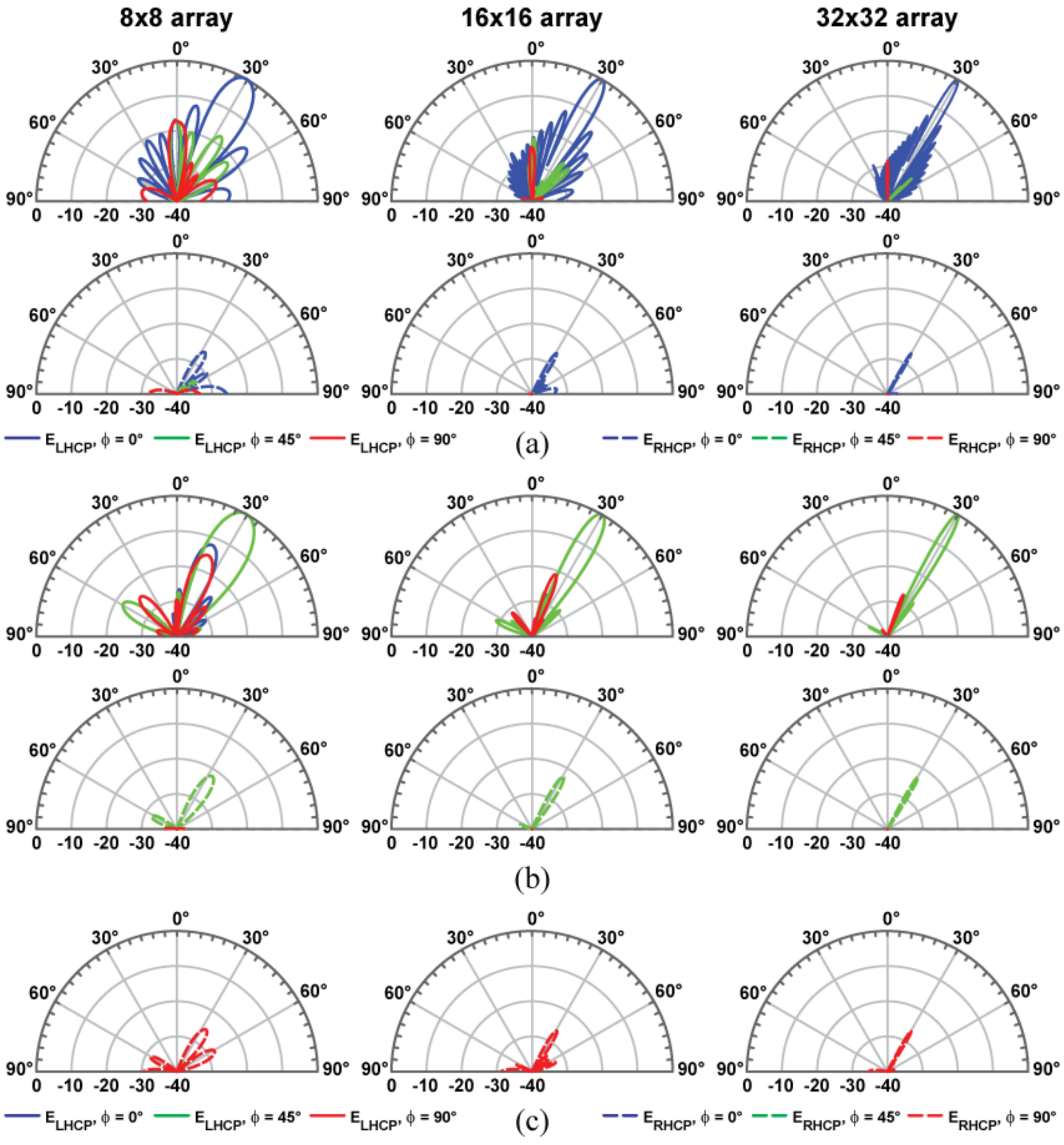

Figure 4.16: Normalized *30° scan* patterns for LHCP *equilateral array* with *LHCP* EP; Cpol (top row) and Xpol (bottom row) for 8x8 (left column), 16x16 (mid column) and 32x32 arrays (right column); with beam scan in (a) principle Z-X plane (ϕ = 0°) , (b) diagonal plane (ϕ = 45°); and Xpol for beam scan in (c) principle Y-Z plane (ϕ = 90°).

These two plots signifies yet another important detail for both square and equilateral CP arrays, that is despite comprising of ideal CP elements with no Xpol components, an array Xpol component of <-20 dB will *always* be present in the

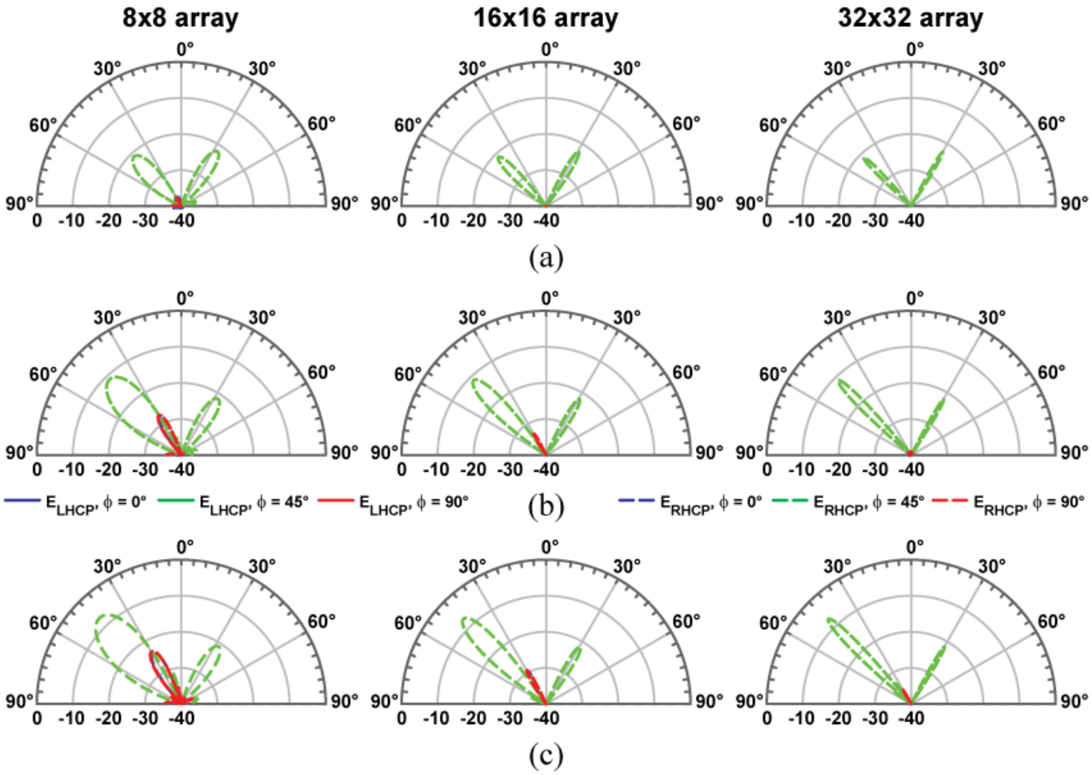

Figure 4.17: Normalized Xpol for *30° bean scan in diagonal plane (ϕ=45°)* LHCP *square array* for 8x8 (left), 16x16 (middle) and 32x32 arrays (right) comprising of CP elements with Xpol of (a) -20 dB, (b) -10 dB and (c) -6 dB.

orientation of the main beam when beam scanning is performed to θ = 30°. This Xpol component does not vary with element spacing. It varies with scan angle, at <-30 dB for scan angles within θ < 15°, and increases as main bean scans further away from broadside. As our interest is within scan range of θ = 30°, wider scan angles are not considered in the study.

Finally, the impact of CP element Xpol on CP array is presented. Figure 4.17 presents normalized Xpol patterns from LHCP *scanned arrays* for cases of 8x8, 16x16 and 32x32 *square layouts*, and comprising *of LHCP antenna elements* defined from (4.4) with Δ_{Cir}=0.1, 0.315, and 0.5 for EP Xpol of -20 dB, -10 dB and -6 dB respectively. Main beam is scanned to θ = 30° in the diagonal plane (ϕ = 45°).

In a similar order, Figure 4.18 presents normalized Xpol patterns from LHCP *scanned arrays* for cases of 8x8, 16x16 and 32x32 *equilateral layouts*, and comprising

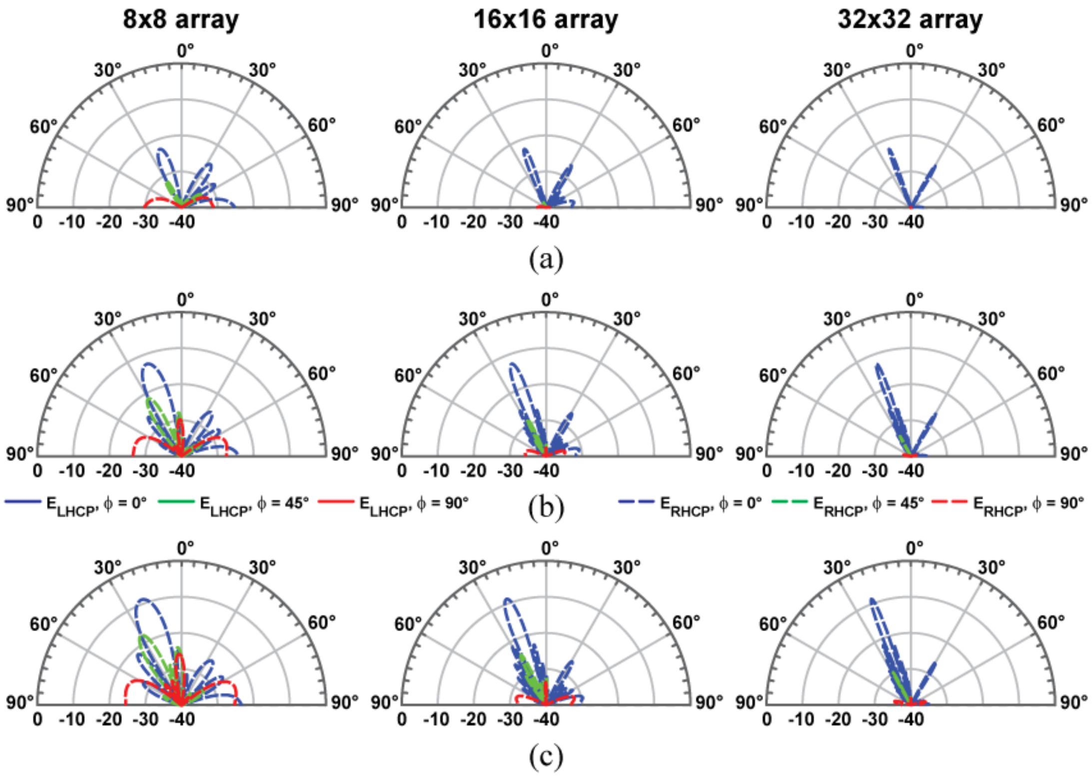

Figure 4.18: Normalized Xpol for *30° bean scan in Z-X plane (ϕ=0°)* LHCP *equilateral array* for 8x8 (left), 16x16 (middle) and 32x32 arrays (right) comprising of CP elements with Xpol of (a) -20 dB, (b) -10 dB and (c) -6 dB.

of LHCP antenna elements defined from (4.4) with Δ_{Cir}=0.1, 0.315, and 0.5 for EP Xpol of -20 dB, -10 dB and -6 dB respectively. Main beam is scanned to $\theta = 30°$ in the principle plane of row-staggering (Z-X plane, $\phi = 0°$).

Similar to the case of CP arrays with LP elements for beam scan, a strong Xpol spike is observed, with peak intensity about 2-3 dB below the CP element Xpol level.

The intensity of the strong Xpol spikes can be reduced with decreasing element spacing. Figure 4.19a-b shows the decrease of the array Xpol spike intensity for 8x8 LHCP square and staggered arrays, as a function of both element spacing and element Xpol levels, and Figure 4.19c the elevation angle which the Xpol spikes occurs. With smaller element spacing, Xpol for square arrays (Figure 4.19a, beam scan at $\phi = 45°$) can be reduced much more significantly than equilateral arrays (Figure 4.19b, beam scan spike at $\phi = 0°$). Though case of 8x8 arrays are presented in Figure 4.19, trends are consistent for larger arrays, and with peak Xpol within 0.5 dB improvement for larger element spacing to within 2 dB improvements for 0.45 λ_0 element spacing.

Also, from Figure 4.19c, the spikes for the Xpol moves towards the X-Y plane as element spacing decreases for square arrays. It stays within elevation of θ = 40° for staggered arrays. This further reinforces the use of square layout over equilateral layout for active beam-scan applications.

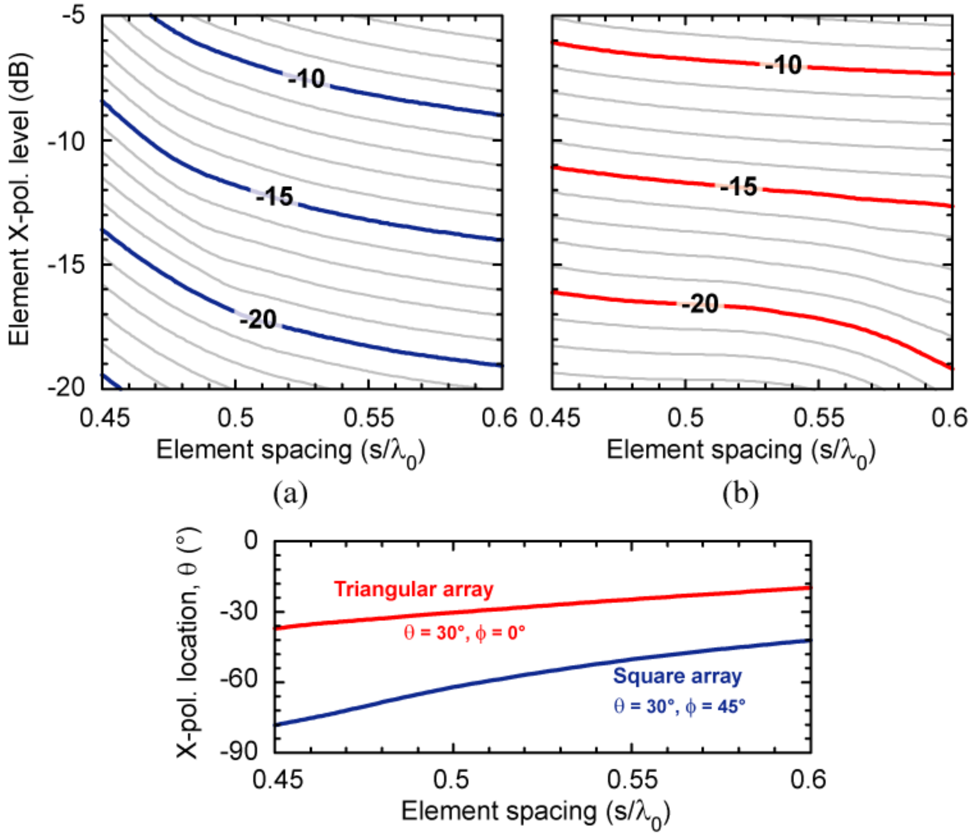

(a) (b)

(c)

Figure 4.19: Normalized Xpol "spike" levels with varying element spacing and EP Xpol levels, for 30° beam scanned 8x8 LCHP array with LHCP elements, in (a) ϕ = 45° plane for square layout, and (b) ϕ = 0° plane for staggered layout, and (c) location of the Xpol spikes in the elevation plane.

4.5 CP Arrays with Microstrip Antenna Elements

4.5.1 Summary of Key Observations

For CP array with the following details:

- LP or CP microstrip antenna elements,
- 0.59 λ_0 element spacing,
- Square or equilateral layout configuration as shown in Figure 4.2 with row staggering along X-axis (Z-X plane, $\phi = 0°$),
- One hierarchy of sequential rotation and quadrature phase feed for every element in a 2x2 unit cell layout (Figure 4.2a,b),
- Main beam at broadside, or scanned to elevation angle of $\theta = 30°$,

the following observations are obtained:

Observation I:

-40 dB of Xpol from a single CP microstrip antenna element is never possible, if the antenna element CP is excited from two quadrature phased orthogonal LP modes (Figure 4.5a). Xpol of < -30 dB is possible only if the FOV is limited to a conical-cut region of within $\theta < 30°$.

Observation II:

For CP *broadside* array comprising of *LP elements*, < -30 dB of array Xpol is possible for sufficiently large array size (Figure 4.6) for square array layout. Array Xpol performance is generally not influenced by element Xpol performance and element spacing.

For equilateral layout, Xpol exist at $\theta = 60°$ in principle plane of row staggering (i.e. at Z-X plane, $\phi = 0°$).

Observation III:

For CP *scanned* arrays comprising of *LP elements* with main beam scanned to $\theta = 30°$, there exist a strong array Xpol “spike” (Figure 4.8 and Figure 4.9 for square and staggered arrays respectively). This spike can be forced into the X-Y plane ($\theta = 90°$) with decreasing element spacing (Figure 4.10) for case of square arrays, thus enhancing the performance of the array at the expense of reduced array size. Element Xpol level has no impact on array Xpol performance in this case.

Observation IV:

For CP *broadside* array comprising of *CP elements*, < -40 dB of array Xpol is possible (Figure 4.11 and Figure 4.12 for square and equilateral layouts respectively), granted the array size is sufficiently large to negate the element’s Xpol effects in a square array (Figure 4.13). Array Xpol of

<-30 dB can still be achieved despite comprising of CP elements with -6 dB Xpol.

For equilateral layout, Xpol exist at θ = 60° in principle plane of row staggering (i.e. at Z-X plane or ϕ = 0°).

Observation V:

For CP *scanned* arrays comprising of *CP elements* with main beam scanned to θ = 30°, array Xpol is found to be ~-25 dB in the orientation of the beam scan (Figure 4.15 and Figure 4.16 for square and equilateral arrays respectively). This is only true if the CP element has no Xpol component; increase in element Xpol levels will introduce another higher array Xpol component (observation VI).

Observation VI:

For CP *scanned* arrays comprising of *CP elements* with main beam scanned to θ = 30°, strong Xpol "spike" is found when main beam is scanned in diagonal plane (ϕ = 45°) for square arrays (Figure 4.17), and in the plane of row staggering (ϕ = 0°) for equilateral arrays (Figure 4.18). The array Xpol "spike" is typically 1-3 dB below element Xpol level, and decreases with decreasing element spacing (Figure 4.19). For square arrays, the strong Xpol "spike" will deviate towards X-Y plane (θ = 90°) with decreasing element spacing, enhancing the performance of the array (at the expense of reduced array size).

4.5.2 Array Implementation/Architecture for Large CP Arrays

For the design of broadside CP arrays for wideband operations, noting observation IV above, focus of antenna element design can be placed on bandwidth widening at huge expense of AR performance, while still attaining <-35 dB Xpol for final CP array.

For the design of active beam-scanned ultra-wideband CP array with LP antenna elements, noting observation III above, a square array layout with small inter-element spacing will avoid the strong Xpol "spike" phenomenon. This is particularly promising for current-sheet arrays approach, with each capacitively-loaded dipoles smaller than $\lambda_0/2$ at the highest frequency of operation. Drawback is the high density of antenna elements for the same array size, resulting in high quantity count of RF front-end channels and components.

For the design of a single antenna element for concurrent CP operation at, say, 20 GHz and 30 GHz, bandwidth may be a larger challenge at the lower frequency due to the higher fractional bandwidth (for a fixed absolute bandwidth at both frequencies). Conversely, placement of the antenna elements will be dictated by the higher frequency, to avoid grating lobes and scan blindness at that frequency. As such, noting observation III above, with the array CP problems arising from element Xpol less prominent *for a square array* with decreasing element spacing, the lower frequency band (i.e. at 20 GHz) can be optimized for impedance bandwidth at the expense of AR performance, while concerns for the higher frequency band (i.e. at 30 GHz) should be placed on the element Xpol.

4.6 Conclusion

Patterns for various CP arrays comprising of LP and CP elements with various performance are presented. Theoretical Xpol levels for CP microstrip antenna elements and arrays are presented. The results presented here can be used to determine on realistic expectation from the CP array especially for cases of beam scan beyond $\theta > 15°$ (and up to 30°) when Xpol starts to degrade to above -30 dB and higher, specifications on the antenna elements to allow for good trade-off in bandwidth and AR, and methods to synthesize the antenna element.

Chapter 4 is based on and mostly a reprint of the material that has been published in *Proc. IEEE Antennas Propag. Symp.* (Jul 2014), Kevin M. Ho and Gabriel M. Rebeiz. The dissertation author was the primary author of this material.

Chapter 5

Dual-Band Components for Ku/Ka-Band Shared Aperture Antenna Arrays

5.1 Scope

The goal of the project is to develop a Ku/Ka-band shared aperture array, for concurrent operation at 20 GHz and 30 GHz. The motivation for the studies presented here (and the preceding chapter) is to provide design details and theoretical evaluations for the development of the shared array aperture.

Targeted application is for data-link communications with satellites or micro-satellites. Bandwidth requirement is at 1 GHz, and stretched goal of up to 2 GHz is desired, for each operating frequency in ~~CP~~ mode. The array should be of low profile, and with frequency scanning capabilities of 30° off broadside.

Possible array implementation approaches are first presented for dual/multi-band shared apertures. Possible reductions in complexity of PCB routings are presented.

The design of the dual band CP antenna element is presented next. Tuning mechanism for achieving desired polarization Xpol and bandwidth are discussed. Lastly, various methods for achieving dual-band quadrature phased (0/90°) and differential phased (0/180°) power splitters are presented. Besides the antenna element, bandwidth is also of a huge challenge for the dual-band components, especially if they are to be constrained to a compact layout.

5.2 Shared Apertures Array Implementation

5.2.1 Implementation Approaches

Aperture sharing can be achieved with any of the 3 approaches, and is summarized in Table 5.1.

I - 2 sets of arrays co-existing on a common aperture, one for each frequency band

II – 1 array of antenna elements with wide bandwidth

III – 1 array of antenna elements with multiple operating frequencies

Consistency in phase center across the different operating frequencies may or may not be required, depending on the applications. Shared apertures for operating frequencies spaced far apart (e.g. S-band and Ku-band), are usually intended for different applications (e.g. global positioning and satellite communications respectively), and hence there is no necessity for a common phase center for both

Table 5.1: Aperture sharing implementation methods.

Description	I: different arrays for different freqs	II: wideband antenna array	III: multiple resonance antenna
> 2 frequencies	✓✗	✓	✓✗
frequency separation	> 2: 1 preferred	Smaller separation preferred	Moderate separation preferred
common feed-point	✗	✓	✓✗
Multiple polarization	✓	✗	✓✗
Consistent array phase center	✓✗	✓	✓
Commercial-grade laminates	✓	✗	✓

✓: supported;
✗: not supported;

frequencies. Conversely, concurrent up/down link for the same application (e.g. Ku-band and Ka-band for concurrent uplink and downlink respectively) will require a coherent phase center for both operating frequencies.

5.2.2 Multiple Arrays vs Wideband Arrays

Approach I is best suited for applications with only 2 operating frequencies, and the higher operating frequency at least twice of lower operating frequency [79]-[80]. Drawbacks include the absence of a common phase center for both frequencies. Figure 5.1a shows a typical implementation, with antenna elements of both array super-imposed on each other, but not completely blocking one another. Independent polarization modes can be achieved for both frequencies. Depending on how the unit cells for the arrays are defined, the phase center may or may not coincide for both operating frequencies.

Approach II is the most appropriate for multiple operating frequencies. Depending on the requirements of the various frequencies, the different operating frequencies can be combined at some stage with a frequency diplexer/multiplexer, sharing a single TLIN, and reducing the complexity of multiple RF routings for different frequencies (an e.g. in [81] for S- and Ku-band). Difficulty includes the need for

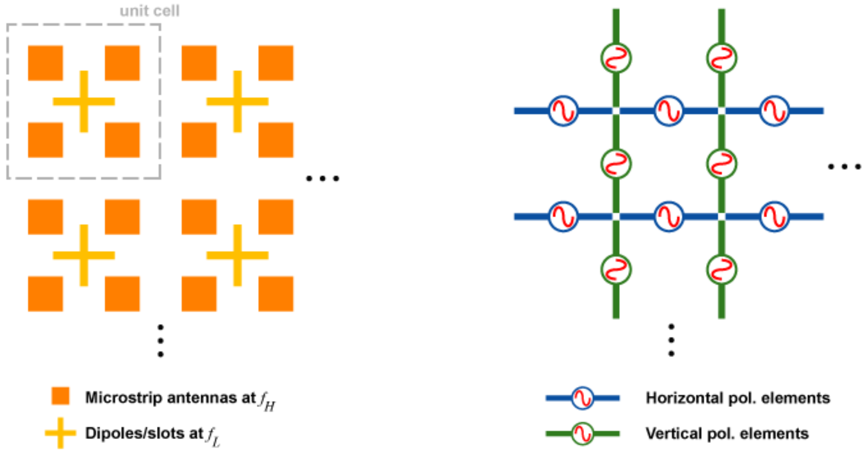

(a) (b)

Figure 5.1: Shared aperture implementation with (a) different antenna arrays for different frequencies and (b) wideband current-sheet array.

different polarization modes at different frequencies, since in most cases the wide-band antenna element will be of the same polarization across the frequency band.

Stacked patch antennas [82],[83] and current sheet arrays [84] are two possible implementations methods. Considering the ratio of the highest to the lowest operating frequencies, the former implementation is best suited for frequency ratio below 2:1, and the latter for much higher ratios. Drawback for the latter includes the complexity of the quadrature feed required for CP excitation. Since it is a single array, the phase center will be consistent for all operating frequencies. A practical limitation, is the requirements for low ε_r substrates for achieving the desired wide-band characteristics without incurring surface-waves modes.

Approach III can be configured for two or more concurrent operating frequencies though challenges increases with increasing number of concurrent operating frequencies. Different polarization for different operating frequencies can be achieved with this approach. Achieving the desired operating bandwidth at the individual frequencies is a possible limitation for this approach. Achieving CP imposes more challenges then LP. The phase center is consistent with this approach for all operating frequencies.

5.2.3 Wideband versus Dual-Band Stacked Microstrip Antenna

Figure 5.2a & b presents the cross section of probe-fed layered microstrip antennas for wideband [83] and dual-band [85] operations respectively. Fundamental difference is the coupling between the microstrip elements. Wideband designs (Figure 5.2a) requires strong coupling between both antenna layers, which can be achieved with the feed directly coupled to the bottom microstrip layer (and hence weak coupling from feed to top microstrip trace element), and the bottom element coupling with the top layer instead. An analogy from classical filter designs for intuitive appreciation is to relate the bandwidth widening mechanism to the coupling of a pair of asynchronous resonators coupling [86].

Inter-layer coupling for dual-band designs (Figure 5.2b) is to be kept to a minimum, by having stronger coupling from the probe feed directly to both microstrip

Figure 5.2: Cross-section for (a) wideband and (b) dual-band layered microstrip antennas.

trace layers. The probe is directly fed to the top layered element, and capacitively coupled to the bottom layered element. Unfortunately, they cannot be adequately decoupled from each other, hence the difficulty of tuning for both frequencies. CP requirements at both operating frequencies further exacerbate the design challenge. Parametric studies for the various tuning mechanisms for both layers separately will allow for ease of impedance tuning while obtaining the desired polarization.

5.2.4 Antenna Feed vs Board Routing Complexity

The easiest way to achieve CP from a single microstrip antenna element, is to have two sets of differential feeds for both orthogonal LP modes, and the 2 sets of feeds with quadrature phase difference, as presented in Chapter 2 (Figure 2.5a & Table 2.1) [31]. With higher operating frequency, and element spacing within $\lambda_0/2$ or less, feed network becomes increasingly complicated from the lack of real-estate between elements. Furthermore, for dual-band or multiple band operation, design of components to fulfill both operating bandwidths and different operating frequencies becomes increasingly challenging.

Antenna element that allows for CP with a single feed-point avoids the need for design for dual/multi-band components, reducing the complexity of routing the RF traces. Furthermore, with a single feed-point for multiple operating frequencies, the RF signals for different operating frequencies can be combined and routed as a single trace from the RF front-end components to the antenna input, further reducing the complexity for the multi-layered board routings.

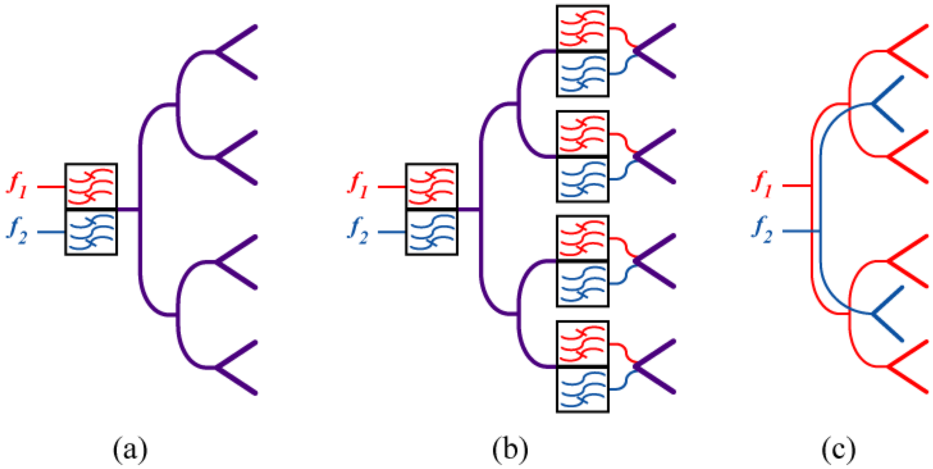

Figure 5.3: Feed network routing complexity for dual/multi-band array using antenna elements with (a) single feed point and (b) multiple feed points for multiple frequencies, and (c) multiple routings for separate antennas for different bands.

5.3 20/30 GHz Dual-band CP Antenna Element

5.3.1 20 GHz CP Antenna Parametric Study

Figure 5.4 presents the layout and cross-section of a 20 GHz CP square microstrip antenna element. CP is achieved with diagonal opposite-corner truncation (c). Parametric studies are performed in HFSS with Rogers RO4003 laminate (ε_r = 3.55, tanδ = 0.0027) for the substrate. Feed via diameter is 0.012” for all cases, for compatibility with mechanical drilled via capabilities.

Figure 5.5 presents the input impedance for the CP square ($w = l$) microstrip antenna for varying substrate height (h). With increasing substrate ε_r, matched condition for CP decreases to low impedance values for the same substrate thickness, and can be compensated with increasing substrate thickness. Addition of prepreg superstrate (thickness 0.004” to 0.012”, not shown here) has minimal influence on the CP input impedance presented, and is required not for 20 GHz, but for 30 GHz operation.

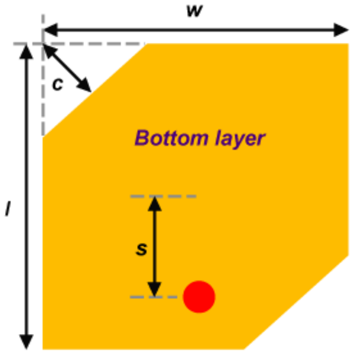

Figure 5.4: Layout of CP square microstrip antenna element.

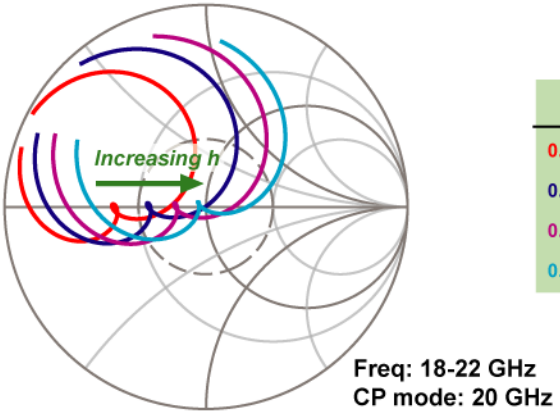

h	*w (= l)*	*s*	*c*	Z_{in} (CP mode)
0.008”	0.151”	0.018”	0.010”	19 Ω
0.012”	0.149”	0.020”	0.012”	28 Ω
0.016”	0.147”	0.023”	0.014”	37 Ω
0.020”	0.145”	0.025”	0.016”	46 Ω

Figure 5.5: Variation of input impedance with varying substrate thickness (*h*) for CP square microstrip antenna (*w* = *l*).

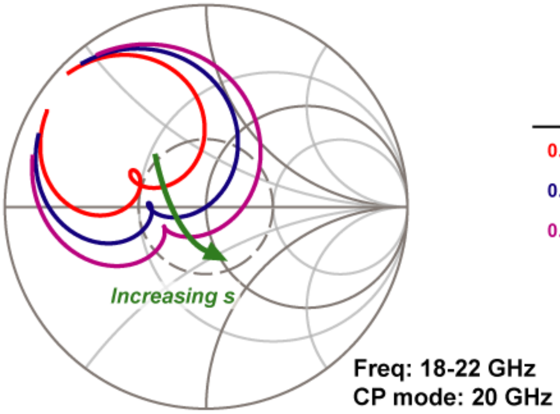

h	*w (= l)*	*s*	*c*	Z_{in} (CP mode)
0.012”	0.149”	0.017”	0.012”	---
0.012”	0.149”	0.020”	0.012”	28 Ω
0.012”	0.149”	0.023”	0.012”	---

Figure 5.6: Variation of input impedance with varying feed offset (*s*) for CP square microstrip antenna (*w* = *l*) on 0.012” thick substrate.

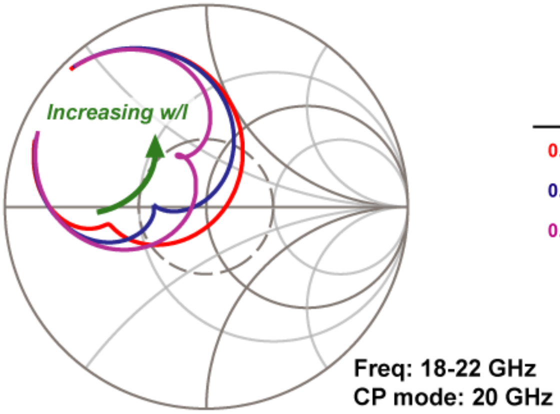

h	*l*	*w/l ratio*	*s*	*c*
0.012”	0.149”	0.98	0.02”	0.012”
0.012”	0.149”	1	0.02”	0.012”
0.012”	0.149”	1.02	0.02”	0.012”

Figure 5.7: Variation of input impedance with width/length ratio (*w*/*l*) CP microstrip antenna on 0.012” thick substrate.

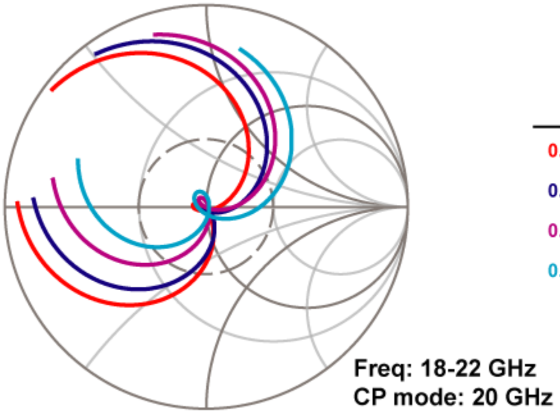

h	*l*	*w/l ratio*	*s*	*c*
0.008”	0.149”	1.022	0.026”	0.010”
0.012”	0.146”	1.019	0.025”	0.013”
0.016”	0.145”	1.012	0.025”	0.015”
0.020”	0.144”	1.004	0.026”	0.017”

Figure 5.8: Matched 20 GHz CP microstrip antenna on RO4003 substrate with various substrate thicknesses.

Increasing overall diectric (substrate + prepreg) thickness at CP excitation may not be a viable option for high ε_r materials in view of surface-waves and scan blindness conditions presented in Chapter 3.

Figure 5.6 presents the input impedance of a conventional 20 GHz embedded CP square ($w = l$) microstrip antenna element with substrate thickness $h = 0.012$”, for varying feed offset (s). Similarly, Figure 5.7 presents the input impedance for the same antenna for varying width/length ratio (w/l). For any given substrate thickness and dielectric permittivity, combination of feed offset and width/length ratio forms the primarily impedance tuning mechanism, for optimum CP mode to be tuned to the desired matched condition, as shown in Figure 5.8 for 0.008-0.02” thick substrates.

5.3.2 20/30 GHz CP Antenna: Design

Figure 5.9 presents the proposed dual-band antenna element, comprising of two vertically-stacked metal layers for the dual resonance conditions. The higher frequency resonance (30 GHz) is predominantly influenced by the top-metal layout (Figure 5.9c), and the lower frequency resonance (20 GHz) by the bottom metal layout (Figure 5.9d). Both elements are vertically aligned at the center of their layout.

CP is achieved with diagonal opposite-corner truncation of both elements (c_T and c_B for top and bottom layout respectively). Consistency in polarization sense for both operating frequencies is required, as the two elements are interacting with each other.

As presented in the preceding section, slight offset of the length and width for the layouts is required so as to ensure a good impedance match at the desired port impedance for CP. This is especially true if the substrate dielectric constant is not available as a design parameter. In this case, the patch width is the same or slightly smaller than the length for the bottom layout ($w_B >= l_B$), and the converse for the top layout (i.e. $w_T <= l_T$).

The operating frequency ratio is 1.5 for both patches, and therefore, the ideal feed point for both patches will be significantly different, with a larger offset from the center of the antenna element being required for the bottom patch. Meanders are therefore introduced to the perimeter of the bottom layout, miniaturizing the lower frequency patch size and allowing for feed-points of both layers to be at the same offset location while maintaining vertical alignment at the center. Alternatively, a physical offset of the two layouts may be considered with vertical alignment at the feed-point instead, but this result in an offset of the phase center for the two operating frequencies. Another advantage of miniaturizing the lower frequency patch is the ease of array layout, as the array is spaced at 0.56-0.59λ_0 at 30 GHz for scanning applications.

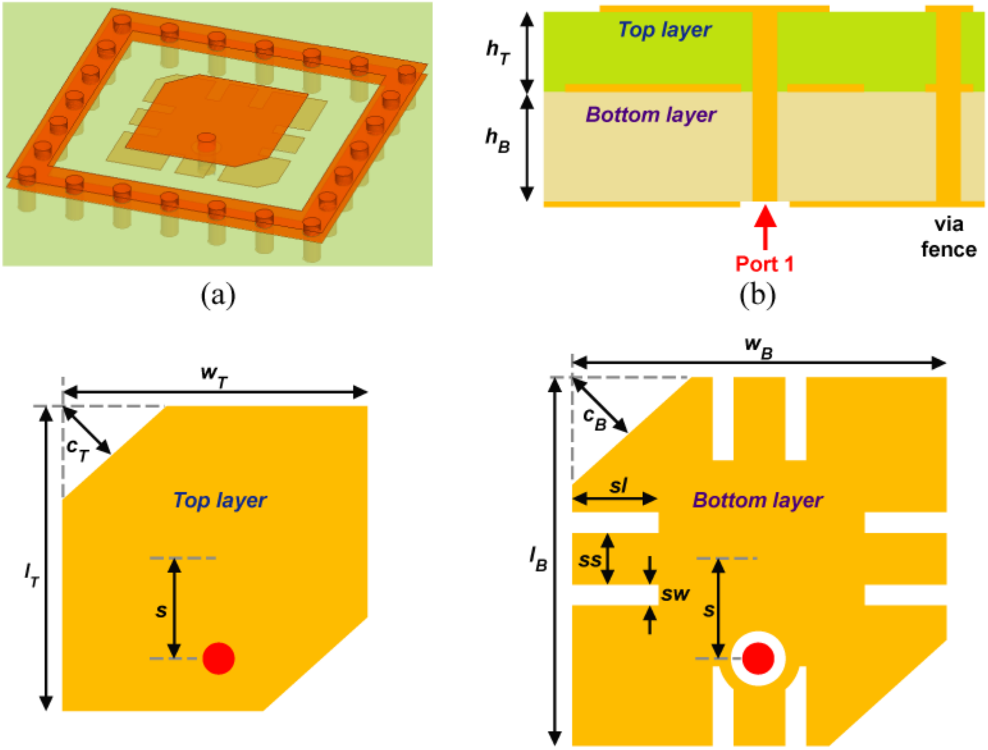

(a) (b)

(c) (d)

Figure 5.9: Dual-band microstrip antenna element (a) picture, (b) cross-section stack-up, and layout details for (c) top and (d) bottom metal layers.

For benchmark purposes, Figure 5.10 presents calculated radiation efficiency for LP conventional square microstrip antennas for 20 and 30 GHz, and IE3D simulations for LP and CP conventional microstrip antennas. IE3D cases include a 0.012” diameter probe-feed via. Expected radiation efficiency for the actual composite structures will be lower than these calculations, since surface waves excitation is from both layout layers.

The use of via fencing surrounding the antenna element (as shown in Figure 5.9a) significantly reduces the surface-waves losses, and enhances the efficiency at 30 GHz to > 60%. It is important to note that HFSS simulations are unable to capture the surface wave losses. Reflecting only resonator efficiency mechanism, HFSS constantly predicts 90% efficiency for the case without via fencing, and 75% for case with via

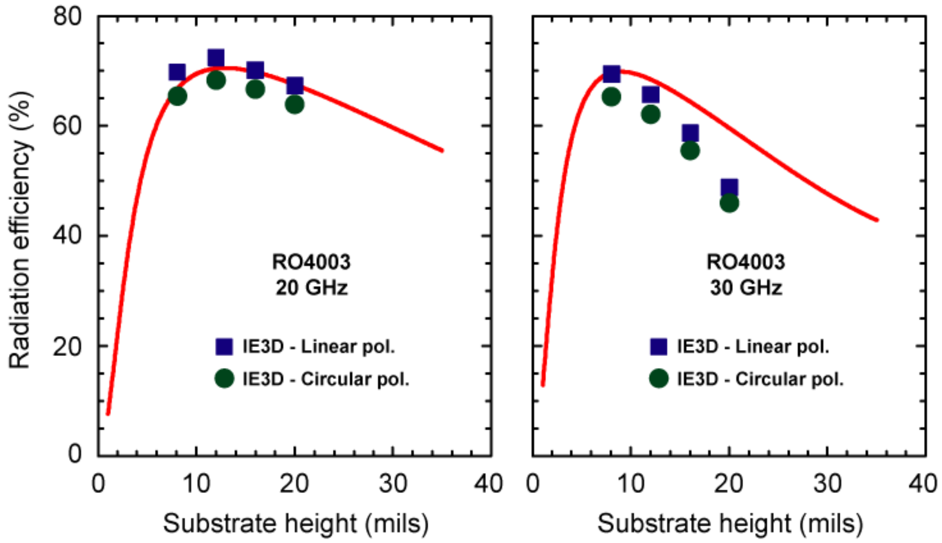

Figure 5.10: Calculated (red trace, for LP) and IE3D simulated radiation efficiency for microstrip antennas on RO4003 at (a) 20 GHz and (b) 30 GHz.

fencing. Losses from surface waves do not matter much for single element applications, but will have significant impact on large arrays.

Finally, the AR bandwidth is typically much smaller than the impedance bandwidth, and this affects the acceptable operating bandwidth. Fortunately, the full array will have significantly lower cross-polarization from techniques including rotational layout and sequential phasing of the antenna elements. Also, close proximity of $< 0.4\lambda_0$ element spacing at 20 GHz will also reduce cross-polarization spurious responses. The lower frequency response should thus be optimized for operating bandwidth, and the higher frequency response for axial ratio performance.

5.3.3 20/30 GHz CP Antenna: EM Simulations

The proposed concept is simulated in HFSS with Rogers RO4003 laminate (ε_r = 3.55, tanδ = 0.0027) for the substrate with thickness h_B = 0.020”, and RO4450 prepreg for the top substrate (ε_r = 3.54, tanδ = 0.004) and thickness h_T = 0.008”. Other physical dimensions are presented in Table 5.2.

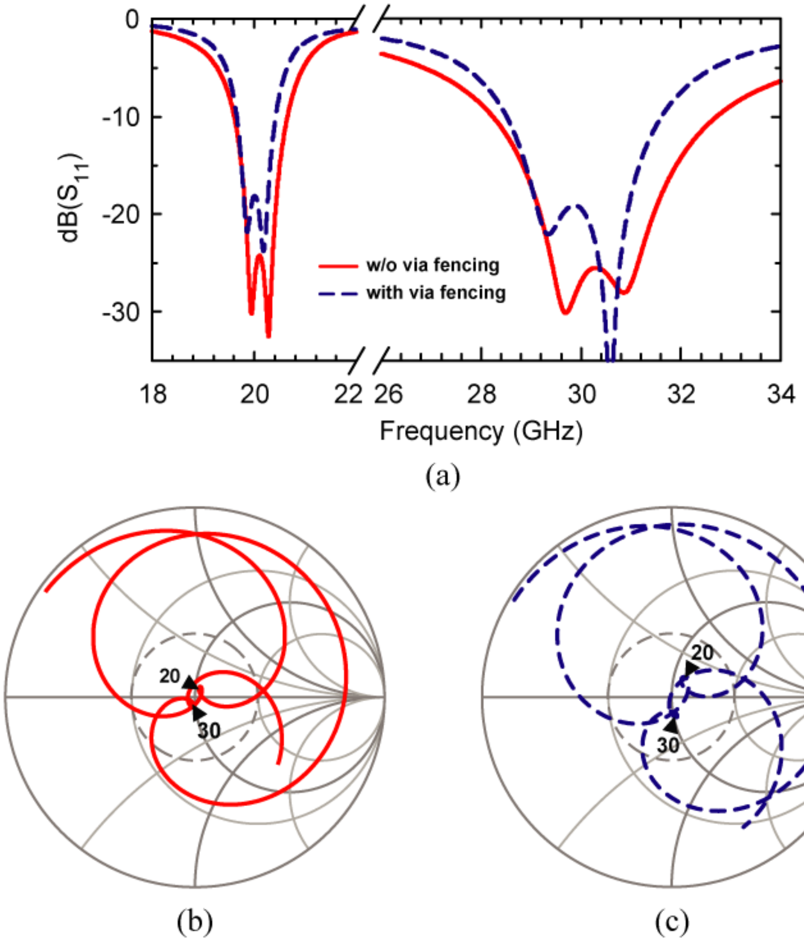

(a)

(b)

(c)

Figure 5.11: Simulated reflection coefficient for dual-band antenna element; (a) in dB, and on Smith chart for case (b) with and (c) without via fencing.

Table 5.2: Physical dimensions (units in mils) for 20/30 GHz microstrip antenna.

	w_T (=l_T)	c_T	w_B	l_B	c_B	s	sl	ss	sw
w/o via fence	117	9.5	94	106	15	25	23	20	10
with via fence	117	7.5	95	102	12.5	22	23	20	10

Figure 5.11 presents the simulated input reflection coefficient of the antenna element configured for LHCP, and Figure 5.12 the simulated AR. The presence of via fencing slightly reduces the impedance and axial ratio bandwidth, but enhances the radiation efficiency from 40-25% for 20-30 GHz, to 51-64%, which matches closer to the theoretical calculations in Figure 5.10. The bandwidth is still too narrow to cover the entire Ka-band, and more design effort is needed.

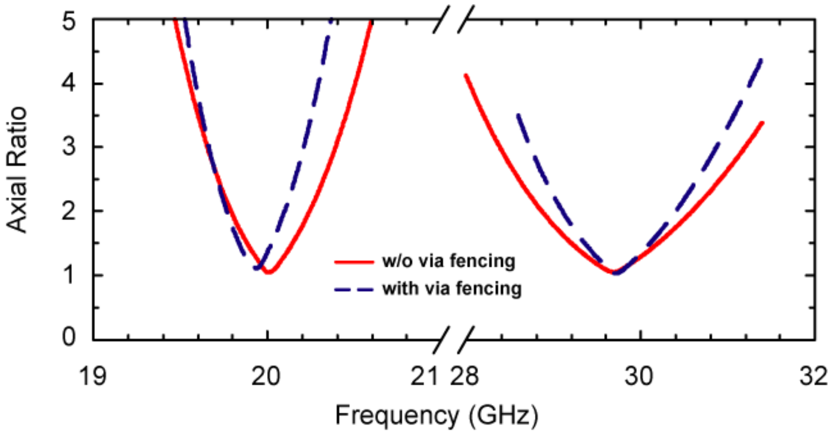

Figure 5.12: Simulated AR for LHCP (solid line: w/o via-fencing, dashed line: with via fencing).

5.4 Dual-Band 3-dB Couplers

The preceding section reveals the challenges for achieving wide operating bandwidth for both operating frequencies from an antenna element with a single feed-point. A potential solution is to use 3-dB couplers with quadrature or differential phase offsets, for interface with antenna elements with dual or quadruplet feed points.

With f_1 = 20 GHz, f_2 = 30 GHz, and frequency ratio of f_2/f_1 = 1.5 as the primary goal, preference for compact size for ease of implementation is the secondary goal for choice of implementation. This is especially significant since $0.6\lambda_0$ of element spacing at f_2 translates to $0.4\lambda_0$ at f_1, or barely 0.25" in physical dimensions.

Finally, the last goal, and perhaps presenting the highest challenge for this approach, is to have up to 2 GHz of operating bandwidth in both bands. Figure 2.12 (and Figure 2.13) presents the acceptable Xpol levels for LP (and CP) based on amplitude imbalance and feed offset from ideal quadrature (and differential) phased excitation, which in turn falls upon the amplitude and phase imbalance of the components available.

5.4.1 General Classification

A survey of existing literature reveals the following 2 generic classification of implementation for couplers with dual-band operation (Figure 5.13a):

Class I -

phase difference at f_1: $\Delta\phi_{f1} = -/+\ \phi_{QD}$, [87], [88], where

$\phi_{QD} = \phi_Q = 90°$ for quadrature-phased (0/90°) couplers, and

$\phi_{QD} = \phi_D = 180°$ for differential-phased (0/180°) couplers

Quadrature phase difference at f_2: $\Delta\phi_{f2} = \Delta\phi_{f1}$ +/- 180°

Implementation: couplers comprising of slow-wave TLIN structures

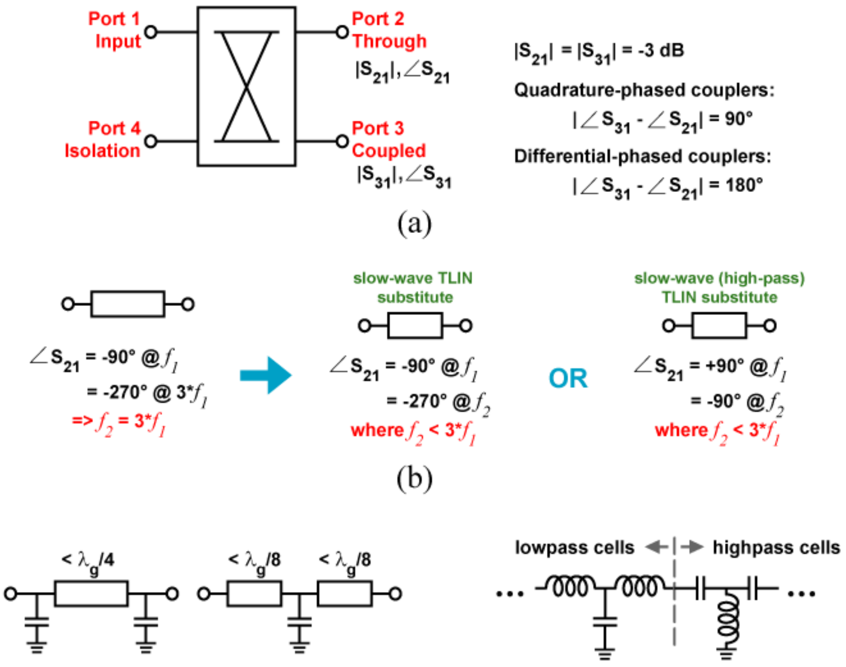

(a)

(b)

(c)

(d)

Figure 5.13: (a) Generic representation for couplers, (b) TLIN replacements with (LoP and HiP) slow-wave structures, and implementation with (c) loaded TLINs (**π**/T LoP network), or (d) cascade of LoP and HiP T network unit cells.

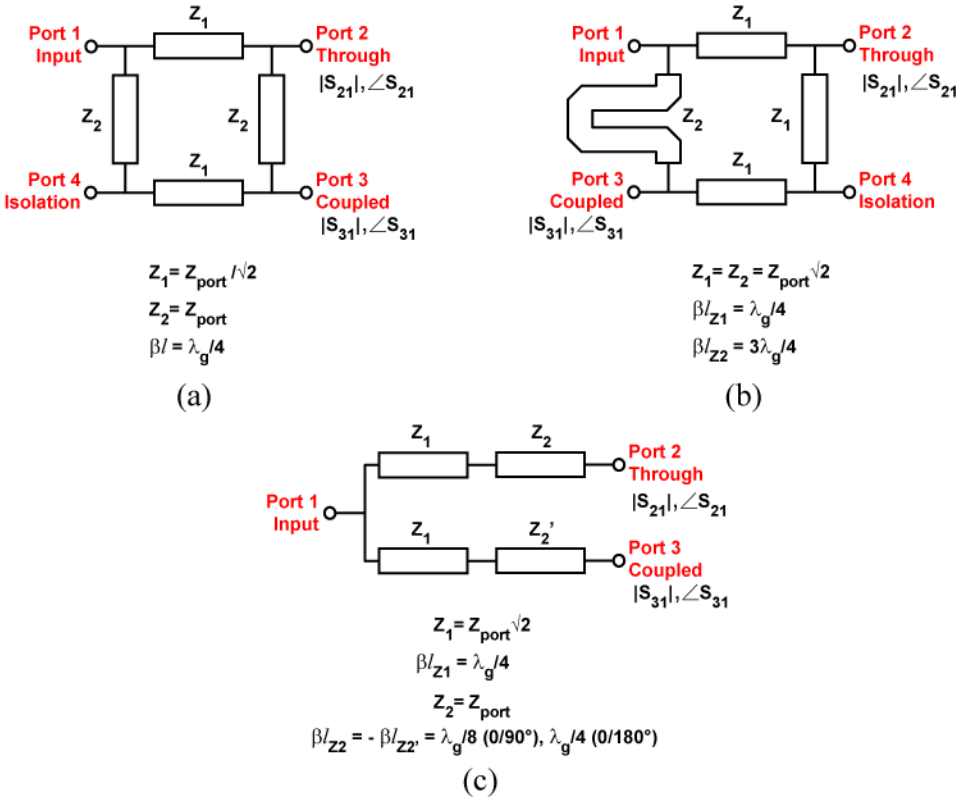

(a) (b) (c)

Figure 5.14: Single stage (a) branch-line, (b) rat-race couplers, and (c) lossless T-junction implementations for 3-dB splitting.

a - capacitively loaded TLIN sections, typically with T or π network (Figure 5.13c)

b - cascade of low-pass (LoP[1]) / high-pass (HiP[2]) networks (Figure 5.13d)

- ☺ possible to synthesize any frequency ratio

Class II -

Quadrature phase difference at f_1: $\Delta\phi_{f1} = -\phi_{QD}$

Quadrature phase difference at f_2: $\Delta\phi_{f2} = \Delta\phi_{f1}$

Implementation: wideband couplers, with electrical lengths defined at center of both bands, i.e. at $f_0 = (f_1 + f_2)/2$

a - multi-section wideband couplers

- ☺ small f_2/f_1 ratio

---

[1] “LP” is designated as linear polarization, hence “LoP” for low-pass.
[2] “HP” is designated as horizontal polarization, hence “HiP” for high-pass.

b - extension of single-stage couplers [89],[90]
- ☺ moderate/wide f_2/f_1 ratio

For Class I implementation, quadrature-phased couplers are implemented with branch-line couplers (Figure 5.14a), which (for a 50 Ω system) require $\lambda_g/4$ long with characteristic impedance of 35.35 Ω and 50 Ω, where λ_g refers to the guided wavelength of the TLIN. Rat-race couplers are used for differential-phased implementation (Figure 5.14b), and require 70.7 Ω impedance TLINs with lengths of $\lambda_g/4$ and $3\lambda_g/4$. Lossless Tee-junction with additional TLIN phased feeds are also considered (Figure 5.14c), and requires additional 50 Ω with lengths of +/- $\lambda_g/4$ and +/- $\lambda_g/8$.

5.4.2 TLIN with LC implementation

Consider a TLIN section, of characteristic impedance Z_0 at frequency f_0. Its per-unit-length inductance (L_{PUL}) and capacitance (C_{PUL}) normalized to 1 wavelength at frequency f_0 is

$$L_{PUL} = \frac{Z_0}{f_0}, \quad C_{PUL} = \frac{1}{Z_0 f_0} \tag{5.1}$$

For a given electrical length θ°, the low-pass L-section series inductance ($L_{LP,L}$) and shunt capacitance ($C_{LP,L}$) are given as (Figure 5.15a)

$$L_{LP,L} = L_{PUL}\frac{\theta}{360}, \quad C_{LP,L} = C_{PUL}\frac{\theta}{360} \tag{5.2}$$

Conversion of the low-pass to high-pass L-section network involves the replacement of series inductors ($L_{LP,L}$) and shunt capacitors ($C_{LP,L}$), to series capacitors ($C_{HP,L}$) and shunt inductors ($L_{HP,L}$) respectively, with the resonance condition for reactance-replacements;

$$L_{LP,L} \cdot C_{HP,L} = L_{HP,L} \cdot C_{LP,L} = \frac{1}{(2\pi f_0)^2} \tag{5.3}$$

Note, for the TLIN with electrical length θ° at f_0, through phase response for low-pass L-section will be = - θ° (which is consistent with the TLIN response), and = + θ° for the high-pass L-section.

Cascade of *N*-stages of L-sections allows for bandwidth widening, and requires the lumped component values to be reduced by and multiplied by *N* times for low-pass

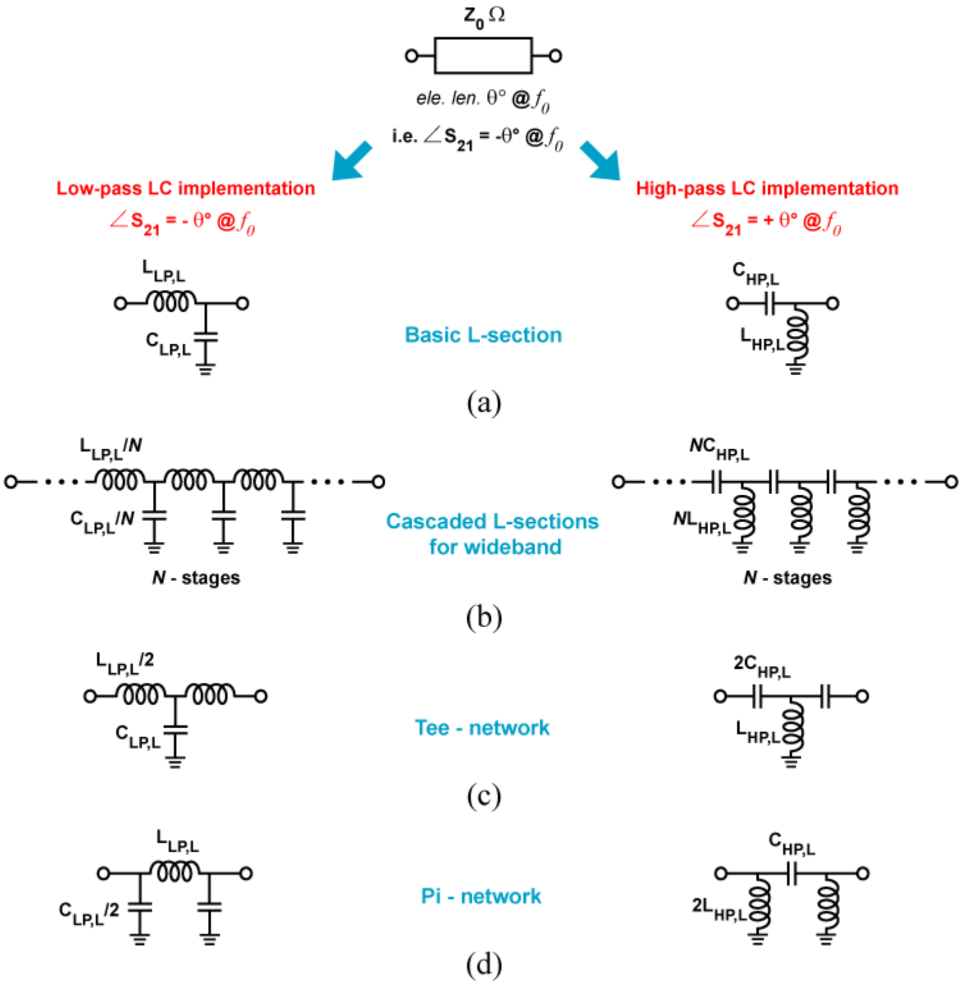

Figure 5.15: LoP (left) and HiP (right) TLIN implementation with LC networks; (a) basic L-section, (b) cascaded L-sections for wider bandwidth, (c) T- and (d) π-network implementation.

and high pass implementation respectively (Figure 5.15b). Finally Figure 5.15c & d presents the T- and π network implementation for network symmetry, with the appropriate scaling factor for consistent phase response.

5.4.3 Dual-band Couplers with Low-pass/Hi-pass TLINs

There are many methods for replacing TLINs with LoP/HiP networks, including methods involving composite left-right handed unit-cells [87] [88], but a simple low-pass and high-pass cascade will be presented, as intent is to use a canonical form for

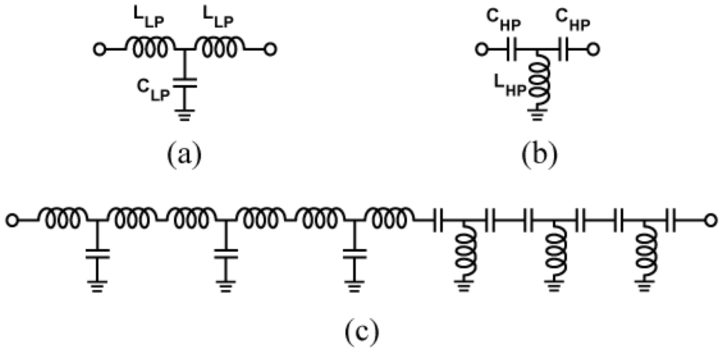

(a) (b)

(c)

Figure 5.16: Unit-cell of (a) LoP and (b) HiP Tee-networks, and (c) TLIN comprising of 3-stage LoP/HiP ($N = 3$).

evaluation of theoretical limits on amplitude and phase imbalance at both operating frequencies (20/30 GHz).

Figure 5.16a,b presents a unit-cell implementation for LoP and HiP sections respectively, and more unit-cells can be cascaded in the LoP and HiP sections as higher stages for wider bandwidth requirements. The proposed TLIN replacement will be a cascade of LoP and HiP network (Figure 5.16c). Note that 2 sections are inadequate for good TLIN response; 4-6 sections synthesizes the TLIN well; there is no difference observed on the synthesized TLIN performance (and the couplers response) with more than 6 sections; 3 sections may not be adequate for good response, but can be considered for cases where compromise in performance is tolerated for size constraints.

The theoretical calculations presented in Figure 5.15 cater for LoP or HiP replacement, but not for LoP/HiP cascade, as the latter involves defining cutoff-frequency definition for the overall pass-band filtering characteristics. Nevertheless, they provide appreciation for expected range of LC values and number of stages required for desired frequency & bandwidth. Table 5.3 lists the reactance values for unit-cells presented in Figure 5.16a-b more suited for TLIN implementations at 20/30 GHz as presented in Figure 5.13b. Note that these LC are not unique for the desired phase and characteristic impedance at the both operating frequencies.

Figure 5.13b shows two implementation approaches; LoP at f_1 and HiP at f_2 (denoted as “$L_{f1}H_{f2}$”), and HiP at f_1 and LoP at f_2 (denoted as “$H_{f1}L_{f2}$”). If sufficient stages are employed for TLIN synthesis, differences from most components with TLIN synthesized from $L_{f1}H_{f2}$ or $H_{f1}L_{f2}$ are almost negligible. Differences may be more significant if 3 stages are used for the TLIN synthesis.

Table 5.3: TLIN implementation with composite LH/RH comprising of Tee-network LoP/HiP unit cells

TYPE I - $\angle S_{21}$= - θ° AT 20 GHZ, = + θ° @ 30 GHZ ($L_{f1}H_{f2}$)

θ	TLIN Z_0 (Ω)	*No. stages*	L_{LP} (nH)	C_{LP} (pF)	L_{HP} (nH)	C_{HP} (pF)
90°	35.35	3	0.215	0.190	0.434	0.644
	50		0.304	0.134	0.615	0.456
	70.7		0.429	0.0950	0.869	0.322
	35.35	4	0.151	0.185	0.497	0.760
	50		0.214	0.131	0.702	0.538
	70.7		0.303	0.0925	0.993	0.380
	35.35	6	0.104	0.142	0.661	1.044
	50		0.146	0.100	0.935	0.738
	70.7		0.207	0.0708	1.322	0.522
45°	50	6	0.216	0.111	0.601	0.376

TYPE II - $\angle S_{21}$= + θ° AT 20 GHZ, = - θ° @ 30 GHZ ($H_{f1}L_{f2}$)

θ	TLIN Z_0 (Ω)	*No. stages*	L_{LP} (nH)	C_{LP} (pF)	L_{HP} (nH)	C_{HP} (pF)
90°	35.35	3	0.157	0.153	0.276	0.269
	50		0.222	0.108	0.390	0.191
	70.7		0.313	0.0766	0.551	0.135
	35.35	4	0.215	0.190	0.434	0.644
	50		0.304	0.134	0.615	0.456
	70.7		0.429	0.0950	0.869	0.322
	35.35	6	0.0757	0.103	0.411	0.554
	50		0.107	0.0731	0.581	0.392
	70.7		0.151	0.0517	0.822	0.277
45°	50	6	0.0526	0.0402	1.052	0.803

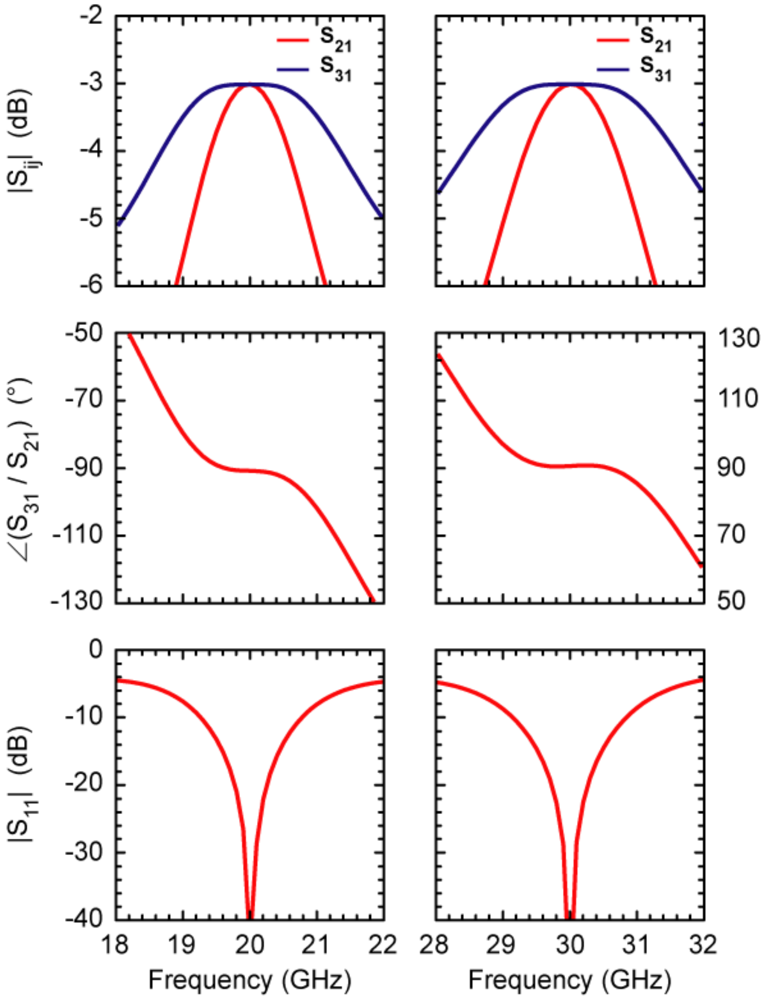

Figure 5.17: Simulated branch-line coupler response with 6-stage LoP/HiP TLINs.

Figure 5.17 presents the response for lossless T-junction splitters synthesized with 6-section TLINs. High amplitude impedance is observed as the bandwidth approaches 1 GHz. Flat 90° phase ratio was observed for a narrow-band region. This is a great narrow-band solution, but perhaps not suited for wideband requirements, unless more branch-line stages (*not* LoP/HiP TLIN stages) is considered.

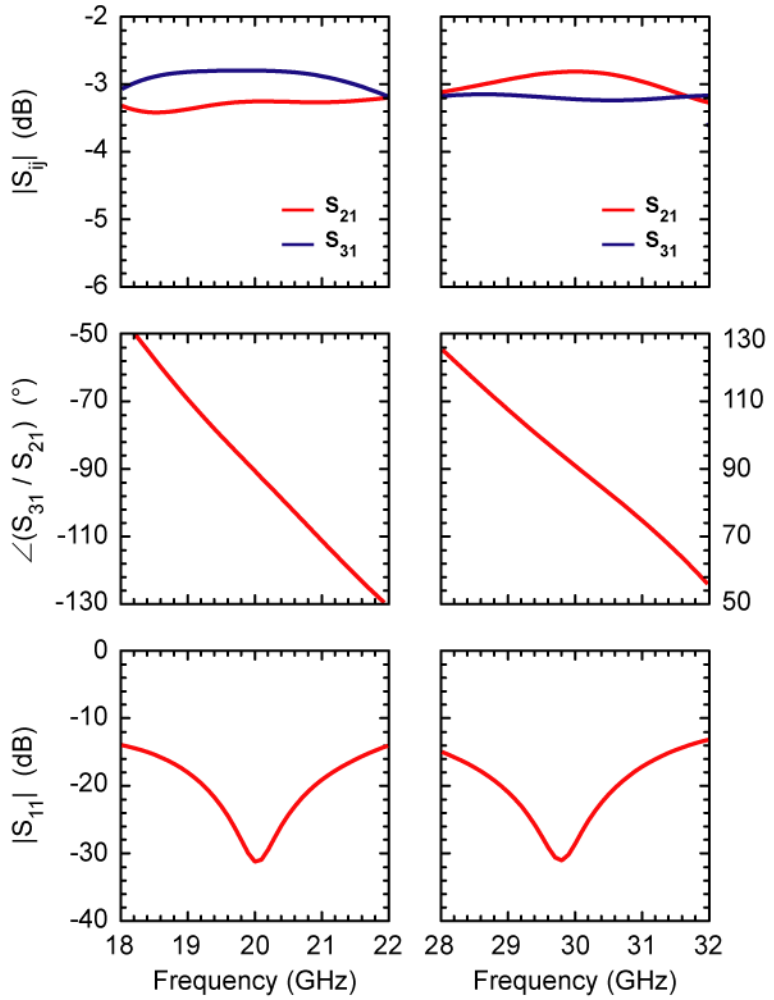

Figure 5.18: Simulated extended T-junction splitter response (0/90°) with 6-stage LoP/HiP TLINs.

Figure 5.18 presents the response for lossless T-junction splitters (0/90°) synthesized with 6-section TLINs (TLIN schematic in Figure 5.14c). Significant improvement is found in the amplitude imbalance over the desired 1 or 2 GHz bandwidth, at the expense of flat 90° phase difference for a small narrow-band range.

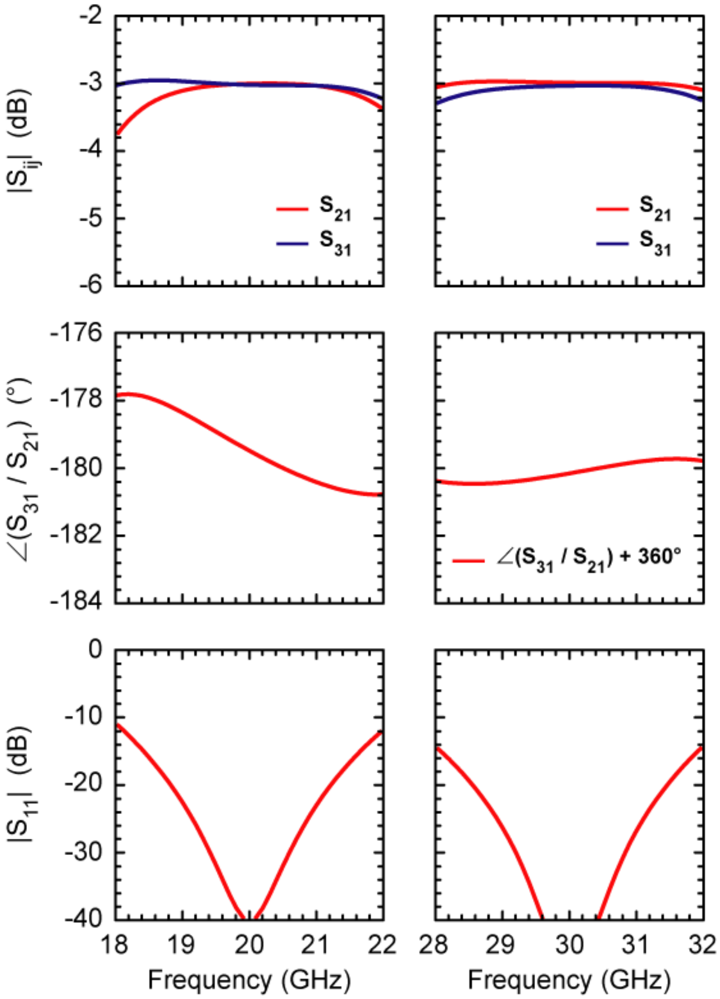

Figure 5.19: Simulated rat-race coupler response with 6-stage LoP/HiP TLINs.

Figure 5.19 presents simulated response for a rat-race coupler with 6-stage TLIN implementation, and Figure 5.20 for lossless T-junction splitters (0/180°). Both set of results are very promising for wideband operations, with the rat-race implementation more superior in performance with less phase imbalance from the differential-phase condition across a wider bandwidth.

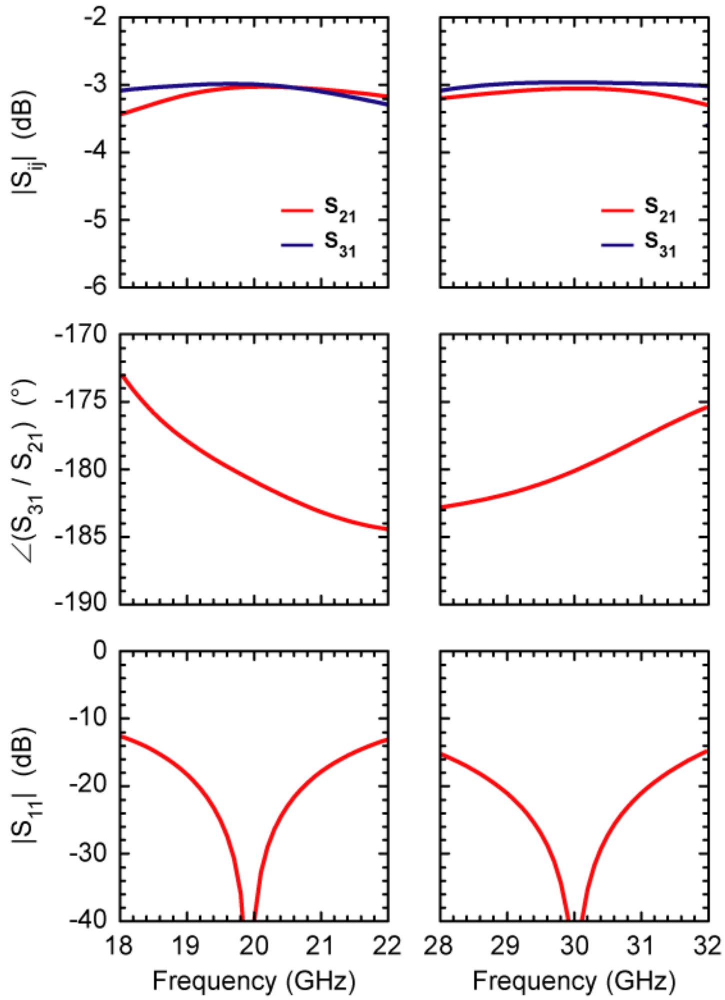

Figure 5.20: Simulated extended T-junction splitter response (0/180°) with 6-stage LoP/HiP TLINs.

These plots presents the fundamental limitations of the amplitude and phase imbalance that can be obtained with single stage (coupler) quadrature and differential phased couplers implemented with LoP/HiP transmission lines. Differential phased couplers can be implemented with rat-race using this approach. Branch-line topology may not be as suitable for wide-band operations, and the limitations stems not from the TLIN synthesis, but from the intrinsic nature of the branch-line coupler topology.

For purpose of comparison, theoretical response for single-stage couplers with ideal TLINs implementation are presented in Figure 5.21 for quadrature-phased couplers

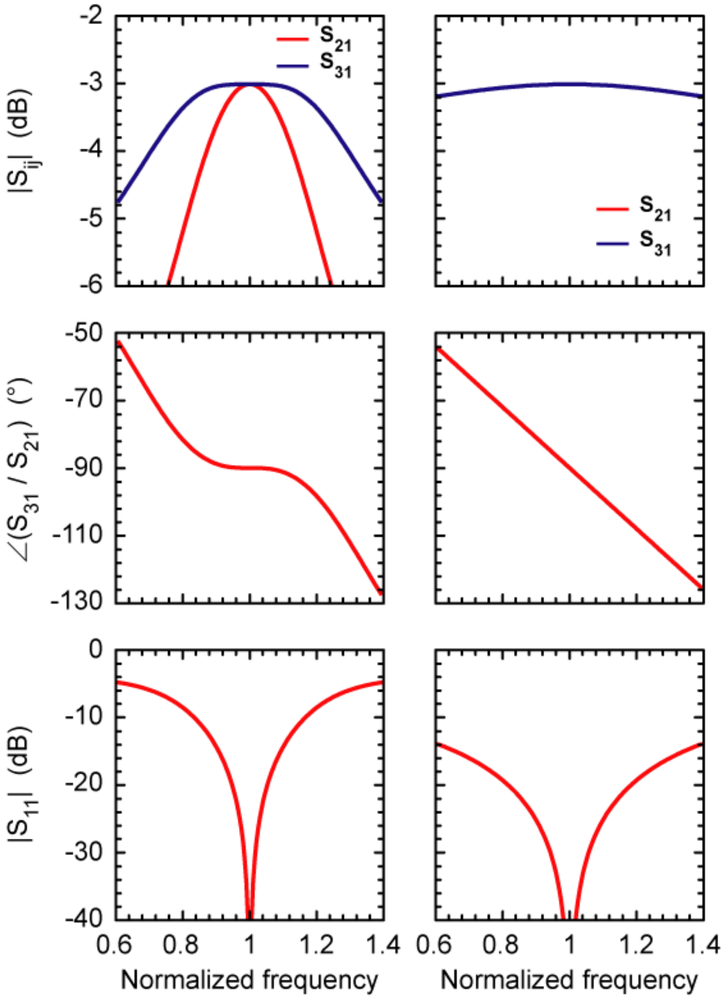

Figure 5.21: Quadrature-phased couplers with ideal TLINs; branch-line (left) and extended T-junction splitter (0/90°) (right).

(layout in Figure 5.14a & c), and Figure 5.22 for differential-phased couplers (layout in Figure 5.14b & c).

The narrowband nature for the branch-line implementation in Figure 5.17 is verified in Figure 5.21. The broad-band nature for the rat-race couplers in Figure 5.19 stems from the use of HiP network, or "-λ/4" length of TLIN, in lieu of the 3λ/4 TLIN segment, and is verified from Figure 5.22.

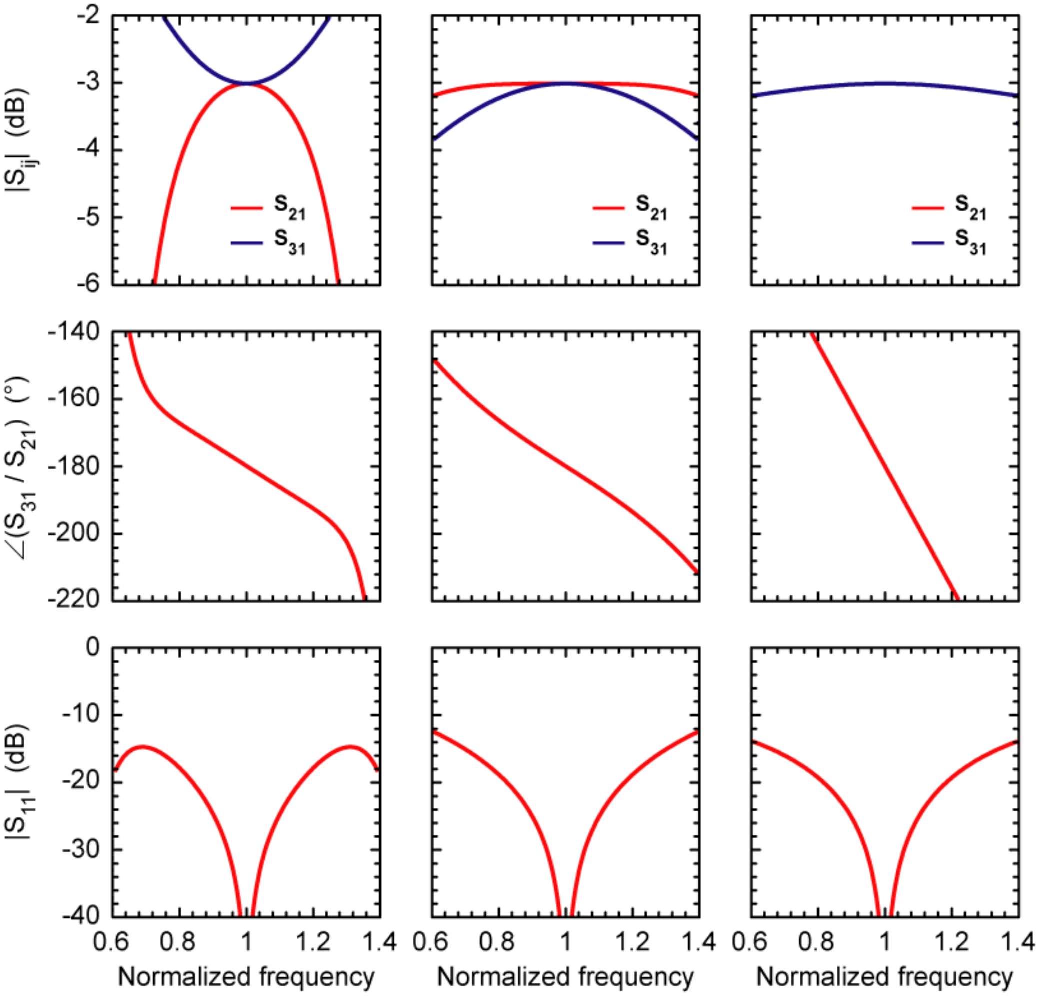

Figure 5.22: Differential-phased couplers with ideal TLINs; rat-race (left), modified rat-race with 3λ/4 TLIN replaced with -λ/4 (mid) and extended T-junction splitter (0/180°) (right).

5.4.4 Extended Single-stage / Multi-stage Couplers Implementation

Single stage branch-line couplers with extended features are presented in Figure 5.23 [89],[90]. Unfortunately for frequency ratio of 1.5:1, the TLIN characteristic impedance required is not easy for implementation. Figure 5.23a may be feasible for implementation in stripline layers of multi-layered stack-up, where TLIN characteristic impedance are typically low due to the close proximity of the ground layers to the stripline traces. Layout for 2-stage branch-line and rat-race couplers are presented in Figure 5.24.

The following impedance values are required for the 2-stage branch line coupler (Figure 5.24a), and the corresponding simulated response presented in Figure 5.25.

$Z_1 = 36.6\ \Omega$, $Z_2 = 97.6\ \Omega$,

$Z_3 = 60.2\ \Omega$,

The 2-stage coupler response is much more suited for wideband operation at both operating frequencies.

Similarly, the following impedance values are required for the 2-stage rat-race coupler (Figure 5.24b), and the corresponding simulated response presented in Figure 5.26.

$Z_1 = 54\ \Omega$, $Z_2 = 48\ \Omega$,

$Z_3 = 28.2\ \Omega$, $Z_4 = 70\ \Omega$,

$Z_5 = 67\ \Omega$,

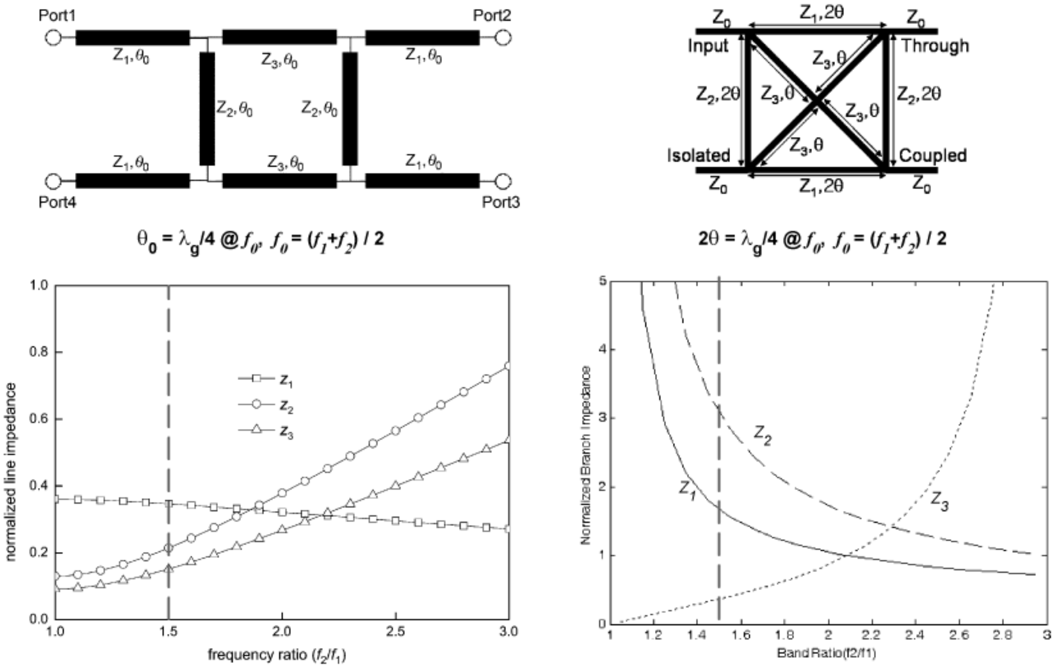

(a) (b)

Figure 5.23: Extension of single-stage branch-line couplers (a) with port extension [89], and (b) with cross-coupled TLIN [90].

2-stage wideband couplers has proven to provide the best response for wide bandwidth requirements for small operating frequency ratio (f_2/f_1 = 1.5), especially for the quadrature-phased couplers where the other alternative with LoP/HiP TLIN synthesis has not been very promising. Unfortunately the size requirements may not be feasible for implementation, especially with elements located closed to each other of 0.4-0.5 λ_0. They can be considered for high performance requirements in other parts of the feed network, or if the other two presented solutions (single-fed dual-band antenna element, multiple feed points antenna element fed with 4-6 stage LoP / HiP couplers) are proven to be inadequate for providing the required bandwidth.

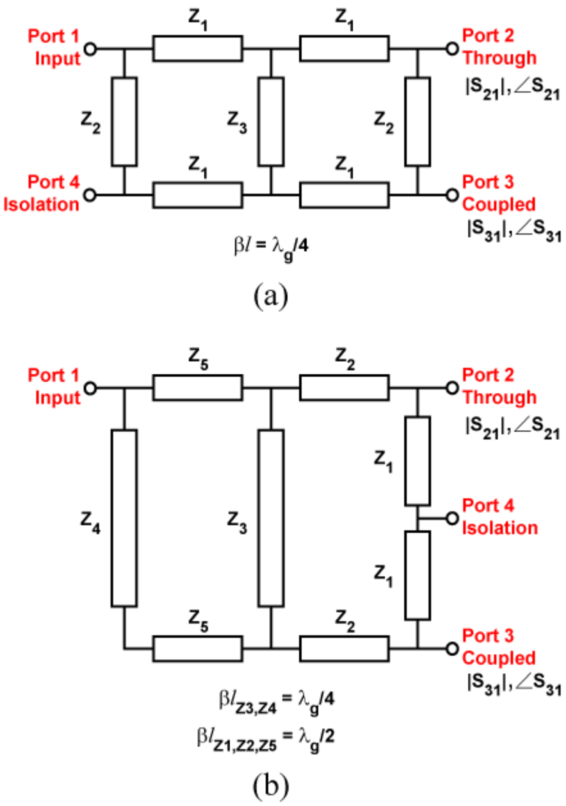

Figure 5.24: 2-section (a) branch-line and (b) rat-race couplers implementation.

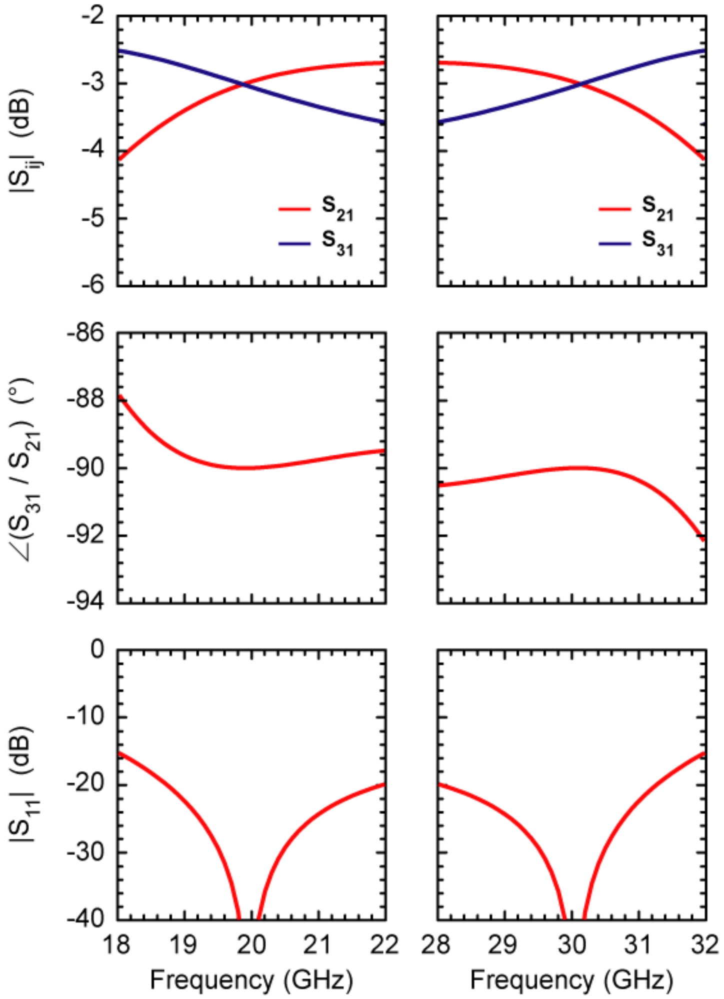

Figure 5.25: Simulated branch-line response with 2-stage rat-race coupler.

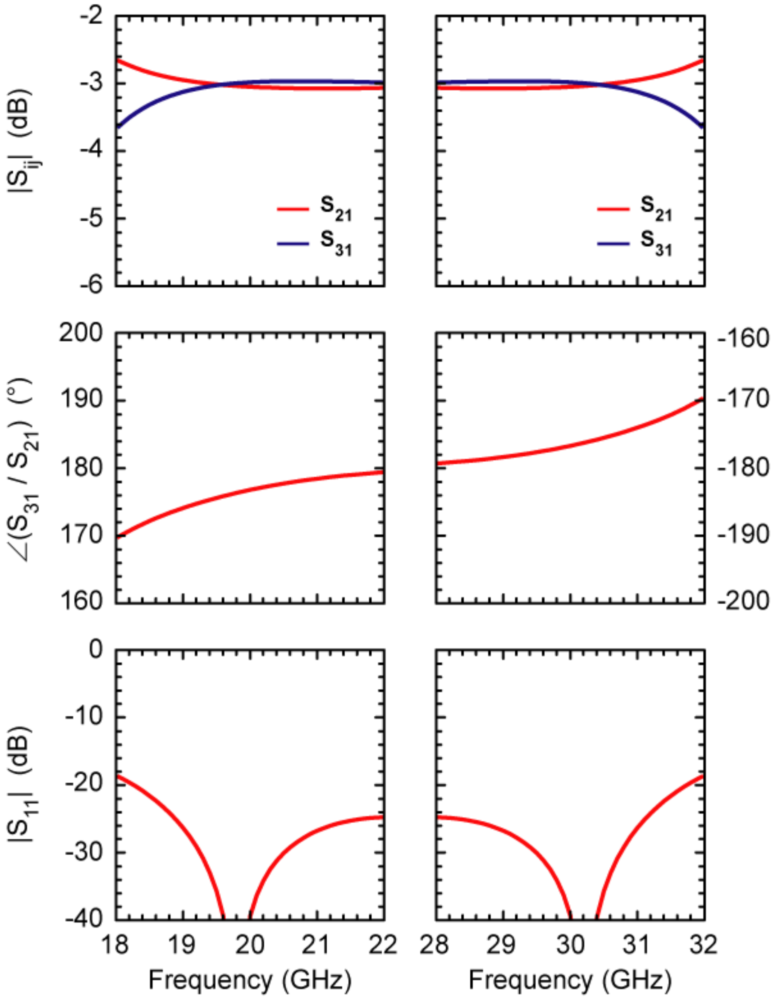

Figure 5.26: Simulated rat-race response with 2-stage rat-race coupler.

5.5 Conclusion

Designs and simulations for dual-band CP antenna element (with single feed-point) and dual-band couplers are presented for operating frequency ratio of 1.5:1. From the complexity of achieving desired (2 GHz) bandwidth at both operating bands, feasible solution may be to perhaps consider a combination of

- using antenna elements with multiple inputs, a set of quadrature inputs for CP operating for each frequency, and
- integration of active circuitry deep into the antenna front-end routing with RFIC implementation, and integrating the functionalities of the diplexers or dual-band 3-dB couplers into the RFIC active circuitry, and feeding from RFIC chips/channels directly into the multiple feeds of every antenna element.

Chapter 5, in part, is based on and mostly a reprint of the material that has been published in *Proc. IEEE Antennas Propag. Symp.* (Jul 2014), Kevin M. Ho and Gabriel M. Rebeiz. The dissertation author was the primary author of this material.

Chapter 6

Conclusion

6.1 Summary of Work

This thesis presents the first microstrip antenna with full-polarization diversity across a wide frequency tuning range, low-cost development of active antenna receiver array, and studies and component designs for development of Ku/Ka-band shared aperture CP antenna array.

Chapter 2 presents microstrip antenna designs for full polarization diversity, frequency tuning, and combination of both polarization diversity and frequency agility. Hardware verifications are presented, with measured tuning range covering 1.6:1 and 1.4:1, for linear and circular polarized cases. High reliable commercial-packaged RF MEMS SPDTs are used for the design of novel re-configurable feed network for polarization diversity control. Discussion on theoretical cross-polarization from a probe-fed microstrip antenna for both linear and circular polarization is presented.

Chapter 3 features the packaging and implementation of multi-channel phased array RFIC chips with commercial QFN plastic packages on commercial-grade multi-layered PCBs, as part of a FMCW radar sensor. Potential performance degradation, ranging from matching with package-PCB interface, to array radiation limitations from choice of PCB, is discussed in depth. Design curves presented as future reference for quick evaluation purposes. Hardware verifications are presented.

Chapter 4 presents on theoretical pattern studies for circular polarized arrays. Implementation methods to enhance CP performance and beam scanning is identified, and resulting Xpol from various layout configuration for broadside beam and 30° beam scan conditions presented. Chapter 5 presents the design of a dual-band antenna element with a single feed-point, and designs for 3-dB couplers with differential or quadrature phase offsets, for 20/30 GHz concurrent dual-band operation.

6.2 Future Work

The microstrip antennas with full polarization diversity can be implemented with high Q MEMS tunable capacitors, to allow for better radiation efficiency across the tuning range. It can be cascaded to form a fully re-configurable multi-beam multiple frequency phased array aperture, with part of the feed network (namely the switches, 0/180° differential splitters and delay lines) absorbed into the RF front-end circuitry (amplifiers and phase shifters) for monolithic-level of integration with RFICs or MMICs for further scalability array development.

X-band phased array antenna efforts reveal the potential matching possibilities and challenges with the use of QFN plastic packages up to 20 GHz. Using the results presented, careful design can be planned for further extension of the QFN packaged phased array RFIC chips across Ku-band. On the other hand, similar approach can be considered for design of antenna arrays on low cost multi-layered commercial-grade PCBs for higher frequency applications with active devices assembled with wire-bonding or flip-chip methods.

Finally, the results of studies presented in Chapter 4 forms the fundamental basis for realistic Xpol expectations for final CP array performance. Combined with the appreciation of limitations imposed by the dual-band elements designed in Chapter 5, theoretical limitations in design specifications for the antenna elements and any dual-band components can be identified at an early stage. Similar to the previous case, the dual-band components (e.g. diplexer and couplers) can be implemented directly on a monolithic level of integration (with or without some RF front-end components) on the RFICs or MMICs, removing the compact space constraints requirements.

Appendix A

Apparent Deviation of Microwave Materials Relative Permittivity

A.1 Introduction

Dielectric permittivity values for microwave materials are, rightfully, an intrinsic property of the materials. For the same material, say, a sheet of RO4003 laminate for microstrip substrate, the relative permittivity should not be varying with the substrate thickness. Unfortunately, measurements of microstrip TLIN resonators and filters have revealed a consistent deviation away from EM simulations, with the measured frequency constantly lower than simulated values.

Simulation setups will result in variations of resonances, with infinitesimal metal thickness for microstrip trace resulting in lower resonance frequencies than 3D metal geometry. Material cross-sectional inhomogeneity (e.g. orientation of woven glass in epoxy-filled organic resin for FR-4) will also result in material effectively having different permittivity values, based on the orientation of signal trace and board thickness.

Besides such variations in simulation set-ups and known variation for material fillings, this Appendix presents 3 factors which are not as obvious and not well appreciated by the community, but are prominent factors which causes measurement deviations from simulations for highly frequency selective circuits;

I:

Deviation of relative permittivity values from stripline test resonators for microstrip circuits.

II:

Anisotropy of dielectric materials.

III:

Surface roughness in conductor-dielectric interface.

Impact of these factors on measurements will be presented, together with methods (and corresponding implications) of performing adjustments in the simulations for ensuring consistency in measurements and simulations, namely for resonances.

A.2 3 Factors for Apparent ε_r deviation

A.2.1 X-band Stripline Test Resonator Standard

For purpose of ensuring consistency of evaluated material ε_r and tanδ in the microwave region, IPC-TM-650 method 2.5.5.5 details the procedures for material evaluation in a stripline configuration at X-band. Figure A.1 presents the layout and assembly for stripline measurements [91].

Allowing for direct measurements in the X-band region, this measurement method is used for quality evaluation and control purposes. Other methods are usually based on time-domain measurements (time-domain reflectometry, TDR) and are at MHz region. Arguments against them include deviation of permittivity properties as

Table A.1: List of some Rogers laminates and dielectric constant values.

Laminate	ε_r from stripline resonator	ε_r from FSR
RT6006	6.15	6.32
RO3006	6.15	6.4
RO3206	6.15	6.27
RO4360	6.15	6.6
RT6010	10.2	10.56
RO3010	10.2	11.2
RO3210	10.2	10.8
RO4003	3.38	3.55
RO4350	3.48	3.66

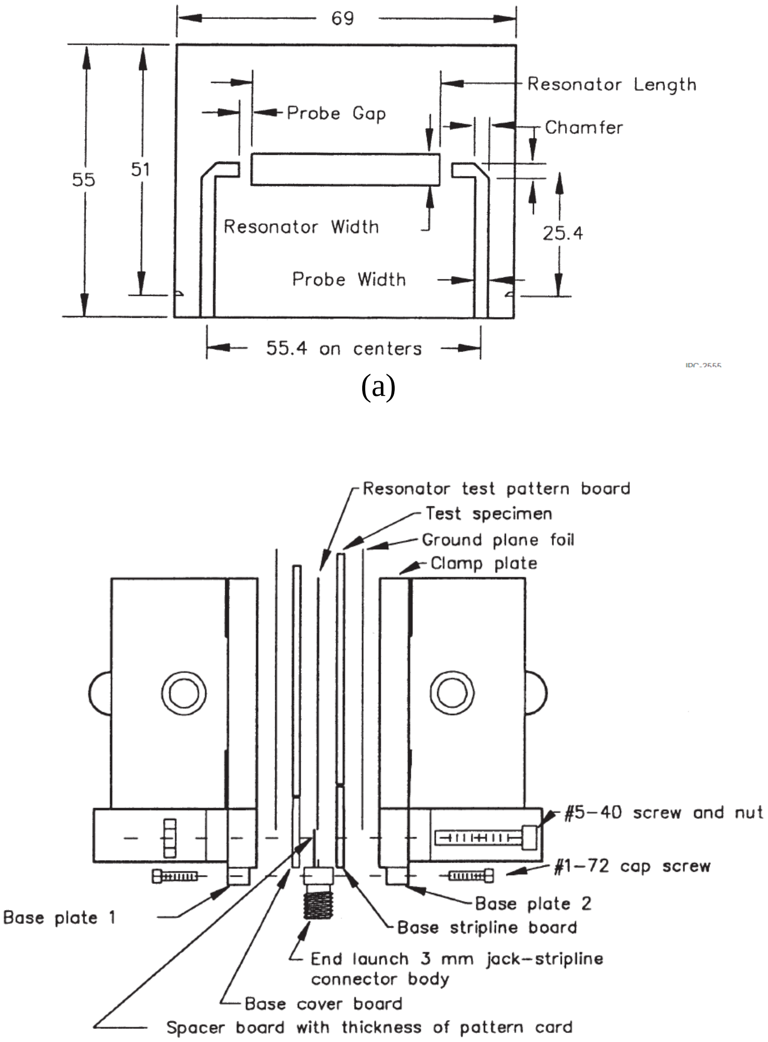

(a)

(b)

Figure A.1: Stripline test resonator (a) layout and (b) assembly details [91].

frequency increases into microwave region.

Problem with this method is the existence of trapped air-gap in the metal-substrate interface, leading to deviation of actual material ε_r value. Air gaps at sides of traces have no significant impact on the measured response [92]. Boards with higher permittivity values are subjected to larger deviation from this air-gap mechanism.

Alternative dielectric constant evaluation methods include full-sheet resonance (FSR) method, with the details and procedures found in IPC-TM-650 2.5.5.6 standard.

It is essentially treating the material under test (MUT) as a cavity resonator, and probing the resonant frequencies of the various modes based on the size of the MUT.

Recent years Rogers presents the use of differential phase length method [67] for customers' reference. It is essentially the phase measurement of two lengths of TLINs, and equating the measured phase difference of both cases to the difference of the physical lengths of both TLINs.

A.2.2 Dielectric Uniaxial Anisotropy

As the cross-sectional profile of some dielectric materials are not homogenous, instead of a constant value, the dielectric constant can be accurately represented by a tensor with the diagonal elements ε_{xx}, ε_{yy}, ε_{zz} capturing the full variation of dielectric constant in 3D space.

Considering the layout of a pair of coupled microstrip TLINs on the X-Y plane, the anisotropy can be reduced to an uniaxial anisotropy; namely a horizontal and a vertical component, i.e. $\varepsilon_{hori} = \varepsilon_{xx} = \varepsilon_{yy,}$ and $\varepsilon_{vert} = \varepsilon_{zz}$. In this way, the odd-even mode of the coupled lines can be intuitively decomposed, with the odd mode dominated by the lateral dielectric constant (ε_{hori}), and the even mode determined by the vertical dielectric constant (ε_{vert}) [92],[93].

Lightly coupled single resonators (e.g. linear or ring resonators) can only evaluate a single resonance corresponding to the vertical dielectric constant value. The lateral dielectric constant value can only be evaluated from a pair of coupled lines, with the coupling coefficient providing the information for evaluating the lateral dielectric constant.

Using a microstrip filter as an illustration with the center frequency consistent in both simulations and measurements; $\varepsilon_{hor} > \varepsilon_{vert}$ if the measured bandwidth is consistently wider from the simulations (Figure A.2).

Impact of this factor can be captured in Sonnet and HFSS. Sonnet allows for entry of horizontal- and vertical- dielectric constant values. HFSS allows for entry of full-3D anisotropic values.

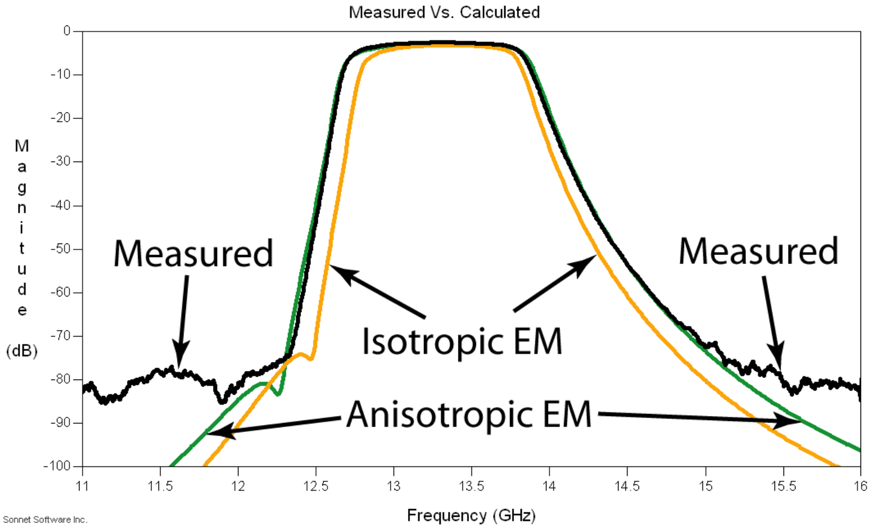

Figure A.2: Impact of $\varepsilon_{hori} > \varepsilon_{vert}$ on microstrip filter and EM modeling with (yellow trace) and without (green trace) uniaxial anisotropy [93].

Some anisotropic values reported include [93];

RO3010: $\varepsilon_{hori} = 12.1$, $\varepsilon_{vert} = 11.3$
RO4350: $\varepsilon_{hori} = 3.3$, $\varepsilon_{vert} = 3.6$

A.2.3 Surface Roughness

As presented in Chapter 3, impact of surface roughness on apparent ε_r deviation is not as obvious. Its impact is easily identified from the other factors when the measured resonance frequency of a microstrip resonator decreases significantly with reduction in substrate height. Impact from this factor increases as substrate thickness decreases.

Surface roughness options in most EM solvers compensates for the losses, but not on the phase velocity. Sonnet accounts for both losses and inductance impact, thus capturing the impact of apparent dielectric variation without the need to explicitly change the dielectric constant values for the simulations. Figure 3.24 presents the apparent change of substrate ε_r and height based on conventional microstrip TLIN model, to adequately account for the surface roughness impact on *both* characteristic impedance and phase velocity.

A possible method to capture the resonant frequencies consistently in both simulations and measurements is to increase the relative permittivity values based on measurements of test resonators. Though this allows for consistent simulated and measured resonances, information for TLIN characteristic impedance is compromised (as presented in Chapter 3), and depending on the nature of the circuit, that may or may not be as severe of an impact.

Using measured data from differential phase length method, the following ε_r values are presented by Rogers (through their MWI software application [94]), for RO4003/4350materials with 0.5 oz ED copper cladding (corresponding to 2.8 μm roughness). The impact of surface roughness is more prominent on RO4000-series laminates, due to the higher surface roughness values (2.8 μm) than others (0.6-1.8 μm).

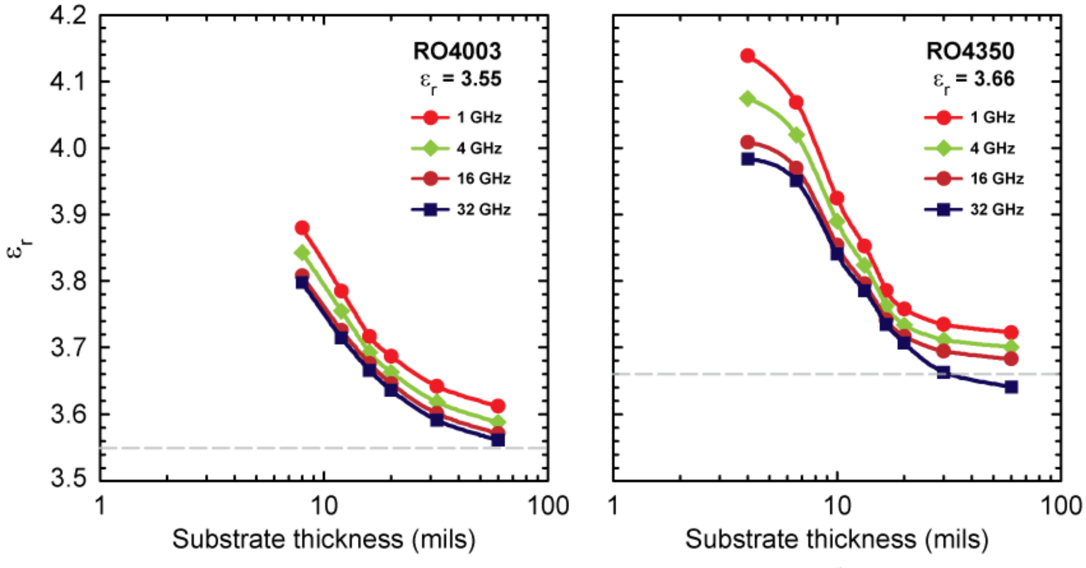

(a) (b)

Figure A.3: Apparent dielectric constant values for ED 0.5 oz copper-cladded (a) RO4003 and (b) RO4350 laminates, with compensation for surface roughness. Data compiled from [94].

A.3 Fitted Design Parameters for RO4350 microstrip TLINs

Rogers RO4350 commercial-grade laminates are extensively used for various applications, namely due to its low substrate losses, combined with its FR4-fabrication compatibilities, UL-94 flammability certification, and low cost.

For 0.5 oz ED Cu-cladding on RO4350 laminates, there will be 2.8 µm of surface roughness between the conductor and substrate. Plated via processes will incur another 0.5 oz of copper, resulting in a total copper thickness of 1 oz, or 35 µm. Sonnet surface roughness model were used to simulate microstrip TLINs on RO4350, with 2.8 µm surface roughness, 35 µm copper thickness, and substrate thickness from 0.0067” to 0.02”. The S-parameter responses from Sonnet were fitted with conventional microstrip transmission line model [68].

Through the S-parameter fittings, apparent substrate relative permittivity and substrate height that ensures the conventional microstrip model for the S-parameter responses to be fitted to Sonnet’s simulated responses with surface roughness considerations were identified, and presented in Figure A.4. From Figure A.4b, the apparent substrate thickness is consistently higher than the physical thickness, to allow for the microstrip TLIN modeled characteristic impedance to correspond to the higher characteristic impedance values (Figure A.4c) arising from the per-unit-length inductance enhancement associated with the surface roughness. Information for substrate thickness of beyond 0.02” is not presented in the plots, since the per-unit-length inductance effect arising from the surface roughness decreases as the substrate thickness increases, and is less significant for thickness of > 0.02”.

Polynomial equations that can be easily used in circuit simulators, relating the apparent substrate ε_r and height information as presented in Figures 4a,b to microstrip TLIN trace widths, are derived and presented below:

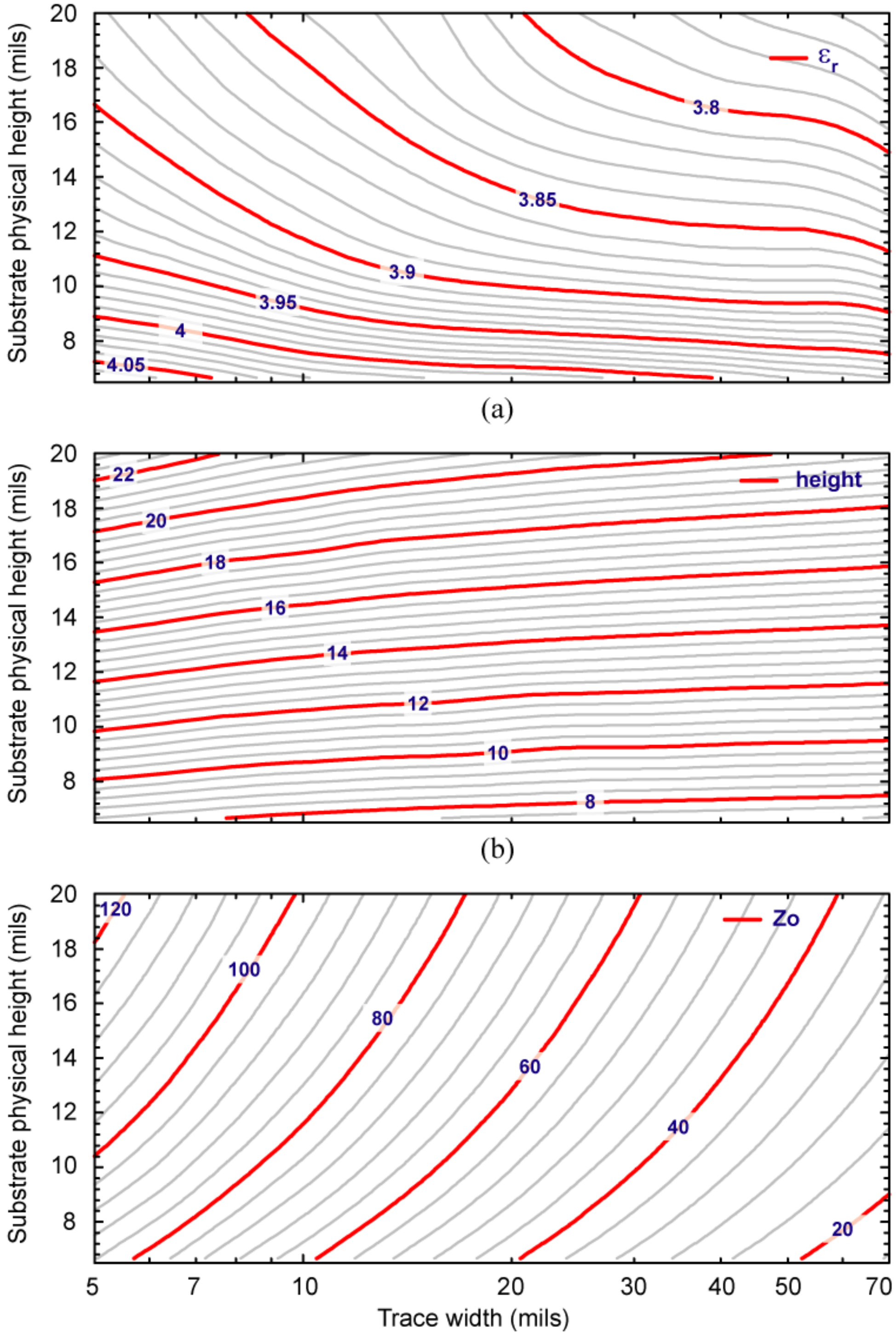

(a)

(b)

(c)

Figure A.4: (a) Apparent substrate dielectric constant and (b) substrate height for use with conventional microstrip model, and (c) simulated characteristic impedance for microstrip TLINs on RO4350 with 35 µm copper thickness and 2.8 µm surface roughness.

With ‘w’ the trace width of the microstrip TLIN (in mils), ‘ε_r’ and ‘*ht*’ the substrate’s relative permittivity height:

- for physical substrate thickness of 0.0067”;

$$\begin{aligned} \varepsilon_r &= -1.7767e^{-9}w^5 + 3.7018e^{-7}w^4 - 2.8905e^{-5}w^3 + 1.0471e^{-3}w^2 - 1.8222e^{-2}w + 4.1368 \\ ht &= -2.1313e^{-8}w^5 + 4.4735e^{-6}w^4 - 3.5726e^{-4}w^3 + 1.3569e^{-2}w^2 - 2.5301e^{-1}w + 9.3379 \end{aligned} \tag{A.1}$$

- for physical substrate thickness of 0.01”;

$$\begin{aligned} \varepsilon_r &= -1.5887e^{-9}w^5 + 3.3007e^{-7}w^4 - 2.6438e^{-5}w^3 + 1.0269e^{-3}w^2 - 1.9892e^{-2}w + 4.0496 \\ ht &= -2.9391e^{-8}w^5 + 6.1498e^{-6}w^4 - 4.8940e^{-4}w^3 + 1.8579e^{-2}w^2 - 3.4873e^{-1}w + 13.455 \end{aligned} \tag{A.2}$$

- for physical substrate thickness of 0.0133”;

$$\begin{aligned} \varepsilon_r &= -8.1755e^{-10}w^5 + 1.8196e^{-7}w^4 - 1.6099e^{-5}w^3 + 7.0874e^{-4}w^2 - 1.5914e^{-2}w + 3.9886 \\ ht &= -3.7087e^{-8}w^5 + 7.8139e^{-6}w^4 - 6.2644e^{-4}w^3 + 2.3935e^{-2}w^2 - 4.5121e^{-1}w + 17.521 \end{aligned} \tag{A.3}$$

- for physical substrate thickness of 0.0167”;

$$\begin{aligned} \varepsilon_r &= -7.0968e^{-10}w^5 + 1.5362e^{-7}w^4 - 1.3456e^{-5}w^3 + 6.0716e^{-4}w^2 - 1.4779e^{-2}w + 3.9592 \\ ht &= -4.1919e^{-8}w^5 + 8.8837e^{-6}w^4 - 7.1806e^{-4}w^3 + 2.7758e^{-2}w^2 - 5.3318e^{-1}w + 21.474 \end{aligned} \tag{A.4}$$

- for physical substrate thickness of 0.02”;

$$\begin{aligned} \varepsilon_r &= -9.5857e^{-10}w^5 + 1.9939e^{-7}w^4 - 1.6165e^{-5}w^3 + 6.5884e^{-4}w^2 - 1.5014e^{-2}w + 3.9412 \\ ht &= -5.1841e^{-8}w^5 + 1.0975e^{-5}w^4 - 8.8396e^{-4}w^3 + 3.3909e^{-2}w^2 - 6.4293e^{-1}w + 25.385 \end{aligned} \tag{A.5}$$

Units of w is in mils, i.e. w=10 for trace width of 0.01”

Valid for trace widths within 0.005” to 0.07”, these polynomial equations will allow for the ease of modeling of RO4350 microstrip TLINs in most circuit simulators (e.g. ε_r and height for MSUB in ADS), retaining the physical dimensions of the microstrip TLIN traces (namely trace widths and lengths), while ensuring high accuracy and measurement consistency for the simulated responses by capturing the impact of the surface roughness on *both* the phase velocity and characteristic impedance values.

A.4 Conclusion

3 dominant factors on the apparent ε_r deviation from measurements are introduced. Electrical permittivity of materials values are intrinsic to the material, and should rightfully not be subjected to changes. In some cases (e.g. factors I,II), the true intrinsic permittivity property were not adequately evaluated, justifying the need for adjustments of permittivity values (increasing the ε_r values for factor I, and introducing anisotropy for factor II).

In other cases (surface roughness for factor III) external influences on the measured resonant frequencies, especially for microstrip resonators, coupled with the limitations of solvers to capture all the extrinsic factors adequately, will require the need for appropriate correction factors to the ε_r values, to allow consistency for most EM solvers with measured results. Deviation of characteristic impedance information has to be noted, though it may not be of any consequence to the design/measurements for most classes of microwave circuits, save for an offset trend which may be erroneously attributed to "fabrication tolerances".

Bibliography

[1] A. S. Morris and V. Steel, "Integrated tunable systems for scalable 4G radios," *IEEE Int. Microwave Symp. Digest*, Seattle, WA, Jun. 2013.

[2] P. A. Tornatta, R. Gaddi, "Aperture tuned antennas for 3G-4G applications using MEMS digital variable capacitor," *IEEE Int. Microwave Symp. Digest*, Seattle, WA, Jun. 2013.

[3] Omron Electronics Components LLC, Schaumburg, IL.

[4] wiSpry, Inc., Irvine, CA.

[5] Cavendish Kinetics Inc., San Jose, CA.

[6] D. F. Sievenpiper, D. C. Dawson, M. M. Jacob, T. Kanar, S. Kim and R. G. Quarfoth, “Experimental validation of performance limits and design guidelines for small antennas,” *IEEE Trans. Antennas Propag.*, vol. 60, no. 1, pp. 8-19, Jan. 2012.

[7] B. R. Elbert, *The Satellite Communication Applications Handbook*, 2nd ed., Artech House, 2004.

[8] C. R. White and G. M. Rebeiz, “Single- and dual-polarized tunable slot-ring antennas,” *IEEE Trans. Antennas Propag.*, vol. 57, no. 1, pp. 19-26, Jan. 2009.

[9] C. R. White and G. M. Rebeiz, “A differential dual-polarized cavity-backed microstrip patch antenna with independent frequency tuning,” *IEEE Trans. Antennas Propag.*, vol. 58, no. 11, pp. 3490-3498, Nov. 2010.

[10] F. Yang and Y. Rahmat-Samii, “A reconfigurable patch antenna using switchable slots for circular polarization diversity,” *IEEE Microw. Wireless Compon. Lett.*, vol. 12, no. 3, pp. 96-98, Mar. 2002.

[11] W. Yoon, S. Han, S. Pyo, J. Lee, I. Shin and Y. Kim, “Reconfigurable circularly polarized microstrip antenna on a slotted ground,” *ETRI Journal*, vol. 32, no. 3, pp. 468-471, Jun. 2010.

[12] F. Yang and Y. Rahmat-Samii, “Patch antennas with switchable slots (PASS) in wireless communications: concepts, designs, and applications,” *IEEE Antennas Propag. Mag.*, vol. 47, no. 2, pp. 13-29, Apr. 2005.

[13] Y. J. Sung, T. U. Jang and Y. S. Kim, “A reconfigurable microstrip antenna for switchable polarization,” *IEEE Microw. Wireless Compon. Lett.*, vol. 14, no. 11, pp. 534-536, Nov. 2004.

[14] J. Liu, D Wang, S. Xiang, W. Wang and S. Zhang, “A reconfigurable microstrip antenna with frequency and polarization diversities,” *Microwave Journal*, vol. 52, pp. 210- 218, May. 2009.

[15] J. Balcells, Y. Damgaci, B. A. Cetiner, J. Romeu and L. Jofre, “60 GHz MEMS-integrated polarization reconfigurable CPW antenna,” *MEMSWave 2009*, Jul. 2009.

[16] D. H. Schaubert, F. G. Farrar, A. Sindoris and S. T. Hayes, “Microstrip antennas with frequency agility and polarization diversity,” *IEEE Trans. Antennas Propag.*, vol. 29, no. 1, pp. 118-123, Jan. 1981.

[17] K. M. Ho and G. M. Rebeiz, “Microstrip patch antennas with frequency agility and polarization diversity over a wide frequency range,” *Proc. IEEE Antennas Propag. Symp.*, Toronto, ON, Jul. 2010.

[18] K. M. Ho and G. M. Rebeiz, “Microstrip antennas with full polarization diversity using packaged RF MEMS switches,” *Proc. IEEE Antennas Propag. Symp.*, Chicago, IL, Jul. 2012.

[19] K. M. Ho and G. M. Rebeiz, “A 0.9-1.5 GHz microstrip antenna with full polarization diversity and frequency agility,” *IEEE Trans. Antennas Propag.*, accepted for publication.

[20] K. M. Ho and G. M. Rebeiz, “Tunable microstrip antenna with circular polarization across 1.4:1 frequency span,” *Proc. IEEE Antennas Propag. Symp.*, pp. 394-395, Orlando, FL, Jul. 2013.

[21] *RF MEMS Switch Model 2SMES-01 datasheet*, Omron Electronic Components LLC, http://www.components.omron.com

[22] G. M. Rebeiz, C.D. Patel, S. K. Han, C. H. Ko and K. M. Ho, “The search for a reliable MEMS switch,” *IEEE Microwave Magazine*, vol. 14, no. 1, pp. 57-67, Jan. 2013.

[23] C. H. Ko, K. M. Ho and G. M. Rebeiz, “An electronically-scanned 1.8–2.1 GHz base-station antenna using packaged high-reliability RF MEMS phase shifters,” *IEEE Trans. Microw. Theory Techn.*, vol. 61, no. 2, pp. 979-985, Feb. 2013.

[24] T. Fujiwara, T. Seki, F. Sato and M. Oba, "Development of RF-MEMS ohmic contact switch for mobile handsets applications", *Proc. 42nd European Microwave Conference*, Amsterdam, The Netherlands, pp. 180-183, Oct 2012.

[25] C. H. Ko, K. M. Ho, R. Gaddi and G. M. Rebeiz, “A 1.5-2.4 GHz tunable 4-pole filter using commercial high-reliability 5-bit RF MEMS capacitors,” *IEEE Int. Microwave Symp. Digest*, Seattle, WA, Jun. 2013.

[26] *Tuning Diode Model SMV123x Series*, Skyworks Solutions, Inc.

[27] Modelithics CLR Library, Modelithics, Inc., Tampa, FL.

[28] D. R. Jackson, “Microstrip antennas,” in J. L. Volakis (Ed.) *Antenna Engineering Handbook*, chap. 7, pp. 7-11 – 7-19, 2007.

[29] D. R. Jackson and N. G. Alexopoulos, “Simple approximate formulas for input resistance, bandwidth, and efficiency of a resonant rectangular patch,” *IEEE Trans. Antennas Propag.*, vol. 39, no. 3, pp. 407-410, Mar. 1991.

[30] D. R. Jackson, S. A. Long, J. T. Willians and V. B. Davis, “CAD of rectangular microstrip antennas,” in K. F. Lee and W. Chen (Eds.) *Advances in Microstrip and Printed Antennas*, chap. 5, pp. 223-271, 1997.

[31] T. Chiba, Y. Suzuki and N. Miyano, “Suppression of higher modes and cross polarized components for microstrip antennas,” *Antennas and Propag. Soc. Int. Symp.*, vol. 20, pp. 285-288, May 1982.

[32] B. M. Schiffman, “A new class of broad-band microwave 90-degree phase shifters,” *IRE Trans. on Microw. Theory Techn.*, vol. 6, no. 2, pp. 232-237, Apr. 1958.

[33] J. A. Nelson and G. Stavis, “Impedance matching, transformers and baluns,” *Very High- Frequency Techniques*, vol. 1, chap. 3, pp. 53-92, 1947.

[34] K. R. Carver and J. W. Mink, “Microstrip Antenna Technology,” *IEEE Trans. Antennas Propag.*, vol. 29, no. 1, pp. 2-24, Jan. 1981.

[35] *RO4000 Series High Frequency Circuit Materials*, and *RO4400™ Series Prepreg Data Sheet*, Rogers Corp., Nov. 2011., Rogers Corp., Jan. 2012.

[36] *SG 32, Product-sheet*, Satimo, 2010, France.

[37] J. Herd, S. Duffy, M. Weber, G. Brigham, C. Weigand and D. Cursio, “Advanced architecture for a low cost multifunction phased array radar,” *IEEE MTT-S Int. Microw. Symp. Dig., Anaheim*, CA, pp. 676-679, May 2010.

[38] E. Viveiros, R. Wellman, J. Clark, D. Tahmoush, J. Silvious, J. Kurtz, D. Wikner and E. Adler, “An unattended, unmanned, and man-portable tactical Doppler radar,” *56th Ann. Meeting MSS Tri-Service Radar Symp.*, Orlando, FL, Jun. 2010.

[39] W. H. Theunissen, D. Brocious, T. DeStefano, J. Mulvey, S. Pappas, J. Thomas, P. Butterfoss, M. Briske, S. Nelson, G. Clark, M.Walker, J.Dishong, R.Mongia and G. Forman, “Development of an X-band phased array antenna using multilayer circuit board architecture,” *IEEE Int. Symp. Phased Array Syst. Technol.*, Waltham, MA, pp. 676-679, Oct. 2010.

[40] L. Infante, A. D. Luca and M. Teglia, “Low-profile ultra-wide band antenna array element suitable for wide scan angle and modular subarray architecture,” *IEEE Int. Symp. Phased Array Systems and Technology*, Waltham, MA, pp. 157-163, Oct. 2010.

[41] E. Brookner, "Phased-array radars: past, astounding breakthroughs and future trends," *Microwave Journal*, vol. 51, no. 1, pp. 30-48, Jan. 2008.

[42] T. Clark, "Low-cost cruise missile defense (LCCMD)," DARPA web site, Aug 2005.

[43] W. Simon, J. Kassner, O. Litschke, H. Fischer and S. Holzwarth,"Highly integrated KA-Band Tx front-end module including 8x8 antenna array," *IEEE MTT-S Int. Microw. Symp. Dig., Boston*, MA, pp. 5-8, Jun. 2009.

[44] A. Geise and A. F. Jacob, "Flex-Rigid Architecture for Active Millimeter-Wave Antenna Arrays," *IEEE MTT-S Int. Microw. Symp. Dig., Boston*, MA, pp. 809-812, Jun. 2009.

[45] J. Hacker, C. Hillman, A. Papavasiliou, C. G. Kim, A. Abbaspour-Tamijani, C. Y. Kim and G. M. Rebeiz, “A 16-element transmit/receive Q-band electronically steerable subarray tile,” *IEEE MTT-S Int. Microw. Symp. Dig.*, Montreal, QC, Canada, pp. 1-3, Jun. 2012.

[46] D. W. Kang and G. M. Rebeiz, "Single and 4-element Ka-band transmit/receive phased array silicon RFICs with 5-bit amplitude and phase control," *IEEE Trans. Microw. Theory Tech.*, vol. 57, no. 12, pp. 3534-3543, Dec. 2009.

[47] D. Shin and G. M. Rebeiz, “A high-linearity X-band four-element phased-array receiver: CMOS chip and packaging,” *IEEE Trans. Microw. Theory Tech.*, vol. 59, no. 8, pp. 2064-2072, Aug. 2011.

[48] J. P. Comeau, M. A. Morton, W. L. Kuo, T. Thrivikraman, J. M. Andrews, C. M. Grens, J. D. Cressler, J. Papapolymerou, and M. Mitchell, “A Silicon–

germanium receiver for X-band transmit/receive radar modules," *IEEE J. Solid-State Circuits*, vol. 43, no. 9, pp. 1889-1896, Sep. 2008.

[49] Y. A. Atesa, Berke Cetinoneri, K. Koh and G. M. Rebeiz, "X/Ku-band 8-element phased arrays based on single Silicon chips," *IEEE MTT-S Int. Microw. Symp. Dig.,* Anaheim, CA, pp. 1258-1261, May 2010.

[50] D. W. Kang, K.J. Koh and G. M. Rebeiz, "A Ku-band 2-antenna 4-simultaneous beams SiGe BiCMOS phased array receiver," *IEEE Trans. Microw. Theory Tech.*, vol. 58, no. 4, pp. 771-780, Apr. 2010.

[51] T. Yu and G. M. Rebeiz, "A 24 GHz 4-channel phased-array receiver in 0.13 μm CMOS*," IEEE (RFIC) Radio Frequency Integrated Circuits Symp.*, Atlanta, GA, June 2008, pp. 361-364.

[52] T. Yu and G. M. Rebeiz, "A 22-24 GHz Phased Array Receiver with On-Chip Coupling Characterization," *IEEE J. Solid-State Circuits*, vol. 43, no. 9, pp. 2134-2142, Sept. 2008.

[53] D. Shin, C. Y. Kim, D. W. Kang and G. M. Rebeiz, "A high-power packaged four-element X-band phased-array transmitter in 0.13-μm CMOS for radar and communication systems," *IEEE Trans. Microw. Theory Tech.*, vol. 61, no. 8, pp. 3060-3071, Aug. 2013.

[54] K. M. Ho, D. Shin and G. M. Rebeiz, "X-band phased array development on Teflon laminates with CMOS RFIC receivers," *Proc. IEEE Antennas Propag. Symp.*, Spokane, WA, pp. 565-568, Jul. 2011.

[55] D. M. Pozar, "Rigorous closed-form expressions for the surface wave loss of printed antennas," *Electronics Letters*, vol. 26, no. 13, pp. 954-956, Jun. 1990.

[56] D. Shin and G. M. Rebeiz, "Low-power low-noise 0.13 μm CMOS X-band phased array receivers," *IEEE MTT-S Int. Microw. Symp. Dig.,* Anaheim, CA, pp. 956-959, May 2010.

[57] www.amkor.com

[58] D.M. Pozar and D. H. Schaubert, "Scan blindness in infinite phased arrays of printed dipoles," *IEEE Trans. Antennas Propag.*, vol. 32, no. 6, pp. 602-610, Jun. 1984.

[59] D. M. Pozar, *Microwave Engineering*, John Wiley and Sons, Inc., 2012.

[60] J.R. James and A. Henderson, "High-frequency behaviour of microstrip open-circuit terminations," *IEE J. on Microw., Optics and Acoust.*, vol. 3, no. 5, pp. 205-218, Sep. 1979.

[61] R. Garg, P. Bhartia, I. Bahl and A. Ittipiboon, *Microstrip Antenna Design Handbook*, Artech House, 2001.

[62] C.-C. Liu, A. Hessel and J. Shmoys, “Performance of probe-fed microstrip-patch element phased arrays,” *IEEE Trans. Antennas Propag.*, vol. 36, no. 11, pp. 1501-1509, Nov. 1988.

[63] *Copper Foils for High Frequency Materials*, Rogers Corporation, 2011.

[64] A. F. Horn III, J. W. Reynolds, P. A. LaFrance and J. C. Rautio, “Effect of conductor profile on the insertion loss, phase constant, and dispersion in thin high frequency transmission lines,” *DesignCon 2010*, Santa Clara, CA, Feb. 2010.

[65] A. F. Horn III, J. W. Reynolds, and J. C. Rautio, “Conductor profile effects on the propagation constant of microstrip transmission lines,” *IEEE MTT-S Int. Microw. Symp. Dig.*, Anaheim, CA, pp. 868-871, May 2010.

[66] A. F. Horn, P. A. LaFrance, J. W. Reynolds and J. Coonrod, “The influence of test method, conductor profile, and substrate anisotropy on the permittivity values required for accurate modeling of high frequency planar circuits,” *Circuit World*, vol. 38, no. 4, pp. 219-231, Sep. 2012.

[67] N. K. Das, S. M. Voda and D. M. Pozar, “Two methods for the measurement of substrate dielectric constant,” *IEEE Trans. Microw. Theory Tech.*, vol. 35, no. 7, pp. 636-642, Jul. 1987.

[68] E. Hammerstad and O. Jensen, “Accurate models for microstrip computer aided design”, *IEEE MTT-S Int. Microw. Symp. Dig.*, Washington, DC, pp. 407-409, 1980.

[69] *Sonnet User’s Guide*, Release 14, Sonnet Software, Inc., Apr. 2013.

[70] J. C. Rautio, “Recent technology developments in the Sonnet suites of planar electromagnetic analysis software,” *Proc. IEEE Antennas Propag. Symp.*, pp. 2720-2723, Spokane, WA, Jul. 2011.

[71] I. Simon, “Magnetic permeability of nickel in the region of centimeter waves,” *Nature*, vol. 157, no. 3996, pp. 735, Jun 1946.

[72] R. Millership and F. V. Webster, "High frequency permeability of ferromagnetic materials," *Proceedings of the Physical Society. Sect. B*, vol. 63, no. 10, pp. 783 - 795, 1950.

[73] S. Lucyszyn, “Microwave characterization of nickel,” *PIERS Online*, vol. 4, no. 6, pp. 686-690, 2008.

[74] O. Inac, D. Shin and G. M. Rebeiz, “A phased array RFIC with built-in self-test capabilities,” *IEEE Trans. Microw. Theory Tech.*, vol. 60, no. 1, pp. 139-148, Jan. 2012.

[75] J. Huang, “A technique for an array to generate circular polarization with linearly polarized elements,” *IEEE Trans. Antennas Propag.*, vol. 34, no. 9, pp. 1113-1124, Sep. 1986.

[76] P. S. Hall, J. S. Jahele and J. R. James, “Sequentially rotated array consisting of higher order mode antenna elements,” *IEE Proc. H Microw., Antennas and Propag.*, vol. 135, no. 5, pp. 381-389, Oct. 1989.

[77] P. S. Hall, “Applications of sequential feeding to wide bandwidth, circularly polarized microstrip patch arrays,” *IEE Proc. H Microw., Antennas and Propag.*, vol. 136, no. 5, pp. 390-398, Oct. 1989.

[78] P. S. Hall, “Sequentially rotated arrays with reduced sidelobes,” *IEE Proc. H Microw., Antennas and Propag.*, vol. 141 no. 4, pp. 321-325, Aug. 1994.

[79] L. L. Shafai, W. A. Chamma, M. Barakat, P. C. Strickland and G. Seguin, “Dual-band dual-polarized perforated microstrip antennas for SAR applications,” *IEEE Trans. Antennas Propag.*, vol. 48, no. 1, pp. 58-66, Jan. 2000.

[80] S. Hsu, Y. Ren and K. Chang, “A dual-polarized planar-array antenna for S-band and X-band airborne applications,” *IEEE Antennas Propagat. Mag.*, vol. 51, no. 4, pp. 70-78, Aug. 2009.

[81] Y. A. Atesal, B. Cetinoneri, K. M. Ho and G. M. Rebeiz, “A two-channel 8-20 GHz SiGe BiCMOS receiver with selectable IFs for multibeam phased-array digital beamforming applications,” *IEEE Trans. Microw. Theory Techn.*, vol. 59, no. 3, pp. 716-726, Mar. 2011.

[82] S. D. Targonski, R. B. Waterhouse and D. M. Pozar, “Design of wide-band aperture-stacked patch microstrip antennas,” *IEEE Antennas Propagat. Mag.*, vol. 46, no. 9, pp. 1245-1251, Sep. 1998.

[83] R. B. Waterhouse, “Design of probe-fed stacked patches,” *IEEE Trans. Antennas Propag.*, vol. 47, no. 12, pp. 1780-1784, Dec. 1999.

[84] S. S. Holland and M. N. Vouvakis, “The planar ultrawideband modular antenna (PUMA) array,” *IEEE Trans. Antennas Propag.*, vol. 48, no. 1, pp. 130-140, Jan. 2000.

[85] S. A. Long and W. D. Walton, “A dual-frequency stacked microstrip circular disk antenna,” *IEEE Trans. Antennas Propag.*, vol. 27, no. 2, pp. 270-273, Mar. 1979.

[86] M. Dishal, "Alignment and Adjustment of Synchronously Tuned Multiple-Resonant-Circuit Filters," *Proc. IRE*, vol. 39, no. 11, pp. 1448-1455, Nov. 1951.

[87] I.-H. Lin, M. DeVincentis, C. Caloz anf T. Itoh, “Arbitrary dual-band components using composite right/left-handed transmission lines,” *IEEE Trans. Microw. Theory Tech.*, vol. 52, no. 4, pp. 1142-1149, Apr. 2004.

[88] P.-L. Chi and T. Itoh, “Mininaturized dual-band directional couplers using composite right/left-handed transmission structures and their applications in beam pattern diversity systems,” *IEEE Trans. Microw. Theory Tech.*, vol. 57, no. 5, pp. 1207-1215, May. 2009.

[89] H. Kim, B. Lee, M.Park, “Dual-band branch-line coupler with port extensions,” *IEEE Trans. Microw. Theory Tech.*, vol. 58, no. 3, pp. 651-655, Mar. 2010.

[90] M.Park and B. Lee, “Dual-band cross-coupled branch-line couplers,” *IEEE Microw. Wireless Compon. Lett.*, vol. 15, no. 10, pp. 655-657, Mar. 2010.

[91] “Stripline test for permittivity and loss tangent (dielectric constant and dissipation factor) at X-band,” *IPC-TM-650 Test Methods Manual*, IPC, Bannockburn, IL.

[92] J. C. Rautio and S. Arvas, “Measurement of planar substrate uniaxial anisotropy,” *IEEE Trans. Microw. Theory Tech.*, vol. 57, no. 10, pp. 2456-2463, Oct. 2009.

[93] J. C. Rautio, R.L. Carlson, B. J. Rautio, and S. Arvas, “Shielded dual mode microstrip resonator measurement of uniaxial anisotropy," *IEEE Trans. Microw. Theory Tech.*, vol. 59, no. 3, pp. 748-754, Mar. 2010.

[94] MWI-2013 Transmission Line Modeling Software, rev. 1.2, Rogers Corporation, Rogers, CT, 2014.